ANALYSIS AND PERFORMANCE ENHANCEMENT OF SOLAR PHOTOVOLTAIC SYSTEMS UNDER SUB-OPTIMAL OPERATING CONDITIONS

A Thesis Submitted
In Partial Fulfillment of the Requirements
for the Degree of

DOCTOR OF PHILOSOPHY

by

RANJEET SINGH

(Roll No. 2K20/PHDEE/502)

Under the Supervision of

Prof. Vinod Kumar Yadav and Prof. Madhusudan Singh
Department of Electrical Engineering
Delhi Technological University, Delhi - 110042



Department of Electrical Engineering

DELHI TECHNOLOGICAL UNIVERSITY
(Formerly Delhi College of Engineering)
Shahbad Daulatpur, Main Bawana Road, Delhi - 110042. INDIA

December, 2024

©DELHI TECHNOLOGICAL UNIVERSITY, DELHI-2024
ALL RIGHTS RESERVED



DELHI TECHNOLOGICAL UNIVERSITY

(Formerly Delhi College of Engineering)
Shahbad Daulatpur, Main Bawana Road, Delhi-42

CANDIDATE'S DECLARATION

I hereby certify that the work which is being presented in the thesis entitled **ANALYSIS AND PERFORMANCE ENHANCEMENT OF SOLAR PHOTOVOLTAIC SYSTEMS UNDER SUB-OPTIMAL OPERATING CONDITIONS** in partial fulfillment of the requirements for the award of the Degree of Doctor of Philosophy and submitted in the Department of Electrical Engineering of the Delhi Technological University is an authentic record of my own work carried out during the period from January, 2021 to December, 2024 under the supervision of Dr. Vinod Kumar Yadav, Professor, Department of Electrical Engineering and Prof. Madhusudan Singh, Registrar, Delhi Technological University.

The matter presented in this thesis has not been submitted by me for the award of any other degree of this or any other Institute.

(Ranjeet Singh)

This is to certify that the student has incorporated all the corrections suggested by the examiners in the thesis and the statement made by the candidate is correct to the best of our knowledge.

Signature of Supervisors

Signature of External Examiner

DELHI TECHNOLOGICAL UNIVERSITY

(Formerly Delhi College of Engineering)
Shahbad Daulatpur, Main Bawana Road, Delhi-42

CERTIFICATE BY THE SUPERVISORS

Certify that **Ranjeet Singh** (2K20/PHDEE/502) has carried out their work presented in this thesis entitled "**ANALYSIS AND PERFORMANCE ENHANCEMENT OF SOLAR PHOTOVOLTAIC SYSTEMS UNDER SUB-OPTIMAL OPERATING CONDITIONS**" for the award of **Doctor of Philosophy** from Department of Electrical Engineering, Delhi Technological University, Delhi, under our supervision. The thesis embodies results of original work, and studies are carried out by the student himself and the content of the thesis do not form the basis for the award of any other degree to the candidate or to anybody else from this or any other University/Institute.

(Vinod Kumar Yadav)
Supervisor

(Madhusudan Singh)
Co-Supervisor

Date:

Abstract

The increasing reliance on solar energy as a sustainable and renewable power source has led to significant advancements in photovoltaic (PV) technology. However, the efficiency and reliability of PV systems remain challenged by factors such as irradiance mismatch, shading, and temperature variations, which can lead to power losses, reduced system lifespan, and potential safety risks like hot spot (HS) formation. These challenges have spurred the development of innovative solutions to optimize PV array performance, particularly under sub-optimal (non-ideal) conditions.

This thesis presents several novel strategies to mitigate the adverse effects of irradiance mismatch on PV systems. The key contributions include the development of the hot spot mitigation circuit (HSMC), innovative module rearrangement techniques such as the generalized module repositioning approach (GMRA), series-parallel generalized module repositioning approach (SP-GMRA), generalized panel rearrangement strategy (GPRS), series-parallel generalized panel rearrangement strategy (SP-GPRS), and the cross-diagonal module rearrangement approach (CDMRA). Additionally, advanced methods to reduce wiring complexity and minimize mismatch losses (MLs) are proposed. By addressing both performance and safety concerns in PV arrays, these techniques significantly enhance the efficiency and reliability of PV systems, contributing to more sustainable energy production.

This doctoral research focuses on enhancing the performance and reliability of PV systems under irradiance mismatch conditions (IMCs), which often lead to reduced power output and potential safety concerns such as HS formation. The work introduces a variety of innovative strategies to mitigate these challenges, specifically through the development of advanced reconfiguration techniques and optimized circuit designs. A novel HSMC is proposed to effectively address HS formation and ML, improving the overall reliability of PV arrays under shaded conditions. Experimental results show that the HSMC outperforms conventional

bypass diodes (BPDs), reducing MLs by up to 89.82%, demonstrating significant improvements in power output and safety.

Further, a static optimal shade dispersion (SD) strategy is introduced alongside the GMRA, designed to uniformly distribute shading across PV arrays. This method is extended to a variant called SP-GMRA, specifically tailored for series-parallel (SP) PV configurations. Both approaches are validated through simulation and hardware experiments, with the GMRA and SP-GMRA demonstrating a substantial reduction in MLs, with up to 76.3% and 27% lower ML, respectively, compared to traditional configurations. In addition to these reconfiguration techniques, a comprehensive shade-resilient approach utilizing the GPRS and SP-GPRS is proposed for enhancing the productivity of PV arrays under varying shading scenarios. Performance evaluations conducted on both simulation platforms and experimental hardware configurations show up to 75.4% reduction in MLs and up to 31% improvement in power generation for total-cross-tied (TCT) PV arrays and up to 16.1% improvement for SP arrays.

The research also introduces the CDMRA, a versatile technique applicable to PV arrays of any size and structure. This approach optimizes module positioning to minimize shading impacts without disrupting the wiring system, offering a significant reduction in mismatch power loss (MPL), improved system efficiency (SE), and enhanced power boost (PB) across multiple irradiance mismatch scenarios irradiance mismatch scenarios (IMSs). To address wiring complexity in conventional TCT configurations, a modified PV arrangement (MPVA) is proposed, which reduces cross-ties by 59.37% and improves overall system performance by minimizing wiring requirements. The progressive module shift rearrangement approach (PMSRA) is introduced as a static shade mitigation technique, applicable to TCT, SP, and MPVA configurations, achieving up to 86% reduction in mismatch loss compared to conventional TCT arrays.

Finally, a dual-stage three-phase grid-interfaced solar photovoltaic power generation (SPPG) system is presented, integrated with a self tuning filter (STF) to optimize the control of voltage source converters (VSCs). This system is designed to enhance power quality (PQ) by addressing issues such as harmonic rejection and power factor correction, demonstrating superior performance compared to existing classical and adaptive control techniques.

Acknowledgements

First and foremost, my gratitude and appreciation must go to my respected advisors Professor Vinod Kumar Yadav and Professor Madhusudan Singh, Department of Electrical Engineering, Delhi Technological University, Delhi, for their invaluable support and guidance during the course of my PhD studies. I consider this as the highest degree of privilege to have completed my studies under their supervisions.

I owe my deepest gratitude to my PhD research committee for their valuable comments and inputs: Dr. Shilpa Pal, Professor, Department of Civil Engineering, Delhi Technological University, Professor M. Rizwan from the Department of Electrical Engineering, Delhi Technological University.

I would like to express my deepest gratitude to my wife Priyanka Bisht and my family members for their love and patience which kept me going on this journey. Their faith and unconditional love towards me are the reason for whatever I have achieved in my life. Without my friends in and out of DTU Delhi, life would have been dull. I am indebted to all of them for their support, valuable input, and constant encouragement.

Finally, I thank God Almighty for giving me strength at all times.

Date: Ranjeet Singh

Contents

Abstract iv
Acknowledgements vi
Contents vii
List of Figures xii
List of Tables xix

List of Abbreviations xxi

List of Symbols xxiv

1 Introduction 1
1.1 Background 1
1.2 Literature Review 3
1.2.1 Literature Survey on Hot Spot Mitigation Approaches for PV Modules 4
1.2.2 Literature Survey on Shade Dispersion Techniques for PV Arrays 11
1.2.2.1 Dynamic Reconfiguration Approaches 11
1.2.2.2 Static Reconfiguration Approaches 14
1.2.3 Literature Survey on PV Array Configurations 20
1.2.4 Literature Survey on Grid-Integrated Solar PV Systems 24
1.3 Research Gaps 29
1.4 Research Objectives 29
1.5 Structure of the Thesis 30

2 Improved Hot Spot Alleviation Approach for Mismatched PV Modules 32
2.1 Preamble 32
2.2 PV Response Analysis Under Non-Ideal Conditions 33

2.2.1 Analysis of Power Loss in a Shaded Cell Exhibiting HS Behavior 34
2.2.2 Reverse Voltage Across a Shaded Cell: Mathematical Analysis 36
2.3 Proposed Hot Spot Mitigation Circuit and Experimental Setup 40
2.3.1 Proposed Hot Spot Mitigation Circuit Topology 40
2.3.2 Experimental Setup 43
2.4 Results and Discussion 45
2.4.1 Experimental Measurements (Electrical Characteristics, Dynamic Response, and Power Loss Estimation) 45
2.4.1.1 Electrical Characteristics 46
2.4.1.2 Dynamic Response Analysis of the PV System 49
2.4.1.3 Estimation of Power Loss (3× 1 PV String) 52
2.4.2 Thermographic Inspection 53
2.4.2.1 Thermal response on 3×1 PV String 53
2.4.2.2 Thermal response on 3×3 PV Array 55
2.5 Summary 57

3 Optimal Shade Dispersion Strategies for Enhanced Power Extraction Under PSCs 58
3.1 Preamble 58
3.2 Electrical characteristics of a PV Array 59
3.2.1 Steady Irradiance Conditions 60
3.2.2 Partial Shading Conditions 61
3.2.3 Estimation of Mismatch Loss for Optimal Shade Dispersion 61
3.3 Description of PV Array Configurations 63
3.3.1 PV Array in TCT Configuration 63
3.3.2 Proposed GMRA and SP-GMRA for Optimal Shade Dispersion 65
3.3.3 Proposed GPRS and SP-GPRS Module Rearrangement Strategy 68
3.3.4 Proposed Cross-Diagonal Module Rearrangement Approach (CDMRA) 72
3.3.5 Simulation and Performance Analysis of the Proposed GMRA and SP-GMRA Technique 75

3.3.6 Hardware Implementation of the proposed GMRA and SP-GMRA Technique 80
3.3.7 Simulation and Performance Analysis of the Proposed GPRS and SP-GPRS Reconfiguration Method 83
3.3.7.1 Performance Metrics 85
3.3.8 Hardware Implementation of the proposed GPRS and SP-GPRS Technique 90
3.3.9 Simulation and Performance Analysis of the Proposed CDMRA Technique 93
3.3.9.1 Performance Metrics 96
3.4 Efficiency Computations and Techno-Economic Feasibility Study 102
3.4.1 Calculation of Efficiency 102
3.4.2 Techno-Economic Analysis 103
3.4.2.1 Techno-Economic Assessment of various Reconfiguration Schemes with the Proposed GMRA and SP-GMRA 104
3.4.2.2 Techno-Economic Assessment of various Reconfiguration Schemes with the Proposed GPRS and SP-GPRS 105
3.5 Summary 105

4 Topological Modifications to the Existing PV Array Configurations 110
4.1 Preamble 110
4.2 Analysis of PV Array Response Under IMSs 111
4.2.1 Scenario I and scenario II shading 112
4.2.2 Short narrow (SN) and distributed SN shading 114
4.3 Different PV Array Configurations 115
4.3.1 TCT configured PV Array 116
4.3.2 B-L Configured PV Array 116
4.3.3 H-C Configured PV Array 118
4.3.4 Proposed MPVA PV Array 118
4.3.4.1 Criteria for Selection of Cross-ties 118
4.3.4.2 Motivation and Novelty 123
4.3.4.3 Wiring structure of the Proposed MPVA 123

4.4 Progressive Module Shift Rearrangement Approach (PMSRA) 125
4.5 Simulation Analysis and Experimental Validation 129
4.5.1 Simulation Results and Performance Analysis 129
4.5.1.1 Description of IMSs and Performance Analysis 134
4.5.1.2 Performance Metrics 141
4.5.2 Experimental Implementation 144
4.5.2.1 5×5 PV Setup 145
4.5.2.2 6×4 PV Setup 152
4.6 Summary 159

5 Modeling and Investigation of the Solar PV System Performance Under Sub-Optimal Operating Conditions 161
5.1 Preamble 161
5.2 Design of the Grid Integrated System 162
5.3 Control Scheme 165
5.3.1 MPOP Tracking Control 165
5.3.2 Grid-Tied VSC Control 166
5.3.2.1 STF Module Description 166
5.3.2.2 PCC Amplitude and Unit-Template Estimation(V^*, x_{pa}, x_{pb}, x_{pc}) 168
5.3.2.3 Estimation of Active Loss Component 169
5.3.2.4 Estimation of the Fundamental Active Load Current Component 169
5.3.2.5 Reference Grid Current Extraction 169
5.4 Results and Discussion 170
5.4.1 Performance Analysis under Balanced Non-Linear Load with SPPG system subjected to Uniform Insolation 170
5.4.2 Performance Analysis under Balanced Linear Load with SPPG system subjected to Non- Uniform Insolation 170
5.4.3 Performance Analysis under Unbalanced Non-Linear Load with SPV system subjected to Uniform Insolation 173
5.4.4 Comparative Performance Analysis of Proposed STF Assisted Control Scheme with Popular Conventional and Adaptive Control Schemes 173

5.5 Summary 175

6 Conclusions and Future Scopes 178
6.1 Conclusions 178
6.2 Contributions 179
6.3 Future Scopes 181

Bibliography 182

List of Publications 201

List of Figures

1.1 (a) Causes, consequences, and mitigation strategies of PSCs. (b) PV string under the impact of PSC. (c) Electrical characteristics of the PV string as a function of the number of shaded modules. (d) Electrical characteristics of the same PV string as a function of the intensity of shading on modules. 3

2.1 (a) Typical response of PV cells under PSC. (b) Experimental arrangement to examine reverse characteristics. (c) Rear view of the disintegrated module. (d) Measured power loss, P_{loss} of a completely shaded cell (cell '1'). (e) Thermographic behavior of the test module under normal condition. (f) Test module exhibiting HS condition under reverse bias. 35

2.2 PV string behavior under mismatch condition. 37

2.3 Proposed HSMC: Operation mechanism under (a) mode I: NC. (b) mode II: PSC. (c) Circuit arrangement. 40

2.4 (a) Hardware prototype for experimental validation. (b) Experimental test setup for selecting appropriate switches for HSMC. 42

2.5 Characteristics of different switches investigated for the proposed HSMC: (a) Drain-source ON-state resistance versus gate-source voltage. (b) Gate-to-source versus drain current characteristics. 42

2.6 Flow chart summarizing the various stages of the conventional and the proposed HS mitigation approach. 43

2.7 Experimental setup (3×1 PV String) for assessing the thermal reliability of the module under PSC. 44

2.8 Experimental setup (3×3 PV Array) for assessing the thermal reliability of the module under PSC. 45

2.9 Measured electrical characteristics of a 3×1 PV String: (a) P-V curves. (b) I-V curves. 46
2.10 Measured electrical characteristics of a 3×3 SP PV array: (a) P-V curves. (b) I-V curves. 47
2.11 Measured voltage versus bypass path current for: (a) 3 × 1 PV String. (b) 3 × 3 SP PV array. 47
2.12 (a) Experimental arrangement of (50 W module) PV string to examine the thermographic behavior under 1 cell shading (b) Thermographic response under 1 cell shading (c) Simulated reverse voltage charchteristics of a PV cell of the test module (d) BPD current versus string voltage under 1 cell and 2 cell shading for different rating modules. 48
2.13 Experimental waveforms showing PV system dynamic response: (a) 3 × 1 PV string (b) 3 × 3 SP PV array. 50
2.14 Power loss estimation under different shading cases for the conventional BPD circuit and the proposed HSMC. 51
2.15 Thermographic analysis (near MPOP) of the shaded module of two 3 × 1 PV strings under consideration under NC (unshaded) condition for (a) String 1, Panel 2 (HSMC). (b) String 2, Panel 2 (BPD). 53
2.16 Thermographic analysis (near MPOP) of the shaded module of two 3 × 1 PV strings under consideration: (a) One cell shaded (with HSMC). (b) One cell shaded (with BPD): No bypass. 54
2.17 Thermographic analysis (near MPOP) of the shaded module of two 3 × 1 PV strings under consideration: (a) Two cells shaded (with HSMC) (b)Two cells shaded (with BPD). 55
2.18 Thermographic behavior (near MPOP) of the shaded module of 3 × 3 SP PV array under one cell shading with (a) BPD. (b) HSMC. 56

3.1 PV source: (a) Electrical circuit model of a PV cell. (b) PV electrical characteristics under SIC and PSCs (multiple peak generation). 61
3.2 (a) 4×4 TCT under a typical 2×2 PSC. (b) Optimal SD through a repositioning approach. (c) ML as a function of SR prior and post application of SD approach. 62

3.3 Representations of the PV array used in this work: (a) Form-I. (b) Form-II. 64
3.4 Illustration showing PV array restructuring using the proposed GMRA technique. 65
3.5 Reconfigured PV array using the proposed GMRA: (a) 9×9 PV array (symmetrical) (b) 6×4 PV array (unsymmetrical). 67
3.6 (a) $i \times j$ PV array connected in TCT configuration. (b) GMRA with the fixed electrical connection of PV modules for a 5×5 PV array. 68
3.7 Illustration showing PV array restructuring using the proposed GPRS approach. 69
3.8 Proposed GPRS reconfigured PV arrays. (a) 9×9 PV array [symmetrical array structure, $(p = q)$]. (b) 6×4 PV array [unsymmetrical structure, $(p \neq q)$]. 69
3.9 Circuit diagram. (a) TCT configuration. (b) Proposed GPRS arrangement for a 5×5 PV array. 70
3.10 Detailed flowchart of the proposed GPRS and SP-GPRS approach. 71
3.11 The complete layout of the proposed CDMRA technique implemented for a 9×9 structure. 72
3.12 Flowchart of the proposed CDMRA technique. 74
3.13 SD performance on a 9×9 PV array under (a) BRC shading scenario, (b) TRC shading scenario, (c) TLC shading scenario, (d) BLC shading scenario with (i) TCT arrangement, (ii) CMAP arrangement, (iii) PRS arrangement, (iv) TTSA arrangement, and (v) proposed GMRA. 75
3.14 Simulated P-V characteristics of 9×9 PV array under different shading scenarios: (a) BRC. (b) TRC. (c) TLC. (d) BLC. 76
3.15 Experimental prototype (5×5 PV array) for hardware validation of the performance of the proposed technique under different shading cases (a) BRC, (b) TRC, (c) TLC, and (d) BLC with "intense" and "moderate" shading profiles. 80
3.16 Experimental P-V characteristics of 5×5 PV array for different shading scenarios (a) BRC shading scenario. (b) TRC shading scenario. (c) TLC shading scenario. (d) BLC shading scenario. 81

3.17 Experimental P-V characteristics of 6×4 PV array for different shading scenarios (a) BRC shading scenario. (b) TRC shading scenario. (c) TLC shading scenario. (d) BLC shading scenario. 82
3.18 Comparative shade dispersion ability of a 9×9 PV array under (a) LRC shading scheme, (b) URC shading scheme, (c) ULC shading scheme, and (d) LLC shading scheme using (i) TCT configuration, (ii) OPSUD configuration, (iii) PRS configuration, (iv) CMAP configuration, and (v) proposed GPRS configuration. 83
3.19 Simulated power (current) versus voltage response of a 9×9 PV array under different shading schemes: (a) LRC. (b) URC. 84
3.20 Simulated power (current) versus voltage response of a 9×9 PV array under different shading schemes: (a) ULC. (b) LLC. 85
3.21 Physical prototype (5×5 and 6×4 PV arrays) subjected to different IMCs (a) LRC. (b) URC. (c) ULC. (d) LLC. 90
3.22 Experimental power-voltage curves (5×5 PV topology) subject to different IMCs. (a) LRC. (b) URC. (c) ULC. (d) LLC. 91
3.23 Experimental power-voltage curves (6×4 PV topology) subject to different IMCs. (a) LRC. (b) URC. (c) ULC. (d) LLC. 92
3.24 Shade attenuation performance under Type-I shading scenario with (a) TCT. (b) CBM. (c) SUD. (d) OPSUD. (e) CBGM. (f) proposed CDMRA. 94
3.25 Shade attenuation performance under Type-II shading scenario with (a) TCT. (b) CBM. (c) SUD. (d) OPSUD. (e) CBGM. (f) proposed CDMRA. 95
3.26 Shade attenuation performance under Type-III shading scenario with (a) TCT. (b) CBM. (c) SUD. (d) OPSUD. (e) CBGM. (f) proposed CDMRA. 96
3.27 Shade attenuation performance under Type-IV shading scenario with (a) TCT. (b) CBM. (c) SUD. (d) OPSUD. (e) CBGM. (f) proposed CDMRA. 97
3.28 Extracted P-V profiles (Simulation) for different PV rearrangement techniques under (a) Type-I shading. (b) Type-II shading. (c) Type-III shading. (d) Type-IV shading. 98

3.29 Shade tolerant performance evaluation of a 9×9 PV arrangement using TCT and the proposed CDMRA technique under (i) Type-I, (ii) Type-II, (iii) Type-III, (iv) Type-IV shading cases: (a) TCT. (b) shade dispersal using the proposed CDMRA. (c) RCD with TCT. (d) RCD with the proposed CDMRA. 99
3.30 Performance indices (PB (%), MPL (%), and SE (%)) for various PV configurations under considered IISs (a) Type-I. (b) Type-II. (c) Type-III. (d) Type-IV cases. 100
3.31 Radar chart representation of FF, ER, and RCDM parameters for different PV configurations under different shading cases: (a) Type-I. (b) Type-II. (c) Type-III. (d) Type-IV. 101
3.32 Comparative efficiency yield of various PV configurations for a 9×9 PV array under different PSCs. 103

4.1 A 4×4 TCT PV array under various IMSs: (a) Scenario I: progressively increasing row shading. (b) Scenario II: progressively increasing column shading. (c) short narrow (SN) shading. (d) distributed SN shading. 113
4.2 A 4×4 TCT PV array under various IMSs: (a) response under scenario I shading. (b) response under scenario II shading. (c) voltage variation of various rows of PV array in response to load variation with time for SN shading. (d) distributed SN shading. 114
4.3 9×9 PV array arrangements: (a) TCT configuration (64 cross-ties). (b) SP configuration (0 cross ties). (c) B-L configuration (32 cross-ties). (d) H-C configuration (32 cross ties). 117
4.4 2×2 PV array: (a) Test Scenario I. (b) Test Scenario II. (c) Test Scenario III. (d) Test Scenario IV. 119
4.5 2×2 PV array: (a) Test Scenario V. (b) Test Scenario VI. (c) Test Scenario VII. (d) Comparative assessment of the necessity of cross tie under different scenarios. 121
4.6 9×9 PV array: (i) different IMSs. (ii) SD using the proposed PMSRA. (iii) distribution of cross-ties for: (a) IMS-I. (b) IMS-II. (c) IMS-III. (d) IMS-IV. 122

4.7 9 × 9 PV configuration for (a) benchmark TCT (64 cross ties). (b) proposed MPVA (26 cross ties). 124
4.8 Layout of the proposed PMSRA rearrangement strategy for a 9 × 9 PV array: (a) Master column identification/ array division into sections. (b) 'primary columns' identification and shift operations. (c) 'secondary columns' identification. (d) remaining shift operations and final reconfigured PV array. 126
4.9 The complete flow diagram of the proposed approach depicting various operational steps. 127
4.10 Wired connection layout of 9 × 9 PV arrangement for (a) TCT configuration (64 cross-ties). (b) proposed PMSRA (26 cross ties). 128
4.11 IMS-I- Lower right corner shading (LRCS) on 9 × 9 PV array: Shade distribution performance with (a) TCT. (b) PRS. (c) CMAP. (d) ACMS. (e) DS. (f) proposed PMSRA. (g) P-V characteristics. (h) I-V characteristics. (i) minimum and maximum row currents generated. 135
4.12 IMS-II-Upper right corner shading (URCS) on 9 × 9 PV array: Shade distribution performance with (a) TCT. (b) PRS. (c) CMAP. (d) ACMS. (e) DS. (f) proposed PMSRA. (g) P-V characteristics. (h) I-V characteristics. (i) minimum and maximum row currents generated. 136
4.13 IMS-III-Upper left corner shading (ULCS) on 9×9 PV array: Shade distribution performance with (a) TCT. (b) PRS. (c) CMAP. (d) ACMS. (e) DS. (f) proposed PMSRA. (g) P-V characteristics. (h) I-V characteristics. (i) minimum and maximum row currents generated. 138
4.14 IMS-IV-Lower left corner shading (LLCS) on 9×9 PV array: Shade distribution performance with (a) TCT. (b) PRS. (c) CMAP. (d) ACMS. (e) DS. (f) proposed PMSRA. (g) P-V characteristics. (h) I-V characteristics. (i) minimum and maximum row currents generated. 140
4.15 FF and ER attained values for various considered PV arrangements under different IMSs (a) LRCS. (b) URCS. (c) ULCS. (d) LLCS. 142
4.16 Performance analysis of various PV setups based on key performance metrics (EFF (%), PE (%), and ML (%)) under various IMSs (a) LRCS. (b) URCS. (c) ULCS. (d) LLCS. 143

4.17 Hardware prototype for experimental validation configured in 5 × 5 arrangement (IMS-II). 145
4.18 5 × 5 PV arrangement: (a) TCT configuration (16 cross-ties). (b) proposed MPVA (10 cross-ties). (c) proposed PMSRA with marked terminal connections. 146
4.19 Experimental voltage versus power curves for different PV configurations (5 × 5 PV configuration) under different irradiance mismatch conditions (a) IMS-I: LRCS. (b) IMS-II: URCS. (c) IMS-III: ULCS. (d) IMS-IV. 147
4.20 Shade distribution performance of 5 × 5 PV array with (i) TCT, (ii) TT, (iii) DS, (iv) IMT, (v) proposed PMSRA, under (a) IMS-I. (b) IMS-II. (c) IMS-III. (d) IMS-IV. 148
4.21 6 × 4 PV arrangement: (a) TCT configuration (15 cross-ties). (b) proposed MPVA (3 cross-ties). (c) proposed PMSRA with marked terminal connections. 152
4.22 Experimental voltage versus power curves for different PV configurations (6 × 4 PV array) under different shading scenarios (a) IMS-I: LRCS. (b) IMS-II: URCS. (c) IMS-III: ULCS. (d) IMS-IV. 153
4.23 Shade distribution performance of 6 × 4 PV array with (i) TCT, (ii) CKM, (iii) OEP, (iv) COL, (v) proposed PMSRA, under (a) IMS-I. (b) IMS-II. (c) IMS-III. (d) IMS-IV. 156

5.1 Schematic representation of grid-tied SPPG system. 163
5.2 STF assisted control architecture for SPPG system. 166
5.3 Block module representation of STF. 167
5.4 Bode plot representation of STF for G = 100. 168
5.5 Performance with balanced non-linear load under uniform insolation. 171
5.6 Performance with balanced linear load subjected to variable insolation. 172
5.7 Dynamic performance with unbalanced non-linear load subjected to uniform insolation. 174

List of Tables

2.1 Specifications of the Experimental Platform 39
2.2 Parameters of the 3×1 PV String Under All Operating Conditions (Close to Open Circuit) 51
2.3 Parameters of the 3×3 SP PV array Under All Operating Conditions (Close to MPOP) 52
2.4 Response of the conventional BPD and the proposed HSMC to one cell shading scenario (3×3 SP PV array) 56

3.1 Parametric data of a PV module at STC used in this work 64
3.2 Comparative Performance Analysis of the Proposed Technique with the Existing State of the Art Reconfiguration Approaches 77
3.3 Assessment of the proposed GPRS and SP-GPRS techniques against current benchmark reconfiguration methods 87
3.4 Parametric Data of PV module Used in the Simulation Analysis 93
3.5 Efficiency of 9×9 PV Array Under Different Shading Scenarios 107
3.6 Hourly Variation in Shading Patterns for Techno-Economic Analysis 108
3.7 Energy Yield Analysis for Various Reconfiguration Methods 109

4.1 Technical Specifications of PV Module Used in Simulation and Experiments 129
4.2 Analytical Computations of Current, Voltage, and Power Attained for CMAP, PRS 130
4.3 Analytical Computations of Current, Voltage, and Power Attained for ACMS, PMSRA 132
4.4 A Comparative Assessment of Different PV Configurations on 5×5 Hardware Prototype 150

4.5 A Comparative Analysis of Performance Metrics across Different PV Configurations for all Shading Scenarios Using 5×5 Hardware Prototype 151
4.6 A Comparative Assessment of Different PV Configurations on 6×4 Hardware Prototype 157
4.7 A Comparative Analysis of Performance Metrics across Different PV Configurations for all Shading Scenarios Using 6×4 Hardware Prototype. 158
4.8 A Quantitative Comparison of the Attained Performance Metrics Between Simulations and Experiments 160

5.1 THD Computations Under Non-Linear Load 175

List of Abbreviations

ACMS	Ancient Chinese Magic Square
B-L	Bridge-Link
BLC	Bottom Left Corner
BOA	Butterfly Optimization Algorithm
BPDs	Bypass Diodes
BRC	Bottom Right Corner
CBGT	Chess Board Game Methodology
CBS	Cool Bypass Switch
CDMRA	Cross-Diagonal Module Rearrangement Approach
CKM	Chess Knight Movement
CMAP	Chaos Map
COL	Column Index
D-STATCOM	Distribution Static Compensator
DOA	Dragaonfly Optimization Algorithm
DS	Dominance Square
DSO	Digital Storage Oscilloscope
EAR	Electronic Array Reconfiguration
ER	Execution Ratio
FAGI	Frequency Adaptive Generalized Integral
FF	Fill Factor
FUT	Futoshiki
GA	Genetic Algorithm

GMPP	Global Maximum Power Point
GMRA	Generalized Module Rearrangement Approach
GPRS	Generalized Panel Rearrangement Strategy
H-C	Honey-Comb
HS	Hot Spot
HSMC	Hot Spot Mitigation Circuit
I-V	Current-Voltage
IGBT	Insulated Gate Bipolar Transistor
IMCs	Irradiance Mismatch Conditions
IMSs	Irradiance Mismatch Scenarios
KKSP	Ken-Ken Square Puzzled
LLC	Lower Left Corner
LMS	Least Mean Square
LRC	Lower Right Corner
LS-TCT	Latin Square Total Cross Tied
ML-FOGI	Multilayer Fourth Order Generalized Integrator
MLs	Mismatch Losses
MOS	Metal Oxide Semiconductor
MOSFET	Metal Oxide Semiconductor Field Effect Transistor
MPL	Mismatch Power Loss
MPOP	Maximum Power Operating Point
MPP	Maximum Power Point
MPPT	Maximum Power Point Tracking
MPVA	Modified PV Arrangement
NCs	Normal Conditions
NSE	Neighborhood Slowest Embedding
O-E	Odd- Even
OEP	Odd-Even-Prime

OPSUD	Optimal SuDoKu
P-V	Power-Voltage
P and O	Perturb and Observe
PB	Power Boost
PCC	Point of Common Coupling
PMSRA	Progressive Module Shift Rearrangement Approach
PQ	Power Quality
PRFCPM	Physical Relocation Fixed Column Positioning of Modules
PRS	Parquet SuDoKu
PS	Partial Shading
PSCs	Partial Shading Conditions
PV	Photovoltaic
RCD	Row Current Difference
RCDM	Row Current Discrepancy Minimization
RTPV	Roof Top Photovoltaics
SD	Shade Dispersion
SE	System Efficiency
SICs	Steady Irradiance Conditions
SOGI	Second Order Generalized Integrator
SP	Series-Parallel
SP-GMRA	Series-Parallel Generalized Module Rearrangement Approach
SP-GPRS	Series-Parallel Generalized Panel Rearrangement Strategy
SPPG	Solar Photovoltaic Power Generation
SPV	Solar Photovoltaic
SR	Shading Ratio
STC	Standard Test Condition

STF	Self Tuning Filter
T-T	Triple-Tied
TCT	Total-Cross-Tied
THD	Total Harmonic Distortion
TLC	Top Left Corner
TRC	Top Right Corner
TT	Tom-Tom
TTSA	Twisted Two Step Arrangement
ULC	Upper Left Corner
URC	Upper Right Corner
VSCs	Voltage Source Converters

List of Symbols

R_{sh}	Shunt resistance of a PV cell,	Ω
R_s	Series resistance of a PV cell,	Ω
P_{loss}	Power loss in a shaded cell,	W
$D_{i,j}$	Forward voltage drop of the module BPD,	V
I_{String}	Total current of PV String,	A
$V_{BV,k}$	Breakdown voltage of the kth PV cell,	V
n_i	Number of series cells forming the module	
$V_{\text{DS},1,i}$	Drain to source voltage across switch Q_1,	V
$V_{\text{DS},2,i}$	Drain to source voltage across switch Q_2,	V
$R_{DS(on)}$	On state resistance of MOSFET,	Ω
V_{GS}	Gate-to-source voltage of MOSFET,	V
V_{DS}	Drain-to-source voltage of MOSFET,	V
I_D	Drain current of MOSFET,	A
I_L	PV module light induced current,	A
I_{rev}	Reverse saturation current of module,	A
k	Ideality factor	
V_{Th}	Thermal voltage of diode equivalent,	V
γ	Temperature-dependent constant of the module's current	
α	Shading ratio	
N_s	Total number of series connected PV modules	
N_p	Total number of parallel connected PV modules	
T	Absolute temperature of the p-n junction,	K

β	Shading intensity on modules	
d_{row}	Maximum difference in row currents,	A
I_{sabc}	Grid currents,	A
V_{dc}	DC link voltage,	V
I^*_{ref}	Grid reference currents,	A
V_{sabc}	Voltages at PCC,	V
I_{labc}	Load currents,	A
${i_L}^f{}_\alpha$ and ${i_L}^f{}_\beta$	Quadrature current components,	A
I_{invabc}	Compensator currents,	A
x_{pa}, x_{pb} and x_{pc}	In-phase unit templates	
${v_{sa}}^f, {v_{sb}}^f, {v_{sc}}^f$	Fundamental grid phase voltages,	V
L_f	Smoothening inductor,	mH
$C_{dc-\text{ link}}$	DC link capacitance,	µF
L_{boost}	Boost converter inductor,	mH

Chapter 1

Introduction

This chapter provides an overview of the thesis topics, detailing the research aspects derived from the analysis of solar PV systems under sub-optimal operating conditions and emphasizing the contributions of the thesis.

1.1 Background

As a result of sustained financial investment and persistent advancements in photovoltaic (PV) technology during the preceding years, both commercial and residential PV installations are undergoing significant transformation on a global scale [1]. PV modules are widely acknowledged for their dependability, exhibiting a prospective operational lifespan that exceeds three decades [2]. PV cells frequently face operational issues or partial shade (PS) that hinder module efficiency and diminish overall system performance. A prevalent issue in contemporary PV systems is the emergence of HS in PV cells [3]. The phenomenon was initially identified in satellite power systems during the late 1960s and persists currently, adversely affecting the module's operational lifespan [4]. HS formation adversely affects module and system reliability. The PV panels are generally rated for lower temperatures than those reached during HS events, leading to weakened electrical joints. This weakening can initiate arcs, heightening the risk of fire and significant safety concerns. Commercial PV module manufacturers provide BPDs that facilitate an alternative current pathway when specific cells within a module exhibit diminished current due to partial shading conditions (PSCs).

The global proliferation of PV systems is linked to reduced manufacturing costs of PV cells and advancements in power conversion technology [5, 6]. However, one of the predominant issues faced by PV systems that very often impedes their optimal utilization is PSCs [7]. The efficiency and performance of PV systems are compromised by PSCs (refer Fig. 1.1). PSCs hinder the optimal utilization of PV arrays by causing shading from moving clouds, dust accumulation, and nearby structures, resulting in current mismatches among modules within the same array. Under steady irradiance conditions (SICs), a distinct peak power point enables conventional peak power tracking algorithms to converge at the optimal power extraction point. In contrast, under PSCs, uneven irradiance causes multiple peaks in the power-voltage (P-V) characteristics, leading to MLs. Power extraction from the PV array under PS is influenced by factors such as the shaded area, the positioning of shaded modules, shade patterns, and the array interconnections [8].

Conventional PV array interconnections like SP, honey-comb (H-C), bridge-linked (B-L), and TCT are employed to minimize ML. TCT arrangement enhances response to PSC by limiting ML, thus increasing power output. Nonetheless, TCT experiences nonuniform row current under mismatches, leading to multiple peaks in the power curve and subsequent power loss. The shortcomings of traditional PV configurations necessitate the exploration of novel shade resilient designs for optimal PV power extraction [9, 10]. Reconfiguration schemes based on electronic sensors and switches, known as electronic array reconfiguration (EAR) or dynamic reconfiguration, have been proposed. These schemes dynamically reorganize electrical connections of shade-impacted modules to mitigate shading effects. Although such approaches generally achieve optimal SD, their complexity and cost hinder widespread field application.

Grid integration of solar PV systems poses significant challenges, particularly due to their unpredictability and reliance on battery storage, which increases costs and reduces reliability [11, 12]. While integration mitigates storage issues, it introduces PQ problems, such as harmonic distortions, poor power factor, voltage regulation, and load imbalance, largely due to interactions with power electronic devices [13]. Ensuring compliance with PQ standards requires a robust control scheme for grid-connected VSCs, which act as active shunt compensators

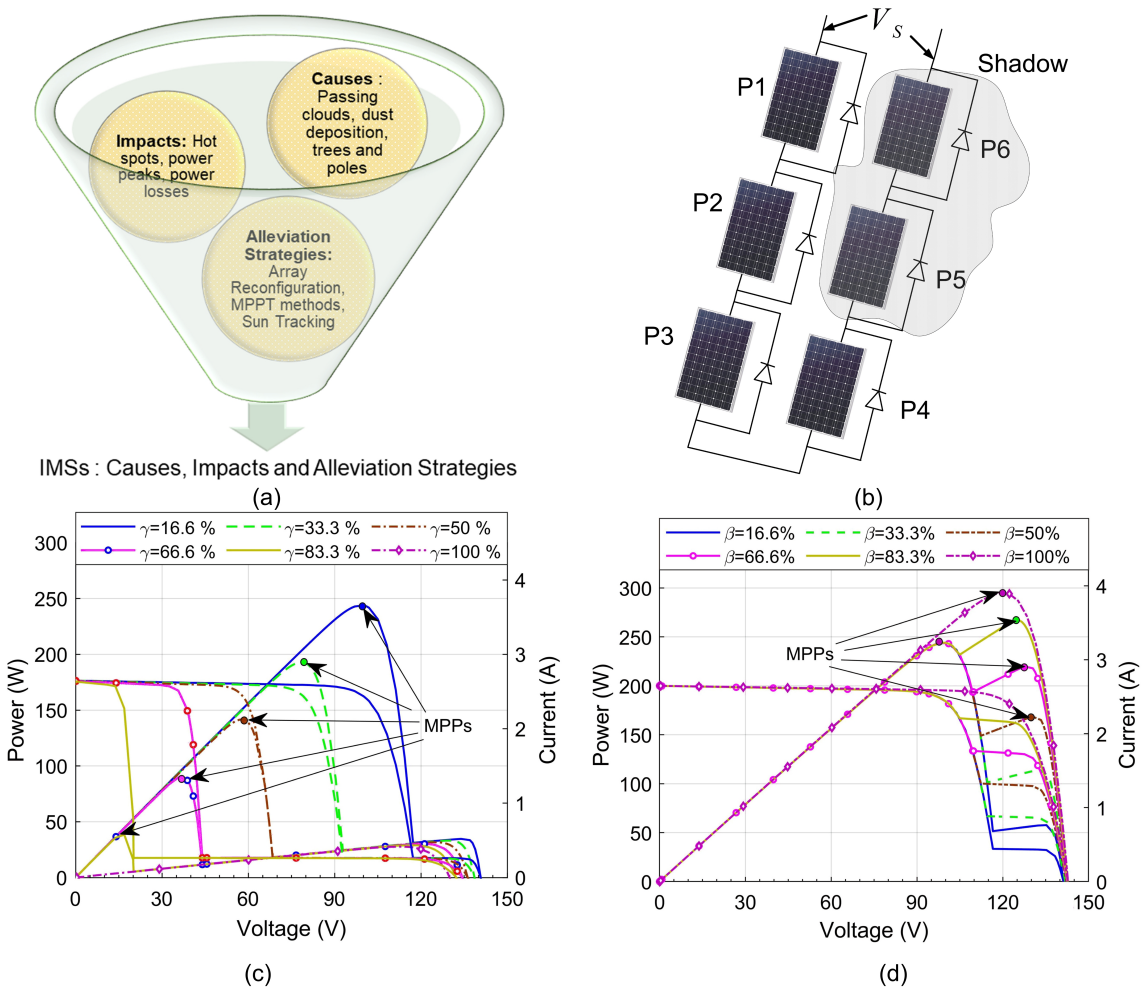

FIGURE 1.1: (a) Causes, consequences, and mitigation strategies of PSCs. (b) PV string under the impact of PSC. (c) Electrical characteristics of the PV string as a function of the number of shaded modules. (d) Electrical characteristics of the same PV string as a function of the intensity of shading on modules.

to address these issues and facilitate seamless integration with the grid [14–17].

1.2 Literature Review

This thesis provides an extensive review of the factors influencing the performance of solar PV systems under mismatch conditions, focusing on shading, temperature variations, and panel degradation. Through a thorough examination of existing research, this work identifies key concepts and

knowledge gaps related to performance analysis in such scenarios. The review explores methodologies previously employed to assess mismatch effects, enabling the selection of suitable approaches for accurate evaluation. Additionally, benchmarking against prior studies ensures that the findings are both valid and contextualized, supporting the development of robust theoretical models to predict PV system behavior under mismatch conditions. Furthermore, this review justifies the research design choices and highlights recent innovations and trends in mismatch mitigation strategies, ensuring that the thesis contributes meaningfully to the advancement of solar energy research.

1.2.1 Literature Survey on Hot Spot Mitigation Approaches for PV Modules

HS mitigation is crucial for enhancing the performance and lifespan of solar PV systems. Numerous approaches have been explored in the literature, focusing on circuit design improvements, shading management, and thermal regulation. This section reviews the key HS mitigation techniques proposed in previous studies. In early studies on HS mitigation, BPDs have been utilized as the sole defensive mechanism against thermal overloads in PV module design, representing a passive protection strategy. Recently, active protection methods have drawn much interest among researchers.

The cool bypass switch (CBS) outperforms standard Schottky diodes in several ways [18]. It dissipates less power, especially at lower temperatures, enhancing PV module efficiency and reliability. Additionally, CBS exhibits significantly lower leakage current under reverse bias, optimizing PV generator performance. Featuring a power metal oxide semiconductor (MOS) driven by a controller, the innovative CBS design effectively bypasses shaded PV cells, reduces overheating, and enhances overall efficiency. Although CBS devices operate at lower temperatures than Schottky diodes, extreme temperatures can still cause damage, increasing maintenance costs and reducing energy efficiency. In reverse bias, CBS devices have lower leakage current than Schottky diodes, but any leakage can still affect the overall PV system efficiency. It was demonstrated in [19] that BPDs are insufficient to fully prevent HS in PV systems, and that active open-circuit protection methods could provide effective

solutions. A new bypass method is presented [20], utilizing a bipolar transistor controlled by MOS transistors, with reliability and efficiency improved under shading conditions. PSPICE simulations and experiments show reduced power dissipation, lower voltage drops, and better power production compared to traditional diode systems. The circuit faces power dissipation issues, especially in MOST A, and risks unexpected bypass activation at low voltages, leading to short circuits. A high-voltage NDMOS is used in the Smart Bypass system to detect and bypass faulty PV cells, ensuring efficiency [21]. A prototype, developed with I3T50 technology, is integrated with storage capacitors, a switch, and a recovery sampling mechanism. Its performance is confirmed through simulations, showing superiority over traditional bypass methods. The prototype faces heating issues, high on-resistance, and performance impacts from a temperature-sensitive resistor. Redesign of the NDMOS and other components is needed for optimization and better handling of higher currents.

In [22], a power metal oxide semiconductor field effect transistor (MOSFET) is used as a voltage divider to lower shaded cell temperatures by up to 24°C, with reliability concerns transferred to an external device, simplifying implementation without the need for additional components. However, the circuit may incur additional costs, particularly with discrete MOSFETs, and require a junction box redesign. Performance depends on selecting a low-$R_{DS(on)}$ MOSFET, with minimal power impact and a slight current reduction under specific conditions. The method proposed in [23] uses a relay, voltage/current monitoring, and Thevenin impedance to detect shading, while a reclosing strategy protects against temporary and permanent shading, overcoming limitations of traditional BPDs. The method detects both abrupt and gradual shading, offering reliable HS protection. However, conventional BPDs are limited in addressing hot spotting, and using multiple bypass devices may lack economic viability. Additionally, BPD techniques can increase temperatures and accelerate aging, affecting long-term reliability. The proposed half-cell module design in [24] offers improved shading tolerance, with a 30% minimum shading ratio for BPD activation, compared to 10% for full-cell modules. It also reduces peak cell heat dissipation by 19% compared to full-cell modules. However, the findings are based on simulations rather than experimental data. The effectiveness of distributed power electronics in mitigating hot-spotting in PV systems is

evaluated, with submodule-level converters shown to nearly eliminate HSs [25]. The impact of accelerated ageing due to hot-spotting is highlighted, with a linear degradation model used to simulate effects over 50 years. Design trade-offs are discussed, with a focus on balancing cost, efficiency, and system longevity.

Distributed power electronics can increase energy yield by over 20% in partially shaded PV systems, prevent hot-spotting, and enhance system reliability and lifetime. It also mitigates ageing effects, ensuring stable energy yield over time. Supported by simulations and experiments, the method is effective, though module-level converters offer limited improvements, and the approach adds complexity and cost. A cost-effective HS mitigation technique using two MOSFETs is introduced to enhance the output power of PV modules affected by HSs, with experimental validation showing a power increase of approximately 3.6 W per module [26]. The proposed solution reduces HS temperatures by 20 °C, increases output power by 3.6 W, improves reliability, and offers a cost-effective, simplified design. However, it requires a complex electronic board design with suitable control logic, involves non-negligible technological costs that deter adoption by crystalline PV module producers, needs precise localization of HSs, and has a limited application scope, necessitating further optimization for broader use.

A modified bypass circuit utilizing an insulated gate bipolar transistor (IGBT) in series with each sub-panel is proposed to enhance protection [27]. The ongoing challenge of HSs in PV systems caused by PS and mismatch conditions is emphasized in the study, with the BPD method, which only partially prevents reverse breakdown, being critiqued. The circuit reduces shaded cell temperature and improves reliability with minimal power loss, but adds complexity. It is less effective under varying conditions and requires additional protection, making it more suitable for high-cell-count panels. Maximum power point tracking (MPPT) accuracy should be assessed under PS, hot-spotting, and varying conditions, with long-term data validation. The highest tracking accuracy for HS modules is achieved by the M-Beta technique, addressing challenges in tracking the global maximum power point (GMPP) [28]. High tracking accuracy and effective HS mitigation under PS are demonstrated by the proposed MPPT methods, including M-Beta and FC-MPPT. However, limitations such as a narrow scope of techniques, lack of statistical analysis, and potential

implementation complexities are acknowledged, with cost implications not fully explored. A new method using relays to isolate HSs in solar PV modules is proposed, enhancing both power and voltage output compared to conventional methods [29]. The technique is effective under various HS conditions, improving reliability and sustainability while using thermal imaging for precise application. The proposed technique enhances power and voltage output by isolating affected substrings, improving reliability and efficiency under intense HS conditions. However, it introduces complexity, potential power loss, and scalability concerns, with increased maintenance needs due to additional components like relay switches. HSs in solar cells are prevented by the new circuit through current cancellation, reducing power dissipation and operating without external control, with minimal power consumption[30]. The circuit is designed for monocrystalline and polycrystalline modules, with its effectiveness confirmed through experimental validation, though it is not suitable for thin-film technologies.

A detailed understanding of the HS phenomenon in PV systems is provided, highlighting the importance of early detection to prevent cell damage [31]. The method, based on a novel current-based detection approach, is validated through MATLAB simulations, effectively identifying HSs early and addressing safety concerns, including the dual role of BPDs in HS formation. HSs are detected early by the method, preventing permanent cell damage while relying solely on current measurements, simplifying the process. However, the method relies on current sensors for operation, and its focus on specific conditions, such as maximum power point (MPP) operation, may not address all scenarios in PV systems. Additionally, the absence of voltage measurements could limit diagnostic capabilities, and the simulation-based validation may not fully reflect real-world complexities, with a potential risk of false positives under certain anomalies. Shingled modules benefit from improved heat diffusion due to their overlapping interconnection design but exhibit significant variations in the current-voltage (I-V) properties of individual shingles, affecting power and HS temperatures [32]. The study reveals that unshaded parallel strings can develop minor HSs during the initial activation of BPDs. Shingled modules enhance packing density and efficiency, boosting power output and offering potential long-term cost savings. However, parallel strings can cause secondary HSs under

shading and complicate thermal management. The study in [33] highlights that the failure of PV module electrode interconnections begins with debonding at the soldering joints, with the silver-glass interface being particularly susceptible to early separation. The research identifies vulnerable interfaces in PV modules and proposes strategies, such as increasing edge distance, to enhance reliability. However, it does not fully account for real-world conditions where temperature gradients significantly influence material behavior and failure mechanisms.

A reconfiguration method is proposed for detecting mismatch and shading in PV panels, using optocouplers to monitor BPDs and a control system to prevent HSs by switching off MOSFETs in shaded subgroups [34]. A microcontroller-based algorithm optimizes power tracking and deploys protection MOSFETs, with experiments validating the method's effectiveness in preventing HS damage. The method improves reliability by preventing HSs in shaded PV panels, offering a cost-effective and easily integrated solution with dynamic reconfiguration for optimal power output. It has been validated through experiments, but its complexity, cooling requirements, and reliance on external power and relays present potential challenges. The technique proposed in [35] addresses shading's impact by reducing reverse voltage across nonproductive cells, preventing breakdown, and lowering temperature through current reduction. It improves PV system reliability by managing temperature effects and reverse voltage, ultimately enhancing efficiency and power output under shading and mismatch conditions. The proposed circuit improves PV module reliability by relocating heat generation to a cost-effective IGBT, reducing temperatures by up to 10.3°C under mismatch conditions. While it simplifies the system and lowers costs, the added complexity of the IGBT introduces a potential point of failure. Limited testing on two modules and sensitivity to temperature variations may impact its broader performance and reliability.

A hybrid feature vector combining RGB, texture, histogram of oriented gradient, and local binary pattern is proposed for classifying PV thermal images using an SVM model, achieving 96.8% training accuracy and 92% testing accuracy [36]. The proposed approach achieves high accuracy (96.8% training, 92% testing), with low computational complexity, making it efficient for monitoring and fault diagnosis in PV panels. However, it may not generalize well across all PV panel types, and its performance depends on dataset quality,

with potential trade-offs in feature dimensionality due to smaller histogram of oriented gradient cell sizes. The method also relies heavily on automated systems for large-scale PV plants, making manual inspection impractical. The proposed sustainable PV module design improves power output by 25% under low-fault and 50% under medium-fault conditions by isolating faulty substrings and remodifying string connections via an additional junction box [37]. The design is cost-effective, enhances performance under fault conditions, and can be automated using relay circuits for easier fault management. However, the design increases complexity, requires manual intervention unless automated, and may lead to higher maintenance needs, with limited fault tolerance in some scenarios.

The study highlights the significance of localized HSs in reducing PV cell efficiency, with temperatures reaching up to 64°C, leading to a 5.7% reduction in efficiency [38]. HSs form rapidly under non-uniform irradiation and dust accumulation, with thermal equilibrium reached within a second. Experimental setups using xenon lamps demonstrated the impact of different concentration ratios on HS formation, emphasizing the importance of addressing recombination processes and voltage loss in understanding the final output voltage of solar cells. The study offers quick diagnosis, precise detection, and real-time monitoring of localized HSs in PV systems. However, the experimental setup using a xenon lamp may not fully replicate real-world conditions, and long-term effects such as encapsulant yellowing were not considered. A novel strategy is proposed to mitigate HSs in PV systems by reducing reverse voltage, power loss, and temperature, while increasing power output at low cost [39]. The active mitigation uses a transistor bypass method to redirect current from shaded cells. An intuitive evaluation method assesses cost, power loss, and temperature, with potential applications in solar heating systems. Simulations and experiments validate its effectiveness in reducing temperature and boosting output power compared to existing methods. However, concerns include potential efficiency loss, space and design challenges due to the divider resistor, temperature fluctuations that could lead to thermal fatigue, and increased complexity and cost in implementation.

A data-driven method called neighbourhood slowest embedding (NSE) is proposed to enhance the sensitivity of HS detection in PV systems [40]. Hardware costs are reduced by using environmental and electrical data for

real-time temperature monitoring, improving fire safety and system stability. Cell-level temperature estimation is enabled, offering more refined analysis and better real-time performance compared to UAV-based infrared imaging. The proposed method offers cost-effectiveness by utilizing existing environmental and electrical data, reducing the need for additional hardware. It enables real-time monitoring of PV module temperatures, improving fire safety through timely warnings. By estimating temperatures at the cell level, it enhances accuracy in HS detection and can be integrated with current systems without requiring extra irradiation measurement instruments. The method reduces error by enhancing module power output monitoring and has been validated with infrared data, proving its feasibility for practical use. Additionally, its ability to estimate temperature ranges makes it valuable for fire warning systems. However, while the NSE method improves temperature estimation, it faces challenges in capturing all nonlinear aspects of PV systems. Estimation errors may occur due to the absence of I-V curve scanning, affecting temperature accuracy. Higher irradiance levels can amplify these errors, and the method struggles with real-time environmental changes, leading to discrepancies. Additionally, the assumption of thermal equilibrium may not always be valid, limiting the method's applicability in certain conditions.

A real-time method for anticipating and preventing HSs in PV panels is proposed [41]. Kernahan's method, which monitors the dynamic conductance of PV cells to avoid reverse bias, is evaluated. BPDs are eliminated to simplify the design of PV panels, reducing costs and complexity. The effectiveness of the method and panel performance are assessed through experimental validation and simulations. The method prevents HSs in PV panels by real-time monitoring of dynamic conductance, ensuring no cell enters reverse bias. It simplifies panel design by eliminating BPDs, reducing manufacturing costs, and improving commercial viability. While it slightly sacrifices energy output under heavy shading, it offers better protection and efficiency compared to traditional designs. However, the method faces challenges related to the cost and stability of differential power processing systems, which may limit its widespread adoption. Additionally, there is a trade-off in energy production under strong shading conditions. Further comparison with conventional panels in various shading scenarios is necessary to fully validate its effectiveness. The study employs Slow

Manifold Analysis to analyze PV systems, focusing on early HS detection by minimizing reconstruction errors [42]. A projection matrix is optimized to minimize change rates, and a new whitening method is proposed for value estimation based on local relationships. Reconstruction error analysis is used to distinguish between normal noise and anomalies, enhancing early-stage HS identification. The proposed method offers high computational efficiency, enabling real-time detection of early-stage HSs in PV systems without relying on physical models or expert knowledge. It outperforms other data-driven methods in detecting anomalies and is adaptable to varying operating conditions. However, it requires adaptive thresholds, different parameters for different conditions, and faces challenges with noise, which could obscure anomaly detection. Further testing is needed to confirm its effectiveness.

1.2.2 Literature Survey on Shade Dispersion Techniques for PV Arrays

The worldwide promotion of roof top photovoltaics (RTPV) supports the clean energy transition by enabling individuals to become local energy contributors [43, 44]. However, a key challenge with PV systems is their heavy reliance on environmental factors that impact energy generation [45]. One such factor that significantly affects the overall efficiency of PV systems is IMSs, which are particularly difficult to address, especially in RTPV systems. Reconfiguring the PV modules stands out as a cost-effective approach with significant potential to boost overall power generation, simultaneously reducing losses in the process. In the existing literature, these methods are categorized as either dynamic, static, or a combination of both [46]. A comprehensive literature review has been conducted to outline the limitations imposed on the PV system following the implementation of various static and dynamic reconfiguration schemes.

1.2.2.1 Dynamic Reconfiguration Approaches

In dynamic rearrangement strategies, the positions of PV modules are securely fixed and remain unchanged, while electrical connections are dynamically adjusted in response to varying irradiation conditions [47]. Efficient dynamic

reconfiguration is accomplished by strategically managing the switch matrix, allowing for the seamless interchange of electrical connections across different PV arrays within each column. This capability enables quick adaptation to varying irradiation levels, ensuring effective row current equalization and optimizing the overall performance and output of the PV array. To facilitate the identification of the most efficient electrical connections, control algorithms employ various optimization techniques.

In [48], a novel approach for PV array reconfiguration using dragon fly optimization algorithm (DOA) was introduced, offering high reliability, reduced complexity, and rapid operational efficiency. This technique improves power and energy generation under IMSs with fewer switches compared to conventional methods. However, it encounters challenges such as prolonged search processes, chaotic flight paths, and unexpected expansions of the search space. Another innovative reconfiguration method was proposed using the butterfly optimization algorithm (BOA), which improves PV array performance under both regular and irregular IMSs. However, this algorithm also faces drawbacks, including local optima entrapment and slow convergence [49].

The democratic political algorithm presented in [50] demonstrates potential for enhanced power extraction in large PV networks under various shading scenarios. However, it demands significant computational resources to achieve optimal solutions. The framework developed in [51] for dynamic PV module reconfiguration addresses array mismatches caused by non-uniform aging. However, its practical feasibility is hindered by the complexity of its structure. In [52], an experimental analysis was conducted on a simple, adaptable PV array configuration using a fuzzy logic recursive least squares approach. The results show that while the fuzzy logic controller successfully adjusts the configuration to maximize power extraction by mitigating power loss in shaded panels, its real-world application is constrained by the added complexity of the switching system. The Particle Swarm Optimization approach introduced in [53], aimed at energy extraction, savings, and income generation, encounters challenges such as difficulties in weight tuning and issues with premature convergence. In [54], a controllable switch matrix is employed to connect a fixed TCT array with a reconfigurable adaptable array. While a simple control scheme is proposed, the use of a large number of switches remains a major limitation. In [55], a

multi-objective Grey Wolf Optimization approach was introduced to address shading effects. Although it outperformed traditional methods, it faces challenges such as significant computational costs, slow convergence rates, and limited scalability, as it was only tested on square-structured arrays. The African vulture optimization method proposed in [56] offers strong search capabilities, allowing it to effectively avoid local optima. However, it struggles with balancing the exploration and exploitation phases. A modified version of the widely used canonical Runge optimizer was proposed in [57] to balance the exploration and exploitation phases. The algorithm showed promising results based on both qualitative and quantitative metrics. However, it was only tested on small-scale PV setups with a limited range of shading patterns. In [58], a novel reconfiguration scheme was introduced, uniquely accounting for power fluctuations resulting from reconfiguration. The approach proposed integrating a hydrogen energy storage system to minimize power regulation costs. However, its practical implementation poses significant challenges.

In [59], a multi-period reconfiguration method for PV arrays integrated with hydrogen storage under IMSs was proposed. The approach aimed to maximize overall profit by accounting for electricity and hydrogen sales alongside frequency regulation costs. In [60], two algorithms were integrated to enhance processing speed and improve irradiance equalization. However, the method required a complex electrical interconnection and a large number of switches, posing practical challenges. In [61], a genetic algorithm (GA) was introduced to achieve uniform SD, but it encountered issues like premature convergence and complex parameter tuning. To address these limitations, a two-step GA approach was proposed in [62]. Six widely used evolutionary multi-objective optimization algorithms were utilized in [63] to identify high-quality Pareto optimal reconfiguration schemes. However, their application is hindered by complex frameworks and challenges in deploying them for large-scale PV arrays. The Harris Hawk Optimizer discussed in [64], demonstrates promising performance but incorporates multiple operational phases and results in even higher peaks in the P-V curve, which may complicate its practical application.
The primary drawbacks associated with these approaches are:

1. ***High Computational Demand:*** Many techniques involve extended search processes, making them computationally intensive. They are also prone to

challenges such as local optima entrapment, complex parameter tuning, and premature convergence.

2. ***Complex Infrastructure:*** Practical implementation often requires a complicated setup, including a large network of switches, which increases system complexity and cost.

3. ***Dynamic Reconfiguration Requirements:*** Dynamic techniques depend on monitoring systems to detect shading or faulty modules, algorithms to determine optimal configurations, and switching matrices to manage module connections, further complicating deployment.

Consequently, the cost associated with dynamic reconfiguration techniques tends to rise due to these additional requirements.

1.2.2.2 Static Reconfiguration Approaches

Static reconfiguration schemes effectively overcome the limitations of dynamic reconfiguration approaches by utilizing a constant interconnection arrangement to enhance power output under varying IMSs. These configurations maintain fixed module positions that do not change with shifting shading patterns. Unlike dynamic methods, static reconfiguration operates without the need for sensors, reconfiguration algorithms, or switching matrices, instead relying on an optimized reconfigurable pattern to ensure even distribution of shading effects across the PV array.

The literature presents various static rearrangement techniques, including arranging modules in a TCT PV array using a Sudoku pattern. This approach ensures even shading distribution without altering the array layout [65]. However, this approach is constrained by limited scalability and the need for extensive wiring. A new puzzle-based reconfiguration scheme, the dominance square (DS) method, is introduced to manage shading effects in PV arrays, tested on a 5×5 array [66]. The DS method improves performance by reconfiguring the conventional TCT interconnection, aiming for uniform row current differences, single peak power, and a smooth I-V curve. The method outperforms other schemes like TCT, BL-TCT, and SP-TCT in reducing mismatch and power loss under various shading patterns and includes an analysis of income generation

and energy savings. The DS method efficiently disperses shade, reduces MPL, and achieves a uniform row current discrepancy (RCD) for maximum power output with a smooth I-V curve. It performs well under various shading patterns and configurations, offers energy savings and income generation, and is considered a reliable solution for PV array reconfiguration. However, the method still experiences wiring losses, and performance may vary under different shading conditions, with the study primarily focusing on specific scenarios. The Latin Square Puzzled and ken-ken square puzzled (KKSP) configurations are introduced to improve power generation and reduce wiring losses in PV arrays under PSCs [67]. Performance enhancements are observed, with power generation being 6.81% higher and wiring loss reduced by 18.86% compared to the SuDoKu Puzzled configuration. The KKSP configuration is found to be superior to the SuDoKu configuration in execution, with a power loss reduction of 771 W under the tested shading conditions. However, the study primarily focuses on specific shading conditions, which may not cover all real-world scenarios. The optimized Sudoku-based reconfiguration method improves power output by effectively dispersing mutual shading and reducing MLs, particularly under varying shading conditions [68]. However, challenges such as unequal shading distribution, current limitations, and reliance on BPDs can impact performance, especially under PSCs. Despite these issues, the method offers better handling of mutual shading and reduced HS risks compared to traditional approaches. The SD technique reduces power loss in PV arrays caused by PS by redistributing shading effects without altering electrical configurations [69]. It enhances power generation by 13.43% compared to the TCT configuration under short wide shading conditions and can be easily implemented in the field. However, the static nature of the technique limits its adaptability to dynamic shading conditions, and its scalability may be restricted to specific configurations like a 3×3 PV array. Additionally, the method lacks electrical reconfiguration, which could limit its optimization in all shading scenarios. The latin square TCT (LSTCT) method enhances PV system performance under PS by dispersing shadow effects across the array, resulting in higher power output, improved fill factor (FF), and reduced power losses compared to the classical TCT configuration [70]. It generates more power at a given voltage range under various shading patterns and achieves a maximum

power of 2279 W with reduced power losses to 330 W. However, the method does not address potential limitations, such as the complexity of implementation, effectiveness under extreme shading conditions, or the economic feasibility of adopting the LS-TCT configuration.

The odd-even (O-E) structuring technique improves PV array power output, reduces MLs by 1.03%, and simplifies MPPT by avoiding local maxima [71]. It increases energy harvest by up to 33.31% under various shading conditions. However, it may increase system complexity and is limited in large installations due to series connections and shading pattern dependency. The Fixed Electrical Reconfiguration technique enhances power generation in PV arrays by redistributing shading effects and simplifying system complexity without extensive sensors or switches [72]. It outperforms traditional configurations in terms of ML reduction, power output, and ease of implementation, but may face challenges in large-scale applications and specific shading conditions. The Arrow Sudoku puzzle reconfiguration technique improves Solar PV array performance by dispersing shading effects evenly across the array, reducing MLs and simplifying system operation [73]. While it outperforms conventional configurations in dynamic shading conditions, it faces challenges like limited flexibility, increased wiring complexity, and constraints on the array size and pattern used. The study introduces the rearranged hybrid interconnection configuration with shade Dispersion Magic Square Puzzle Pattern, boosting solar photovoltaic (SPV) performance under PS by increasing output power and reducing mismatch power loss [74]. However, implementation complexity and adaptability to different PV arrays or conditions are not discussed.

Optimal and improved SuDoKu arrangements for TCT PV arrays are proposed to improve power output and reduce MLs under PS [75, 76]. These techniques simplifies design but offers limited enhancement (2.6%) and do not address installation complexity or dynamic shading adaptation. The Modified Sudoku reconfiguration improves power output by dispersing shading, increasing GMP by 14.41% over TCT and 0.75% over Improved Sudoku [77]. The SIMT configuration is proposed to enhance power output and reduce mismatch and wiring losses in PV arrays [78]. Power enhancement of up to 21.43% is observed, with easy detection of maximum power for MPPT controllers. However, effectiveness is validated through simulations, and practical

implementation for existing installations may be complex. The Skyscraper method improves power output and simplifies MPPT by dispersing shade effectively across PV arrays [79]. However, its effectiveness in complex shading patterns, real-world conditions, and the cost of implementation are not fully explored. A new technique involving two new reconfiguration patterns, canonical SuDoKu and multi-diagonal SuDoKu, for improving power extraction in TCT PV arrays under PS was proposed [80]. These methods rearrange PV modules without altering electrical connections, enhancing efficiency and reducing MLs. However, they require physical relocation of modules, may increase system losses, and lack monitoring systems for dynamic shading conditions.

A Novel Magic Square View Topology of a PV System under PSC was proposed in [81]. It has superior performance than Sudoku and TCT but its applicability is restricted to only 9×9 PV Arrays. The odd-even-prime (OEP) arrangement reduces power loss by distributing shading evenly across rows in PV arrays, enhancing power output and efficiency under PSCs [82]. However, the method's complexity and performance in extreme shading or non-standard PV configurations are not fully addressed. The Phyical Relocation Fixed Column Positioning of Modules with Fixed Electrical Connection algorithm enhances power generation in solar PV arrays under PS by optimizing module relocation, showing significant improvements over traditional configurations [83]. However, its initial setup requirement, dependency on array configuration, and challenges with complex shading patterns may limit its applicability in certain situations. The diagonally dispersed TCT configuration enhances PV performance by evenly distributing shaded modules, simplifying installation and operation [84]. However, it may increase wiring losses and is static, unable to adapt to changing shading.

The tom tom (TT) puzzle pattern technique requires fewer sensors and switches, reducing system complexity and cost [85]. However, physical relocation of panels can involve wiring complexity depending on panel positioning. Additionally, although the method performs better than SP, B-L, and H-C configurations but fails when compared with the TCT configuration in terms of statistical measures. The method using Arnold's Cat Map significantly enhances output power (up to 38.15%) and reduces MLs in PV arrays [86]. It has

been validated through extensive testing across 100 shading cases and real-world environments. However, issues such as the reappearance of the original image over time and the complexity of implementation may arise. Another static reconfiguration technique improves power output, reduces losses, and simplifies reconfiguration compared to existing techniques [87]. While offering enhanced efficiency and lower system complexity, it may face challenges with scalability, versatility in varying shading scenarios, and requires real-time evaluation for broader implementation. The four square Sudoku method enhances power output by redistributing shade across PV arrays, achieving a nearly single-peak power curve and improving efficiency [88]. While it offers significant energy savings and economic benefits, it may be labor-intensive for installations, has limited scalability for different array sizes, and its performance under complex shading patterns is not fully explored.

The ancient chinese magic square (ACMS) method improves PV array performance under PS by enhancing SD and current uniformity, resulting in smoother I-V and P-V curves with fewer maxima [89]. While it outperforms traditional methods like TCT and Su-Do-Ku, its implementation complexity, cost implications, and scalability for real-world applications remain unaddressed. The Benzene configuration improves power output under PS by reducing mismatch and shading losses, with fewer tie connections compared to traditional configurations, making it cost-effective for large PV arrays [90]. While it achieves higher peak power and maintains a high FF, it may still experience some MLs under specific shading conditions, where TCT may perform better. A chaos map (CMAP) is used for reconfiguring PV arrays to mitigate PS effects, leading to enhanced power output by achieving uniform row currents and efficient SD [91]. Conventional configurations are outperformed, and the method is applicable to various array sizes. However, stability issues arise in larger arrays, and SD in the first and last columns is challenging, making implementation labor-intensive.

The Permutation and Combination approach optimizes GMPP extraction, reduces power loss, and enhances efficiency by effectively dispersing shade across PV arrays [92]. Validated through simulations, it demonstrates robust performance under PSCs. However, its effectiveness may diminish with larger systems or extensive SD due to computational complexity and reconfiguration challenges. The parquet SuDoKu (PRS) method improves power output under

PS by evenly distributing shade, reducing average power loss to 40.50%, and enhancing GMPP by up to 15.47% over competing methods [93]. It is cost-effective, eliminates the need for extra hardware, and provides higher annual financial returns. However, its implementation complexity and adaptability to diverse conditions may require further investigation. The extra region SuDoKu topology addresses complex fractional PS scenarios, surpassing traditional methods like TCT and SuDoKu by improving efficiency, FF, and reducing ML [94]. Validated through simulations and experiments, it significantly enhances energy generation. However, challenges may arise with extreme shading patterns, higher computational demands, and scalability for large PV arrays.

The triple-X SuDoKu reconfiguration method enhances PV array performance under PS by dispersing shading effects through module repositioning [95]. Tested on a 9×9 TCT array under various shading patterns, it improved power output by 20.57% over TCT and 3.6% over classical SuDoKu, minimizing power losses to 0.15%. Despite its benefits, the static nature, labor-intensive setup, and limited adaptability to changing shading conditions may pose challenges. The Cross-Kit technique improves PV array performance under PS by redistributing shading effects without altering electrical connections [96]. It enhances power output by 5.49% to 26.73% compared to TCT and O-E configurations, simplifies MPPT by reducing local maxima, and offers straightforward implementation. However, challenges include scalability for large arrays, potential cost increases due to additional components, and limited testing under rapidly changing conditions. The chess board game theory (CBGT) method optimizes PV array performance under PS by dispersing shadows efficiently, achieving higher GMPP, enhanced efficiency, and reduced power loss compared to conventional configurations like SP and TCT [97]. Despite its promise, the method faces challenges in implementation complexity, scalability to larger systems, and the need for extensive experimental validation across diverse shading scenarios.

The main drawbacks associated with the previously reported rearrangement methods are:

1. The TCT configuration excels beyond other established conventional topologies such as series, SP, B-L, and H-C due to its outstanding ability to

extract maximum power under IMSs. Consequently, nearly all reported PV reconfiguration schemes implemented reconfiguration on the TCT configuration. However, its intricate wiring structure, mainly due to a substantial number of cross-ties, results in heightened wiring losses.

2. Most static reconfiguration techniques exhibit dependency on array dimensions, presenting a notable challenge for scalability in real-world installations.

1.2.3 Literature Survey on PV Array Configurations

Over the years, various PV array configurations have been studied to analyze their behavior/response under the effects of PSCs, each aiming to improve power output, minimize HS risks, and ensure operational reliability. This section reviews the state-of-the-art advancements in PV array configurations under PSCs, highlighting their methodologies, effectiveness, and limitations.

The performance of SP, TCT, and B-L configurations under shadowing, aging, and mismatch conditions is examined, with cross-tied designs demonstrating notable advantages [98]. However, the study's assumptions, limited scope, and absence of real-world validation highlight the need for further research. A comprehensive review of Solar PV array configurations under PS is presented, focusing on the use of BPDs to mitigate energy losses [99]. A MATLAB model is developed to simulate various configurations, shading patterns, and array sizes, with SP, TCT, B-L, and H-C configurations analyzed. It is concluded that proper array layout and configuration, particularly the H-C configuration for asymmetrical arrays, can significantly enhance SPV system performance. However, limitations include the generalization of results, assumptions of ideal conditions, lack of experimental validation, narrow focus on specific configurations, and challenges in real-world applications and computational requirements.

A mathematical model for analyzing TCT PV arrays under mismatching conditions is introduced, improving computational efficiency and enabling real-time energy evaluations [100]. Validated through simulations, it demonstrates advantages over traditional SP configurations. However, it assumes uniform module behavior, may not fully capture BPD effects, and faces

computational challenges in larger arrays. The model's validation is limited to a specific configuration, and practical integration into embedded systems may encounter challenges. Contributions are made to understanding PV systems, focusing on interconnections and shading effects [101]. PV mismatch is addressed, interconnection schemes analyzed, and mathematical models for shadows and optimization laws introduced. A connection matrix is proposed, with simulations exploring power output impacts. However, limitations include a focus on external mismatch, artificial shadows, and narrow topology exploration, highlighting the need for further research in real-world PV system optimization. The study compares six PV array configurations under PS to optimize system efficiency [102].

The TCT configuration generally outperforms others, but performance varies with shading patterns. Key findings guide PV optimization, though limitations include focus on a single array size, simplified shading scenarios, single BPD use, and lack of economic and long-term performance data. Further research is needed to address these gaps. The study compares series, SP, and TCT PV array configurations under PS [103]. Results show that TCT outperforms S and SP, reducing power losses to 13% under 70% shading. However, the study relies on MATLAB simulations, lacks hardware testing, and focuses on a 4×4 array and specific shading scenarios, limiting its generalizability. Additionally, other configurations, like B-L, were not considered. Further research with real-world testing and varied conditions is needed. The TCT configuration outperforms others under PS, as shown through mathematical analysis and Matlab simulations. However, the focus on TCT, use of a single diode model, limited shading scenarios, and lack of experimental validation suggest the need for further research to confirm real-world applicability [104].

PV configurations like simple series, P, SP, TCT, B-L, and H-C were analyzed for power optimization under PS. MATLAB/Simulink simulations showed TCT's superior performance, though limited to three shading conditions [105]. The complexity of TCT and the exclusion of other configurations and practical factors like cost and reconfiguration highlighted the need for further research and real-world validation. Shading effects on PV arrays were investigated to identify efficient configurations [106]. Experiments on a 4×5 array under varying shading scenarios showed that shading reduces output, especially in

series-connected modules. The TCT configuration performed best under random shading, while BPDs helped mitigate power loss. However, limitations such as the focus on specific shading patterns, controlled conditions, and the exclusion of long-term diode performance and broader metrics highlight areas for further research. The performance of PV array configurations (S, P, SP, TCT, B-L) under PS and faults was evaluated using MATLAB/Simulink [107]. Key indicators like current, voltage, and series resistance were analyzed. Results emphasized the importance of configuration choice for efficiency under shading and faults. However, the study's scope was limited by a narrow range of faults, reliance on simulations, and a focus on specific indicators, excluding economic and environmental factors.

The triple-tied (T-T) configuration addresses PS in PV systems, outperforming most existing configurations while reducing wiring redundancy compared to TCT. Experiments show its potential for large-scale use, but T-T ranks second to TCT in power output and may struggle in extreme shading conditions. Its wiring complexity could also raise costs compared to configurations like B-L and H-C, and the simulation results may not fully reflect real-world conditions. The T-T configuration addresses PS in PV systems, outperforming most existing configurations while reducing wiring redundancy compared to TCT [108]. Experiments show its potential for large-scale use, but T-T ranks second to TCT in power output and may struggle in extreme shading conditions. Its wiring complexity could also raise costs compared to configurations like B-L and HC, and the simulation results may not fully reflect real-world conditions. The performance of three solar PV array configurations—Series (S), SP, and H-C was evaluated under various PSCs [109]. Simulations showed that shading reduces power generation, with the H-C configuration outperforming both S and SP configurations in all scenarios. Electrical performance was emphasized, but practical aspects such as cost, installation, and maintenance were not considered. Results were based on simulations without experimental validation, and the range of shading conditions was limited, potentially restricting the applicability of the findings. Alternative configurations were not explored. Simulations of various PV topologies (S, P, SP, TCT, B-L, H-C) under different shading patterns show that TCT outperforms others in power generation and reducing MLs, but its complex

design increases wiring costs [110]. Despite promising techniques like adaptive reconfiguration and micro-inverters, the findings may not fully apply to real-world scenarios due to simulation limitations. Hybrid configurations (SP: TCT, B-L: TCT, H-C: TCT, B-L: H-C) seek to improve power output and minimize losses, demonstrating superiority over traditional setups like TCT [111]. Nevertheless, substantial redundancy, wiring losses, and complexity impede practical application. Simulation-based analysis employing two-diode modeling provides insights but lacks empirical validation, constraining its relevance to various PV architectures. Additional research is imperative to tackle these obstacles and enhance PV performance under diverse conditions.

The performance of SP, B-L, H-C, and T-T PV array configurations was evaluated under various shading patterns, with T-T demonstrating higher efficiency and power generation [112]. Simulations were conducted in the Matlab/Simulink environment, but the absence of experimental validation, a focus on limited shading patterns, and static configurations limit the findings' generalizability. PV array configurations are analyzed, with the TCT configuration noted for its optimal performance in partial shading [113]. The significance of hybrid and metaheuristic strategies for SD is underscored. While conventional and puzzle-based configurations receive attention, there is a lack of thorough examination regarding dynamic shading, novel configurations, and practical issues associated with metaheuristic techniques. Experimental validation remains insufficient, and the findings may not be universally applicable to all PV systems, necessitating further investigation into emerging technologies and practical implementations. Series-connected on-chip PV cells are proposed for voltage boosting, but issues such as current mismatching among p/n junctions and dependency on illumination intensity limit optimization [114]. Integrated BPDs mitigate shading effects, though they introduce power losses and reverse leakage risks.

A novel 7×7 and 9×9 T-T PV array configuration were developed and compared with S, SP, TCT, B-L, and H-C configurations under diverse shading scenarios [115–117]. While the TCT configuration demonstrated superior power generation under most conditions, its higher wiring requirements lead to increased costs and losses [118]. A novel TCT interconnection scheme enhances PV system performance under shading, outperforming standard TCT and forced

TCT by over 40 W in specific cases. However, increased wiring raises costs and the risk of arc failures. An analytical algorithm is presented to estimate the MPP of TCT connected solar cells, avoiding computational complexity and convergence issues [119]. The TCT connection improves performance under PS but lacks a BPD, potentially allowing current flow through shaded cells. While HS generation is considered negligible, the paper does not address this issue. The TCT configuration, while generating the highest GMPP, suffers from increased wiring losses due to a greater number of cross ties [120]. Although the TCT configuration generally performs best, there are specific shading patterns where other configurations like H-C may outperform it due to fewer ties. A new technique for estimating the GMPP in shaded PV arrays improves accuracy and reduces complexity by dividing the P-V curve [121]. However, its performance depends on shading parameters and may be difficult to apply in real-world systems with wiring resistances. The limited comparison with existing methods and the iterative process could reduce efficiency.

1.2.4 Literature Survey on Grid-Integrated Solar PV Systems

The integration of SPV systems with the grid has emerged as a cornerstone in the transition toward sustainable energy solutions. Grid-connected SPV systems not only contribute to reducing carbon footprints but also ensure reliable power supply by leveraging renewable energy resources. However, challenges such as intermittency, PQ, synchronization, and grid stability demand comprehensive research and innovative approaches to optimize their performance. This chapter presents a literature survey that reviews recent advancements, methodologies, and technological developments in the domain of grid-integrated SPV systems, focusing on key aspects such as system design, power electronics interfaces, grid compliance, and performance enhancement strategies.

Grid-integrated SPV systems enhance PQ and stability through advanced control strategies like the multilayer fourth order generalized integrator (MLFOGI) algorithm [122]. This approach addresses voltage distortions and imbalances, ensuring robust performance in weak distribution grids while adhering to IEEE 519 requirements for grid reliability. Grid-integrated SPV systems, such as the Solar Power Transfer System, are designed to enhance PQ,

compensate for reactive power, and ensure maximum power extraction under varying load conditions through the utilization of advanced control algorithms like frequency adaptive generalized integral (FAGI) [123]. A grid-integrated AC/DC microgrid incorporating renewable energy resources and hybrid energy storage systems, such as supercapacitors and batteries, is designed to enhance power balance, stability, and performance [124]. This is achieved through the implementation of a double-loop control structure and small-signal modeling. Grid-integrated SPV systems face challenges like intermittency, non-dispatchability, and stability issues. Advanced controls, energy storage, and grid code compliance address these, enhancing reliability and integration [125]. Grid-integrated SPV systems employ multilevel inverters to minimize switching losses and harmonics. A cascaded H-bridge multilevel inverter, combined with isolated multi-output DC–DC converters, enhances efficiency and PQ using advanced control methods and MPPT [126].

Transformer-less inverters and advanced topologies have improved PV system efficiency, but challenges like narrow voltage ranges, bulky capacitors, and complex controls remain. Further innovation is needed to enhance performance [127]. An adaptive grid-tied PV system minimizes total harmonic distortion (THD) below 4% using a tri-MPPT algorithm [128]. Experimental results show improved efficiency, particularly under light loads. However, the basic prototype limits its real-world applicability, and further research is needed on different converter topologies and environmental conditions. A single-phase H-bridge inverter is designed for distributed generation systems to improve PQ by compensating for harmonic and reactive power [129]. Further research is needed on current limitation strategies and inverter design for reactive power compensation. A hybrid mantis search-reptile search algorithm combined with a unified power quality conditioner is proposed to enhance PQ in grid-connected solar systems [130]. Simulations show improved performance over existing methods, but limitations include reliance on simulations and untested long-term stability. A simplified adaptive transversal filter control scheme is proposed to improve PQ in grid-tied SPV systems with shunt active power filters. It performs well in steady-state and dynamic conditions, but limitations include potential reduced effectiveness in complex scenarios and reliance on specific simulations, limiting generalizability [131]. A grid-tied PV system is proposed to address PQ

issues caused by non-linear loads, using an equilibrium optimized PI controller to stabilize the DC bus voltage [132]. The system improves power factor correction and harmonics elimination, outperforming traditional methods. However, limitations include the complexity of implementing the control in real-world applications and the need for further validation under diverse conditions.

PQ in grid-connected PV systems is enhanced using a hybrid active power filter with a three-level converter, effectively mitigating harmonics and improving voltage stability for better grid performance [133]. However, it is limited to three-phase four-wire systems and incurs higher costs due to additional power electronics components. A PV-based shunt active power filter using synchronous reference frame control enhances PQ in grid-connected systems by mitigating harmonics and compensating reactive power, meeting IEEE standards for total harmonic distortion [134]. Traditional PI controllers perform poorly under variable load conditions, while an adaptive intelligent nonlinear controller effectively addresses variable load, non-linearities, and reactive power. A PV-integrated unified power quality conditioner uses an adaptive compensating technique based on the variable leaky least mean square algorithm to enhance PQ in distribution networks [135]. It addresses current harmonics, poor power factor, and grid disturbances, maintaining sinusoidal voltage at the load terminal. The system's effectiveness is validated through simulation and hardware implementation. However, limitations include the complexity of the algorithm requiring significant computational resources and untested performance under extreme dynamic conditions or variable loads. Environmental factors, such as sunlight availability, may also affect the system's performance.

A modified reduced order generalized integrator-based frequency-locked loop and a fuzzy-tuned PID controller are proposed for grid-tied PV systems to enhance PQ [136]. The system mitigates harmonics, minimizes steady-state error, and ensures compliance with IEEE-519 standards. A grid-tied solar PV system is proposed to enhance PQ by addressing harmonics, reactive power, and load unbalancing using an adaptive generalized maximum Versoria criterion controller [137]. This approach outperforms conventional control techniques and ensures compliance with IEEE-519 standards. A hybrid PV-wind-battery energy

storage system integrated with a three-phase utility grid inverter uses a fuzzy logic proportional integral derivative-improved second-order generalized integrator-quadrature signal generator-phase locked loop control strategy to enhance PQ at consumer terminals [138]. The technique separates the fundamental components of phase load currents, improves dynamic performance, and maintains power balance, ensuring compliance with IEEE-519 standards for THD. However, the controller is limited by its unsuitability for DC-offset rejection and its previous use in distribution static compensator (D-STATCOM), which may affect its performance in renewable energy applications.

A three-phase single-stage grid-tied solar PV system utilizes a Perturb and Observe algorithm for maximum power extraction under varying environmental conditions [139]. A hardware prototype validates the control scheme, showing improved performance in DC offset and harmonic rejection compared to conventional methods. The proposed Multiple-Improved-Notch-Filter control algorithm effectively extracts the fundamental load current component, ensuring robust performance during grid abnormalities. However, challenges remain in integrating renewable energy systems into weak grids, and the system's performance in more extreme or varied real-world scenarios requires further validation. An enhanced second order generalized integrator (SOGI) control scheme is proposed for grid-tied PV systems, maintaining low THD under distorted grid voltages with simple tuning [140].

A novel smooth least mean square (LMS) algorithm is proposed for controlling PV inverters, enhancing synchronization with the grid by extracting active and reactive load components, compensating for harmonics, and reducing voltage fluctuations [141]. Validated through simulations and hardware testing, it performs well under various conditions. However, its robustness in real-world scenarios and highly dynamic or non-linear loads has not been fully evaluated. A new variable step size LMS adaptive control algorithm is proposed for grid-integrated PV systems to enhance reference current generation for voltage source converters [142]. It improves dynamic performance and maintains PQ by compensating for harmonic and reactive power, ensuring compliance with IEEE-519 standards. However, the study's reliance on controlled laboratory conditions and MATLAB/Simulink modeling may limit the generalizability to

real-world applications. The Sign Regressor Least Mean Mixed Norm control technique for a D-STATCOM is developed to improve PQ by mitigating harmonics, reactive power, and load balancing [143]. It outperforms traditional methods like Recursive Least Square and Variable Step Least Mean Square in convergence speed, steady-state error, and total harmonic distortion reduction, with experimental validation. However, its complexity in implementation under unbalanced and distorted voltage conditions may affect D-STATCOM performance.

A two-stage grid-tied PV system is designed to enhance PQ and mitigate voltage fluctuations and harmonics in weak grid conditions [144]. It uses a third-order complex filter to manage disturbances like voltage sag/swell and load unbalancing, ensuring stable operation and improved energy extraction. However, the reliance on advanced control algorithms may pose challenges in practical applications, especially due to sensitivity to system parameter variations and implementation complexity. A PV system is designed to operate effectively under weak grid conditions, ensuring balanced and sinusoidal power delivery while mitigating voltage sag, swell, and distortion [145]. It uses adaptive DC link voltage regulation and a PV feed forward term to improve response to grid variations, validated through laboratory tests. However, limitations include the complexity of the control algorithms for adaptive voltage regulation and the need for further testing in real-world scenarios to assess performance under diverse conditions.

A microgrid system integrating PV, wind, and battery energy storage improves energy reliability and sustainability [146]. It uses a sixth-order complex filter to manage disturbances and enhance PQ in both on-grid and off-grid modes. Limitations include potential battery life issues and challenges with voltage imbalances. An adaptive Steepest Descent Laplacian Regression control algorithm is proposed for grid-tied SPV arrays to improve efficiency and quality [147]. It addresses challenges from variable solar irradiance and grid conditions. However, it faces limitations due to the high computational burden and inability to handle all grid abnormalities.

1.3 Research Gaps

Some of the gaps identified in the literature are as follows:

1. The previous studies on HS alleviation mainly focused on temperature reduction of the shaded cell under PSCs with very little regard to the power modification to the existing system.
2. No research is available that establishes a relationship between shading ratio and the activation of the mitigation strategies that are being used (*e.g.*: comparison with conventional BPD circuit).
3. Additionally, there is very little research that adequately explains the driving mechanisms of the switches involved in the suggested HS mitigation circuits.
4. Most of the existing techniques, despite being effective in enhancing the GMPP to some extent, induce multiple peaks in the PV array characteristics.
5. As most of the existing static techniques reconfigure the array arbitrarily through some puzzle-based pattern or magic-square pattern, *etc.*, the shading is not uniformly dispersed. So, an intelligent and even SD can eliminate this drawback.
6. The researchers have not yet explored the reliability improvement aspect of PV systems through reconfiguration approaches.
7. The requirement of a higher number of cross-ties (i.e. more wiring is required), leads to more cost for cabling and more wiring loss in TCT configuration. Limited research is available on topological modifications to conventional PV array topologies aimed at reducing the huge wiring dependence.

1.4 Research Objectives

Based on the research gaps identified in Section 1.3. The main objective of the thesis is to provide performance enhancement measures and a comprehensive

analysis of PV systems under sub-optimal operating conditions. For this, the following research studies need to be conducted:

1. **Improved Hot Spot Alleviation Approach for Enhanced PV System Reliability.**

   To develop an improved HS alleviation approach that can be easily integrated with any number of series connected cells and protect hot spotted cells from thermal breakdown during the slightest of the shading event thus improving the overall PV system reliability.

2. **Improved Shade Dispersion Strategy for Enhanced Power Extraction Under PSCs.**

   To develop a generalized optimal shade dispersion strategy valid for both symmetrical and unsymmetrical array sizes capable of harvesting maximum power under different PSCs with minimum mismatch losses.

3. **Topological Modifications to Existing PV Array Configurations for Enhanced PV Power Extraction Under Mismatch Conditions.**

   To propose a new PV array topology by modifying existing configurations for optimal power extraction under PSCs with reduced wiring/cabling requirements.

4. **Modelling and Investigation of a Solar PV System Performance Under Sub-Optimal Operating Conditions.**

   To design and evaluate the performance of a grid-integrated solar PV system operating under sub-optimal operating conditions.

1.5 Structure of the Thesis

The remainder of the thesis is organized as follows:

Chapter 2 provides an in-depth analysis of PV module performance under severe mismatch conditions. It presents an enhanced HS mitigation technique aimed at improving power extraction and reliability. The chapter quantifies power loss in shaded cells and explores the shortcomings of traditional BPDs.

Additionally, it offers a comparative analysis of power loss and thermographic behavior between modules using both conventional and newly proposed mitigation strategies.

Chapter 3 introduces innovative static shade dispersion techniques designed for optimal power extraction from PV arrays under PSCs. These methods are shown to be universally applicable across different PV array configurations and rely on straightforward reconfiguration strategies, eliminating the need for complex switch and sensor networks. The chapter also offers a performance comparison of the proposed approaches with recent advanced reconfiguration techniques, supported by both simulation and experimental validation.

Chapter 4 presents a novel PV configuration known as the MPVA, which reduces cross-tied wiring in comparison to traditional TCT PV arrays. It also introduces the PMSRA, a new method for evenly distributing shade across PV arrays, tailored to the proposed arrangement. The chapter features comprehensive simulations and experimental analyses, comparing the performance of the proposed approach with current state-of-the-art methods under various shading conditions.

Chapter 5 focuses on the design and performance evaluation of a STF-assisted control system for a dual-stage three-phase grid-integrated SPV system operating under sub-optimal conditions. The control scheme is assessed for key features such as harmonic reduction, power factor correction, resilience to load imbalance, and optimal power extraction under varying insolation levels. The chapter includes extensive simulation results conducted using MATLAB/Simulink to demonstrate the system's effectiveness.

Chapter 6 summarizes the key findings and contributions of the research. It also outlines potential directions for future investigation, suggesting areas where further study and development could enhance the current work.

Chapter 2

Improved Hot Spot Alleviation Approach for Mismatched PV Modules

2.1 Preamble

The development of PV technology has played a crucial role in the global transition to renewable energy. However, the efficiency and lifespan of PV systems can be severely affected by PS, which leads to the formation of HS within the modules. This chapter aims to delve into the complexities of HS formation, the shortcomings of traditional BPDs, and the innovative solutions designed to improve the thermal performance of PV systems.

HSs develop when certain cells in a PV module are shaded, causing them to overheat while the surrounding cells continue to function normally. This thermal stress can result in permanent damage, such as degradation of electrical connections or even fire hazards. The importance of effective mitigation strategies is highlighted by the fact that while BPDs are intended to bypass current away from shaded cells, they often do not fully prevent the formation of HS.

The chapter presents findings from experiments involving a 3×1 PV string and 3×3 SP PV array configurations. Thermal imaging was used to analyze the thermal behavior of modules under different shading conditions, comparing the performance of standard BPDs with the proposed HSMC. The results indicate

substantial temperature differences in shaded cells, underscoring the limitations of conventional methods in addressing the risks associated with HS.

To overcome the shortcomings of BPDs, this chapter introduces the HSMC, which leverages advanced semiconductor technology to better manage the thermal performance of shaded cells. The HSMC works by reducing the reverse voltage on shaded cells, thereby preventing them from reaching critical thermal breakdown levels. This novel approach not only enhances the safety of PV systems but also boosts their efficiency during shading events.

By exploring the thermal dynamics of PV modules under shading conditions and proposing an innovative solution, this chapter contributes to a deeper understanding of how to optimize PV system performance. The findings are intended to inform future designs and operational strategies, ensuring that PV technology can meet increasing energy demands in a sustainable and safe manner.

In summary, this chapter sets the stage for a comprehensive exploration of the challenges posed by shading in PV systems and the innovative strategies that can be employed to mitigate these issues, ultimately enhancing the reliability and efficiency of solar energy solutions.

The remainder of the chapter is organized as follows: The underlying theoretical aspects of PV behavior under non-ideal conditions supported by experimental analysis on a scaled-down PV module are presented in Section 2.2. Section 2.3 deals with theoretical considerations of the proposed HSMC and the experimental setup developed for validation of theoretical findings. Section 2.4 focuses on the results and discussions of the experimental work performed for examining the HS endurance efficacy of the shaded portion of the module with the proposed HSMC. Finally, Section 2.5 offers a summary of the chapter to encapsulate our findings and contributions.

2.2 PV Response Analysis Under Non-Ideal Conditions

Analysis of PV behavior under mismatch conditions is extremely crucial for the utmost energy harvest from the PV installation and the system reliability.

2.2.1 Analysis of Power Loss in a Shaded Cell Exhibiting HS Behavior

Fig. 2.1(a) shows the PSC on one of the cells in a module. The respective I-V characteristics are displayed under each cell. As string current is increased from zero to the optimum point, the operating point of each PV cell shifts. Since all the cells are connected in series, each cell operating point in the module is obtained by the intersection of the individual cell I-V curves with the operational line horizontal to the x-axis. The operating point shifts as specified, $c_I \rightarrow b_I \rightarrow a_I$ for cell $I, c_{II} \rightarrow b_{II} \rightarrow a_{II}$ for cell II and $c_{III} \rightarrow b_{III} \rightarrow a_{III}$ for cell III. When the operating line corresponds to O_c, the shaded cell III, operates at its maximum power operating point (MPOP), c_{III}. However fully illuminated cells, I and II still do not operate at their MPOPs. As the operation line shifts to O_b, fully illuminated cells, I and II generates power at corresponding points b_1 and b_{II}. The new string current corresponding to this operation line [indicated by a solid line in Fig. 2.1(a)] happens to be higher in magnitude than the short-circuit current of the shaded cell III, causing the reverse voltage across this cell. Since the voltage polarity is reversed with current still flowing in the same direction, cell III now acts as a sink of power instead of a power source. If allowed to operate under this condition for a prolonged duration, then cell III acting as a load will dissipate substantial power as heat, thus immensely causing the cell's local temperature to rise. At O_a, the reverse voltage impressed on the shaded cell, III increases with cells I, II, and III operating respectively at points a_I, a_{II}, and a_{III}. Interestingly, although PV cells I and II generate power at their respective MPOPs, the shaded cell, III dissipates tremendous power as heat, downgrading the overall system efficiency heavily and posing serious safety and reliability concerns.

To practically validate the theoretical considerations presented here, a scaled-down PV module (2.5 Wp rating) was employed as a test module to estimate the impact of completely shading one cell. To practically validate the theoretical considerations presented here, a scaled-down PV module (2.5 Wp rating) was employed as a test module to estimate the impact of completely shading one cell. Fig. 2.1(b) shows the experimental setup for analyzing the power loss in a completely obscured cell exhibiting HS. The PV module was

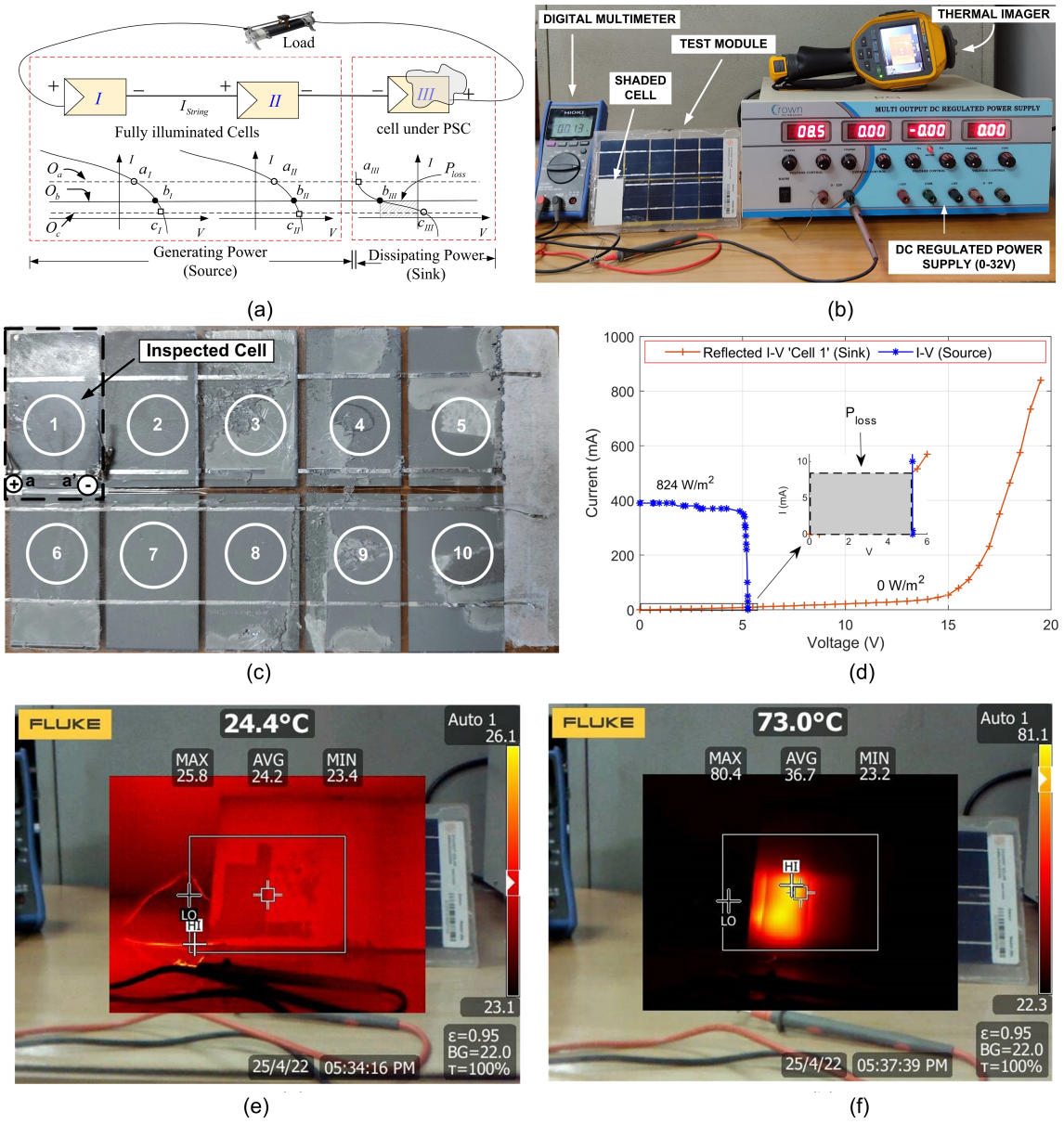

FIGURE 2.1: (a) Typical response of PV cells under PSC. (b) Experimental arrangement to examine reverse characteristics. (c) Rear view of the disintegrated module. (d) Measured power loss, P_{loss} of a completely shaded cell (cell '1'). (e) Thermographic behavior of the test module under normal condition. (f) Test module exhibiting HS condition under reverse bias.

disintegrated for accessing the shaded cell (cell " 1 ") terminals marked by "+" and "-" [see Fig. 2.1(c)]. Reverse characteristics of a completely shaded cell (cell " 1, " acting as load) were estimated by gradually varying the reverse bias applied

to the cell and measuring the resultant current at various instants. At natural solar irradiance of 824 W/m^2, the forward $I-V$ characteristics of the unshaded cells (acting as source) were measured. To determine the power loss in the shaded cell, the measured reverse characteristics were reflected and superimposed on the forward $I-V$ curve of the source in the first quadrant. The operating point of the PV module is the point of intersection of the $I-V$ characteristics of the source (nine unshaded cells) and the sink (one shaded cell) [see Fig. 2.1(d)]. The shaded area is the measure of power loss occurring in the completely shaded cell, with the remainder of the cells generating power (maximum power of 1.764 W@824 W/m^2). The power loss, P_{loss} is estimated to be 52.54 mW , accounting for 2.98% of the maximum generated power output at the specified irradiance. Interestingly, this loss further intensifies as the cell area under the shading ambit reduces. The number of cells connected in series for the inspected module is 10 [see Fig. 2.1(c)] and the cumulative open circuit voltage of the module is merely 6 V. The shaded cell is compelled to dissipate substantial power as heat causing significant localized temperature leading to an extremely inefficient system as the number of series connected cells increases. Infrared images (see Fig. 2.1(e) and (f) reveal that the temperature of the examined cell increases by over 200% $(80.4°C)$ from the normal conditions (NCs) $(25.8°C)$ even on gradual application of reverse bias within 3 min , indicating that the cell has entered the avalanche breakdown region beyond -15 V. Hence, there is a need to devise effective technological solutions to mitigate this localized generated heat in the affected cell to prevent unwanted damage and consequential economic loss.

2.2.2 Reverse Voltage Across a Shaded Cell: Mathematical Analysis

Consider n_i number of series cells forming the module. For the PV configuration under observation (3×1 string), n_i equals 36. To keep the analysis simple, the ideal single diode circuit model ($R_{sh} = \infty, R_s = 0$) of the participant cells of the module is considered [148] (see Fig. 2.2).

The reverse voltage imposed upon the obscured cell of the module can be quantified by employing Kirchhoff's voltage rule on the loop through individual

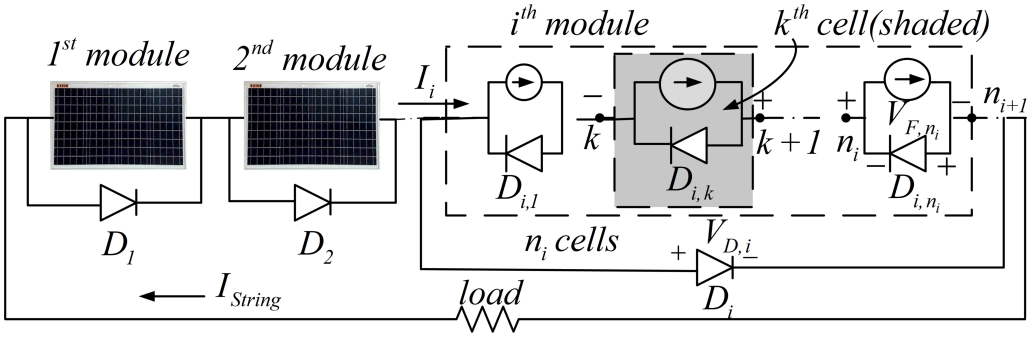

FIGURE 2.2: PV string behavior under mismatch condition.

module integrated BPD. Due to the virtual disconnection of the series circuit at the kth node of the ith module in the string because of the mismatch event at the kth cell, the current is forced to pass through the intrinsic diode, $D_{i,j}$ of individual cells, thus incurring a voltage drop of $V_{F,j}$ The voltage between kth and $(n_i + 1)$ th terminal of any shade affected i th module can be estimated as:

$$v_k^{n_i+1} = -V_{D,i} - \sum_{j=1}^{k-1} V_{F,j} \tag{2.1}$$

$\forall i = 1, 2, 3$ (module indices)
$\forall j = 1, 2, 3, \ldots n_i$((cell indices of the shaded module)
where $V_{D,i}$ is the forward voltage drop of the i th module integrated BPD, D_i and $V_{F,j}$ is the forward voltage drop of the intrinsic diode, $D_{i,j}$ corresponding to the jth cell. It must be noted that the ith module integrated BPD, D_i conducts only when condition (2.2) is met.

$$I_{\text{String}} > I_i \tag{2.2}$$

where I_{String} is the total current of the PV string and I_i is the current of the i th module. The voltage across $(k + 1)$th and $(n_i + 1)$ th terminal of the ith module in the string can be calculated as:

$$v_{k+1}^{n_{i+1}} = \sum_{j=k+1}^{n_i} V_{F,j} \tag{2.3}$$

Using (2.1) and (2.3), the voltage across the kth mismatched cell of the ith module of the string can be determined as:

$$v_k^{k+1} = v_k^{n_{i+1}} - v_{k+1}^{n_{i+1}} = -\left(V_{D,i} + \sum_{j=1}^{k-1} V_{F,j} + \sum_{j=k+1}^{n_i} V_{F,j}\right) \tag{2.4}$$

To have good reliability in the design, the value of n_i should be kept sufficiently low to avoid entering the breakdown region of the shaded cell. The following voltage condition (2.5) must be met for any arbitrary shaded cell, k, at all times to evade any premature aging and subsequent damage due to the elevated temperature operation for a prolonged duration:

$$v_k^{k+1} = -\left(V_{D,i} + \sum_{j=1}^{k-1} V_{F,j} + \sum_{j=k+1}^{n_i} V_{F,j}\right) << V_{BV,k} \tag{2.5}$$

where $V_{BV,k}$ is the breakdown voltage of the kth cell. Substituting the forward voltage drop, for the intrinsic diode $D_{i,j}$ ($V_{F,j} = 0.6$ V) and standard BPD ($V_{D,i} = 0.5$ V), the peak value of the reverse voltage across the mismatched cell may be realized as 21.5 V for the module under inspection (single BPD per module). Following the same rationale, the peak reverse voltage across non-productive cells may also be estimated for other commercially available modules viz; 60 cells (11.9 V) and 72 cells (14.3 V) having BPD across each one-third of the cells in module.As discussed in the preceding section, the magnitude of reverse bias across PV cells dominates the cell operating temperature under shading conditions. The avalanche breakdown behavior is expected from the alkaline, and acidic texturized PV cells at -15 V to -20 V for the former and -13 V for the latter [35]. One approach to safeguard masked cells is to have BPD across each cell body. However, this is not an economical option from manufacturer's point of view and may result in complexity and extended power losses with more diodes being in conduction and is highly unlikely to be incorporated in the immediate future. Another approach would be to employ short string lengths that enhance HS mitigation effectiveness using BPDs. Again, module manufacturers do not accept this solution commercially because of the involved costs.

TABLE 2.1: Specifications of the Experimental Platform

Equipment	Parameter	Value
PV Module	Maximum Power	40 W
	Open-circuit voltage	22.18 V
	Voltage at MPP	18.00 V
	Current at MPP	2.22 A
	Short circuit current	2.40 A
	Number of cells	$36 (= 9 \times 4)$
	Tolerance	+0 to 5 W
Thermal Imager	Type	FLUKE Ti400
	Detector resolution	320×240 pixels
	Thermal Sensitivity (NETD)	≤ 0.05°C at 30°C
	Accuracy	± 2°C or 2%
	Frame rate	60 Hz
	IFOV (spatial resolution)	1.31 mRad
Solar Power Meter	Make	MECO instruments
Rheostats	Rating	$100\,\Omega/5$ A (2 units in series connection)
Multimeters	Units	2 (Type: FLUKE 101)
Digital Storage Oscilloscope	Channels	4 (Type: KEYSIGHT DS0-X 2024A, 200 MHz)

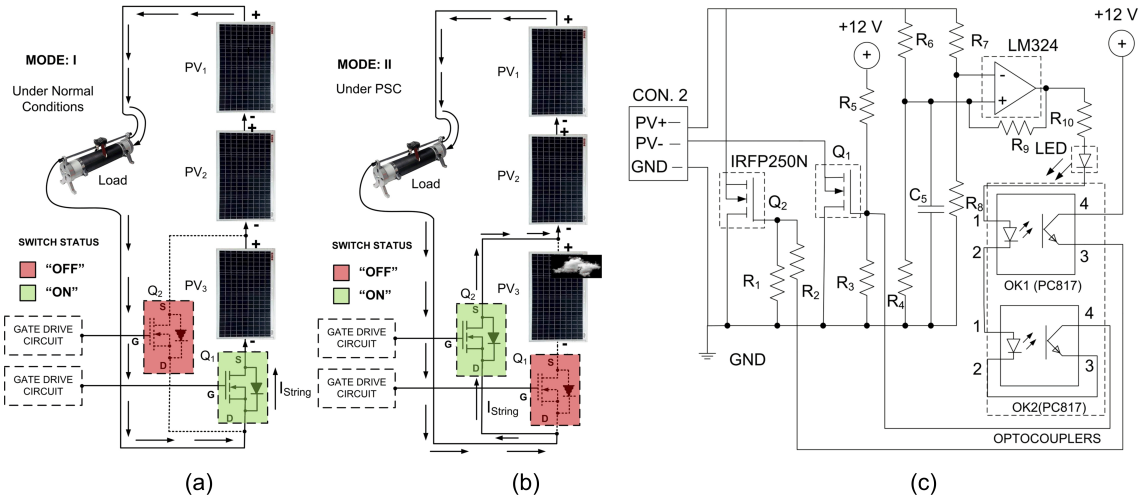

FIGURE 2.3: Proposed HSMC: Operation mechanism under (a) mode I: NC. (b) mode II: PSC. (c) Circuit arrangement.

2.3 Proposed Hot Spot Mitigation Circuit and Experimental Setup

This section describes the overall circuit configuration of the proposed HSMC and the experimental setup used for testing its performance.

2.3.1 Proposed Hot Spot Mitigation Circuit Topology

The proposed approach is based on dual power MOSFET configuration. MOSFET Q_1 is connected serially between the module and the load whereas MOSFET Q_2 is connected across the module, as shown in Fig. 2.3

In the event of PSC, Q_2 is driven into conduction, offering a near short circuited path across the affected module, thus providing bypass, whereas Q_1 provides a reduction in reverse voltage across the shaded cell, which is reflected as an improved temperature reduction of the shaded cell than the standard BPD circuit. As discussed in the preceding section 2.2.2, the maximum reverse voltage impressed on the kth shaded cell of any i th module is the sum of intrinsic diode forward voltage drop, V_F of the remaining unshaded cells and forward voltage drop of the conducting BPD, V_D. To bring the temperature of the shaded cell well within the safe limits, the reverse voltage imposed on the cell needs to be pushed

sufficiently low to prevent the mismatched cell from reaching the avalanche breakdown region. Under normal operation ((mode I: unshaded condition), the switch Q_1 is in conduction having low value of drain to source voltage, $V_{DS,1}$ while the switch Q_2 is not conducting any current as shown in Fig. 2.3(a). So, the string current I_{String} , coincides with the drain current of the MOSFET Q_1, i.e., $I_{\text{String}} = I_{\text{DS,1}}$ and the corresponding system output includes generation from all the three PV sources. Under PSC (mode II: ≥ 1 cell shading), the switch Q_1, stops conduction, and the bypass circuit involving the switch Q_2 gets activated. Thus, the string current, I_{String} equals the drain current of the switch Q_2 i.e., $I_{\text{String}} = I_{\text{DS,2}}$ with the consequence that the affected module is effectively bypassed [see Fig. 2.3(b)]. Interestingly, the current through the switch, Q_1 is decreased, and the corresponding operating point shifts to a higher value of drain to source voltage, $V_{\text{DS,1}}$. The modified reverse voltage across the k th shaded cell of the i th module using the proposed HSMC can be estimated similarly as discussed in section 2.2.2

$$v_k^{k+1} = -\left(V_{\text{DS,2},i} + \sum_{j=1}^{k-1} V_{F,j} + \sum_{j=k+1}^{n_i} V_{F,j}\right) + V_{\text{DS,1},i} \tag{2.6}$$

where $V_{\text{DS,1},i}$ and $V_{\text{DS,2},i}$ are the drain to source voltages across switches Q_1 and Q_2, respectively, of the proposed circuit integrated to the i th module. On comparing (2.4) and (2.6), an apparent reduction in the reverse voltage appearing across the mismatched cell can be ascertained. Thus, the proposed HSMC performs significantly better in reducing the voltage imposed on the shaded cell under PSC with the consequent shift of the operating point to a safe value, much lower than the avalanche breakdown region of the cell, thus ensuring safe and reliable operation. The complete circuit arrangement showing the gate driver circuits for the individual switches, Q_1 and Q_2 along with the complete hardware realization is shown in Fig. 2.3(c) and Fig. 2.4 (a), respectively. The 15 V ac supply is drawn from a step-down transformer (not shown in the circuit) fed from a 230 V, 50 Hz single phase source. To reduce the ON-state power losses of HSMC, a meticulous selection of switches from a variety of available MOSFET ratings is carried out through extensive initial experimental analysis on a laboratory setup before their deployment into operation, as depicted in Fig. 2.4(b). MOSFETs (IRFP250N) having low onstate drain-source resistance

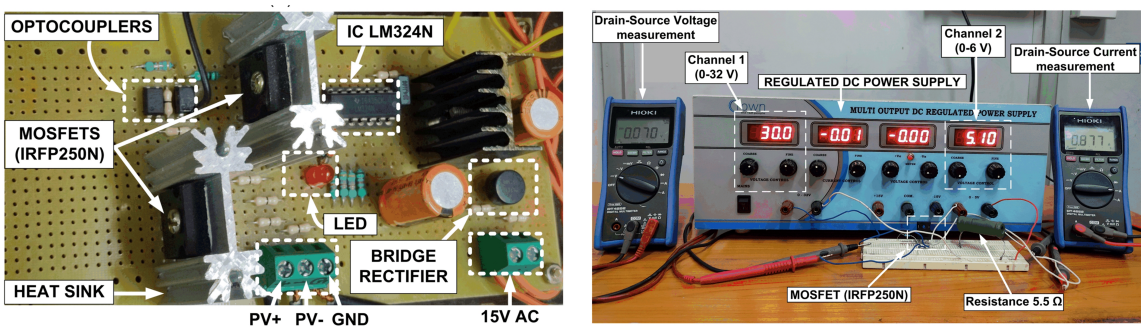

FIGURE 2.4: (a) Hardware prototype for experimental validation. (b) Experimental test setup for selecting appropriate switches for HSMC.

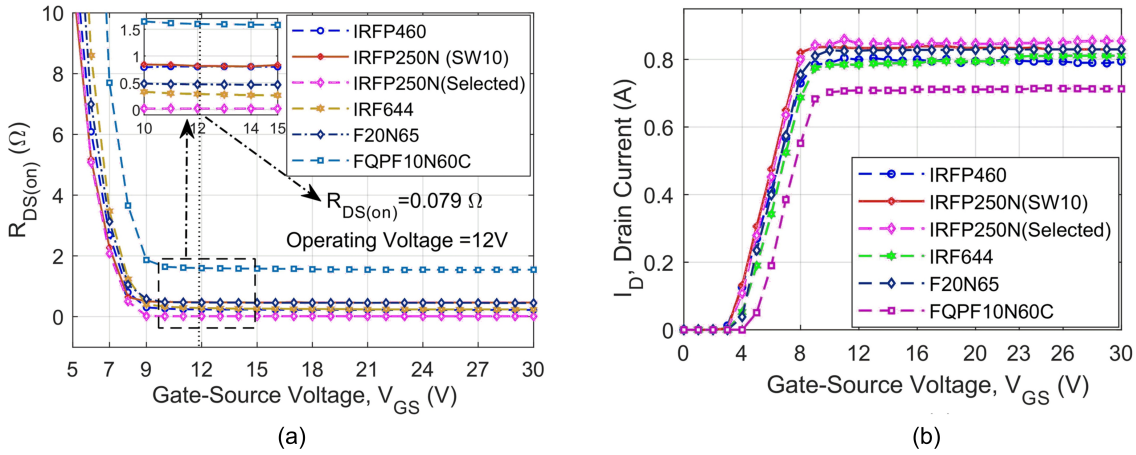

FIGURE 2.5: Characteristics of different switches investigated for the proposed HSMC: (a) Drain-source ON-state resistance versus gate-source voltage. (b) Gate-to-source versus drain current characteristics.

$R_{\mathrm{DS(on)}} = 0.079\Omega$ is selected for HSMC. The operating gate-to-source voltage, V_{GS} for the proposed circuit, is 12 V . The variation of on-state drain-source resistance $R_{\mathrm{DS(on)}}$ and drain current, I_D for different values of gate-to-source voltage, V_{GS} for various examined MOSFETs, are also shown in Fig. 2.5(a) and (b). A generalized flowchart depicting various operational stages of the conventional BPD and the proposed HSMC approach is shown in Fig. 2.6.

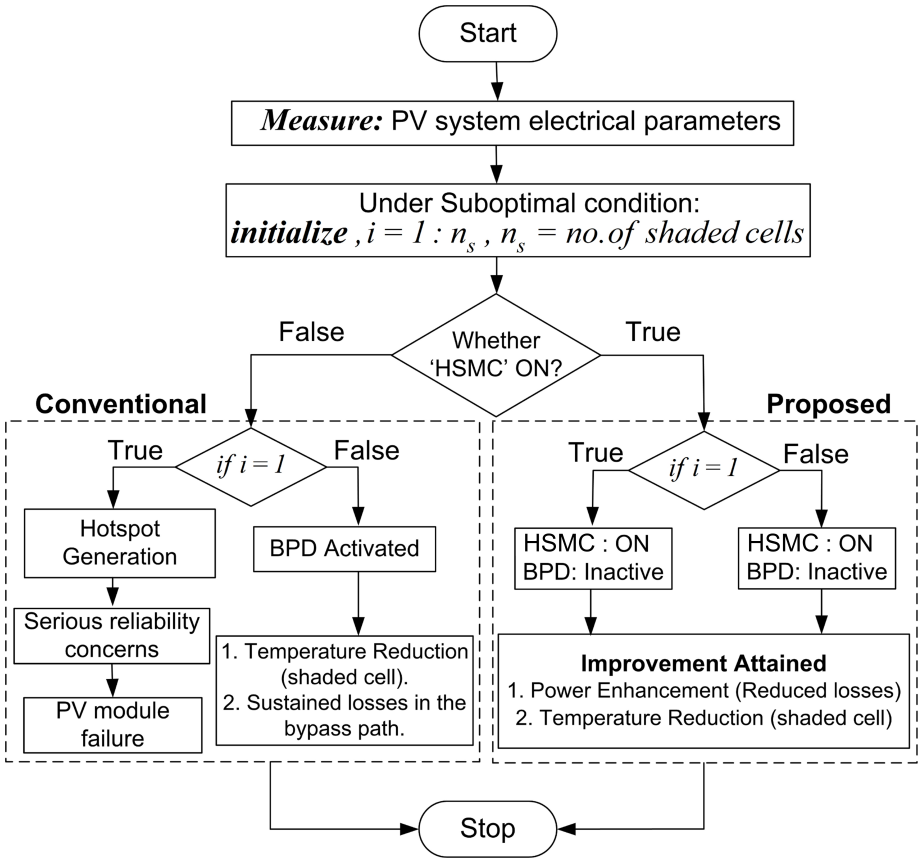

FIGURE 2.6: Flow chart summarizing the various stages of the conventional and the proposed HS mitigation approach.

2.3.2 Experimental Setup

In this section, an analysis and validation of the MOSFETs based HSMC approach is described in detail. Fig. 2.7 and 2.8 shows the developed experimental set-up for 3×1 PV string and 3×3 PV array respectively consisting of three and nine identical PV modules mounted on the same supporting frame, aligned in the same direction and at the same inclination.This arrangement enables them to be tested at exactly similar time and conditions. The electrical characteristics of the PV modules under standard test conditions (STC) and the critical specifications of the thermal imager to access the HS are given in Table 2.1. The 3×1 PV string and 3×3 SP array was examined under the effect of the artificial shadow of varying shading ratio (SR) (one cell-shaded: 2.77% and two cell-shaded: 5.55% under the same operating and ambient conditions). Here, SR is computed as the ratio of

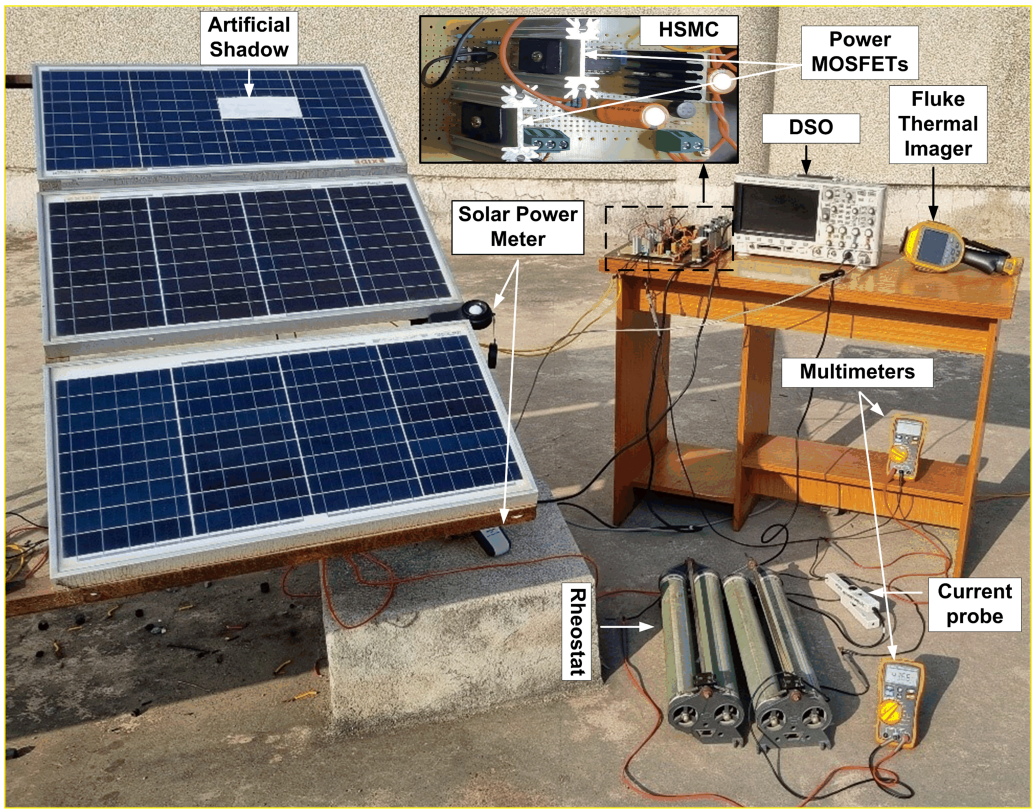

FIGURE 2.7: Experimental setup (3×1 PV String) for assessing the thermal reliability of the module under PSC.

number of shaded cells to the total number of cells in the module.

For instance, the total number of cells in the considered module are 36. So, 1 cell shading corresponds to a SR of 0.027 (or 2.77%) and likewise. The artificial shadow-infected module was examined with both standard BPD and integration with the proposed HSMC. Thermal imaging measurements of the shaded cell were performed to quantify the impact of the mismatch effect in the PV system under examination since detecting HS using thermal imaging is a universal approach. The key outcomes of the experimental analysis with detailed discussions are presented in Section 2.4.

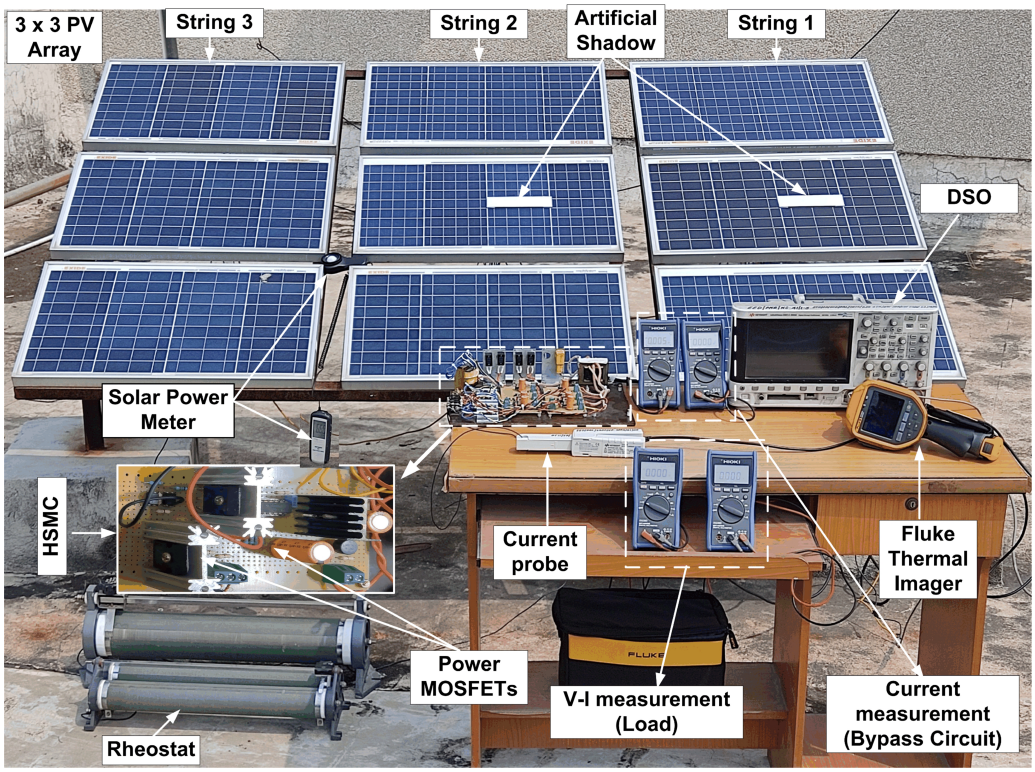

FIGURE 2.8: Experimental setup (3×3 PV Array) for assessing the thermal reliability of the module under PSC.

2.4 Results and Discussion

To corroborate the practical workability of the proposed control approach, key measurements and thermal inspection of 3×1 PV string system (refer Fig. 2.7) were carried out after intentionally shading the different number of cells under similar operating and ambient conditions. A 3×3 PV array (refer Fig. 2.8) configured in a SP arrangement is also considered for experimental analysis and thermographic inspection for testing the performance of the proposed HSMC extensively.

2.4.1 Experimental Measurements (Electrical Characteristics, Dynamic Response, and Power Loss Estimation)

In this section, a comprehensive description of the experimental analysis is presented. The evaluation includes an examination of the electrical

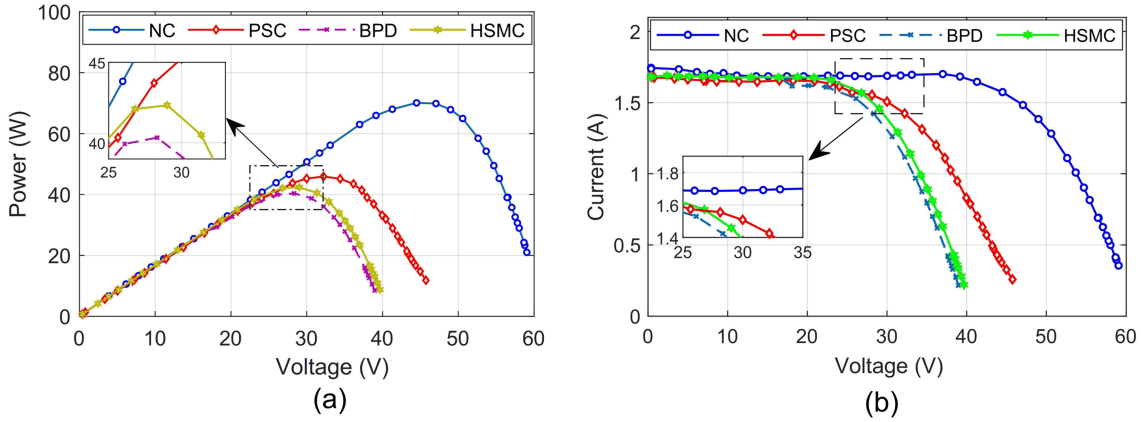

FIGURE 2.9: Measured electrical characteristics of a 3×1 PV String: (a) P-V curves. (b) I-V curves.

characteristics, assessment of the dynamic response, and thermographic analysis of the considered PV systems.

2.4.1.1 Electrical Characteristics

The solar irradiance varied from $700 - 815\ \mathrm{W/m^2}$ during the entire experimental investigation. The PV system's electrical characteristics were measured under various operating conditions, viz. NC (unshaded), PSC ([No Bypass: 1 cell shaded (HSMC "OFF")], bypass with standard BPD [(two cells shaded) and (HSMC "OFF")] and finally bypass with proposed HSMC ($\geq$ 1 cell shaded) by performing the complete scan of the operating region achieved through variation of a resistive load. The measured $P - V$ and $I - V$ characteristics at $700\ \mathrm{W/m^2}$ for 3×1 PV string system under predefined conditions are shown in Fig. 2.9(a) and (b), respectively. A maximum power enhancement of 5.0% under two cells shading condition is attained with the proposed HSMC. The variation of current through the bypass circuits with string voltage was also measured as depicted in Fig. 2.11(a). Under 1-cell shading, BPD is not activated, since negligible current flows through it, as a result, HS formation is inevitable for all the operating points of the affected module located in between the short circuit region and close to MPOP region. The shaded area in Fig. 2.11(a) represents the HS-prone region for the shade-affected module under 1-cell shading (protected through

traditional BPD). As the shading area is increased to 2 cells, BPD starts to conduct string current though not completely.

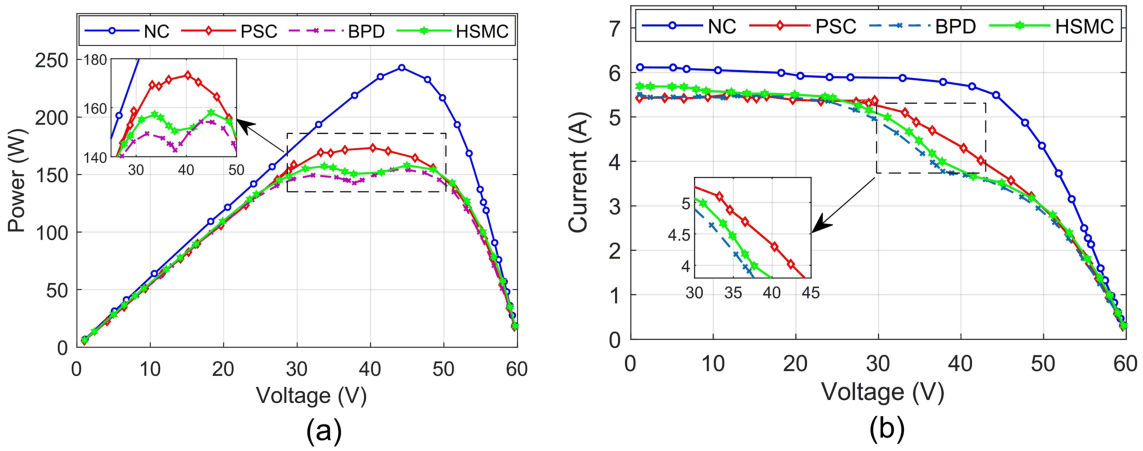

FIGURE 2.10: Measured electrical characteristics of a 3×3 SP PV array: (a) P-V curves. (b) I-V curves.

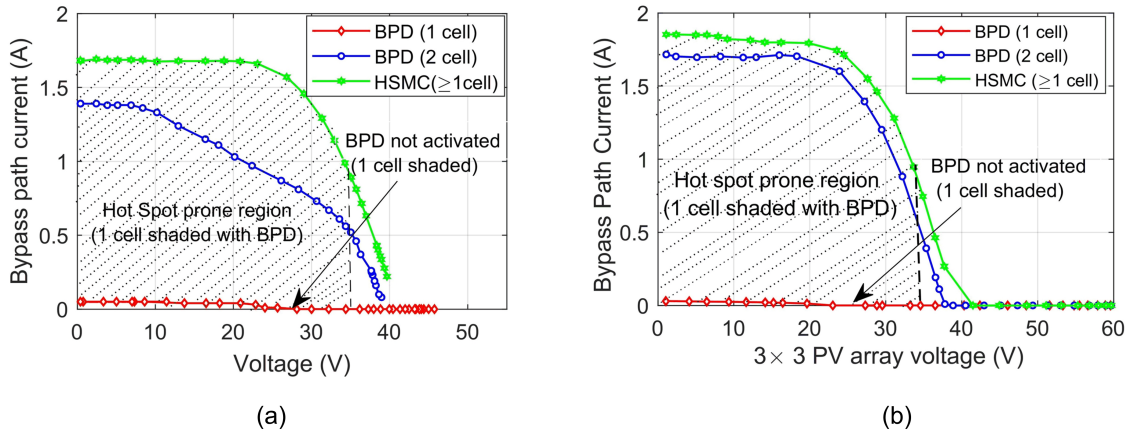

FIGURE 2.11: Measured voltage versus bypass path current for: (a) 3 × 1 PV String. (b) 3 × 3 SP PV array.

On the contrary, the HSMC completely bypassed the affected module even at the slightest of the shading event ensuring safe operation. The $P-V$ and $I-V$ curves for a 3 × 3 SP PV array under different operating conditions are shown in Fig.2.10(a) and (b), respectively. On integration with proposed HSMC, a maximum power enhancement of 2.42% is observed when one of the modules of the array is subjected to two cell shading conditions. Similar experimental

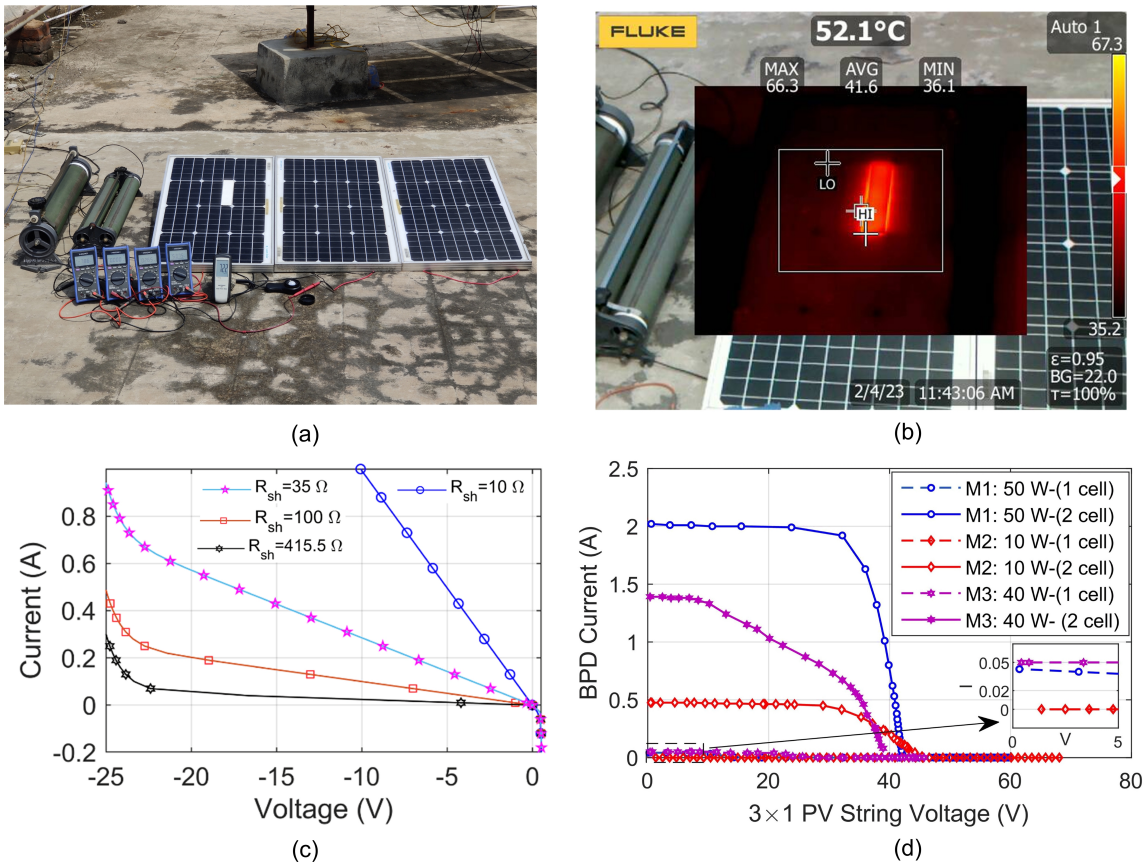

FIGURE 2.12: (a) Experimental arrangement of (50 W module) PV string to examine the thermographic behavior under 1 cell shading (b) Thermographic response under 1 cell shading (c) Simulated reverse voltage charchteristics of a PV cell of the test module (d) BPD current versus string voltage under 1 cell and 2 cell shading for different rating modules.

measurements were carried out as done on 3×1 PV string system to examine the response of the bypass circuit to varying shading conditions. As before, conventional BPD completely failed in bypassing the shade-affected module under 1-cell shading. The HS-prone region under one-cell shading for the module protected through BPD is depicted in Fig. 2.11(b).

To extensively investigate the behavior of BPD during 1 cell shading conditions, series of experiments were conducted on three 3×1 PV strings, each comprising of different ratings of PV modules viz. M1: 50 W, M2: 10 W, M3: 40 W respectively. One such 3×1 PV string comprising of 50 W rated PV modules is depicted in Fig. 2.12(a). The thermographic behaviour of the considered string

when subjected to single cell shading is alo shown (refer Fig. 2.12(b)). A simulation analysis is conducted to investigate the reverse voltage characteristics of a PV cell within the test module under varying shunt resistance, R_{sh} values. The results reveal that the reverse breakdown behavior of the cell is strongly influenced by the shunt resistance. Specifically, cells with lower shunt resistance values experience higher losses and significant temperature buildup during PSCs compared to cells with higher shunt resistance values (2.12)(c). Experimental results confirm that BPD failed to conduct during 1 cell shading even close to the short circuit conditions (refer Fig. 2.12(d) in all the three considered PV string systems subjecting the mismatched cell to elevated temperatures.

2.4.1.2 Dynamic Response Analysis of the PV System

To better analyze the various operating modes of the PV systems, the dynamic response is captured on a digital storage oscilloscope (DSO). Clear transitions among different functional stages of 3×1 PV string system and 3×3 SP PV array are respectively observed through experimental waveforms recorded as shown in Fig. 2.13(a) and (b). A complete scan of the system operation is carried out using DSO for a total duration of 50 s and the system response at various transitions are captured for the 3×1 PV string and the 3×3 SP PV array. For the initial 12 s, the system is operating under NC (unshaded), with the operating voltage and current of the PV string being 56.56 V and 0.690 A, respectively as shown in Fig. 2.13(a). The onset of PSC (one cell completely obscured) occurs at $t = 12$ s, string voltage, and current dip and settles to new values of 43.2 V and 0.52 A , respectively. Under this condition, no bypass circuit is active. At $t = 22$ s, BPD gets activated (under 2- cell shading) and provides a bypass path to the string current. Under this condition, the string voltage and current recorded were 37.2 V and 0.479 A , respectively. Interestingly, BPD activation starts only for $\geq$ 2 cell shading conditions, thus exposing the mismatched cell to thermal degradation over time for low ($<$ 2 cell) shading conditions and hence may initiate irreversible failure of the module. At $t = 32$ s, shading is reduced to 1 cell again, and the proposed HSMC is activated resulting in immediate activation of the bypass circuit with the corresponding string voltage and current values being

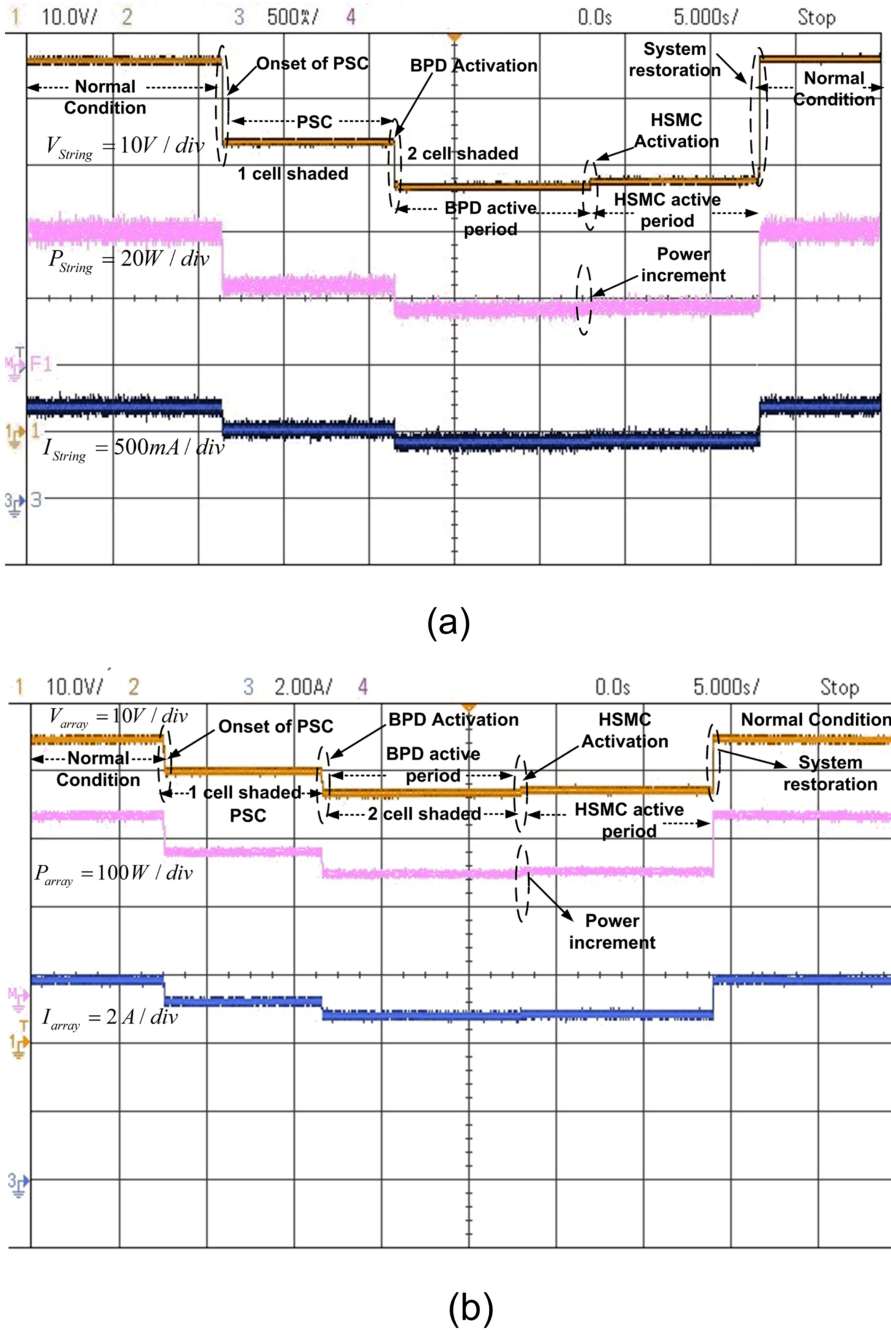

FIGURE 2.13: Experimental waveforms showing PV system dynamic response: (a) 3×1 PV string (b) 3×3 SP PV array.

37.9 V and 0.489 A respectively. The system is left unattended for a further 10 s , and at $t = 42$ s, the artificial shading is withdrawn. The system restores to NC with corresponding string voltage and current values being 56.56 V and 0.690 A ,

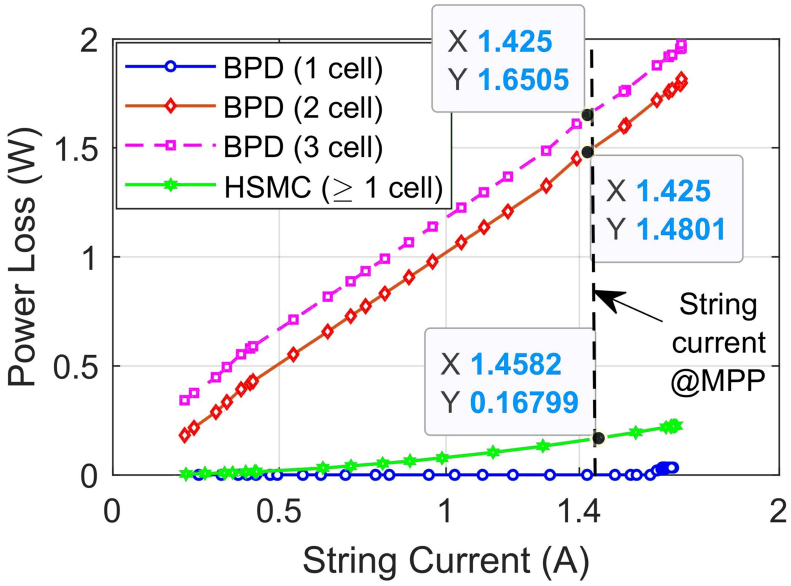

FIGURE 2.14: Power loss estimation under different shading cases for the conventional BPD circuit and the proposed HSMC.

respectively. The corresponding system parameters are given in Table 2.2. For brevity, since the same workflow was observed with the 3×3 SP PV array (near MPOP region) [see Fig. 2.13(b)], hence it is not presented here in detail but is listed for reference in Table 2.3.

TABLE 2.2: Parameters of the 3×1 PV String Under All Operating Conditions (Close to Open Circuit)

String Voltage (V)	String Current (A)	String Power (W)
Condition 1: NC (Unshaded)		
56.56 V	0.690 A	39.02 W
Condition 2: PSC		
43.2 V	0.52 A	22.46 W
Condition 3: Bypass with standard BPD(2 cells shaded, HSMC 'OFF')		
37.2 V	0.479 A	17.81 A
Condition 4: Bypass with HSMC (1 cell shaded)		
37.9 V	0.489 A	18.53 W
Condition 5: System Restoration		
56.56 V	0.690 A	39.02 W

TABLE 2.3: Parameters of the 3 × 3 SP PV array Under All Operating Conditions (Close to MPOP)

Array Voltage (V)	Array Current (A)	Array Power (W)
Condition 1: NC (Unshaded)		
44.25 V	5.29 A	261.51 W
Condition 2: PSC		
40.2 V	5.12 A	205.82 W
Condition 3: Bypass with standard BPD(2 cells shaded, HSMC 'OFF')		
37.2 V	4.79 A	178.18 A
Condition 4: Bypass with HSMC (1 cell shaded)		
37.9 V	4.98 A	188.53 W
Condition 5: System Restoration		
44.25 V	5.91 A	261.51 W

2.4.1.3 Estimation of Power Loss (3× 1 PV String)

The power loss, $P_{\text{byp,loss}}$ occurring in the bypass path of the shaded module protected through the conventional BPD and the proposed HSMC for the 3×1 PV string is measured for different shading cases for the entire operating zone of the PV string as depicted in Fig. 2.14. It is observed that since under 1 cell shading, the standard panel integrated BPD does not go into conduction, the $P_{\text{byp,loss}}$ is therefore apparently the least. However, as the number of shaded cells is increased and BPD goes into full conduction, significant power loss occurs in the bypass path of the module. The $P_{\text{byp,loss}}$ is computed for the conventional bypass circuit and the proposed HSMC as given in (2.7) and (2.8) respectively.

$$\underbrace{P_{\text{BPD}}}_{\text{byp,loss}} = V_D \times I_{\text{String}} \tag{2.7}$$

$$\underbrace{P_{\text{byp,loss}}}_{\text{HSMC}} = I^2_{\text{String}} \times R_{\text{DS(on)}} = I^2_{\text{DS,2}} \times R_{\text{DS(on)}} \tag{2.8}$$

where V_D represents the forward voltage drop of the BPD which varied from 0.667 to 1 V as the string current is increased and $R_{DS(on)}$ is the drain-source on-state resistance of MOSFET (IRFP250N) switches used in proposed HSMC

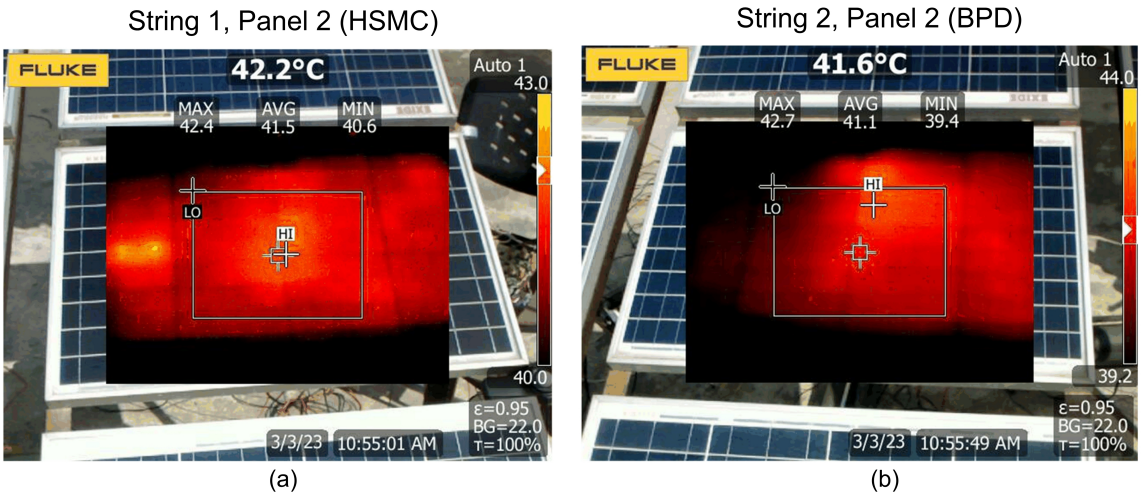

FIGURE 2.15: Thermographic analysis (near MPOP) of the shaded module of two 3×1 PV strings under consideration under NC (unshaded) condition for (a) String 1, Panel 2 (HSMC). (b) String 2, Panel 2 (BPD).

having the value of 0.079Ω. It is observed that at the MPOP of the PV string, $P_{\text{byp,loss}}$ of the shade-affected module on application of proposed HSMC circuit is reduced to 88.65% and 89.82% under two-cell and three-cell shading respectively in comparison to module integrated BPD.

2.4.2 Thermographic Inspection

Thermal inspection of the shade-affected module is done considering two prominently employed PV connection topologies viz. series and SP connection.

2.4.2.1 Thermal response on 3×1 PV String

To obtain a precise evaluation of the thermal performance of a module affected by shading, thermal measurements were taken from two identical 3×1 PV strings. One of the strings had its middle module equipped with the proposed HSMC (string 1, panel 2), while the same module in the other string (string 2, panel 2) was fitted with a traditional BPD. Each PV string's middle module was thoroughly examined using a high-resolution thermal imager to capture the thermal behavior of the shaded module. The use of different middle modules from distinct PV strings with different bypass strategies was employed to

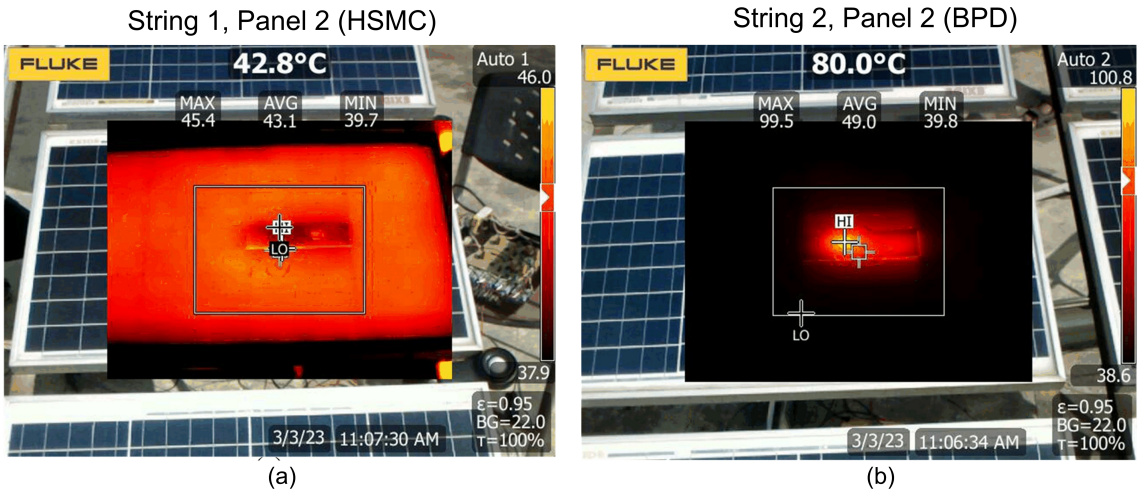

FIGURE 2.16: Thermographic analysis (near MPOP) of the shaded module of two 3×1 PV strings under consideration: (a) One cell shaded (with HSMC). (b) One cell shaded (with BPD): No bypass.

prevent any disturbances in the thermal measurements of the shaded module during its operation. Furthermore, assessing the PV string's behavior with the same shading pattern simultaneously guaranteed the accurate capture of the thermal behavior of the shade-affected module, allowing for a comparison of the two different bypass strategies. Infra red images of the inspected module (string 1: panel 2 (with HSMC), string 2: panel 2 (with BPD)) were captured at various instants during the entire system operation.

Under normal unshaded conditions, the maximum temperature of the middle panel for string 1 and string 2 was observed to be 42.4°C and 42.7°C, respectively, under full exposure to the incoming irradiance as shown in Fig. 2.15. The middle modules in the respective PV strings were kept unattended under 1 cell shading condition for approx. 12 min . This resulted in a rise in the temperature of the shaded cell of the panel 2 (string 2) to 80°C with the consequent initiation of the localized heating of the shaded cell to exceedingly high temperatures of up to 99.5°C as shown in Fig. 2.16(b). This condition must not be sustained for a significant time, otherwise, it may lead to cell destruction and irreversible module failure. It was observed that the standard BPD failed to counter the localized temperature rise in the shaded cell due to its inability to get into conduction for low shading conditions ($<$ 2 cells). On the contrary, the

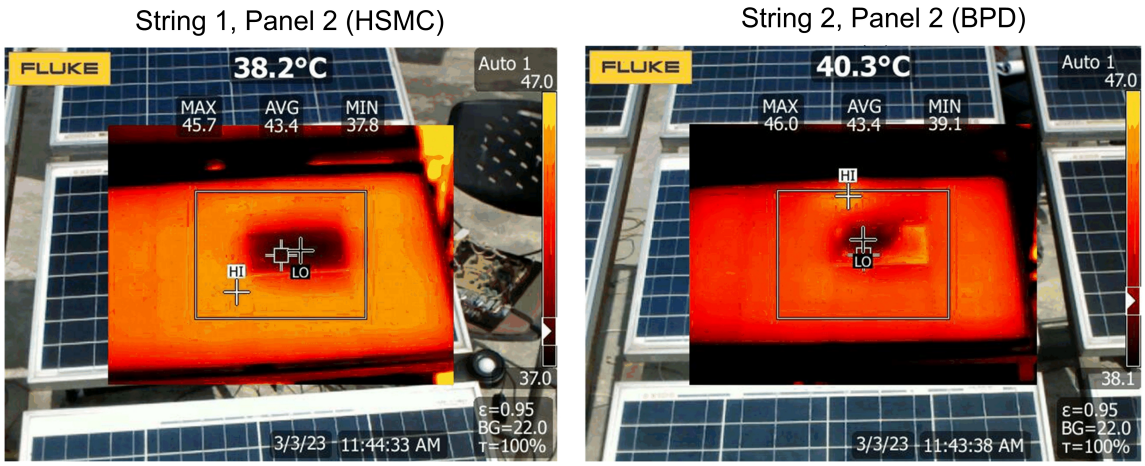

FIGURE 2.17: Thermographic analysis (near MPOP) of the shaded module of two 3×1 PV strings under consideration: (a) Two cells shaded (with HSMC) (b)Two cells shaded (with BPD).

maximum temperature of the shaded cell of panel 2 (string 1) protected through HSMC under the one-cell shading scenario was recorded to be 45.4°C, as shown in Fig. 2.16(a) which is well within the safe limits. As the number of shaded cells increases, BPD goes into conduction under two cells shading scenario, thus bypassing the affected module. The PV strings were again left unattended for approx. 37 min . It is observed that the maximum temperature reached in the shaded cells for the respective modules under two cell shading for both the bypass strategies is respectively 45.7°C and 46°C [see Fig. 2.17(a) and (b)] which falls within the safe operating limit of the individual shaded modules.

2.4.2.2 Thermal response on 3×3 PV Array

Different modules of the array were shaded. The maximum temperature of the module equipped with BPD on shading with one cell reached 80.6°C [see Fig. 2.18(a)]. On the contrary, the maximum temperature of the HSMC protected module was recorded to be 52.3°C under one cell shading [see Fig. 2.18(b)]. As the shading area is increased, the thermal behavior of both the shaded modules shows similar nature. This confirms that BPD performs satisfactorily when the shading area is higher than close to 2 cells leading to safe operation, however, it completely failed under low shading conditions posing a serious threat to the

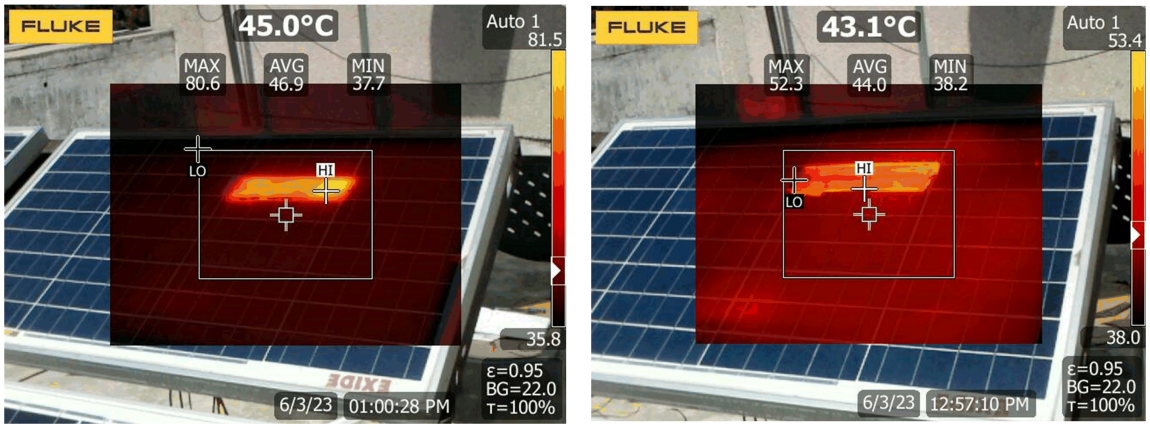

(a) (b)

FIGURE 2.18: Thermographic behavior (near MPOP) of the shaded module of 3 × 3 SP PV array under one cell shading with (a) BPD. (b) HSMC.

TABLE 2.4: Response of the conventional BPD and the proposed HSMC to one cell shading scenario (3 × 3 SP PV array)

Bypass mechanism	String Voltage	String Current	Bypass Current	Operation Status
Case I: Near Open-circuit condition				
With BPD	60.1 V	0.298 A	0.0 A	Safe operation
With HSMC	60.1 V	0.298 A	0.0 A	Safe operation
Case II: Near Short-circuit condition				
With BPD	1.125 V	5.31 A	0.191 A	HS formation
With HSMC	1.166 V	5.35 A	1.72 A	Safe operation
Case III: Intermediary condition				
With BPD	30.58 V	4.59 A	0.068 A	HS [see Fig. 2.18(a)]
With HSMC	31.28 V	4.63 A	1.31 A	Safe [see Fig. 2.18(b)]

system's reliability. The key experimental measurements of 3 × 3 SP PV array under different operating conditions are reported in Table 2.4.

2.5 Summary

This chapter delves into the prevalent challenge of HS formation in PV systems and introduces a novel approach aimed at mitigating this issue to enhance system reliability and performance under shading conditions. A critical assessment of conventional BPDs is presented, identifying their inability to effectively address localized heating during shading events, often resulting in reduced module reliability. The research presents several significant contributions to the field of PV systems, particularly in addressing the challenges posed by HS formation. The primary contributions are outlined as follows:

1. ***Improved HS Mitigation Approach:*** A novel method to mitigate localized heating in PV modules is proposed, resulting in enhanced power extraction and improved system reliability under PSCs.

2. ***Quantification of Reverse Breakdown Behavior and Power Loss:*** The study quantifies the reverse breakdown behavior and associated power loss in fully shaded cells within a scaled-down PV module under HS conditions, offering deeper insights into the phenomenon.

3. ***Limitations of Standard BPDs:*** The inability of conventional BPDs to effectively address localized heating under low shading scenarios is demonstrated, emphasizing their adverse impact on module reliability.

4. ***Power Loss Analysis:*** An analysis of power loss is conducted for both conventional BPDs and the proposed approach, revealing that module-integrated BPDs channel significant string currents during increased shading events, exacerbating power losses.

5. ***Effectiveness of the HSMC:*** Experimental findings reveal that the proposed HSMC substantially reduces the maximum temperature of shaded cells compared to traditional BPDs. The HSMC achieves up to an 89.82% reduction in power loss through bypass paths under shading conditions, significantly enhancing system reliability and thermal stability.

Chapter 3

Optimal Shade Dispersion Strategies for Enhanced Power Extraction Under PSCs

3.1 Preamble

The pursuit of energy independence is increasingly reliant on the effective harnessing of renewable energy sources, with solar energy emerging as a front runner in this transition towards sustainable energy solutions. The global acceptance of PV systems has been significantly bolstered by advancements in manufacturing technologies and a notable reduction in the costs associated with PV cell production. However, a critical challenge that persists in the optimal utilization of PV systems is the phenomenon of PSCs.

PSCs can severely hinder the performance of PV arrays, leading to a decline in efficiency due to the mismatch in current generation among the modules. This mismatch is often exacerbated by external factors such as moving clouds, dust accumulation, and nearby obstructions like trees and buildings, which can cast shadows on the PV modules. The implications of PSCs are profound, as they not only reduce the overall power output but also complicate the management of energy production in PV systems.

To address these challenges, this thesis introduces a number of novel static optimal SD strategies aimed at mitigating ML by uniformly distributing shade across the entire PV array. The proposed generalized module repositioning

approaches are adaptable to various array configurations, whether symmetrical or asymmetrical, and is designed to enhance power extraction under PSCs.

The research presented herein includes simulations conducted on a 9×9 PV array under common shading scenarios, followed by experimental validation on both symmetrical 5×5 and unsymmetrical 6×4 configurations. The findings demonstrate the effectiveness of the proposed schemes and their variants in optimizing power output while maintaining the integrity of the electrical connections. Furthermore, the proposed methods are benchmarked against a range of contemporary reconfiguration techniques, showcasing significant improvements in performance metrics, including a reduction in MLs by up to 76.3% compared to traditional configurations.

This chapter delves into the intricacies of the proposed strategies, their implementation, and the resultant efficiencies achieved, thereby contributing to the broader discourse on enhancing the viability of solar energy systems in the face of PS challenges.

The remainder of the chapter is organized as follows: Section 3.2 explores the impact of shading and temperature on the performance of PV arrays, providing valuable insights for developing effective strategies to mitigate PSCs. Section 3.3 discusses traditional configurations like TCT and introduces innovative approaches such as GMRA, SP-GMRA, GPRS, SP-GPRS, and CDMRA, all aimed at optimizing power extraction under shading. This section also presents simulation results and experimental validation of the proposed module rearrangement strategies, demonstrating their effectiveness in enhancing power output and reducing ML. Section 3.4 evaluates the efficiency and techno-economic viability of these strategies, assessing their practical implementation in real-world PV systems. Finally, section 3.5 summarizes the key findings, highlighting the potential of the proposed strategies to improve PV system efficiency under PSCs.

3.2 Electrical characteristics of a PV Array

Understanding the electrical behavior of PV arrays under various operating scenarios and the underlying principles of optimal SD is essential for developing

an efficient SD strategy for maximizing power harvesting from a PV array. The PV array displays intriguing behavior as a result of high correlations with numerous external parameters, with temperature and irradiance standing out as the most significant.

The modeling of a PV array and its response is considered next.

3.2.1 Steady Irradiance Conditions

Several PV cells connected serially make up a PV module. The single-diode model shown in Fig. 3.1(a) is employed in this work [149]. The voltage (V_G) and generated current (I_G) of a PV module are related

$$I_G = I_L - I_{\text{rev}} \left[\exp\left(\frac{V_G + R_s I_G}{k V_{Th}} \right) - 1 \right] - \frac{V_G + R_S I_G}{R_p} \tag{3.1}$$

where I_L is the module's light-induced current, I_{rev} is the reverse saturation current of the electrical diode equivalent, k is the ideality factor, and V_{Th} represents thermal voltage. Further, R_s and R_p represent module equivalent series and shunt resistances, respectively. Since the light-induced current I_L in (3.1) is dependent on irradiance S_a and temperature T [150], the panel-generated current I_G is also expressed as

$$I_G\left(S_a, T\right) = I_{SC,0} \left(\frac{S_a}{S_{as}} \right) \left[1 + \gamma \left(T - T_s \right) \right] \frac{\left(R_s + R_p \right)}{R_p} \tag{3.2a}$$

where $I_{SC,0}$ is the module's current corresponding to the short circuit at standard irradiance and temperature conditions $\left(S_{as} = 1000\,\text{W/m}^2; T_s = 25^0\text{C} \right)$ and γ represents the temperature-dependent constant of the module's current

$$I_G = I_{SC,0} \times \left(\frac{S_a}{S_{as}} \right) = \alpha \times I_{SC,0} \quad \forall T = T_s \tag{3.2b}$$

where the shading ratio, $\alpha = \left(\frac{S_a}{S_{as}} \right), \alpha \in [0, 1]$ where $\alpha = 1$ and $\alpha = 0$ corresponds to a fully illuminated and completely shaded module, respectively. The I-V characteristic equation under SIC for any arbitrary-sized array comprising N_s

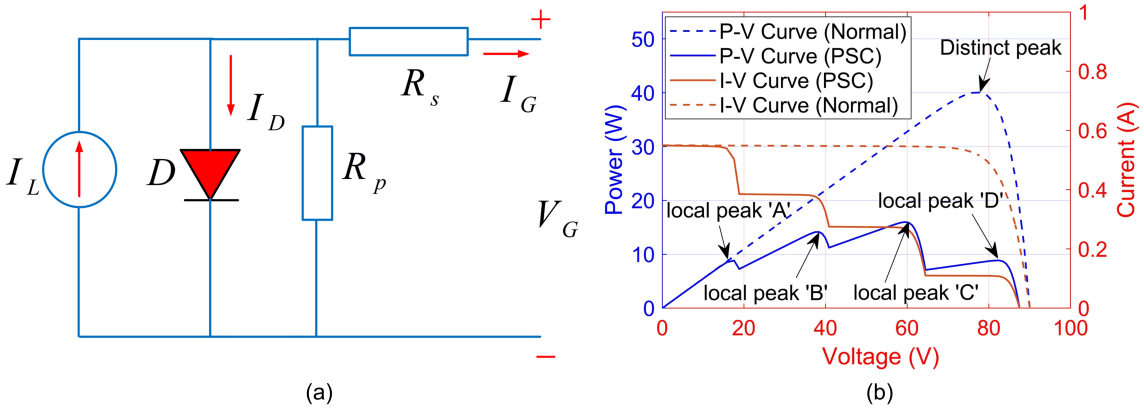

FIGURE 3.1: PV source: (a) Electrical circuit model of a PV cell. (b) PV electrical characteristics under SIC and PSCs (multiple peak generation).

series modules in each N_p shunt connections is as follows:

$$I_{\text{pv}} = N_p \times (I_L - I_{\text{rev}}) \left[\exp\left(\frac{V_G + \frac{N_s}{N_p} R_s I_G}{k N_s V_{Th}} \right) - 1 \right] + \frac{V_G + \frac{N_s}{N_p} R_s I_G}{\frac{N_s}{N_p} R_p} \tag{3.3}$$

Using (3.1), (3.2a, 3.2b), and (3.3), the PV module and array considered in this work are modeled.

3.2.2 Partial Shading Conditions

The BPD gets activated due to radiation mismatch among modules under PSCs. BPDs provide an alternate path for the current to flow, thus bypassing the shaded module and averting its possible damage due to HS formation, though not completely. This results in the formation of staircase I-V curve with the appearance of multiple peaks in the resultant P-V curve [83]. Fig. 3.1(b) shows typical electrical characteristics of a PV array under SIC and PSC.

3.2.3 Estimation of Mismatch Loss for Optimal Shade Dispersion

For any $i \times j$ PV array arrangement, to quantify the effectiveness of any SD strategy, estimation of ML is vital and can be obtained from the difference between the resultant sum of individual maximum generated module powers

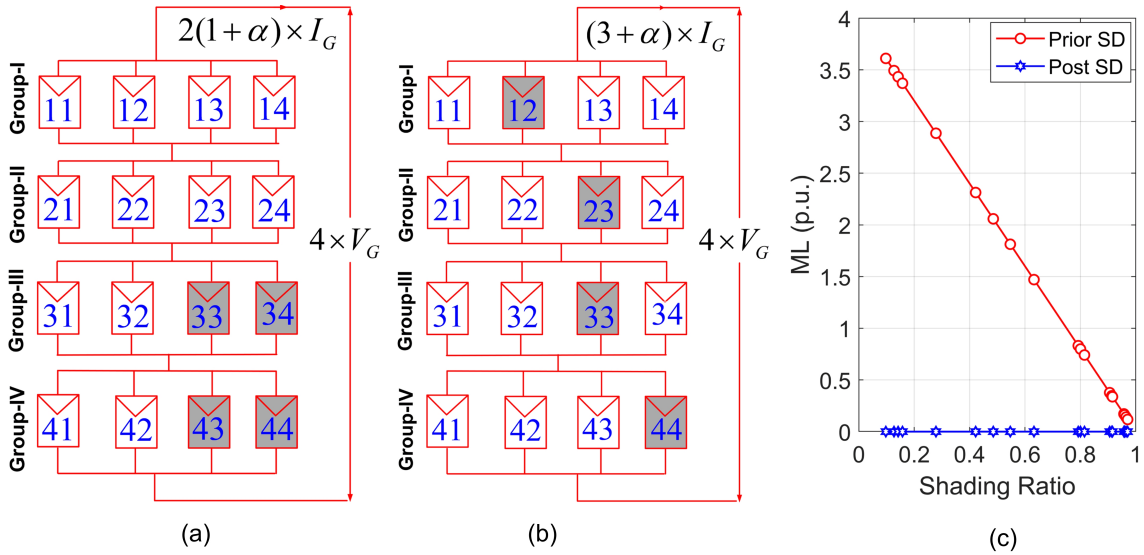

FIGURE 3.2: (a) 4×4 TCT under a typical 2×2 PSC. (b) Optimal SD through a repositioning approach. (c) ML as a function of SR prior and post application of SD approach.

and the total array power under PSCs as follows:

$$\mathrm{ML} = \sum_{q=1}^{i\times j} P_{m,q} - P_{\text{array}} \tag{3.4}$$

where $P_{m,q}$ and P_{array} are, respectively, the optimal generated powers from the q th module and the entire PV array under PSCs. Fig. 3.2(a) shows a typical 2×2 shading event on a 4×4 PV array with four modules under the impact of shading. The array can be partitioned into four individual groups connected serially, each having four parallel PV units. Here, the current generated by the unshaded and shaded modules is I_G and αI_G, respectively. As mentioned earlier, " α " is the shading ratio. The optimal SD achieved after module reconfiguration is shown in Fig. 3.2(b). The ML is estimated under two cases as shown below:

1) Case I- 4 × 4 TCT Array Under 2 × 2 Shading (Prior SD): Two modules each in groups III and IV are shaded. The 12 unshaded modules and 4 shaded modules individually generate maximum powers of $(12V_G \times I_G)$ and $4\alpha I_G \times V_G$, respectively. For the estimation of the GP power of the PV array, P_{array} , first, the currents of the individual groups of the array are determined. Since different groups contribute different currents, the existence of multiple peaks in the PV

curve is inevitable. The panels in group IV will be bypassed first, followed by group-III, II, and finally group-I having voltages of $4V_G, 3V_G, 2V_G$, and V_G, respectively. The array peak power under this condition is estimated to be $8V_G \times I_G(1+\alpha)$. The ML using (4) can be estimated as:

$$ML|_{4\times4}^{\text{prior } SD} = \underbrace{[(12V_G \times I_G) + 4\alpha I_G \times V_G]}_{\sum_{q=1}^{4\times4} P_{m,q}} - \underbrace{[8V_G \times I_G(1+\alpha)]}_{P_{\text{array}}} = 4(1-\alpha)V_G \times I_G. \tag{3.5a}$$

2) Case II- 4×4 PV Array Modules Reconfigured to Obtain Optimal SD Using a Repositioning Approach (Post SD): Post application of the SD approach, the shade gets dispersed across various rows of the PV array, thus minimizing the group current difference. Each group now has only one shaded module. The resultant ML can be estimated as before

$$ML|_{4\times4}^{\text{post SD}} = \underbrace{[(12V_G \times I_G) + 4\alpha I_G \times V_G]}_{\sum_{q=1}^{4\times4} P_{m,q} \quad \forall q=1,2,3...16} - \underbrace{[4V_G \times (3+\alpha) \times I_G]}_{P_{\text{array}}} = 0 \tag{3.5b}$$

In this manner, an effective SD strategy disperses any shade pattern to alleviate the ML, thus ensuring the optimal utilization of the PV array arrangement. Fig. 3.2(c) shows the variation in ML as a function of shading ratio, α, prior and post SD. It can be observed that post-SD, the ML decreases considerably.

3.3 Description of PV Array Configurations

This section gives the description of different PV array configurations including the various proposed module rearrangement techniques.

3.3.1 PV Array in TCT Configuration

The power extraction from a PV array configured in a TCT arrangement is analyzed under various PSCs. The output voltage and current extracted from a

TABLE 3.1: Parametric data of a PV module at STC used in this work

Parameter	Simulation	Experimental
Optimal power output (P_{max})	50 W	10 W
Voltage at MPP $(V_{pv,m})$	19.95 V	20 V
Current at MPP $(I_{pv,m})$	2.51 A	0.50 A
Short circuit current (I_{sc})	2.63 A	0.60 A
Open circuit Voltage (V_{oc})	22.26 V	24.8 V
Dimensions (L × W × H)	430 × 665 × 35 mm	255 × 350 × 22 mm

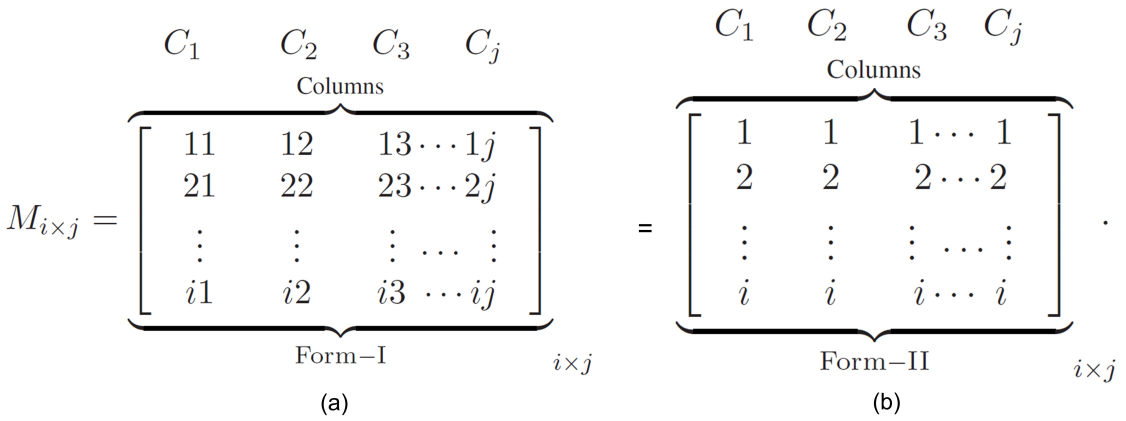

FIGURE 3.3: Representations of the PV array used in this work: (a) Form-I. (b) Form-II.

$i \times j$ TCT-arranged PV array can be expressed as given by

$$I_{\text{pv}} = \sum_{q=1}^{j} I_{G,pq} \quad \forall p = 1, 2, \ldots, (i-1) \tag{3.6}$$

$$V_{\text{pv}} = \sum_{p=1}^{i} V_{G,pq} \quad \forall q = 1, 2, \ldots, (j-1). \tag{3.7}$$

Fig. 3.3 gives the two representations of the PV array used in this work

The module parametric specifications at standard test condition (STC) employed for simulation and experimental analysis are listed in Table 3.1.

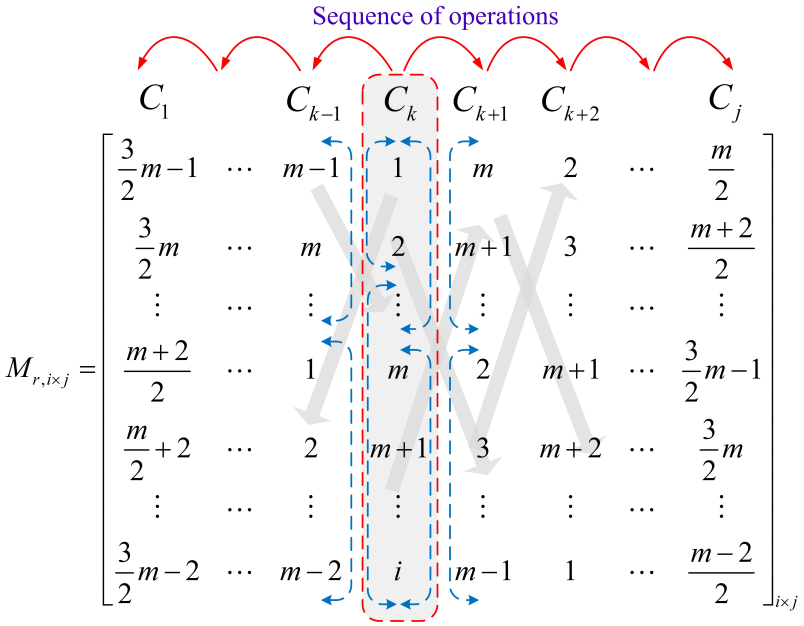

FIGURE 3.4: Illustration showing PV array restructuring using the proposed GMRA technique.

3.3.2 Proposed GMRA and SP-GMRA for Optimal Shade Dispersion

In any PV array arrangement, each PV module position can be identified by a definite row and column index value as depicted in 3.3. For instance, module position " $1j$ " corresponds to a row index value " 1 " and column index value " j." Only the row indices are modified in the proposed GMRA, while the column indices remain unaltered.

1) Case I: $i \times j$ ***PV Array, where,*** $i =$ ***Odd Number:***

Step 1: Identify the primary column, C_k, in the PV array, where $k = \left\lceil \frac{j}{2} \right.$, the ceil operator " $\lceil$ " rounds a real number to the lowest next integer. Next, arrange the primary column row index values sequentially in ascending order as shown in Fig. 3.4. Steps 2 and 3 describe the further restructuring of the PV array located to the right and left of the primary column, respectively.

Step 2: Divide the entire PV array located to the right of the primary column, C_k, including the primary column itself, into two groups i.e., top and bottom w.r.t row index values. The bottom group starts with the mth row index of the primary column, where $m = \left\lceil \frac{i}{2} + 1 \right.$ and continues sequentially until the last row

index in the column. The remaining row index values of the primary column constitute the top group. The row index values in the subsequent column C_{k+1} are obtained by replacing the top and bottom group row index values of the column with the bottom and top group row index values of the preceding column C_k, respectively, in a sequential order and so on.

Step 3: Divide the entire PV array located to the left of the primary column, C_k, including the primary column itself, into two groups i.e., top and bottom w.r.t row index values. The bottom group starts with the $(m-1)$ th row index value of the primary column, C_k, and continues sequentially until the last row index in the column. The remaining row index values of the primary column constitute the top group. The row index values in the preceding column C_{k-1} are achieved by replacing the top and bottom group row index values of the column with the bottom and top group row index values of the subsequent column, C_k, respectively in a sequential manner and so on.

Likewise, the row index values of the remaining columns are obtained following the aforementioned steps and the final reconfigured TCT array using GMRA is obtained. After the application of GMRA, a 9×9 PV array is shown in Fig. 3.5(a).

Step 4: To obtain the final reconfigured SP PV array using SP-GMRA, the row and column index values obtained using GMRA are interchanged before implementation on an SP configuration. This means that the module positions identified as " 81 ," " 45 ," and " 36 " in GMRA marked by dotted circles in Fig. 3.5(a) correspond to "18," "54," and " 63 " respectively, in SP-GMRA, and so on.

2) Case II: $i \times j$ ***PV Array, where,*** $i =$ ***Even Number:***

Step 1:Identify the primary column, C_k, in the PV array, where $k = \frac{j}{2} + 1$ for $j =$ even number, and $k = \left\lfloor \frac{j}{2} \right.$ for $j =$ odd number. Next, sequentially arrange, C_k, row indices in ascending order.

Step 2: Divide the entire PV array into two halves (groups) including the primary column, C_k, w.r.t row indices.

Step 3(a):The module positions for the subsequent column C_{k+1} is achieved by replacing the top and bottom group row index values in the column with the bottom and top group row indices of the preceding column, C_k, respectively, and so on.

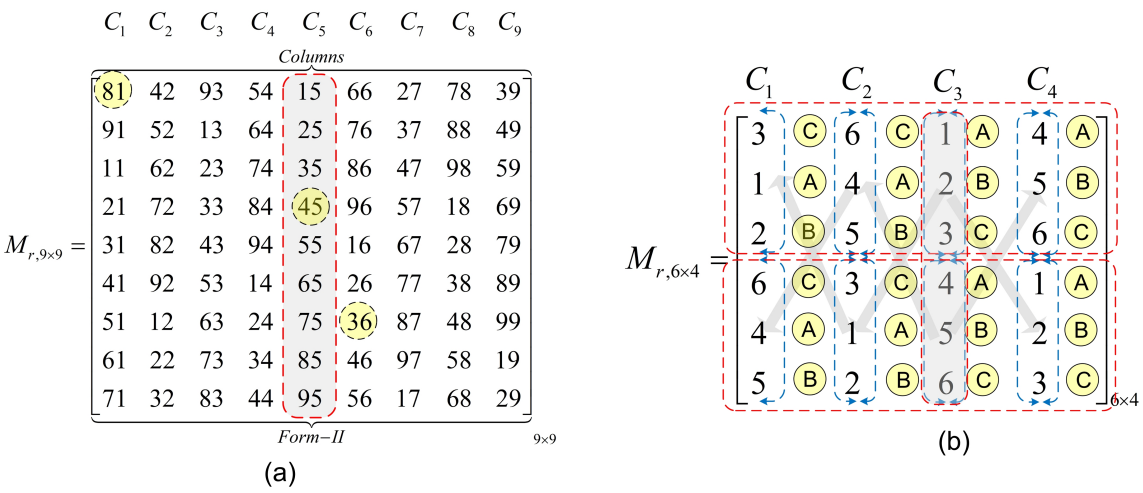

FIGURE 3.5: Reconfigured PV array using the proposed GMRA: (a) 9×9 PV array (symmetrical) (b) 6×4 PV array (unsymmetrical).

Step 3(b): The module positions for C_{k+2} are achieved by first shifting the row index values in an anticlockwise manner, beginning with the bottom-most member for each group of the preceding column C_{k+1}, followed by the replacement of the top and bottom group row index values of the column with bottom and top group row index values of the preceding column, C_{k+1}, respectively. This is done to avoid any repetition of the columns. The same procedure is applied for the remaining columns positioned to the right.

Step 4(a): The row indices for C_{k-1} and preceding columns except C_1 is achieved by following the same procedure as described above in step 3(b).

Step 4(b): The first column C_1 row indices are obtained by performing a similar operation on the column C_2 as described in step 3(a). This step is followed for all array configurations of the form $i \times j$, where $i = j$ or $i \neq j$. An unsymmetrical 6×4 PV array is repositioned post-GMRA application as depicted in Fig. 3.5(b).

The circuit arrangement of the TCT configuration and the proposed GMRA for a 5×5 PV array with fixed electrical connections is shown in Fig. 3.6(a) and (b) respectively.

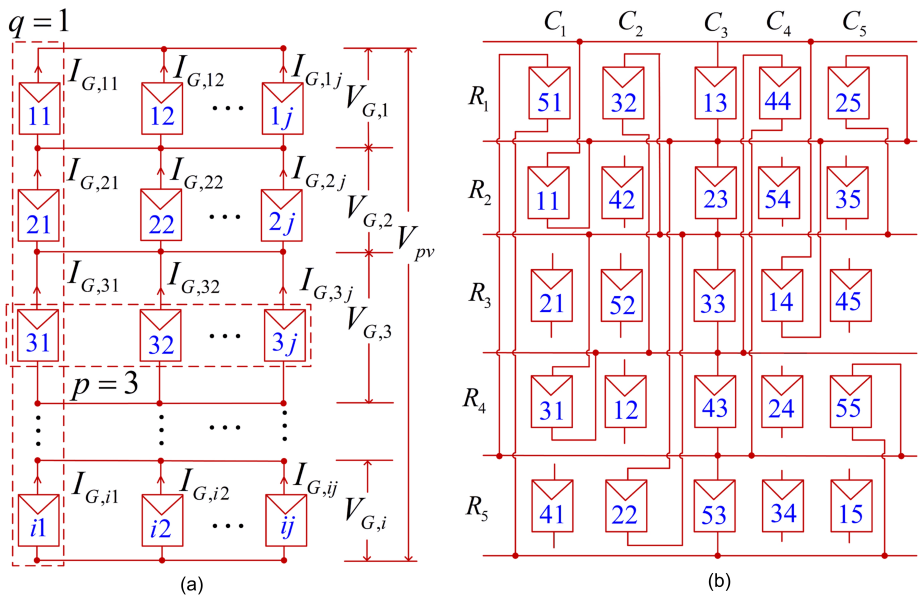

FIGURE 3.6: (a) $i \times j$ PV array connected in TCT configuration. (b) GMRA with the fixed electrical connection of PV modules for a 5×5 PV array.

3.3.3 Proposed GPRS and SP-GPRS Module Rearrangement Strategy

The proposed reorganization approach is valid for any $p \times q$ array dimensions where p, q can hold even, odd, or both values. Here " p " and " q " represent the total rows and columns in an array, respectively. Moreover, the proposed rearrangement strategy is equally valid for any symmetrical $(p = q)$ and unsymmetrical $(p \neq q)$ array structures.

Step 1: The index values corresponding to the rows in the first column C_1 are arranged in descending order as depicted in Fig. 3.7.

Step 2: Partition the entire PV array into " n " sections w.r.t. rows, i.e., $S_1, S_2, \ldots, S_n$, where $n = \lceil \frac{p}{3} \rceil$ (refer Fig. 3.7). The ceiling function, " $\lceil$ " rounds the result to the lowest next integer. Each section consists of a maximum of three elements from each column. The first three row indices namely, " p," " $p-1$," and " $p-2$ " in column C_1 form the first section, S_1. The following three row indices constitute the second section, S_2, and so on.

Step 3: The process of reconfiguration commences with the first column, C_1 and is subsequently applied to all the following columns in the array, proceeding

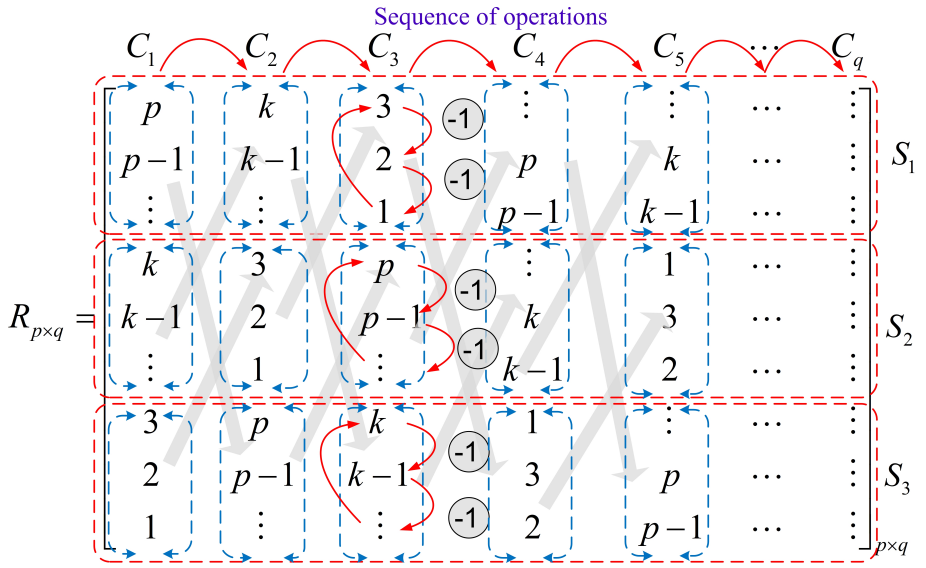

FIGURE 3.7: Illustration showing PV array restructuring using the proposed GPRS approach.

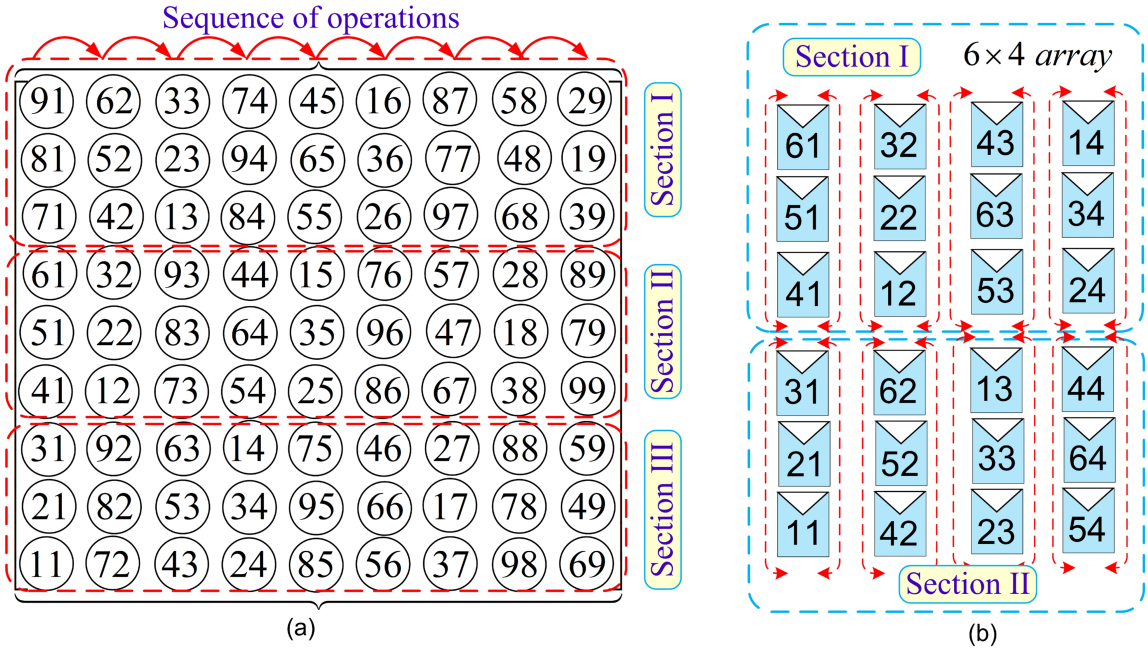

FIGURE 3.8: Proposed GPRS reconfigured PV arrays. (a) 9 × 9 PV array [symmetrical array structure, $(p = q)$]. (b) 6 × 4 PV array [unsymmetrical structure, $(p \neq q)$].

from left to right.

Step 4: The members in the second and third sections of C_1 are reassigned as

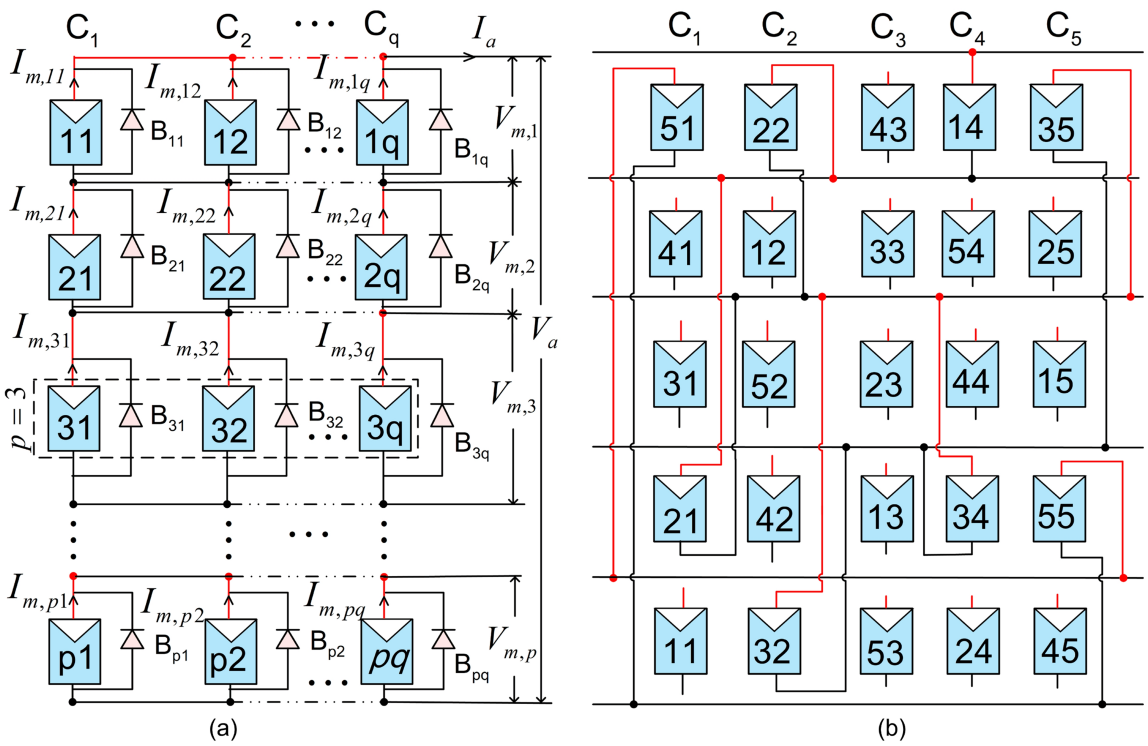

FIGURE 3.9: Circuit diagram. (a) TCT configuration. (b) Proposed GPRS arrangement for a 5×5 PV array.

the first and second section members in the next column, C_2 respectively. Likewise, the first section members of C_1 are assigned as the members of the third section in the following column, C_2. This sequence of operations is iteratively applied to all the subsequent columns in the array until the replication of columns (row indices) is observed.

Step 5: If the application of step 4 leads to the creation of a duplicated column, $C_n, \forall n \in 4, 5, \ldots, q$, each section member in the preceding column, C_{n-1} undergoes a one-position downward shift within their respective sections. This results in the final element of each section shifting upwards by two places as shown in Fig. 3.7. This adjustment occurs before the element's assignment to the subsequent column, C_n. The subsequent reconfiguration of a PV array using GPRS involves following the same procedure described in step 4 until column duplication occurs, at which point step 5 is executed.

Step 6: In the SP-GPRS arrangement, the optimization of PV module placement involves swapping of row and column indices within the final array achieved

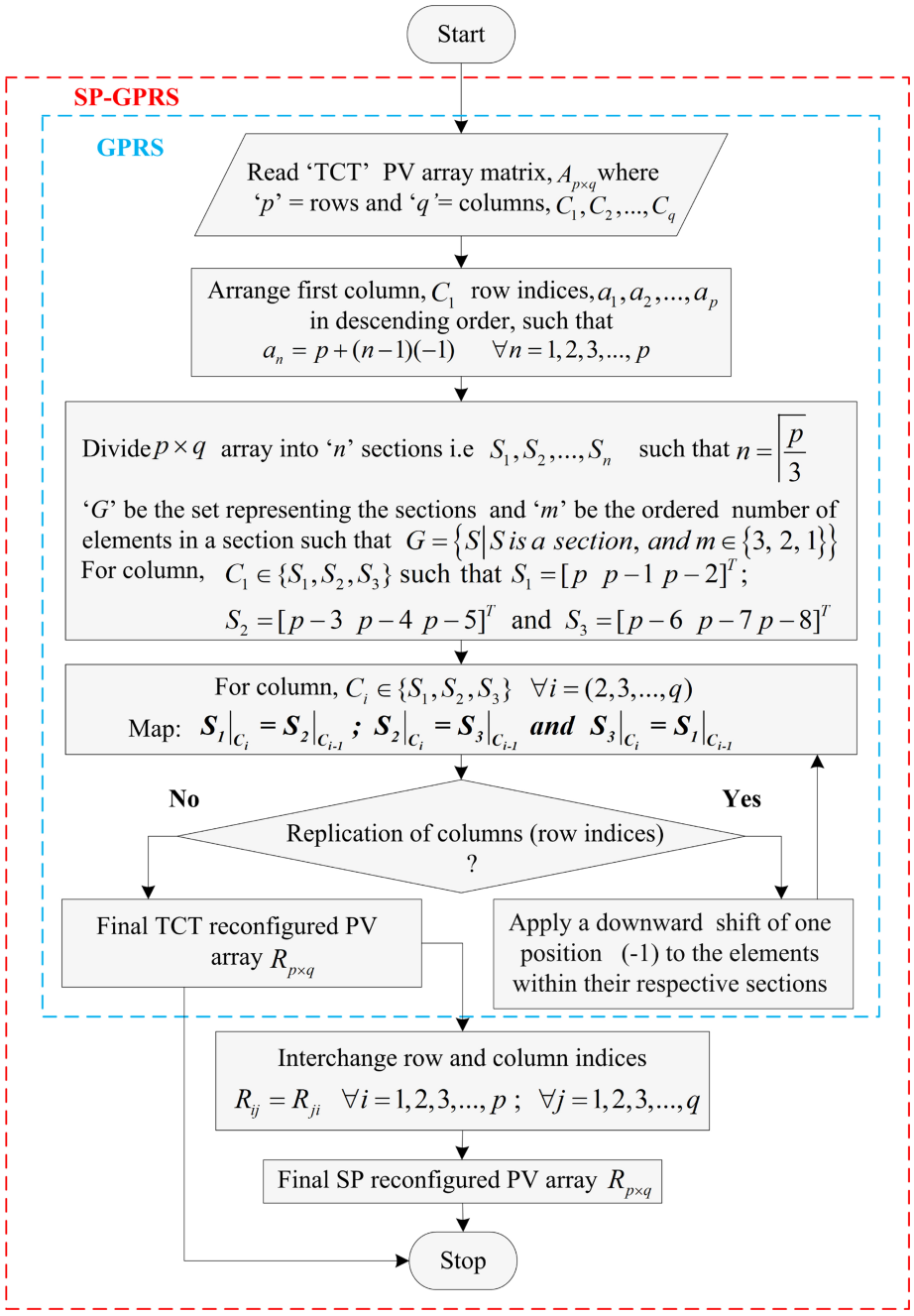

FIGURE 3.10: Detailed flowchart of the proposed GPRS and SP-GPRS approach.

using GPRS. For instance, if a PV module occupies positions " 18 " and " 53 " in the GPRS-reconfigured array, it is relocated to " 81 " and " 35 " in the SP-GPRS arrangement respectively. The final reconfigured symmetrical (9×9) and unsymmetrical (6×4) PV arrays, utilizing the proposed strategy, are depicted in

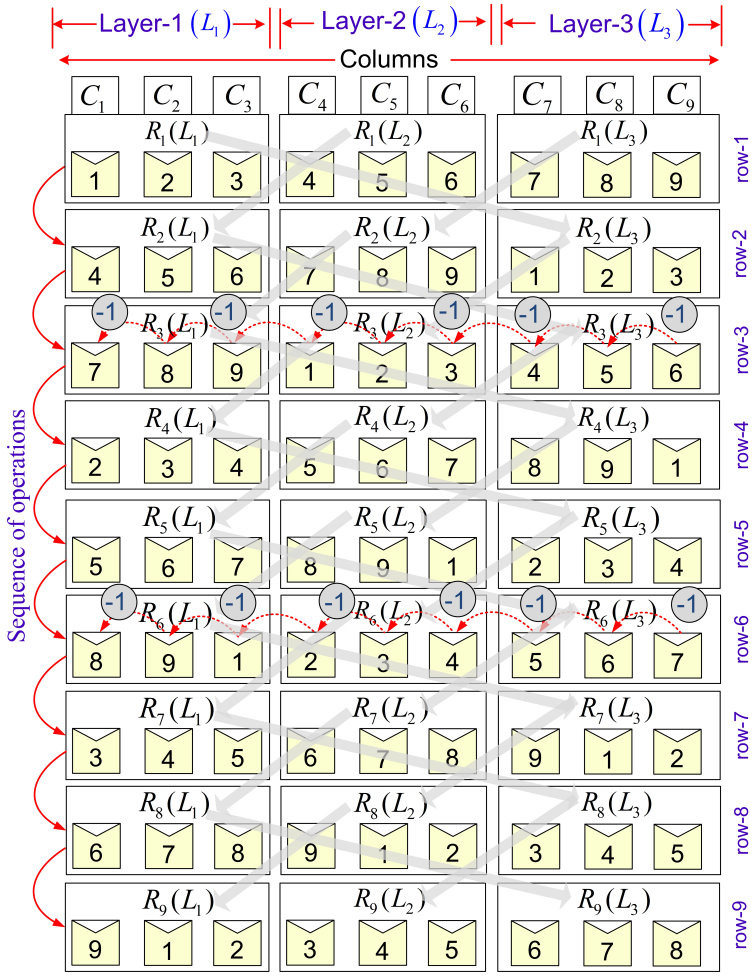

FIGURE 3.11: The complete layout of the proposed CDMRA technique implemented for a 9×9 structure.

Fig. 3.8(a) and (b), respectively. Electrical connection diagrams for TCT and the proposed GPRS approach are shown in Fig. 3.9(a) and (b). The detailed flow diagram depicting the various operational steps of the proposed approach is shown in Fig. 3.10

3.3.4 Proposed Cross-Diagonal Module Rearrangement Approach (CDMRA)

The proposed rearrangement approach is valid for any $r \times c$ PV array dimensions where r, c can hold even, odd, or both values. Here r and c represent

the total rows and columns in an array, respectively. The proposed approach optimizes PV module positions within the array without altering the end-to-end terminal connections. Notably, the modules are shifted within the same column, significantly reducing wiring requirements compared to other rearrangement strategies that involve shifts both row-wise and column-wise. To achieve the final reconfigured array for uniform shade attenuation under different inconsistent irradiance scenarios using the proposed approach, CDMRA, the following steps are executed sequentially:

Step 1: Divide the entire PV array into ' s ' layers w.r.t columns, where $s = \lceil \frac{c}{3} \rceil$ and each layer comprises a maximum of three members from each row, as illustrated in Fig. 3.11.

Step 2: The reconfiguration process begins with the first row and is then applied successively to the remaining rows until reaching the last row, R_r.

Step 3: In the first row, place PV modules sequentially in the ascending row index order, as shown in Fig. 3.11.

Step 4: The precise locations of the PV units for any k th row under different layers are determined by following the rule outlined in (3.8)

$$\left(R_k\left(L_q\right)\big|_{\text{new}} = R_{k-1}\left(L_{q+1}\right)\right) \quad \forall k = 2,3,\ldots,r; \forall q = 1,2,\ldots,s \tag{3.8}$$

For instance, the row indices of R_2 within the third layer, L_3 are mapped as updated values for R_3 within second layer, L_2 Likewise, module positions for different rows are achieved. If the limit for the index values corresponding to the row and layer gets violated, the rule given above in (3.8) will hold by making slight adjustments as indicated in Fig. 3.11.

Step 5: To avoid duplication of row indices in the same layers across different rows, the members of the defaulter row are shifted one position towards the left before executing step 4. Fig. 3.11 depicts the entire layout of the implemented proposed CDMRA technique for a 9×9 PV arrangement. The detailed flow diagram of the proposed CDMRA technique is depicted in Fig. 3.12

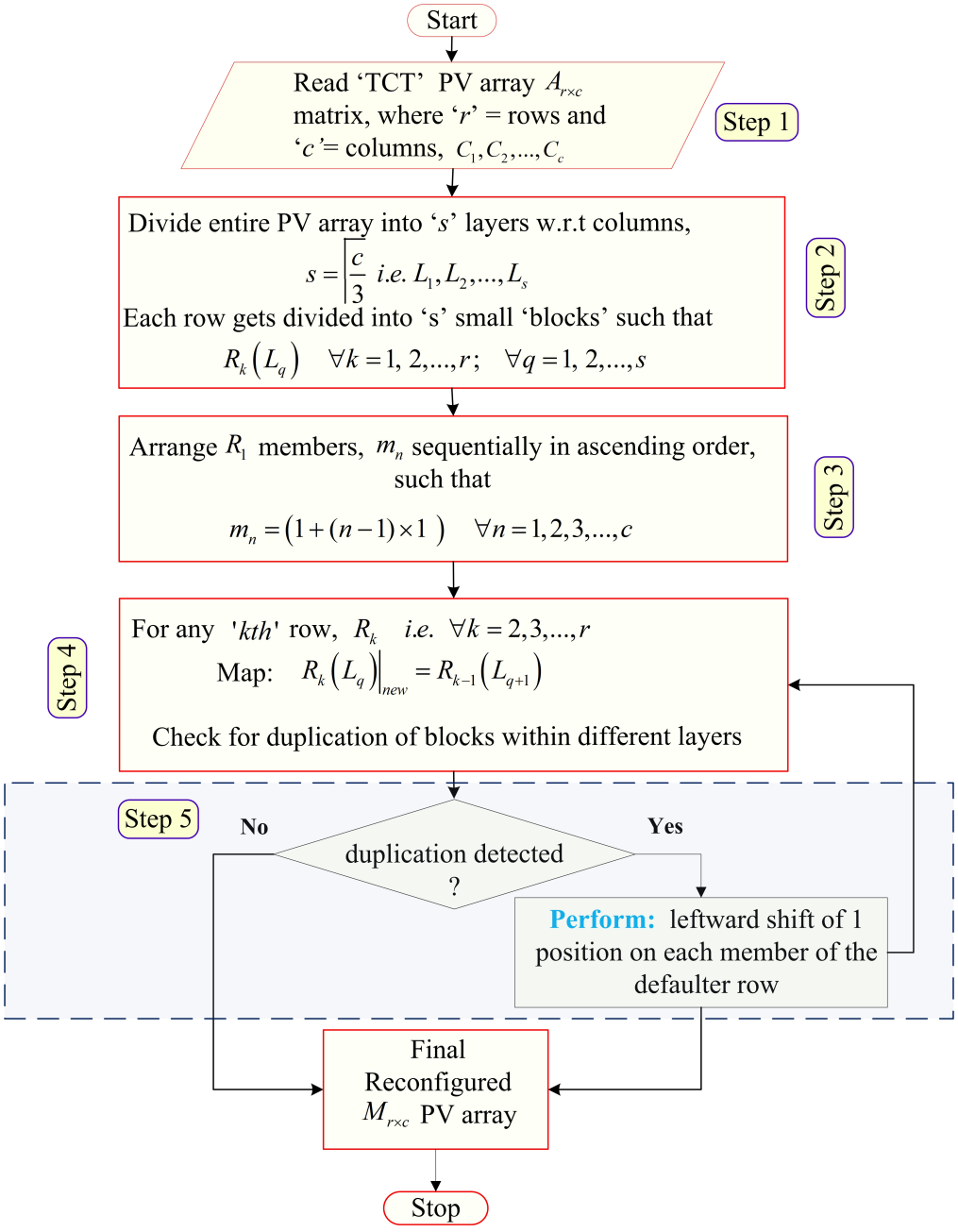

FIGURE 3.12: Flowchart of the proposed CDMRA technique.

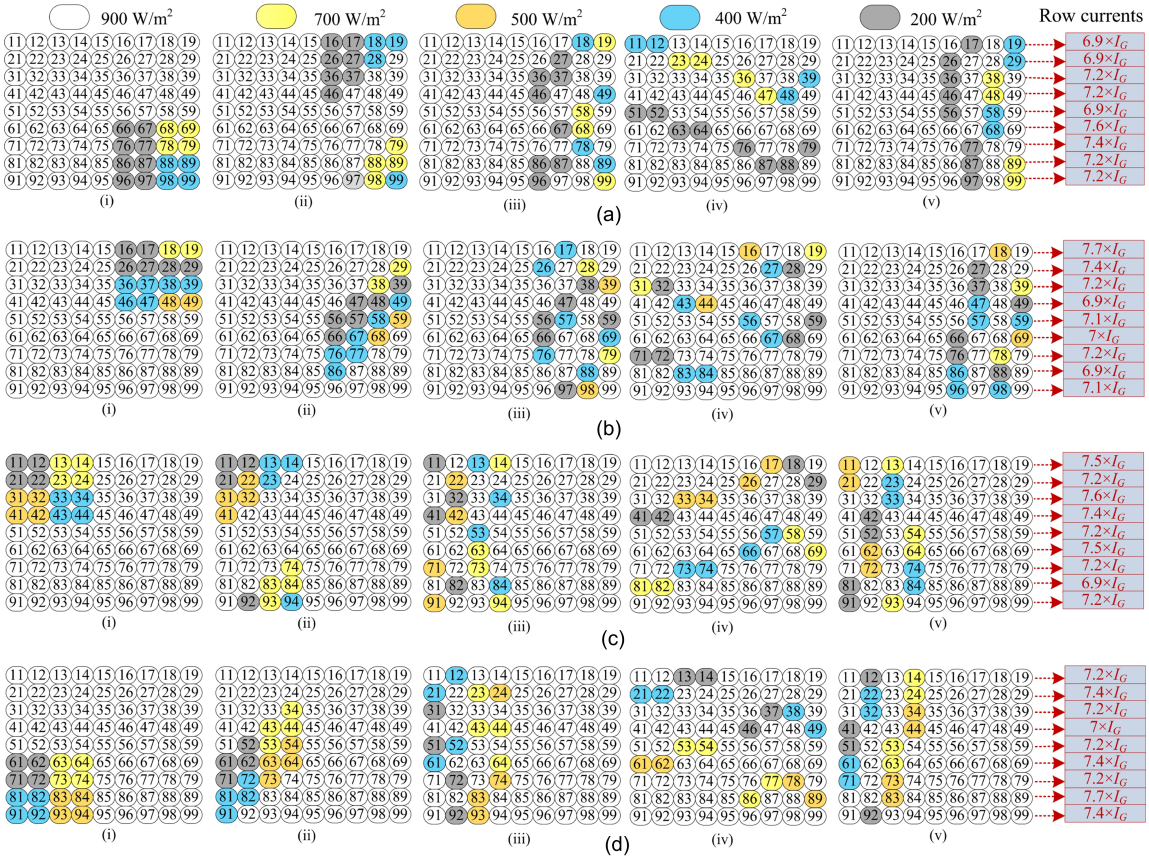

FIGURE 3.13: SD performance on a 9 × 9 PV array under (a) BRC shading scenario, (b) TRC shading scenario, (c) TLC shading scenario, (d) BLC shading scenario with (i) TCT arrangement, (ii) CMAP arrangement, (iii) PRS arrangement, (iv) TTSA arrangement, and (v) proposed GMRA.

3.3.5 Simulation and Performance Analysis of the Proposed GMRA and SP-GMRA Technique

The proposed GMRA's performance is evaluated against the benchmark TCT configuration and three recently published state-of-the-art reconfiguration methods, i.e., CMAP [91], PRS [93], and twisted two step arrangement (TTSA) [87] under four different shading cases, i.e., bottom right corner (BRC), top right corner (TRC), top left corner (TLC), and bottom left corner (BLC).

Figs. 3.13 and 3.14, respectively, show the SD performance and P-V characteristics of a 9 ×9 PV array with different reconfiguration approaches under the impact of aforementioned shading scenarios. The comparative

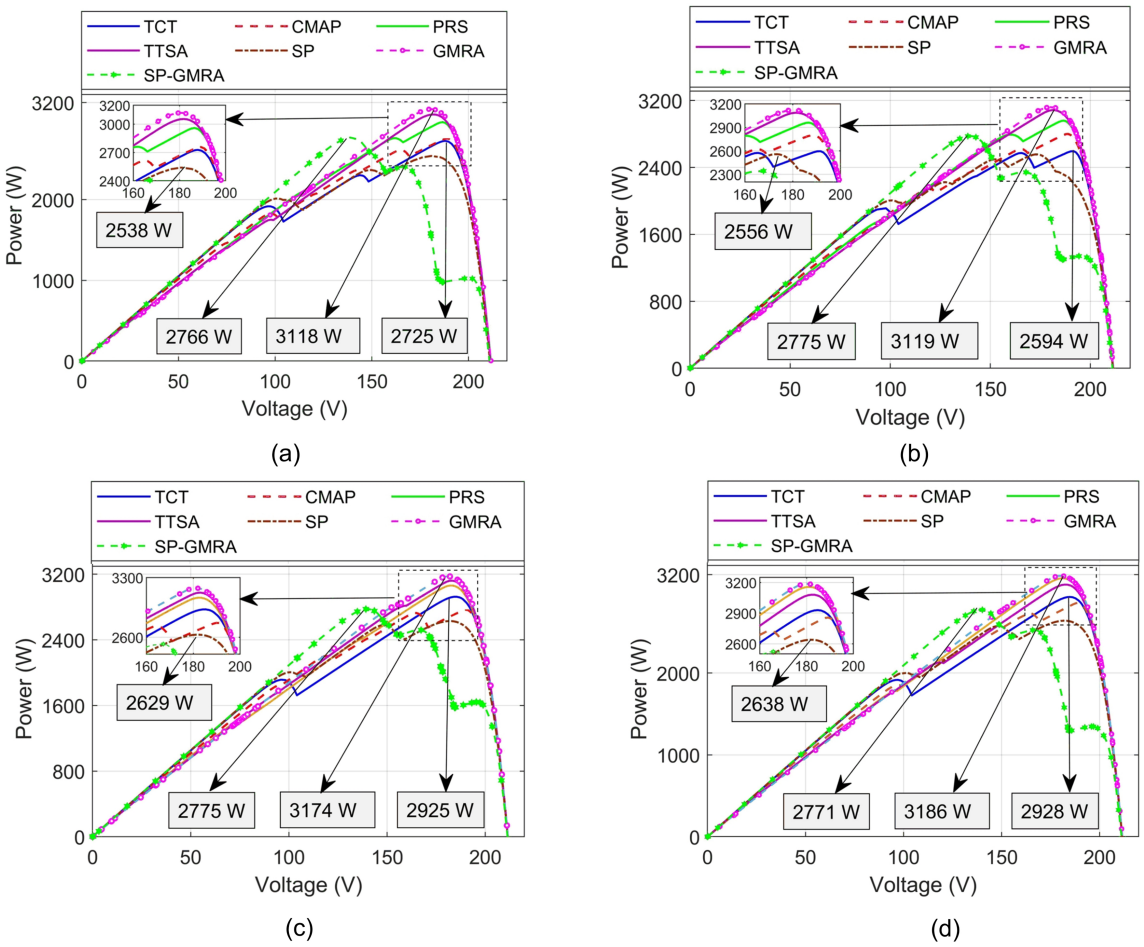

FIGURE 3.14: Simulated P-V characteristics of 9 × 9 PV array under different shading scenarios: (a) BRC. (b) TRC. (c) TLC. (d) BLC.

performance evaluation is done utilizing four important performance metrics such as fill factor (FF), ML, execution ratio (ER), and power enhancement (PE). Additionally, the performance metrics of SP-GMRA are also evaluated against the commonly employed SP configuration. The PE is assessed against TCT and SP configurations for GMRA and SP-GMRA, respectively. Table 3.2 gives a comparative performance estimation of the proposed approach in terms of the aforementioned performance metrics against TCT, CMAP [91], PRS [93], TTSA [87], and SP. To comprehensively examine the overall performance of the proposed technique under different shading scenarios, the average values of various performance metrics from Table 3.2 are considered.

TABLE 3.2: Comparative Performance Analysis of the Proposed Technique with the Existing State of the Art Reconfiguration Approaches

Shading Scenarios	PV configuration	I_{mp}	V_{mp}	P_{mp}	Parametric indicators/Metrics				Optimal configuration
					FF (%)	ML (W)	ER (%)	PE (%)	
BRC	TCT	14.49	188.05	2725	63.8	505	74.6	N.A	GMRA
	CMAP [91]	14.56	189.3	2756	64.5	474	75.5	1.13	
	PRS [93]	15.84	186.64	2956	69.2	274	80.9	8.47	
	TTSA [87]	16.79	181.77	3052	71.5	178	83.6	12	
	SP	14.04	180.76	2538	59.4	692	69.5	N.A	
	GMRA	17.24	180.88	**3118**	**73**	**112**	**85.4**	**14.42**	
	SP-GMRA	19.93	138.8	**2766**	**64.8**	**464**	**75.7**	**8.98**	
TRC	TCT	13.53	191.64	2594	60.7	636	71.0	N.A	GMRA
	CMAP [91]	14.81	188.97	2799	65.5	431	76.6	7.9	
	PRS [93]	15.84	186.77	2959	69.3	271	81.0	14.07	
	TTSA [87]	17.05	180.89	3084	72.2	146	84.5	18.88	
	SP	14.74	173.39	2556	59.9	674	70.0	N.A	
	GMRA	17.36	179.64	**3119**	**73.1**	**111**	**85.4**	**20.24**	
	SP-GMRA	19.81	140.1	**2775**	**65.0**	**455**	**76**	**8.56**	

Table 3.2 (continued)

Shading Scenarios	PV configuration	I_{mp}	V_{mp}	P_{mp}	Parametric indicators/Metrics				Optimal configuration
					FF (%)	ML (W)	ER (%)	PE (%)	
TLC	TCT	15.78	185.38	2925	68.5	365	80.2	N.A	GMRA
	CMAP [91]	14.58	189.75	2766	64.8	524	75.77	-5.43	
	PRS [93]	16.82	181.99	3062	71.7	228	83.8	4.68	
	TTSA [87]	17.05	182.96	3122	73.1	168	85.52	6.73	
	SP	14.39	182.63	2629	61.6	661	72.0	N.A	
	GMRA	17.56	180.73	**3174**	**74.3**	**116**	**86.9**	**8.51**	
	SP-GMRA	19.93	139.18	**2774**	**64.9**	**516**	**76**	**5.51**	
BLC	TCT	15.84	184.7	2928	68.6	362	80.2	N.A	GMRA
	CMAP [91]	15.09	189.2	2855	66.9	435	78.2	-2.49	
	PRS [93]	17.37	181.67	3155	73.9	135	86.4	7.75	
	TTSA [87]	16.91	182.03	3078	72.1	212	84.3	5.12	
	SP	14.53	181.55	2638	61.8	652	72.2	N.A	
	GMRA	17.68	180.18	**3186**	**74.6**	**104**	**87.2**	**8.81**	
	SP-GMRA	19.77	140.14	**2771**	**64.9**	**519**	**75.9**	**5.04**	

1) Fill Factor: It is a measure of the squareness of the I-V characteristics under PSCs, hence an extremely important metric for quantifying the effectiveness of any SD approach. The proposed GMRA produced on average 12.76%, 12.76%, 3.87%, and 2.14% higher FF than TCT, CMAP, PRS, and TTSA arrangements, respectively, under all considered shade cases. Additionally, on reconfiguring the traditional SP configuration using the proposed SP-GMRA, on average 7.1% higher FF was achieved.

2) Mismatch Losses: The ML is estimated similarly as described earlier in (3.5a) and (3.5b). On taking the average of all ML values under different shading cases, the proposed GMRA generates 76.3%, 76.2%, 51.2%, and 37% lower ML compared to TCT, CMAP, PRS, and TTSA configurations, respectively. Moreover, the SP-GMRA arrangement generates 27% lower ML than the SP array.

3) Execution Ratio: The average ER obtained with TCT, CMAP, PRS, and TTSA is 76.5%, 76.5%, 83.0%, and 84.48%, respectively. On the contrary, the proposed GMRA exhibits an average ER of 86.2%. The SP-GMRA offers ER on average, 7% higher than traditional SP configuration.

4) Power Enhancement: The proportionate power enhancement w.r.t TCT is used as a measure to evaluate the relative performance of the proposed GMRA method with CMAP, PRS, and TTSA, while for the SP-GMRA, the performance enhancement is evaluated w.r.t to SP configuration as shown in Table 3.2. On average, the power enhancement attained w.r.t TCT configuration using CMAP [91], PRS [93], TTSA [87] and proposed GMRA is 0.03%, 9.02%, 10.41%, and 12.75%, respectively. Additionally, the power enhancement of 7% is achieved when SP-GMRA arrangement is used over SP connection under different shading conditions. In addition to SD , the row current computations are also shown for the proposed scheme (refer Fig. 3.13).

The proposed scheme produces uniform row (group) currents throughout the array and consistently exhibits the best SD in all cases. As evident from Table 3.2, the proposed scheme outperforms all other reconfiguration methods on prominent performance metrics. The simulated P-V characteristics under different shading conditions are shown in Fig. 3.14. The GP powers attained with TCT, SP, GMRA, and SP-GMRA configurations are also highlighted. The TCT and SP array generates the highest GP powers when the PV arrays are reconfigured using GMRA and SP-GMRA, respectively. Among all considered

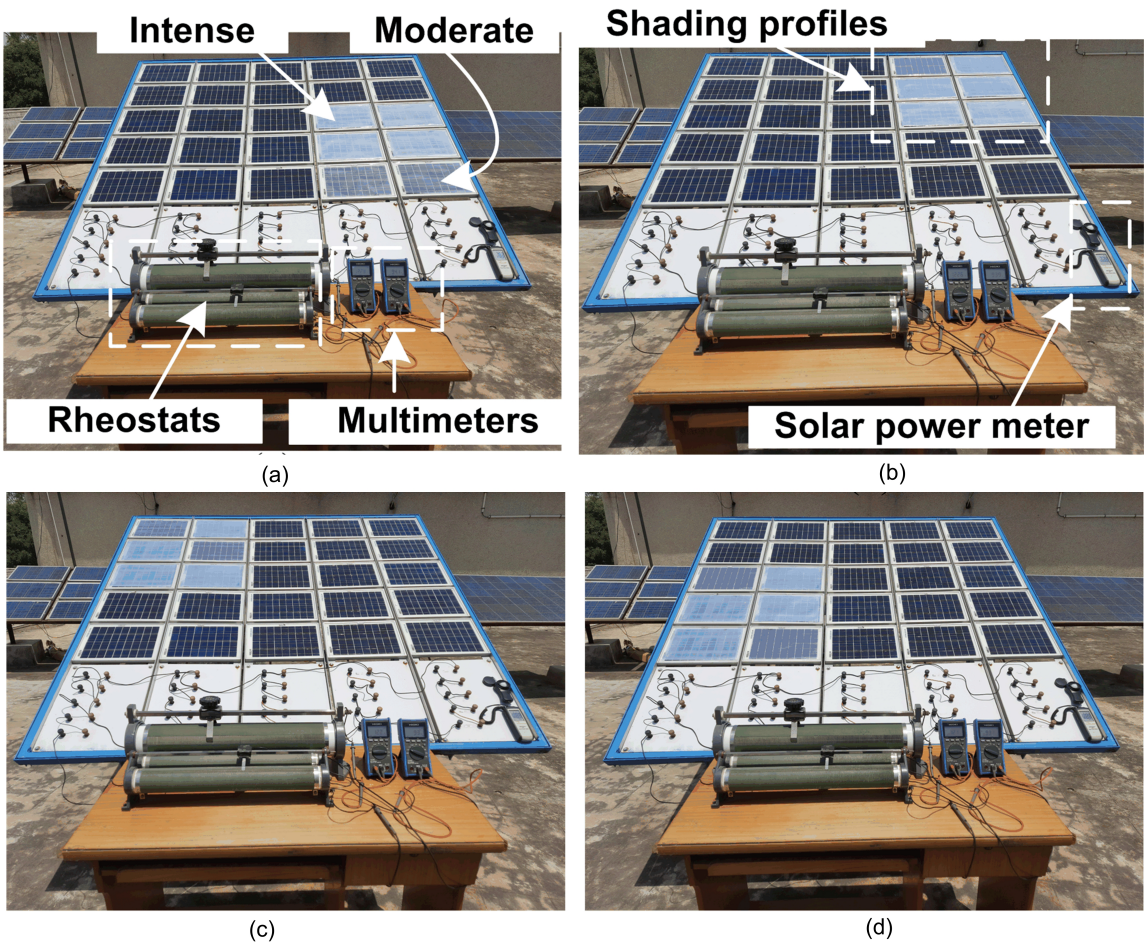

FIGURE 3.15: Experimental prototype (5×5 PV array) for hardware validation of the performance of the proposed technique under different shading cases (a) BRC, (b) TRC, (c) TLC, and (d) BLC with "intense" and "moderate" shading profiles.

reconfiguration approaches, the proposed technique exhibits clear dominance.

3.3.6 Hardware Implementation of the proposed GMRA and SP-GMRA Technique

A scaled-down experimental setup was established, as shown in Fig. 3.15 for hardware validation under different shading scenarios. Commercial-grade transparent plastic sheets (200 microns) are utilized to generate artificial shading scenarios. Multiple layers of sheets are employed to create "intense" and

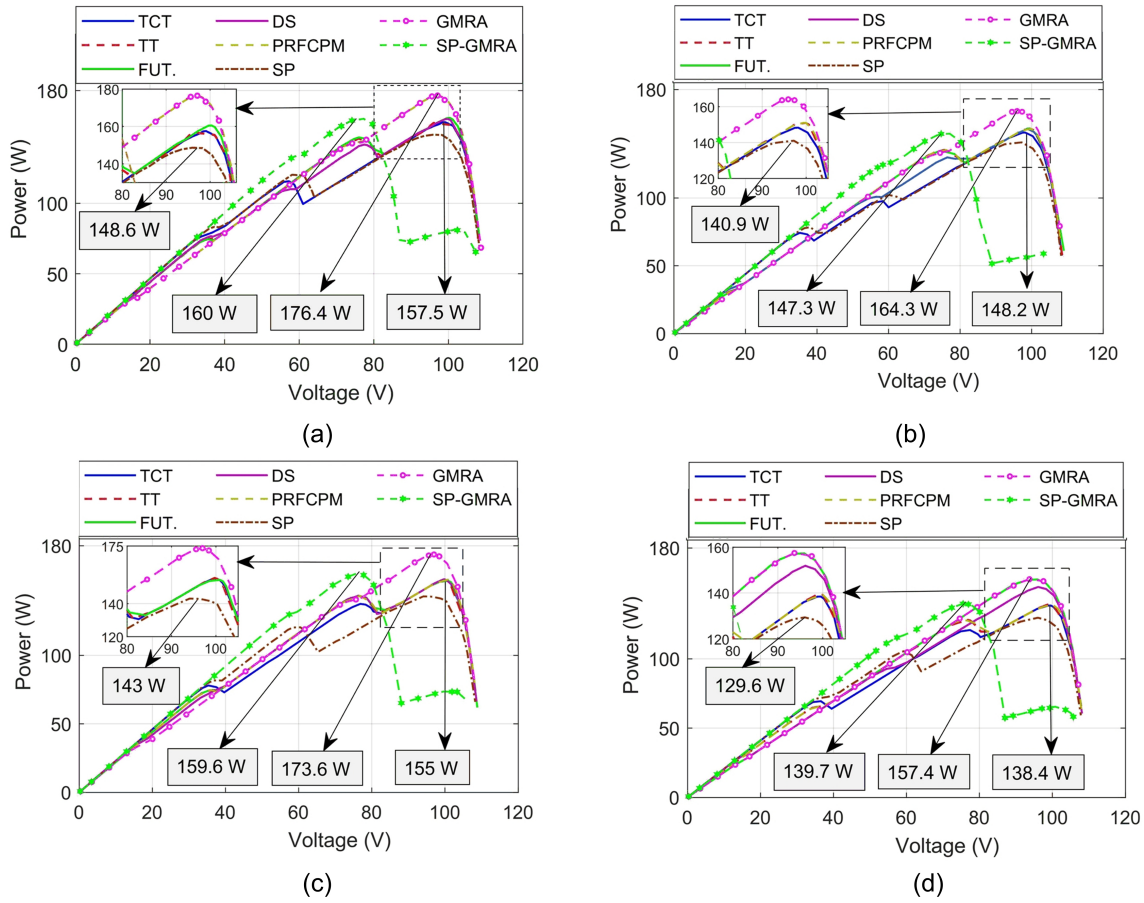

FIGURE 3.16: Experimental P-V characteristics of 5 × 5 PV array for different shading scenarios (a) BRC shading scenario. (b) TRC shading scenario. (c) TLC shading scenario. (d) BLC shading scenario.

"moderate" shading profiles. A total of 25 PV modules of 10 W each are configured in symmetrical 5 × 5 and unsymmetrical 6 × 4 arrangements.

Four common shading profiles were created i.e., BRC, TRC, TLC, and BLC on the two considered PV arrangements configured in TCT and SP configurations. The hardware validation of the performance of the proposed GMRA is performed against many popular and recently published state-of-the-art methods, i.e., phyical relocation fixed column positioning of modules (PRFCPM) [83], OEP [82], TT [85], Futoshiki (FUT) [151], DS [66], and Column (COL) [152]. Figs. 3.16 and 3.17 show the experimental P-V characteristics of 5 × 5 and 6 × 4 PV array under predefined shading conditions. SP-GMRA configuration is tested against conventional and more common SP configuration. Under all

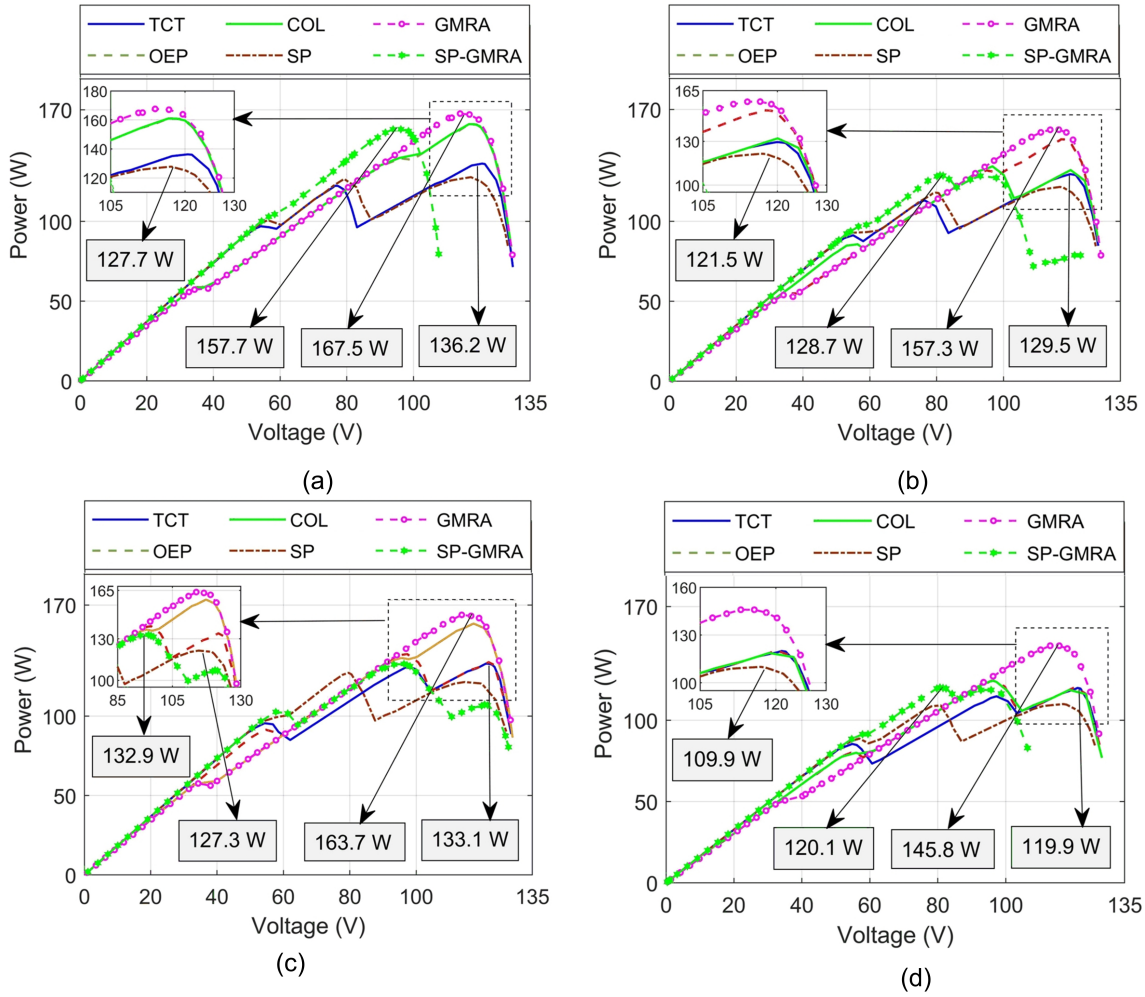

FIGURE 3.17: Experimental P-V characteristics of 6×4 PV array for different shading scenarios (a) BRC shading scenario. (b) TRC shading scenario. (c) TLC shading scenario. (d) BLC shading scenario.

shading conditions, the proposed approaches, GMRA (reconfigured TCT) and SP-GMRA (reconfigured SP), generated the highest peak power points (PPPs) against all other reconfiguration methods and SP configuration respectively as evident from Figs. 3.16 and 3.17.

The average power enhancement of 29.55% and 22.3%, respectively, is attained using the proposed GMRA against TCT arrangement under all considered shading conditions for 5×5 and 6×4 arrays. Similarly, compared to the SP configurations, 7.93%, and 10.9% higher peak power is extracted using SP-GMRA when tested on 5×5 and 6×4 arrangements, respectively.

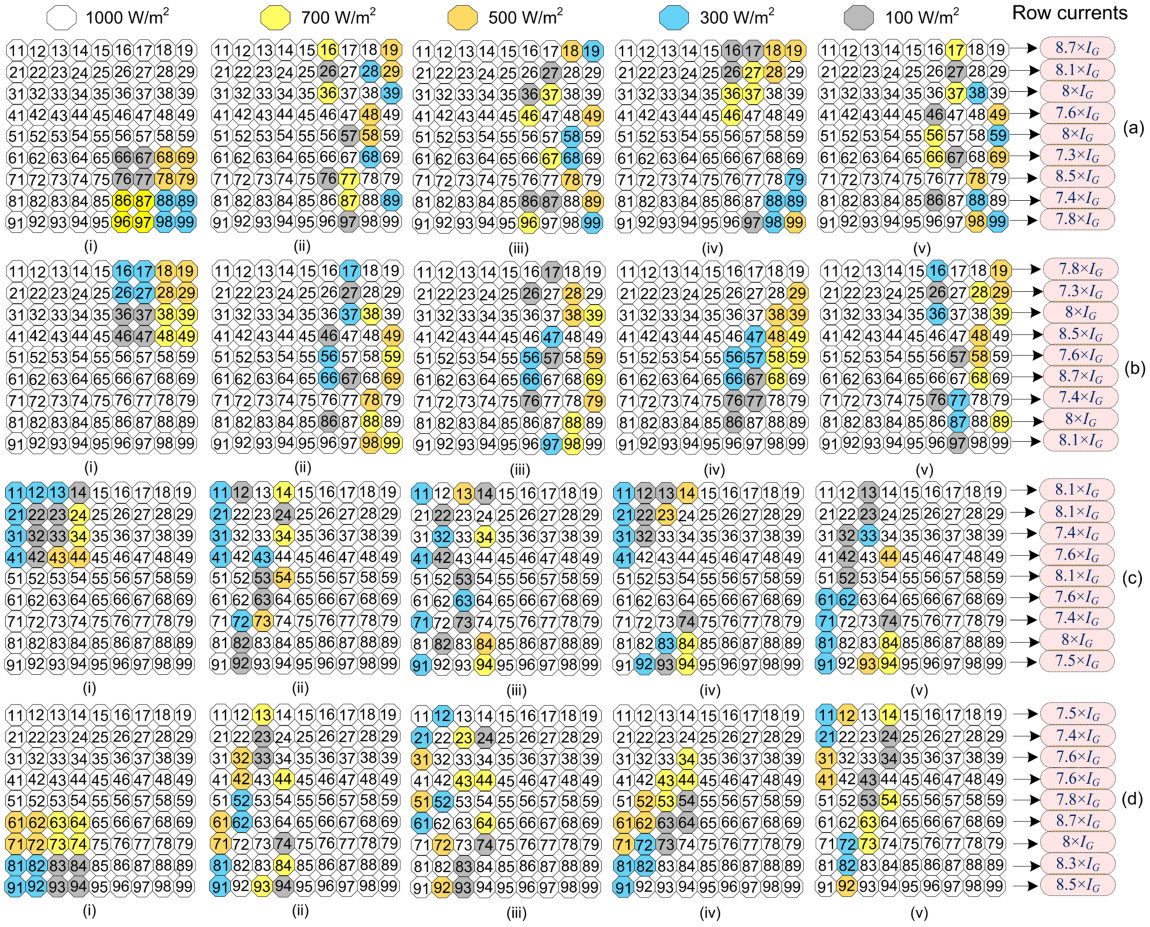

FIGURE 3.18: Comparative shade dispersion ability of a 9 × 9 PV array under (a) LRC shading scheme, (b) URC shading scheme, (c) ULC shading scheme, and (d) LLC shading scheme using (i) TCT configuration, (ii) OPSUD configuration, (iii) PRS configuration, (iv) CMAP configuration, and (v) proposed GPRS configuration.

3.3.7 Simulation and Performance Analysis of the Proposed GPRS and SP-GPRS Reconfiguration Method

The efficacy of the suggested GPRS is assessed in comparison to the standard TCT setup and five contemporary and well-regarded rearrangement methods found in the literature i.e., optimal SuDoKu (OPSUD) [75], ACMS [89], PRS [93], CMAP [91], and TTSA [87] across four distinct IMCs, i.e., lower right corner (LRC), upper right corner (URC), upper left corner (ULC), and lower left corner (LLC). Fig. 3.18 depicts the comparative SD ability of a 9 × 9 PV array with various module rearrangement strategies when exposed to the aforementioned

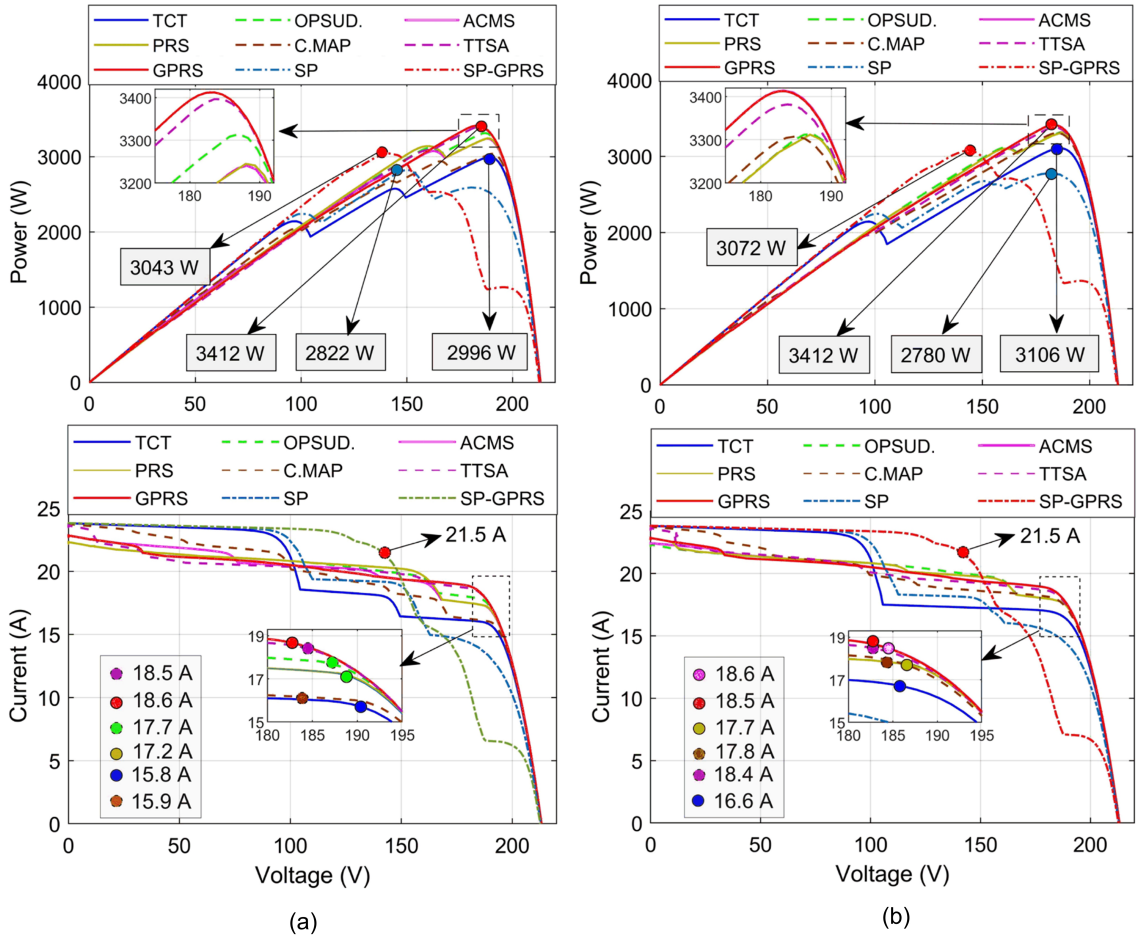

FIGURE 3.19: Simulated power (current) versus voltage response of a 9×9 PV array under different shading schemes: (a) LRC. (b) URC.

IMCs. The row currents for the proposed approach are also depicted in Fig. 3.18. The proposed technique generates even row currents and consistently exhibits the most favorable SD in all considered IMCs. Figs. 3.19 and 3.20 shows the simulated electrical characteristics of the array with different reconfiguration schemes under the considered mismatch scenarios. As evident from Figs. 3.19 and 3.20, the proposed GPRS attained the highest GMPP location compared to all other methods, indicating maximum power extraction under all cases. In addition, the proposed SP-GPRS generates significantly higher GMPP location compared to the conventional SP configuration under all considered shading cases.

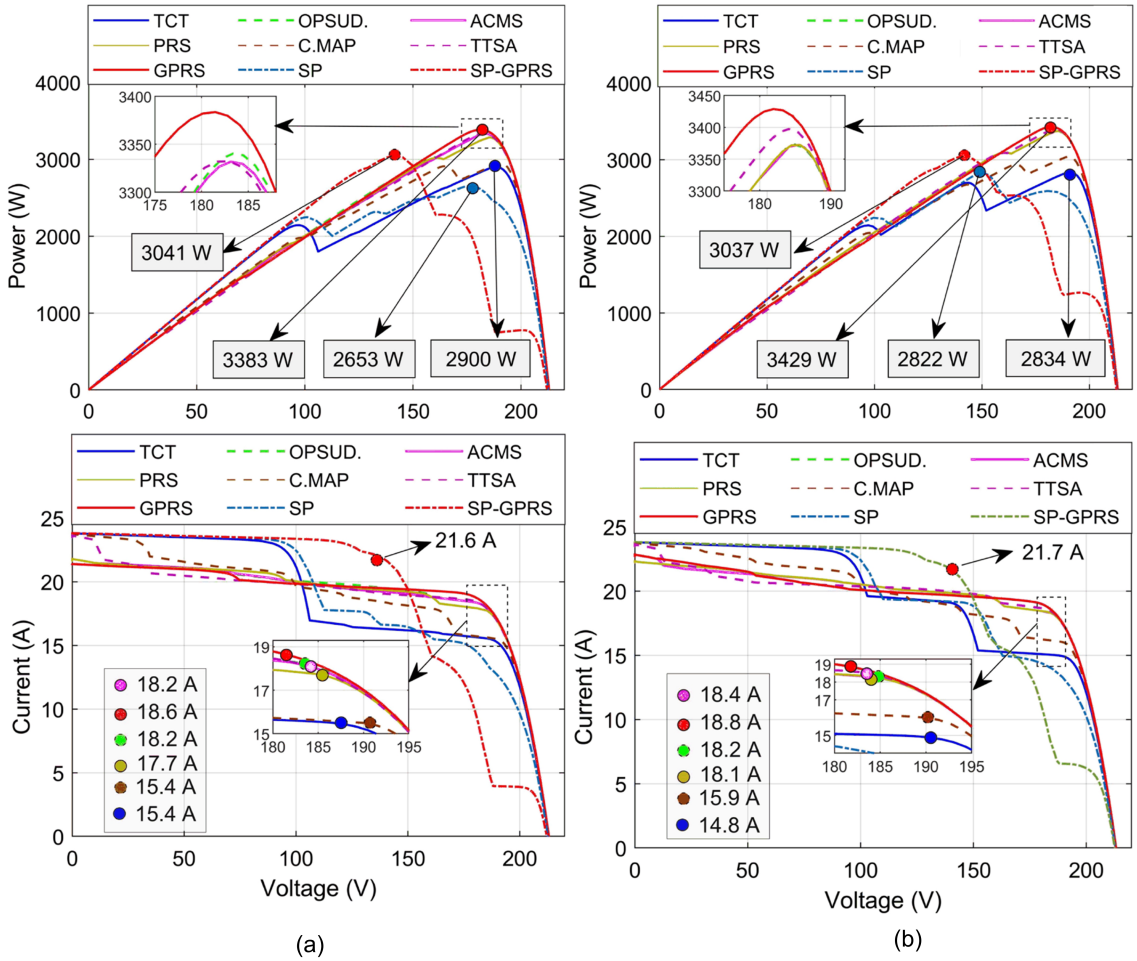

FIGURE 3.20: Simulated power (current) versus voltage response of a 9×9 PV array under different shading schemes: (a) ULC. (b) LLC.

3.3.7.1 Performance Metrics

The critical evaluation of the comparative performance of the PV array is conducted using five essential PV performance indices i.e., ML, power augmentation (PA), FF, ER, and efficiency. Furthermore, the PV array metrics of SP-GPRS are assessed relative to the widely used SP framework. Given that GPRS and SP-GPRS align with TCT and SP connections, the PV array is specifically assessed with respect to TCT and SP configurations, respectively. Table 3.3 presents a comprehensive analysis of the proposed scheme with TCT, OPSUD [75], ACMS [89], PRS [93], CMAP [91], TTSA [87], and SP configurations, utilizing the specified performance indices.

(i) ML : During IMCs, shaded units generate less current than unshaded units, leading to an overall reduction in array-generated power due to multiple series module connections. ML is computed by evaluating the difference between the combined peak powers of individual PV modules within the array and the overall peak power generated by the entire array during IMCs. It is expressed as shown below:

$$\mathrm{ML}(\%) = \frac{\sum_i^N P_{\mathrm{mi}} - P_A}{\sum_i^N P_{\mathrm{mi}}} \times 100 \tag{3.9}$$

where P_{mi} and P_A is the peak power generated by the individual module and entire array, respectively. The proposed GPRS yields 75.4 %, 33.6%, 32.2%, 42.0%, 69.1%, and 18.3% lower ML compared to TCT, OPSUD [75], ACMS [89], PRS [93], CMAP [91], and TTSA [87] arrangements, respectively. Furthermore, the proposed SP-GPRS configuration yields an average ML value that is 35.6% lower compared to the SP array.

(ii) PA: The assessment of the proposed GPRS approach's effectiveness is carried out in contrast to OPSUD [75], ACMS [89], PRS [93], CMAP [91] , and TTSA [87] arrangements based on the PA corresponding to TCT. Conversely, when evaluating the performance enhancement of the suggested SP-GPRS approach, the standard used is the conventional SP arrangement as specified in Table II. When considering different PS cases, the average power enhancement, compared to the TCT configuration using OPSUD [75], ACMS [89], PRS [93], CMAP [91], TTSA [87], and the proposed GPRS, is 12.86%, 12.96%, 11.77%, 4.18%, 14.24%, and 15.34%, respectively. Furthermore, when SP-GPRS configuration is employed under different IMCs, a significant average PA of 10.13% is observed compared to SP topology.

(iii) FF : The FF is estimated using the following equation:

$$\mathrm{FF}(\%) = \left\{ \frac{(\ \mathrm{Power}\ )_{\mathrm{GPPP}}}{V_{oc} \times I_{sc}} \right\} \times 100 \tag{3.10}$$

On average, the proposed GPRS yielded higher FFs than the TCT, OPSUD [75], ACMS [89], PRS [93], CMAP [91], and TTSA [87] configurations, amounting to 15.19%, 2.17%, 2.06%, 3.18%, 10.54%, and 1.03%, respectively, across all examined

TABLE 3.3: Assessment of the proposed GPRS and SP-GPRS techniques against current benchmark reconfiguration methods

Shading Profile	PV configuration	I_{mp}	V_{mp}	P_{mp}	Performance Parameters/Indices				
					FF (%)	ML (%)	ER (%)	PE (%)	EFF (%)
LRC	TCT	15.82	189.3	2996	62	16.2	73.6	N.A	14.6
	OPSUD. [75]	17.72	186.9	3314	68.6	7.3	81.5	10.6	16.2
	ACMS [89]	17.22	188.15	3240	67.1	9.3	79.7	8.10	15.8
	PRS [93]	17.25	187.98	3244	67.2	9.26	79.7	8.27	15.8
	CMAP [91]	15.91	191.04	3039	62.9	15.0	74.7	1.43	14.8
	TTSA [87]	18.50	183.53	3396	70.3	5.01	83.5	13.3	16.6
	SP	18.82	149.97	2822	58.4	21.0	69.4	-5.80	13.8
	GPRS	18.59	183.50	**3412**	**70.6**	**4.56**	**83.9**	**13.8**	**16.7**
	SP-GPRS	21.52	141.34	**3042**	**63**	**14.9**	**74.8**	**7.79**	**14.8**
URC	TCT	16.67	186.30	3106	64.3	13.1	76.4	N.A	15.2
	OPSUD. [75]	17.67	187.39	3313	68.6	7.33	81.5	6.66	16.2
	ACMS [89]	17.71	183.26	3412	70.6	4.56	83.9	9.85	16.7
	PRS [93]	17.71	186.98	3311	68.5	7.39	81.4	6.66	16.2
	CMAP [91]	17.88	184.89	3307	68.5	7.50	81.3	6.47	16.1
	TTSA [87]	18.40	183.76	3381	70.0	5.43	83.1	8.85	16.5
	SP	18.82	149.97	2780	57.5	22.2	68.3	-10.4	13.6
	GPRS	18.59	183.50	**3412**	**70.6**	**4.56**	**83.9**	**13.8**	**16.7**
	SP-GPRS	21.58	142.33	**3072**	**63.6**	**14.0**	**75.5**	**10.50**	**15.0**

Table 3.3 (continued)

Shading Profile	PV configuration	I_{mp}	V_{mp}	P_{mp}	Performance Parameters/Indices				
					FF (%)	ML (%)	ER (%)	PE (%)	EFF (%)
ULC	TCT	15.78	185.38	2900	60.0	17	71.3	N.A	14.5
	OPSUD. [75]	17.72	186.9	3340	69.1	4.44	82.1	15.7	16.7
	ACMS [89]	17.22	188.15	3331	68.9	4.69	81.9	14.86	16.6
	PRS [93]	17.25	187.98	3283	67.9	6.0	80.7	13.2	16.4
	CMAP [91]	15.91	191.04	2946	61.0	15.71	72.4	1.58	14.7
	TTSA [87]	18.50	183.53	3332	68.9	4.66	81.9	17.13	16.6
	SP	18.82	149.97	2653	54.9	24.0	65.2	-8.51	13.2
	GPRS	18.59	183.50	**3383**	**70.0**	**3.21**	**83.2**	**16.65**	**16.9**
	SP-GPRS	21.52	141.34	**3041**	**62.9**	**12.9**	**74.7**	**4.86**	**15.2**
LLC	TCT	15.84	184.7	2833	58.6	20.7	69.6	N.A	13.8
	OPSUD. [75]	17.72	186.9	3372	69.8	5.68	82.9	19.02	16.5
	ACMS [89]	17.22	188.15	3372	69.8	5.68	82.9	19.02	16.5
	PRS [93]	17.25	187.98	3372	69.8	5.68	82.9	19.02	16.5
	CMAP [91]	15.91	191.04	3039	62.9	15.0	74.7	7.27	14.8
	TTSA [87]	18.50	183.53	3397	70.3	4.98	83.5	19.9	16.6
	SP	18.82	149.97	2822	58.4	21.0	69.4	-0.3	13.8
	GPRS	18.59	183.50	**3428**	**70.9**	**4.1**	**84.3**	**21.00**	**16.7**
	SP-GPRS	21.52	141.34	**3037**	**62.8**	**15.0**	**74.6**	**7.61**	**14.8**

shading scenarios. Likewise, the SP-GPRS arrangement yields 10.07% higher FF than the SP configuration.

(iv) ER : The ER quantifies how the PV framework performs when facing IMCs relative to its performance under standard operating conditions. The ER for different configurations is estimated using the following equation:

$$\mathrm{ER}(\%) = \left\{ \frac{(\mathrm{GPPP})_{\mathrm{IMC}}}{(\mathrm{GPPP})_{\mathrm{SOC}}} \right\} \times 100 \tag{3.11}$$

The average values of ER attained across different shading scenarios using TCT, OPSUD [75], ACMS [89], PRS [93], CMAP [91], and TTSA [87] are 72.7%, 82%, 82.1%, 81.1%, 75.7%, and 83%, respectively. Conversely, the suggested GPRS approach delivers an average ER of 83.8%. On average, the SP-GPRS configuration exhibits an ER that surpasses the traditional SP setup by 10%.

(v) Efficiency (EFF): For any $p \times q$ PV array, the efficiency, η_A can be estimated as shown in (3.12) where S_{ij} denotes the irradiance received by the module positioned at ith row and jth column and A_m is the module area

$$\eta_A = \frac{(\text{ Power })_{\mathrm{GPPP}}}{\left(\sum_{i=1}^{p}\sum_{j=1}^{q} S_{ij}\right) \times A_m} \times 100 \quad \forall i = 1,2,3,\ldots,p \quad \forall j = 1,2,3,\ldots,q. \tag{3.12}$$

Table 3.3 presents the efficiency calculations for a 9×9 PV array utilizing various rearrangement techniques subject to different considered IMCs. The average efficiency enhancement w.r.t. the benchmark TCT configuration under various considered shading profiles for OPSUD [75], ACMS [89], PRS [93], CMAP [91], TTSA [87], and the proposed GPRS is 12.71%, 12.78%, 11.61%, 4.17%, 14.12%, and 15.18%, respectively. In addition, an efficiency enhancement of 10.03% is observed when the SP array is reconfigured using SP-GPRS. Table 3.3 reveals that the proposed approach excels in terms of different key performance indicators when compared with different rearrangement schemes. Out of all the assessed reconfiguration methods, the proposed GPRS and SP-GPRS approach exhibits clear superiority.

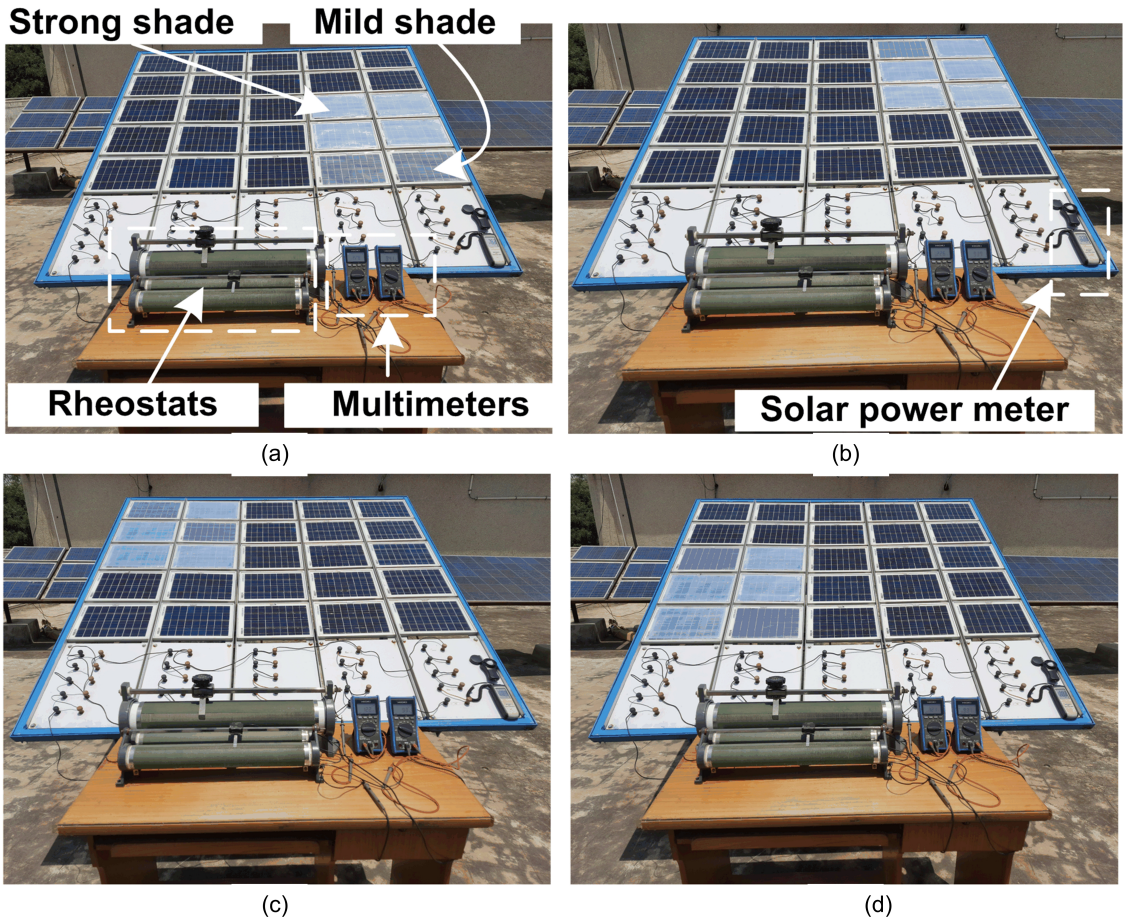

FIGURE 3.21: Physical prototype (5×5 and 6×4 PV arrays) subjected to different IMCs (a) LRC. (b) URC. (c) ULC. (d) LLC.

3.3.8 Hardware Implementation of the proposed GPRS and SP-GPRS Technique

An outdoor experimental prototype comprising 25 identical PV modules configured in both TCT and SP arrangements, was utilized for experimental evaluation. This setup, as depicted in Fig. 3.21 , was exposed to different IMCs. Transparent plastic sheets having commercial-grade thicknesses of 250 microns are employed to simulate various artificial IMCs. Several such see-through films are superimposed to generate "strong" shading occurrences on particular panels while leaving others with mild shading or no shading at all (refer to Fig. 3.21).

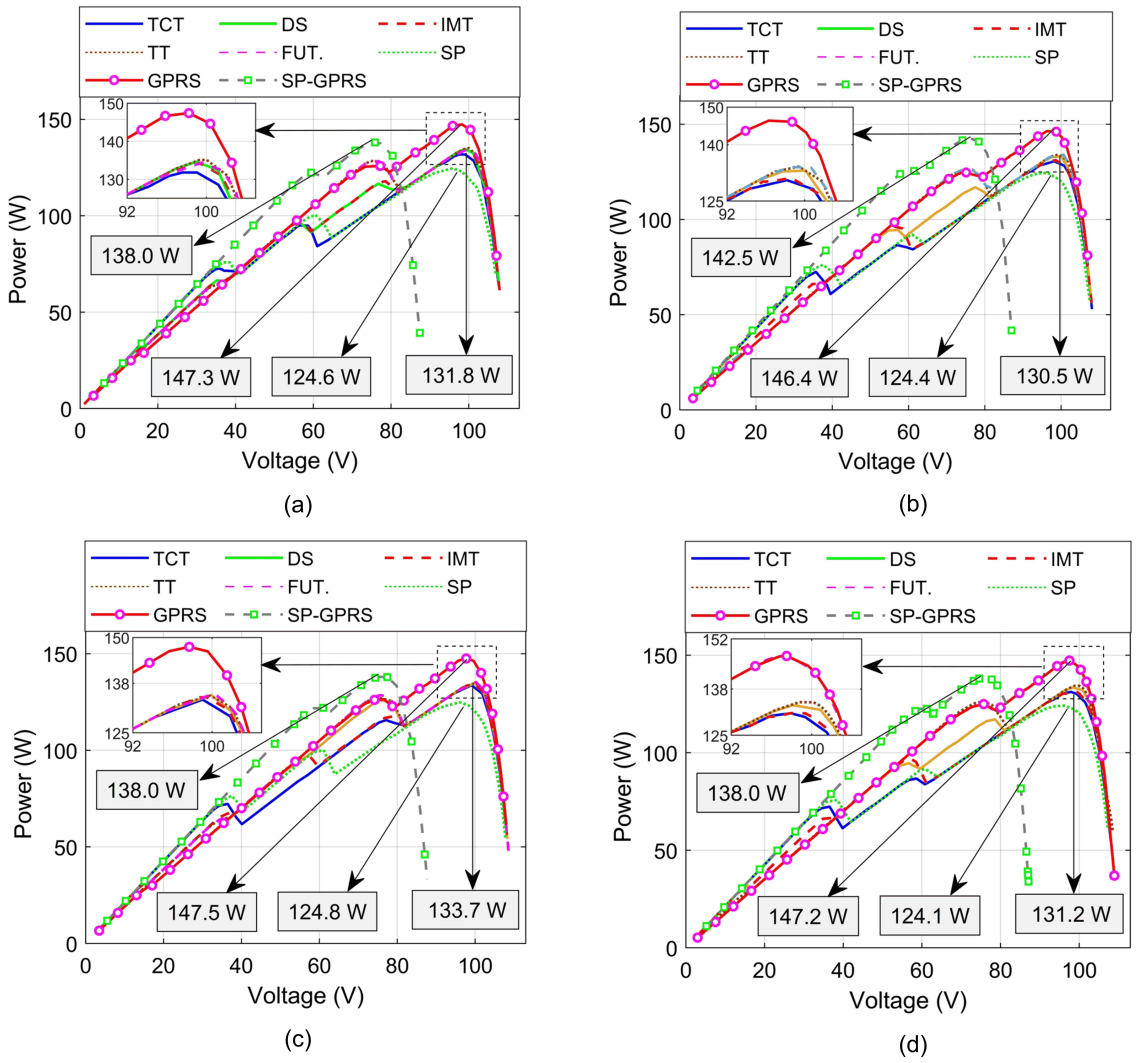

FIGURE 3.22: Experimental power-voltage curves (5×5 PV topology) subject to different IMCs. (a) LRC. (b) URC. (c) ULC. (d) LLC.

The PV panels are interconnected in both symmetrical (5×5) as well as asymmetrical (6×4) TCT and widely adopted SP configurations.

The behavior is analyzed under four prevalent shading scenarios: LRC, URC, ULC, and LLC. The practical validation of the proposed GPRS's effectiveness is carried out through comparison with various established and recently introduced state-of-the-art techniques, including FUT [151], DS [66], TT [85], CKM [97], COL [153], and OEP [31]. Figs. 3.22 and 3.23 depict the P-V profiles obtained from physical prototypes of 5×5 and 6×4 arrays when exposed to varying IMCs.

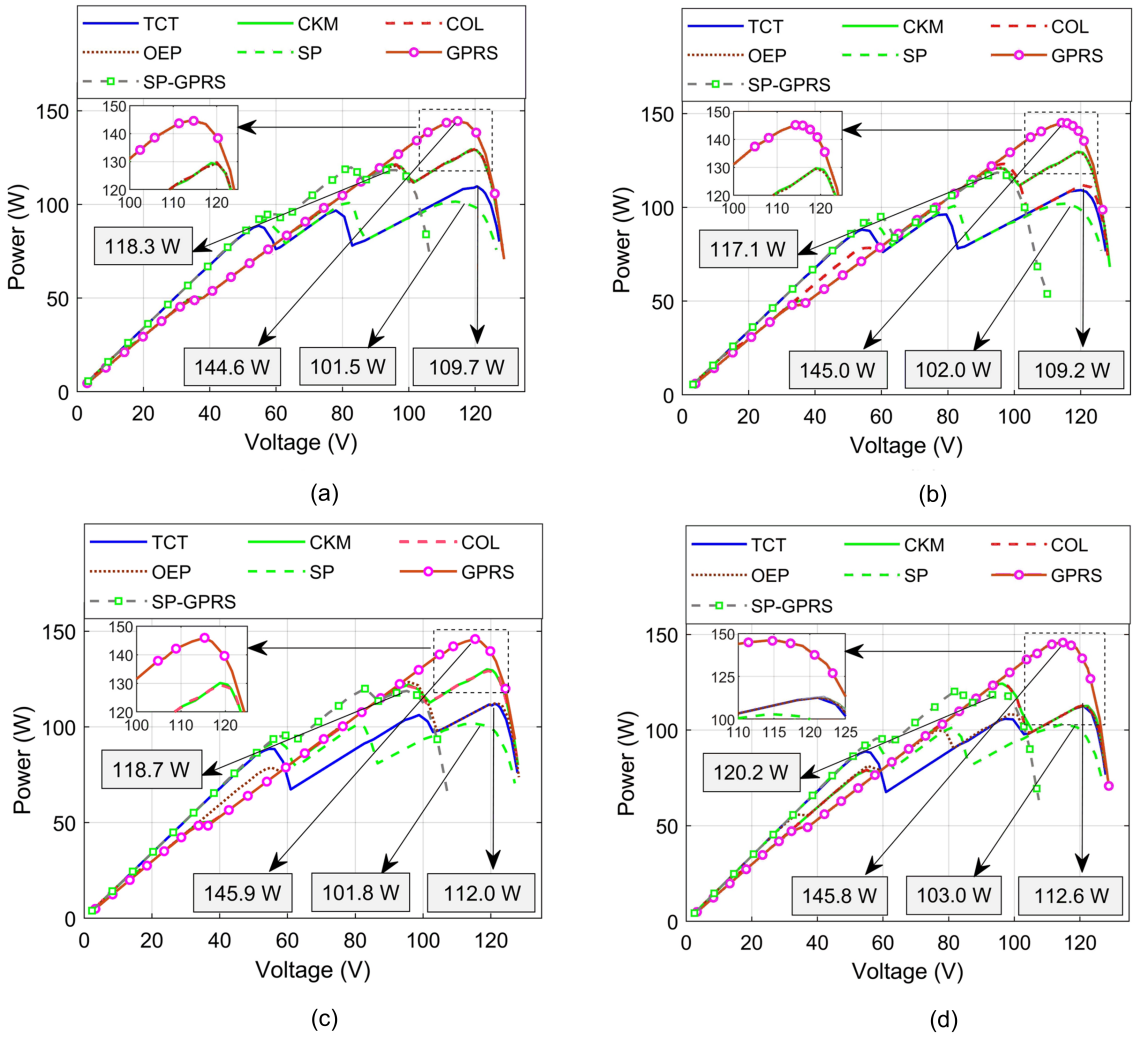

FIGURE 3.23: Experimental power-voltage curves (6×4 PV topology) subject to different IMCs. (a) LRC. (b) URC. (c) ULC. (d) LLC.

Under varying shading scenarios, the proposed methods, GPRS (reconfigured-TCT) and SP-GPRS (reconfigured-SP) demonstrate consistent performance. This superiority is clearly demonstrated in Figs. 3.22 and 3.23. The proposed GPRS yields an average power enhancement of 11.6% and 31% for the 5×5 and 6×4 PV arrays respectively, when compared to the TCT arrangement across all PS events considered. Likewise, in comparison to the SP configurations, SP-GPRS achieves an enhancement of 11.77% and 16.16% in peak power when assessed on the 5×5 and 6×4 PV setups, respectively.

TABLE 3.4: Parametric Data of PV module Used in the Simulation Analysis

Parameter	Simulation
Optimal power output (P_{max})	330 W
Voltage at MPP $(V_{pv,m})$	37.21 V
Current at MPP $(I_{pv,m})$	8.87 A
Short circuit current (I_{sc})	9.42 A
Open circuit Voltage (V_{oc})	45.87 V
Cell quantity $(N_{s,m})$	72
Area (L × W × H)	$1976mm \times 992mm \times 40mm$

3.3.9 Simulation and Performance Analysis of the Proposed CDMRA Technique

For a comprehensive performance evaluation of the proposed CDMRA technique, a comparison is made with recent and well-established PV rearrangement schemes such as OPSUD [75], SudoKu (SUD) [65], chaotic baker map (CBM) [91], chess board game methodology (CBGM) [97] in addition to the TCT topology. The specifications of the PV module employed for simulation analysis are presented in Table 3.4.

Simulations are performed on a 9×9 PV arrangement under four unique shading schemes, namely, Type-I, Type-II, Type-III, and Type-IV.

1) Type-I Shading Scheme: In this shading case, the lower right section of the TCT array is exposed to inconsistent irradiation, as shown in Fig. 3.24(a). The shade distribution performance of different rearrangement techniques, including the proposed technique, CDMRA is shown in Fig. 3.24. The extracted P-V curves for different methods are depicted in Fig. 3.28(a). The simulation results revealed that the peak power output (PPO) using TCT, CBM [91], SUD [65], OPSUD [75], CBGM [97], and the proposed CDMRA is 18262 W, 19949, 21524 W, 21565 W, 22276 W, and 22742 W respectively.

2) Type-II Shading Scheme: In this shading case, the upper right section of the TCT array is exposed to inconsistent irradiation as shown in Fig 3.25(a). The

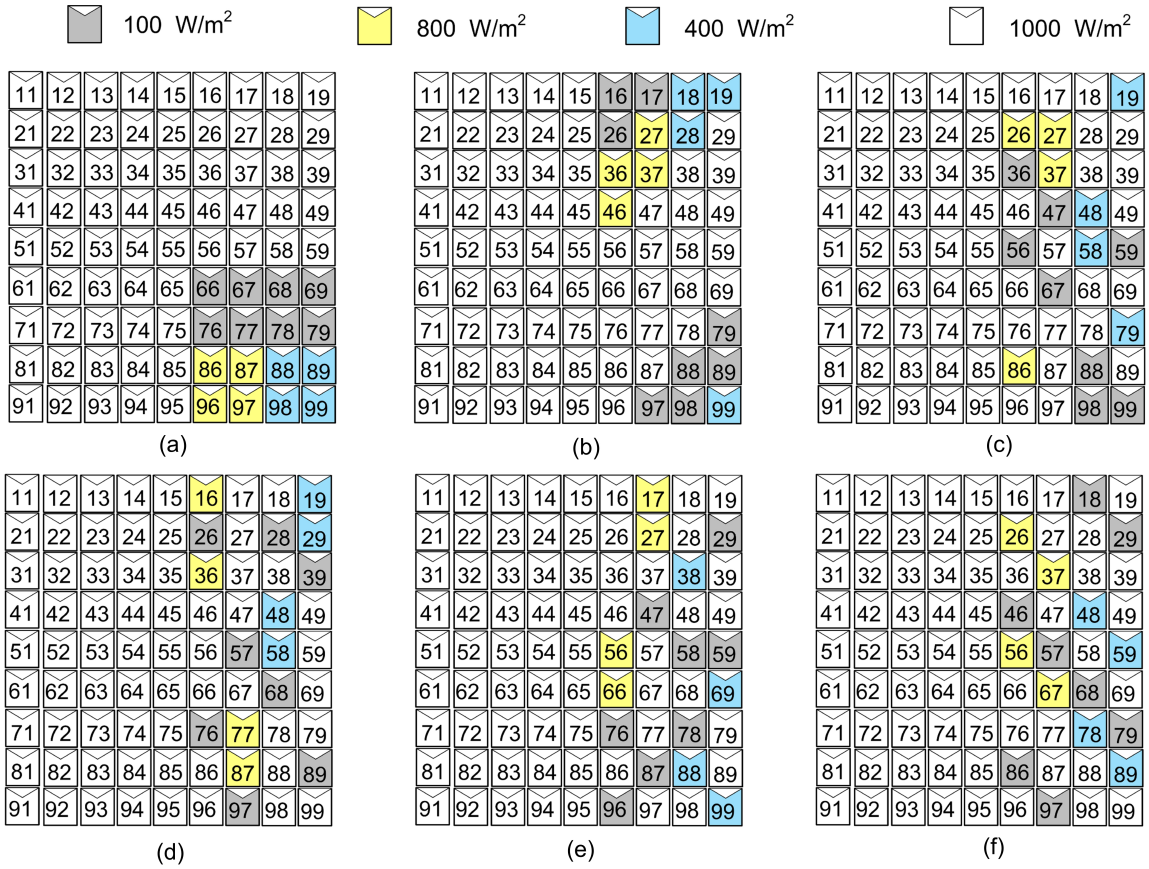

FIGURE 3.24: Shade attenuation performance under Type-I shading scenario with (a) TCT. (b) CBM. (c) SUD. (d) OPSUD. (e) CBGM. (f) proposed CDMRA.

shade distribution performance of different rearrangement techniques including the proposed technique, CDMRA is shown in Fig. 3.25. The extracted P-V curves for different methods are depicted in Fig. 3.28(b). The simulation results revealed that the PPO generated using TCT, CBM [91], SUD [65], OPSUD [75], CBGM [97], and the proposed CDMRA is 18653 W, 21931 W, 22193 W, 22162 W, 22199 W, and 22593 W respectively.

3) Type-III Shading Scheme: In this shading case, the upper left section of the TCT array is exposed to shading as shown in Fig. 3.26(a). The shade distribution performance of different rearrangement techniques including the proposed technique, CDMRA is shown in Fig. 3.26. The extracted P-V curves for different methods are depicted in Fig. 3.28(c). The simulation results revealed that the PPO extracted using TCT, CBM [91], SUD [65], OPSUD [75], CBGM [97], and the

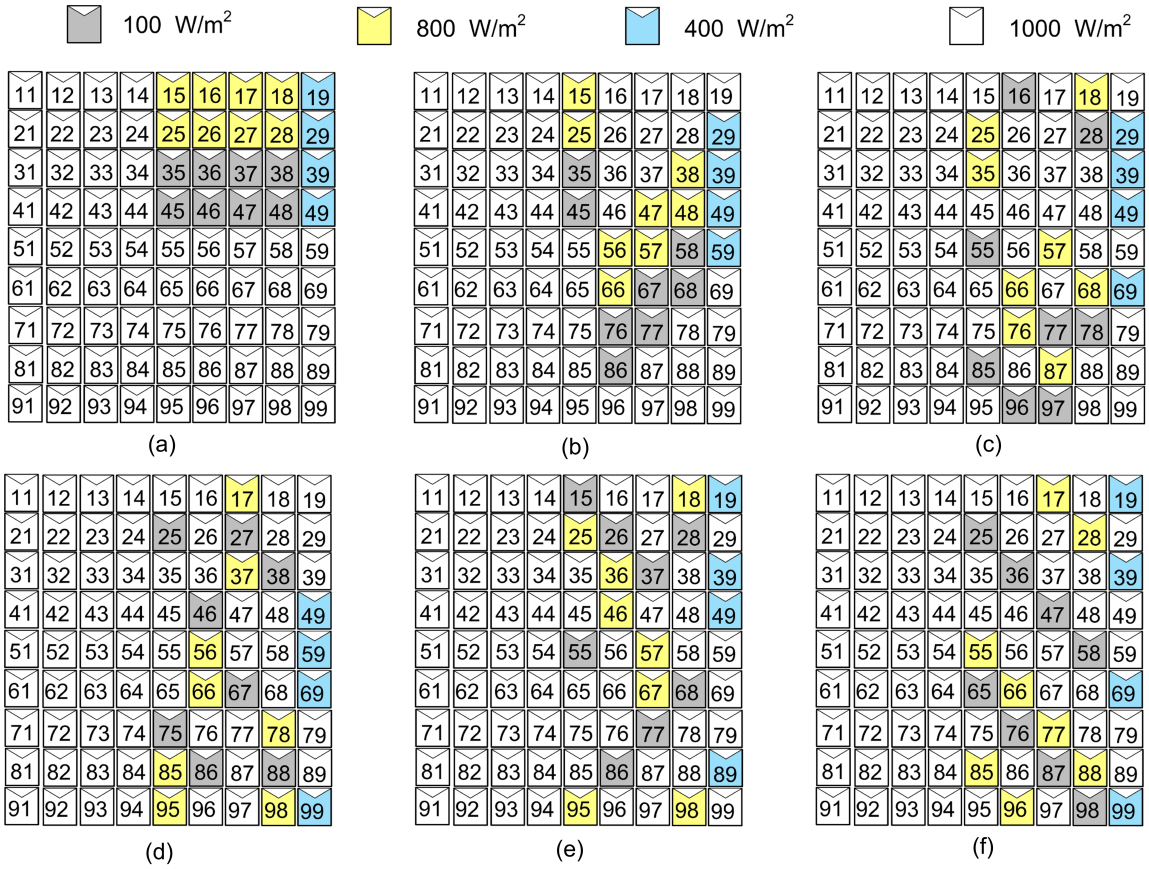

FIGURE 3.25: Shade attenuation performance under Type-II shading scenario with (a) TCT. (b) CBM. (c) SUD. (d) OPSUD. (e) CBGM. (f) proposed CDMRA.

proposed CDMRA is 17354 W, 19307 W, 21345 W, 21402 W, 22053 W, and 22354 W respectively.

4) Type-IV Shading Scheme: In this shading case, the lower left section of the TCT array is exposed to IMCs as shown in Fig 3.27(a). The shade distribution performance of different rearrangement methods including the proposed technique, CDMRA is shown in Fig. 3.27.

The extracted P-V curves for different methods are depicted in Fig. 3.28(d). The simulation results revealed that the PPO extracted using TCT, CBM [91], SUD [65], OPSUD [75], CBGM [97], and the proposed CDMRA is 18653 W, 21931 W, 22193 W, 22162 W, 22199 W, and 22593 W respectively. The response of TCT and the proposed CDMRA to various shading profiles is shown in Fig. 3.29(a) and (b), respectively. The row current discrepancy (RCD) is the disparity

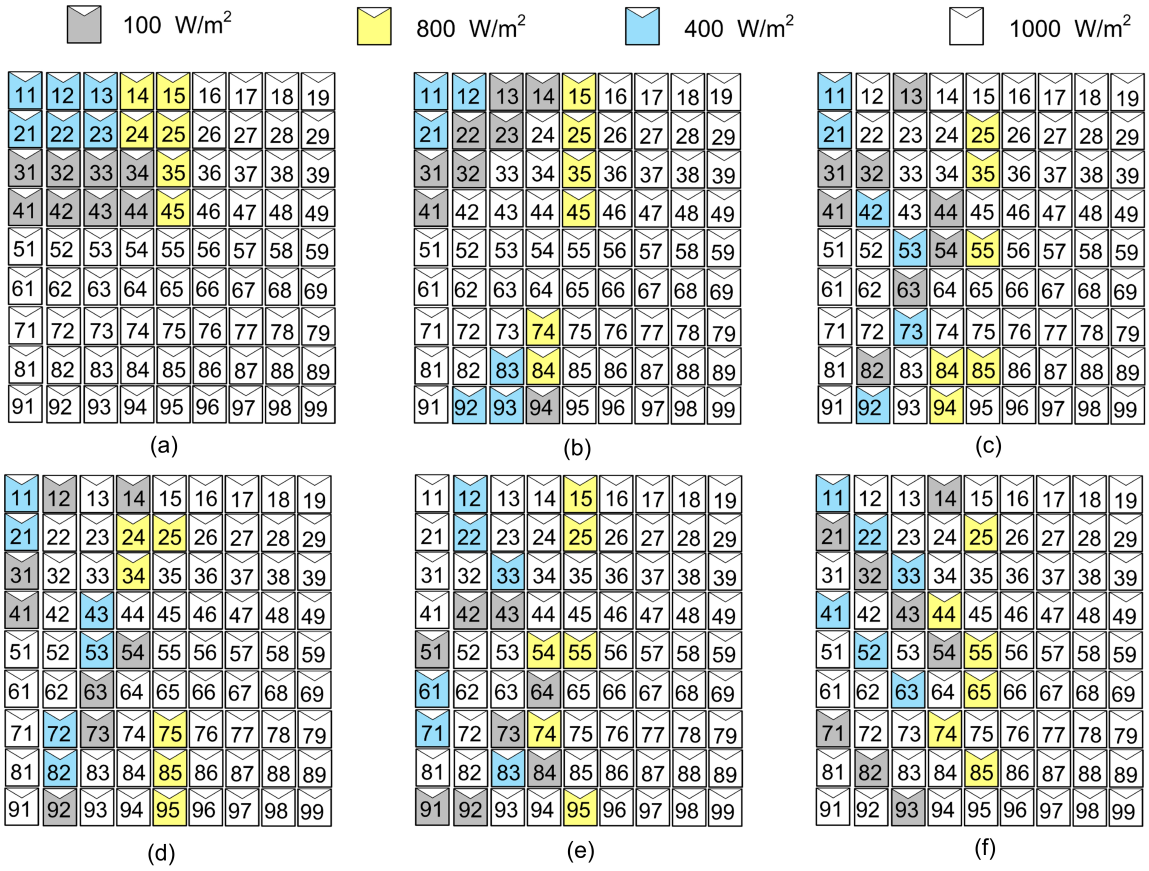

FIGURE 3.26: Shade attenuation performance under Type-III shading scenario with (a) TCT. (b) CBM. (c) SUD. (d) OPSUD. (e) CBGM. (f) proposed CDMRA.

between the maximum and minimum row currents generated by the array. The RCD achieved using TCT and the proposed CDMRA is shown in Fig. 3.29(c) and (d) respectively. It is evident that the proposed CDMRA generates significantly lower RCD as compared to TCT.

3.3.9.1 Performance Metrics

The prominent performance metrics evaluated for various rearrangement techniques and the proposed CDMRA.

(1) Power Boost (PB): The enhancement of peak power output (PPO) w.r.t TCT PV array is used as an important measure for comparison of different PV rearrangement techniques. The PB is evaluated for different methods under

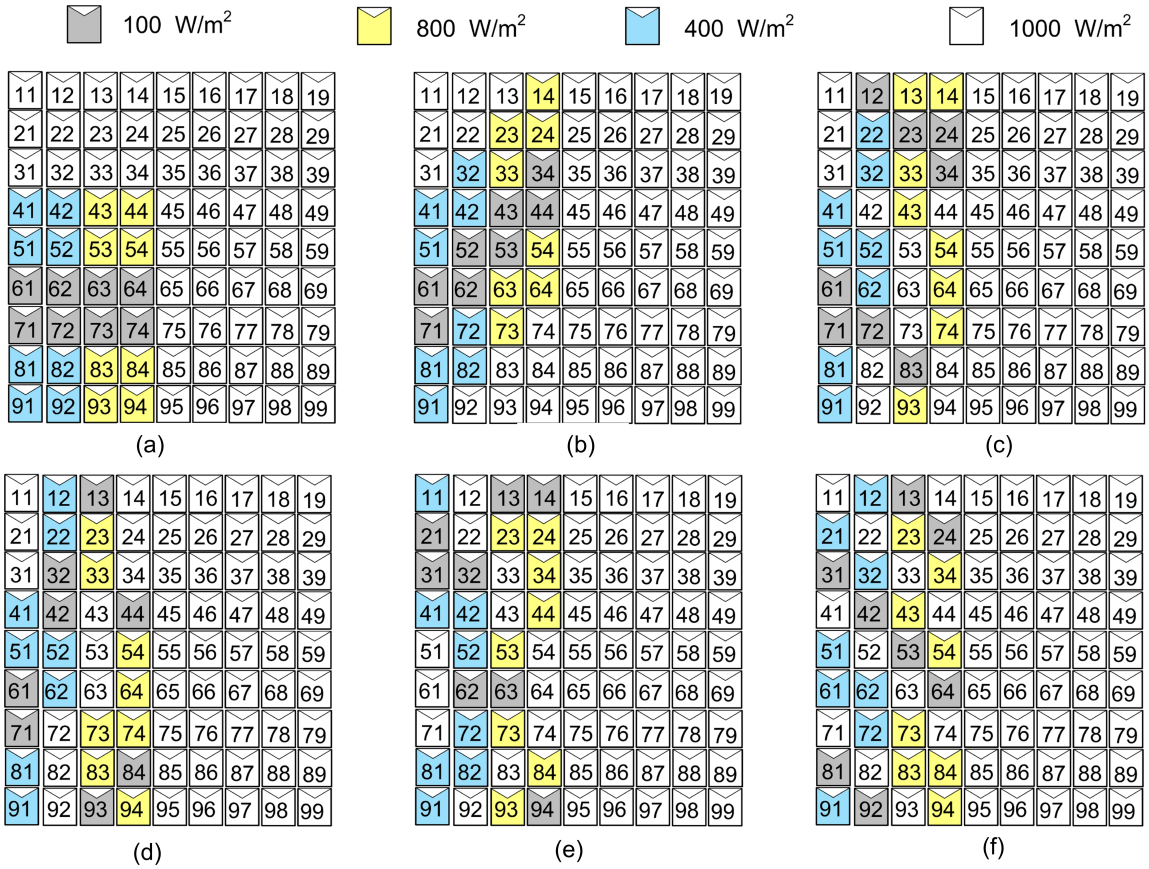

FIGURE 3.27: Shade attenuation performance under Type-IV shading scenario with (a) TCT. (b) CBM. (c) SUD. (d) OPSUD. (e) CBGM. (f) proposed CDMRA.

various IISs as given in (3.13).

$$PB(\%) = \frac{(PPO)_{\text{rearrangement technique}} - (PPO)_{TCT}}{(PPO)_{TCT}} \times 100 \tag{3.13}$$

The proposed CDMRA technique outperforms all studied configurations by generating the highest PB , as shown in Fig. 3.30. In particular, it extracts an average of 23.9% higher PB compared to the TCT configuration.

(2) Mismatch Power Loss (MPL): The MPL highlights the difference between the PPO generated by the summation of individual PV module PPOs and the PPO achieved by the PV array after reconfiguration. The MPL for different PV

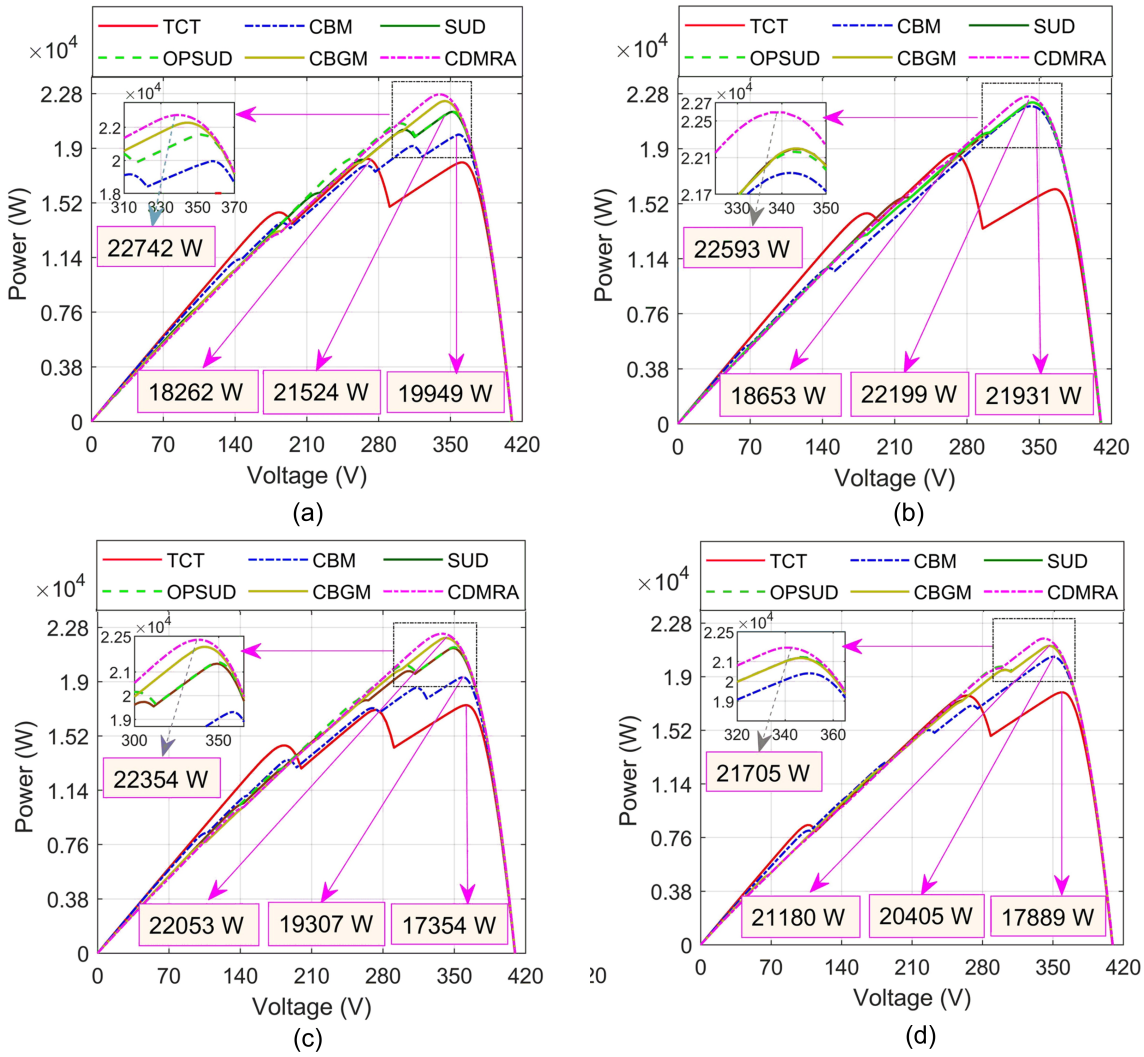

FIGURE 3.28: Extracted P-V profiles (Simulation) for different PV rearrangement techniques under (a) Type-I shading. (b) Type-II shading. (c) Type-III shading. (d) Type-IV shading.

arrangements is computed using (4.10).

$$\text{MPL}(\%) = \frac{\sum_a^N P_{m,a} - P_{array}}{\sum_a^N P_{m,a}} \times 100 \tag{3.14}$$

where $P_{m,a}$ and P_{array} is the PPO generated by the individual module and entire PV array respectively. The proposed CDMRA yields the lowest MPL among all considered PV arrangements as depicted in Fig. 3.30. CDMRA yields on average 89.9% lower MPL compared to TCT configuration.

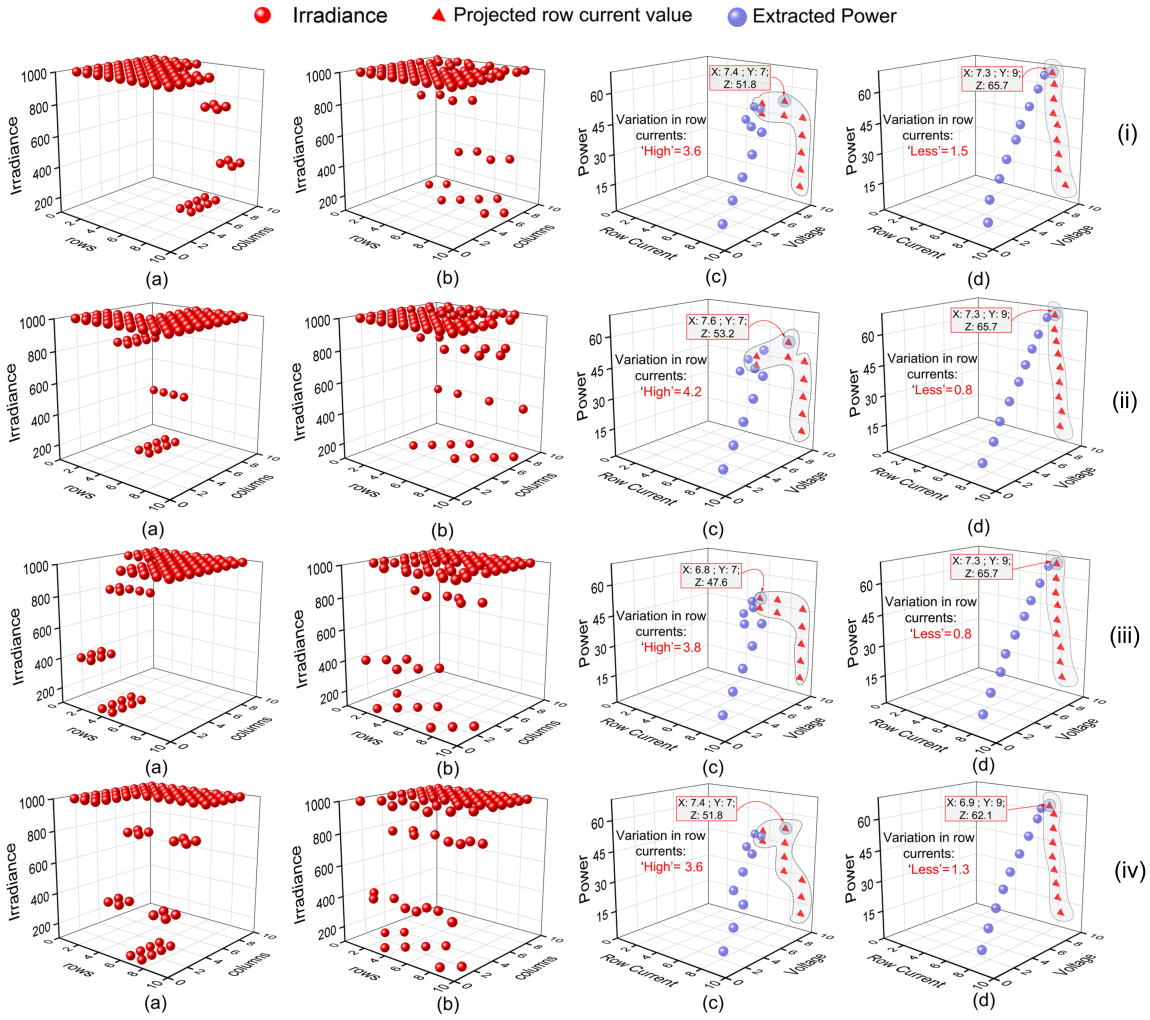

FIGURE 3.29: Shade tolerant performance evaluation of a 9×9 PV arrangement using TCT and the proposed CDMRA technique under (i) Type-I, (ii) Type-II, (iii) Type-III, (iv) Type-IV shading cases: (a) TCT. (b) shade dispersal using the proposed CDMRA. (c) RCD with TCT. (d) RCD with the proposed CDMRA.

(3) System Efficiency (SE): Efficiency computation is a crucial metric that defines the effectiveness of the various PV arrangements. It is estimated for any $r \times c$ PV array using (3.15).

$$SE(\%) = \frac{PPO}{(\sum_{a=1}^{r} \sum_{b=1}^{c} G_{ab}) \times A_p} \times 100 \tag{3.15}$$

where ' G_{ab} ' is the irradiance in W/m^2 and ' A_p ' is the module area in m^2. The proposed CDMRA consistently achieves the highest efficiency compared to all

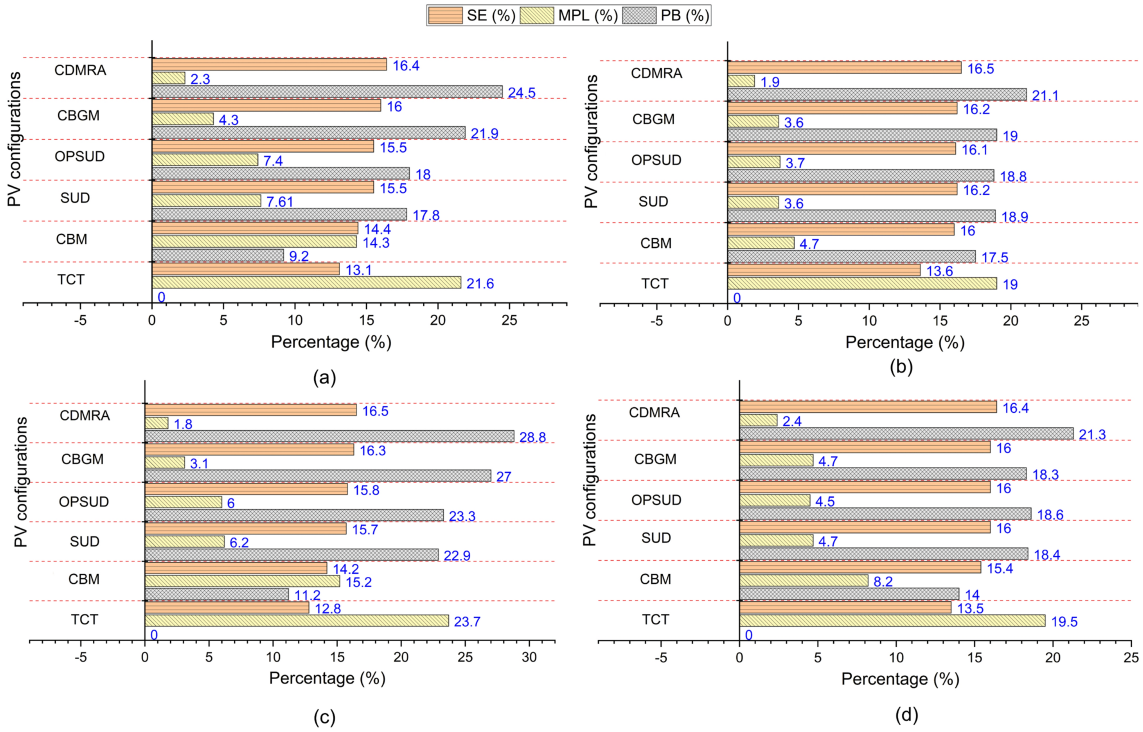

FIGURE 3.30: Performance indices (PB (%), MPL (%), and SE (%)) for various PV configurations under considered IISs (a) Type-I. (b) Type-II. (c) Type-III. (d) Type-IV cases.

considered PV arrangements as evident from Fig. 3.30. From simulation analysis, it is observed that the proposed CDMRA achieves 24.1% higher efficiency compared to TCT topology.

4) Row Current Discrepancy Minimization (RCDM): To ensure effective shade attenuation in partial shading scenarios, a higher RCDM is desirable, as evaluated in (5).

$$RCDM(\%) = \frac{(RCD)_{TCT} - (RCD)_{\text{rearrangment technique}}}{(RCD)_{TCT}} \times 100 \tag{3.16}$$

The proposed CDMRA technique outperforms all studied configurations by generating the highest RCDM, as shown in Fig. 3.31. In particular, it yields an average of 70.4% higher RCDM compared to the TCT configuration.

5) Fill Factor (FF): FF is an important measure that defines the squareness of the current-voltage profile and is employed for performance comparison of different

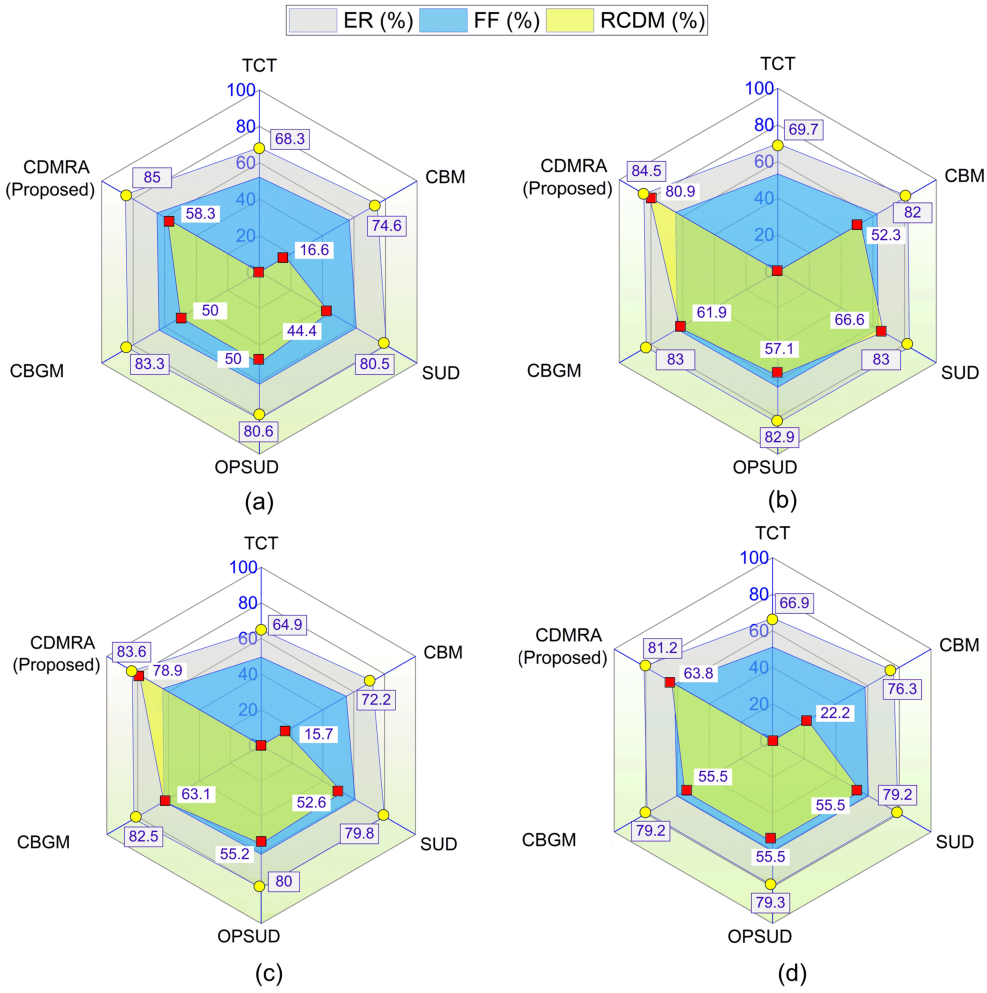

FIGURE 3.31: Radar chart representation of FF, ER, and RCDM parameters for different PV configurations under different shading cases: (a) Type-I. (b) Type-II. (c) Type-III. (d) Type-IV.

PV configurations. It is estimated using (3.17)

$$FF(\%) = \frac{PPO}{(V_{oc} \times I_{sc})} \times 100 \tag{3.17}$$

Simulation results demonstrate that the proposed CDMRA technique consistently achieves the highest FF values compared to other PV configurations as depicted in Fig. 3.31. Specifically, on average, the proposed approach yields a 21.4% higher FF than TCT across all considered inconsistent irradiance scenarios (IISs).

6) Execution Ratio (ER): The ER assesses the PV system's performance in the presence of IISs compared to its performance under standard test conditions (STCs).

$$ER(\%) = \frac{(PPO)_{IISs}}{(V_{oc} \times I_{sc})_{STC}} \times 100 \tag{3.18}$$

The proposed method attains the highest ER among all reconfiguration techniques. In comparison to TCT, the proposed method generates an average of 23.7% higher ER.

3.4 Efficiency Computations and Techno-Economic Feasibility Study

In this section, efficiency calculations are conducted for both conventional and proposed PV configurations under different shading profiles.

3.4.1 Calculation of Efficiency

The accurate assessment of the efficiency plays a crucial role in effectively comparing different reconfiguration schemes for the PV system under PSCs. For any $i \times j$ PV array arrangement, the efficiency, $\eta|_x^y$, can be estimated as depicted in (3.19).

$$\eta|_x^y = \frac{\text{GMPP}|_x^y}{\left(\sum_{m=1}^{i}\sum_{n=1}^{j} S_{mn}\right) \times A_p} \quad \forall\, m = 1,2,3,\ldots,i \quad \text{and} \quad \forall\, n = 1,2,3,\ldots,j \tag{3.19}$$

where " x " and " y " denote the shading scenario and PV configuration, respectively. Additionally, " $S_{mn}\left(W/m^2\right)$ " represents the irradiance input received by the module located at m th row and nth column and $A_p\left(m^2\right)$ denotes the area of the individual module, which is 0.285 m^2 (from Table 3.1). Using (3.19), the efficiency calculations for TCT, CMAP [91], PRS [93], TTSA [87], SP, GMRA, and SP-GMRA under BRC, TRC, TLC, and BLC shading conditions (see Fig. 3.13) are performed. Fig. 3.32 illustrates the comparative performance in terms of system efficiency yields for a 9×9 PV array utilizing different reconfiguration methods.

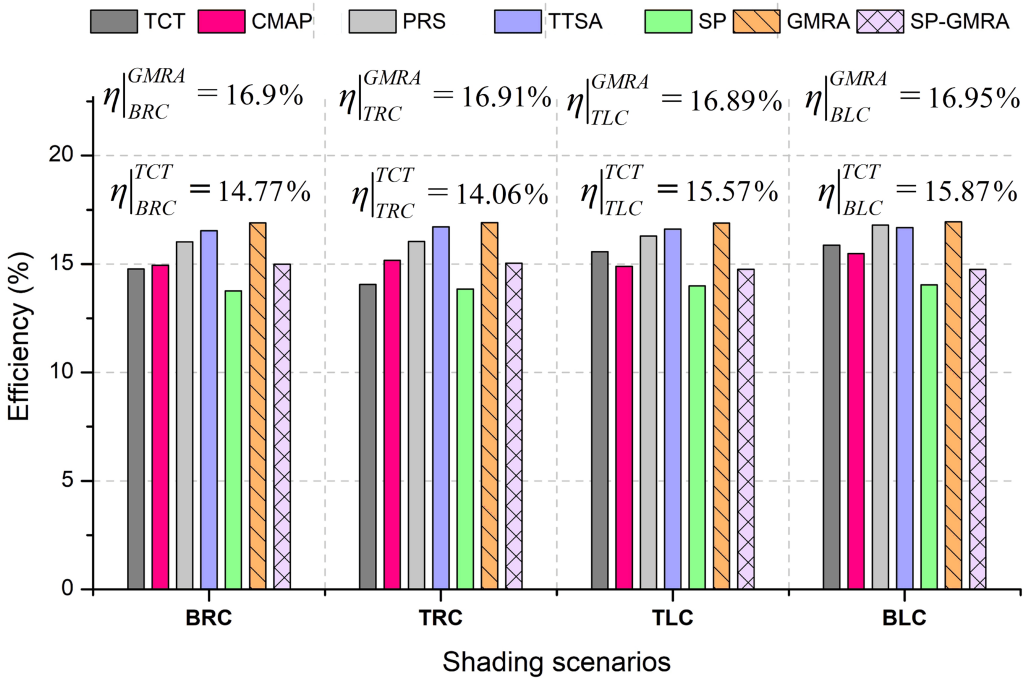

FIGURE 3.32: Comparative efficiency yield of various PV configurations for a 9×9 PV array under different PSCs.

The efficiency values, $\eta|_x^{\text{TCT}}$ and $\eta|_x^{\text{GMRA}}$ corresponding to TCT and GMRA configurations, respectively, under different shading scenarios, " x," are also highlighted for clarity. The proposed GMRA yields the highest efficiency under all considered shading scenarios as evident from Table 3.5. On average, 12.28% higher efficiency is attained under all considered shading conditions using the proposed GMRA compared to the conventional TCT arrangement. SP-GMRA results in 7% higher efficiency compared to the traditional SP configuration when average values under all shading schemes were considered.

3.4.2 Techno-Economic Analysis

This section presents a techno-economic analysis of the proposed reconfiguration schemes, comparing them with several widely recognized and recently developed rearrangement techniques.

3.4.2.1 Techno-Economic Assessment of various Reconfiguration Schemes with the Proposed GMRA and SP-GMRA

The energy yield calculations for TCT, CMAP [91], PRS [93], TTSA [87], and the proposed GMRA technique are performed based on total power extracted after reconfiguration, considering full effective sun hours. The evaluation is performed on a 9 $\times$9 array of capacity 4.05 kW considering four different aforementioned shading scenarios (refer Table 3.1 for module specifications). Each shading scenario is assumed to occur for a duration of 10 minutes consecutively within an effective sun hour period of 8 h , as depicted in Table 3.6. Furthermore, the revenue generated by the plant is estimated by considering a tariff rate of Rs. 15 per unit. As evident from Table 3.7, the proposed reconfiguration scheme leads to the highest energy yield and, therefore, generates the highest annual revenue of \$1686.04 surpassing the TCT, CMAP [91], PRS [93], and TTSA [87] methods. It is important to note that in both the TCT and the proposed GMRA arrangements, the PV modules are arranged sequentially, resulting in less wiring dependence. On the contrary, the PV arrangements such as CMAP [91] and TTSA [87], where modules can occupy any position within the array, lead to much higher cabling requirements. In the proposed GMRA arrangement, modules are repositioned within the column with fixed electrical connections, necessitating increased wiring (209$\times$ module length) for a 9 $\times$ 9 PV array compared to the wiring (81$\times$ module length) required for the same array size using TCT. The cost components considered for the system include the PV array with supporting structures (\$5167) and connecting wires (\$1.54/m). Considering all installation costs and also factoring in a maintenance cost (2% of the installation costs) for the PV system, the payback period for both TCT and the proposed GMRA is estimated. The techno-economic analysis revealed that the proposed system can recoup the invested funds within a time frame of about 3.2 years, which is shorter compared to the 3.56 years required with the TCT arrangement. So, the proposed reconfiguration arrangement is less costly (compared to electronic reconfigurable techniques that require a lot of sensors and switches), practically feasible, and lucrative in terms of annual energy savings for large PV plant installations.

3.4.2.2 Techno-Economic Assessment of various Reconfiguration Schemes with the Proposed GPRS and SP-GPRS

Energy yield assessments for TCT, OPSUD [75], ACMS [89], PRS [93], CMAP [91], TTSA [87], and the proposed GPRS involve calculating the cumulative power extracted post reconfiguration, considering the entire duration of effective sunlight hours. The energy yield assessment is carried out on a 9×9 PV setup, boasting a capacity of 16.2 kW , and considers the four distinct IMCs outlined earlier. In the process of conducting the analysis, each panel is exposed to illumination for 8 h daily, spanning from 9:00 A.M. to 5:00 P.M. Different shading profiles namely LRC, URC, ULC, and LLC are periodically introduced to the PV setup for 10 min every consecutive hour throughout the day, resulting in each shading profile lasting for 2 h . The annual revenue generated by various schemes is determined, considering a price of Rs. $12/\text{kW} \cdot \text{h}$. The yearly revenues generated by TCT, OPSUD [75], ACMS [89], PRS [93], CMAP [91], and TTSA [87] are \$1247.2, \$1405.7, \$1407.4, \$1392.1, \$1299.5, \$1423.3 respectively.The proposed strategy generates an annual revenue of \$1436.9, surpassing the conventional TCT arrangement by 15.2%. Moreover, the SP-GPRS yields 16.6% (\$1284.8) more annual revenue compared to the SP configuration (\$1167.3).

3.5 Summary

This thesis investigates innovative strategies for mitigating the effects of PS on PV arrays, with a focus on enhancing energy output and efficiency through advanced reconfiguration techniques. By addressing ML and optimizing power extraction, the proposed methods offer substantial improvements over conventional and state-of-the-art approaches. The principal research contributions are as follows:

1. This thesis introduces GMRA, SP-GMRA, GPRS, SP-GPRS and CDMRA as advanced static SD and alleviation strategies designed to enhance PV array performance under PSCs.

2. The GMRA strategy achieved a 12.76% improvement in FF compared to TCT and a 7.10% improvement over SP configurations, with power

enhancements of up to 29.55% and 22.3% for 5×5 and 6×4 arrays, respectively. Additionally, energy yield calculations for GMRA, TCT, CMAP, PRS, and TTSA methods showed that GMRA generated the highest annual revenue, amounting to $1686.04, surpassing all other methods.

3. The GPRS method outperformed both conventional and contemporary techniques, achieving efficiency gains of 15.18% over TCT and 10.03% over SP configurations, alongside experimental power boosts of up to 31% for TCT arrays and 16.16% for SP arrays. Furthermore, SP-GPRS generated 16.6% more annual revenue than the SP configuration, with an annual revenue of $1436.9, exceeding the conventional TCT arrangement by 15.2%.

4. A detailed techno-economic analysis revealed that the proposed GMRA arrangement has a shorter payback period (3.2 years) compared to the TCT arrangement (3.56 years), making it a more cost-effective, practically feasible, and profitable solution, particularly for large PV plant installations.

5. The dimension-independent CDMRA approach reduced MPL by 89.9% and increased RCD minimization by 70.4% compared to the conventional TCT arrangement.

6. The congruence between simulation and experimental results validates the effectiveness and superiority of these proposed strategies in addressing shading challenges across diverse PV array configurations.

TABLE 3.5: Efficiency of 9 × 9 PV Array Under Different Shading Scenarios

Shading Scenarios	PV configuration	Efficiency (%)	Shading Scenarios	PV configuration	Efficiency (%)
BRC	TCT	14.77	TRC	TCT	14.06
	CMAP [91]	14.94		CMAP [91]	15.17
	PRS [93]	16.02		PRS [93]	16.04
	TTSA [87]	16.54		[87]	16.72
	SP	13.76		SP	13.85
	GMRA	**16.9**		GMRA	**16.91**
	SP-GMRA	**14.99**		SP-GMRA	**15.04**
TLC	TCT	15.57	BLC	TCT	15.87
	CMAP [91]	14.89		CMAP [91]	15.48
	PRS [93]	16.29		PRS [93]	17.1
	TTSA [87]	16.61		TTSA [87]	16.68
	SP	13.99		SP	14.04
	GMRA	**16.89**		GMRA	**16.95**
	SP-GMRA	**14.76**		SP-GMRA	**14.75**

TABLE 3.6: Hourly Variation in Shading Patterns for Techno-Economic Analysis

Hour	Interval					
	$0-10$ min	$10-20$ min	$20-30$ min	$30-40$ min	$40-50$ min	$50-60$ min
$9-10$	BRC	TRC	TLC	BLC	BRC	TRC
$10-11$	TLC	BLC	BRC	TRC	TLC	BLC
$11-12$	BRC	TRC	TLC	BLC	BRC	TRC
$12-13$	TLC	BLC	BRC	TRC	TLC	BLC
$13-14$	BRC	TRC	TLC	BLC	BRC	TRC
$14-15$	TLC	BLC	BRC	TRC	TLC	BLC
$15-16$	BRC	TRC	TLC	BLC	BRC	TRC
$16-17$	TLC	BLC	BRC	TRC	TLC	BLC

TABLE 3.7: Energy Yield Analysis for Various Reconfiguration Methods

Hour	PV reconfiguration schemes				
	TCT	CMAP [91]	PRS [93]	TTSA [87]	GMRA
9 -10	2748.5	2788.5	3007.8	3078.6	3139
10-11	2837.5	2799.5	3058.1	3089.3	3159.5
11-12	2748.5	2788.5	3007.8	3078.6	3139
12-13	2837.5	2799.5	3058.1	3089.3	3159.5
13-14	2748.5	2788.5	3007.8	3078.6	3139
14-15	2837.5	2799.5	3058.1	3089.3	3159.5
15-16	2748.5	2788.5	3007.8	3078.6	3139
16-17	2837.5	2799.5	3058.1	3089.3	3159.5
Daily energy extracted (kW-h)	22.3	22.3	24.2	24.6	25.2
Yearly energy extracted (kW-h)	8139.5	8139.5	8833	8979	9198
Total yearly income generated@Rs 15/kW-h	122,092.5	122,092.5	132495	134685	137970
Cumulative yearly income generated in $	1492.0	1492.0	1619.13	1645.89	1686.04

Chapter 4

Topological Modifications to the Existing PV Array Configurations

4.1 Preamble

The increasing demand for renewable energy sources has driven significant advancements in PV technology. Among these, the arrangement and configuration of PV modules play a critical role in optimizing energy output, particularly under varying environmental conditions.
This chapter explores the performance enhancement of a novel MPVA, designed to address challenges posed by IMSs. PV systems convert sunlight into electricity, but their efficiency can be significantly impacted by factors such as shading and irradiance levels. Traditional configurations, such as the TCT arrangement, often suffer from performance losses when modules experience uneven shading or irradiance conditions. These challenges necessitate innovative approaches to improve energy capture and overall system efficiency.

The proposed MPVA offers a groundbreaking solution by reducing cross-tied wiring by 59.37% compared to standard configurations. This reduction simplifies the wiring structure while enhancing the system's adaptability to varying irradiance conditions. The MPVA employs a unique static reconfiguration technique, the PMSRA, which optimizes power output under different shading scenarios.

To validate the effectiveness of the MPVA, extensive experimental studies were conducted using both symmetrical (5×5) and unsymmetrical (6×4) PV module configurations. These experiments assessed the MPVA's performance compared

to traditional arrangements, focusing on metrics such as GMPP and efficiency under various IMSs.

The results from the experimental validation indicate that the PMSRA configuration consistently outperforms traditional setups, achieving significant power increases across multiple shading cases. For instance, in a 6×4 PV array, the PMSRA configuration demonstrated power increases of up to 29.2% compared to the TCT configuration. These findings highlight the potential of MPVA to enhance energy capture and efficiency in real-world applications.

This research contributes to the ongoing efforts to improve PV system performance, particularly in environments where irradiance conditions are not uniform. By exploring innovative configurations and reconfiguration techniques, this study aims to pave the way for more efficient and resilient solar energy systems, ultimately supporting the transition to sustainable energy sources.

The remainder of the chapter is organized as follows: Section 4.2 analyzes PV array performance under various IMSs. Section 4.3 describes different conventional PV configurations, such as TCT, B-L, H-C, and SP, alongside the proposed MPVA configuration with significantly fewer cross-ties. Section 4.4 provides a detailed explanation of the PMSRA, including the steps involved in the rearrangement of PV modules. This section outlines how the PV array is segmented and how modules are shifted to optimize performance. Results obtained from extensive simulations and experimental validations on different PV configurations, including a 9×9 PV network and smaller prototypes are presented in section 4.5. Finally, 4.6 concludes the chapter with a summary of key research findings.

4.2 Analysis of PV Array Response Under IMSs

The response of a PV array configured in a TCT arrangement under different IMSs is elucidated. In the TCT configuration, multiple modules are connected in series to create several strings. These strings are then interconnected in a way that each module in the array is connected in parallel with several other modules as shown in Fig. 4.1(a). The output current and voltage generated by an $r \times c$ TCT-configured PV array, where ' r ' and ' c ' correspond to the number of rows

and columns in the array respectively is given as follows:

$$I_a = \sum_{j=1}^{c} I_{m,ij} \quad \forall\, i = 1, 2, \ldots, (r-1) \tag{4.1}$$

$$V_a = \sum_{i=1}^{r} V_{m,ij} \quad \forall\, j = 1, 2, \ldots, (c-1) \tag{4.2}$$

To extensively examine the behaviour of a PV array during shading conditions, the response of a 4×4 TCT PV array is studied specifically, under different IMSs. To capture the true essence of the response of the PV array under a wide range of mismatches in operating conditions, the array modules are subjected to variable shading intensities, β, with progressively increasing values of shading ratios, α within the same row (scenario I) and column (scenario II) as shown in Fig. 4.1(a) and (b). Here, the shading intensity β represents the fraction of irradiance received by a module compared to the standard test level of 1000 W/m^2, such that $\beta \in \{0.1, 0.2, 0.4, 0.6, 0.8\}$. The shading ratio ' α ' denotes the fraction of the shaded modules in each row and column, such that $\alpha \in \{0.25, 0.5, 0.75, 1\}$. Additionally, a more common shading profile, short narrow (SN) is considered for analysing the effect of shading on the operating voltages of various rows before and after shade distribution over the entire PV array.

4.2.1 Scenario I and scenario II shading

The array modules are subjected to progressively increasing row (scenario I) and column shading (scenario II) with variable shading intensities, β. For the scenario I shading, the panels. of the fourth row are progressively shaded starting from the leftmost module i.e. '41' and continuing up to '44' as shown in Fig. 4.1(a). Similarly, for scenario II, the modules of the first column are progressively shaded starting from module ' 41 ' and continuing up to ' 11 ' as depicted in Fig. 4.1(b). The resulting percentage degradation in Global Peak Power Point (GPPP) is also estimated for the two aforementioned scenarios in comparison to uniform irradiance conditions, as illustrated in Fig. 4.2(a) and (b). Interestingly, for any fixed value of β, significant degradation in GPPP occurs for increasing α values (number of shaded modules) within the same row (Scenario

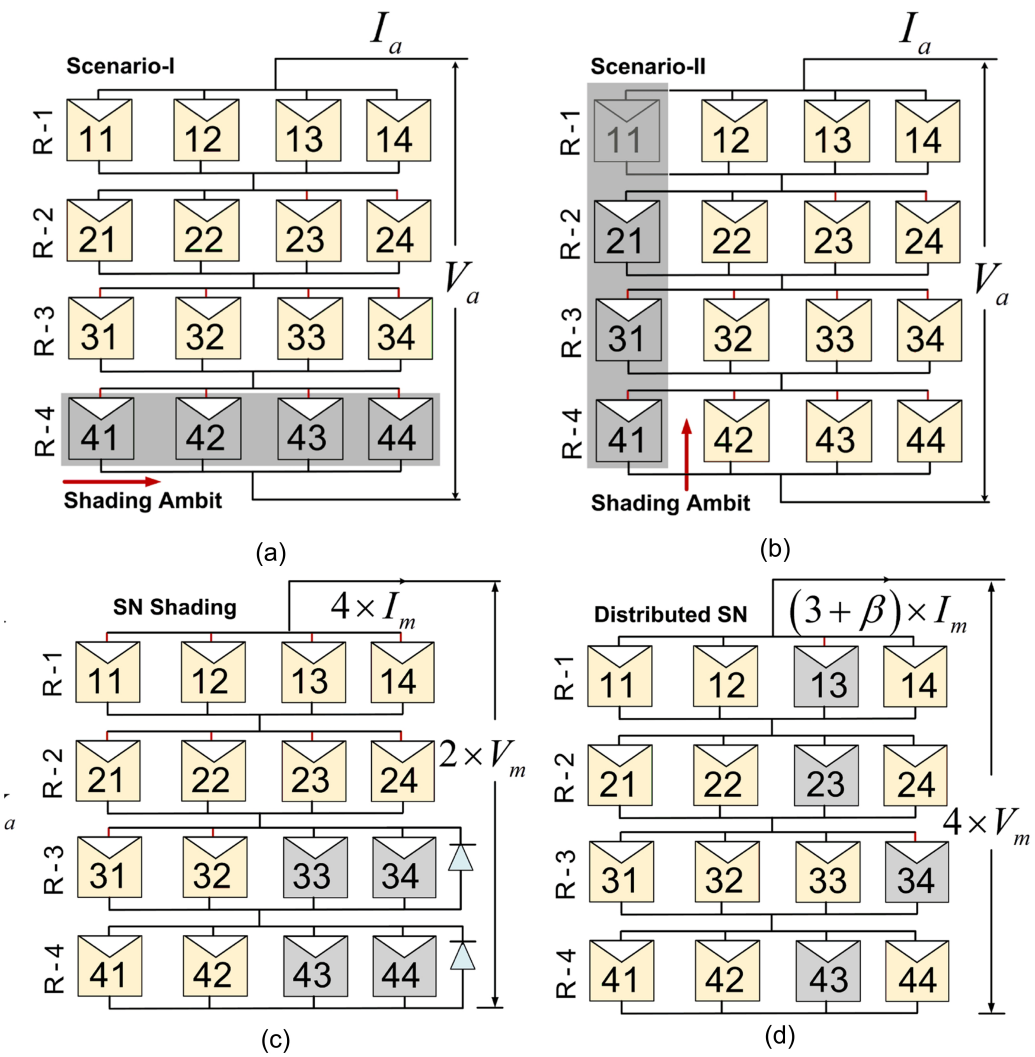

FIGURE 4.1: A 4×4 TCT PV array under various IMSs: (a) Scenario I: progressively increasing row shading. (b) Scenario II: progressively increasing column shading. (c) short narrow (SN) shading. (d) distributed SN shading.

I). For instance, $\forall \beta = 0.1, 0.2, 0.4, 0.6$, the GPPP degrades up to 26% (refer to Fig. 4.2(a)). On the contrary, in scenario II shading, the worst-case degradation is 23%, corresponding to $\beta = 0.1$, and only 10% for $\beta = 0.6$ as shown in Fig. 4.2(b). This indicates an improved array response under both strong and moderate shading when the shading is distributed over different rows. So, to extract improved array performance under IMSs from a TCT configured PV array, any SD scheme must disperse the shade to the maximum number of rows possible.

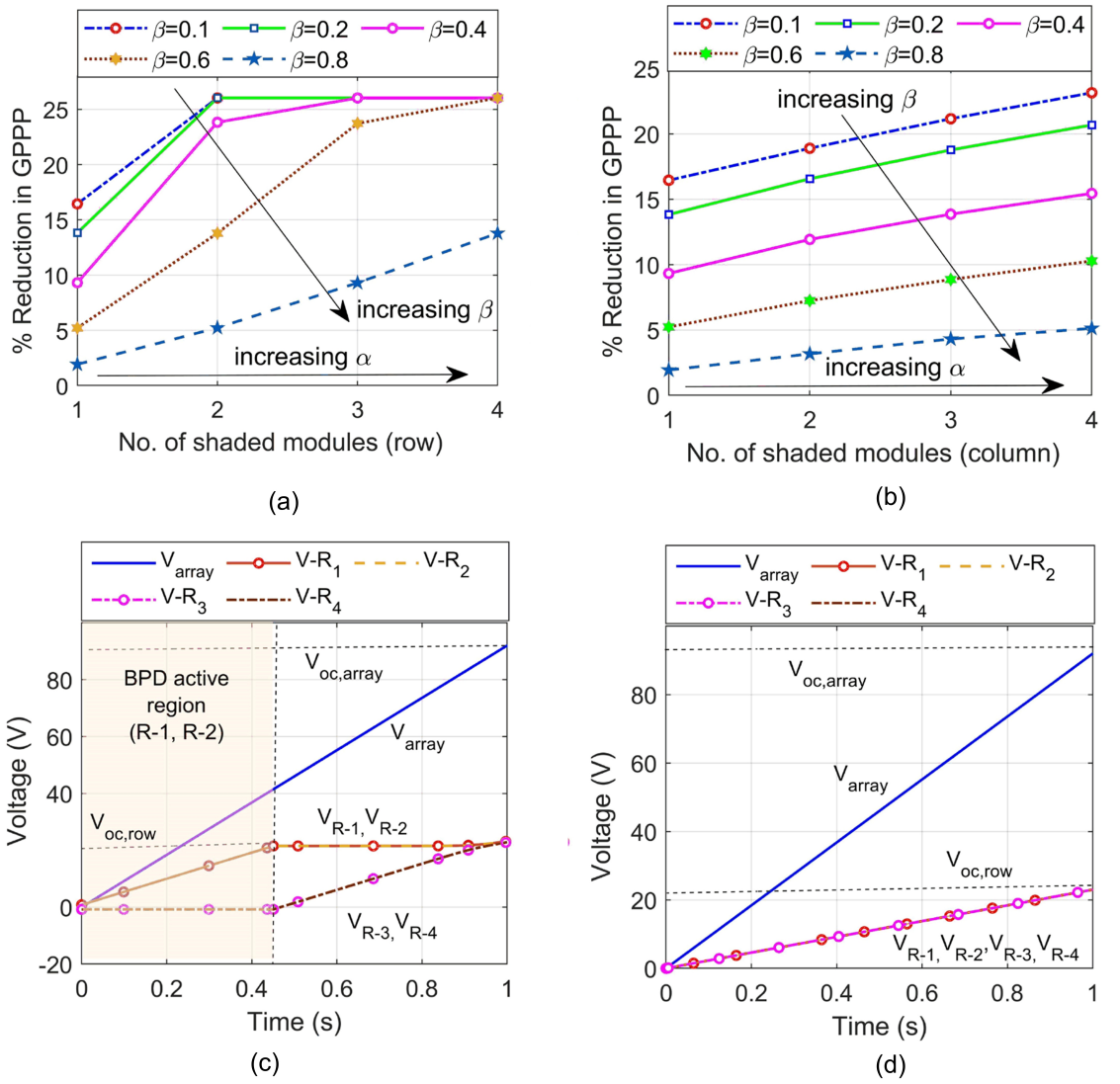

FIGURE 4.2: A 4×4 TCT PV array under various IMSs: (a) response under scenario I shading. (b) response under scenario II shading. (c) voltage variation of various rows of PV array in response to load variation with time for SN shading. (d) distributed SN shading.

4.2.2 Short narrow (SN) and distributed SN shading

In SN shading, a 2×2 sub-array comprising modules ' 33 ', ' 34 ', ' 43 ', and ' 44 ' from rows R $-$ 3 and R-4 are shaded respectively as depicted in Fig. 4.1(c). Distributed SN shading comprises only a single module from each row under the ambit of shading as shown in Fig. 4.1(d). A simulation study on a 4×4 T-C-T PV array comprising 10 W modules is performed to analyse the effect of SN

shading and distributed SN shading on the operating voltages of different rows of the array. Fig. 4.2(c) and (d) show the PV array response in terms of voltage variation of various rows of the array as a function of load variation with time under SN and distributed SN conditions respectively. Additionally, the BPDs active region is highlighted for R-3 and R-4 as shown in Fig. 4.2(c). For thesake of brevity, only two BPDs are shown, each across R-3 and R-4. BPDs when turned on, isolate shaded modules, causing zero power generation from them. Once the voltage of the unshaded rows i.e. R-1 and R-2 reaches the open circuit rated voltage, $V_{oc,row}$, the BPDs get deactivated as shown in Fig. 4.2(c) . Consequently, the module's voltage rises,responding to load variations, allowing the PV array-generated current to flow while staying within the constraints of the shaded module's current. The significant mismatch among rows triggers the activation of BPDs, leading to multiple peaks in the power curve, resulting in ML as well as misled loss due to erroneous tracking of the MPPT controllers. On the contrary, in distributed SN shading (Fig. 4.1(d)), since each row has only a single PV module shaded, the mismatch among rows is eliminated and none of the BPDs gets activated.Fig. 4.2(d) demonstrates the voltage build-up across different rows over time with load variations. Consequently, the resulting power curve becomes free from multiple peak formations, leading to a reduction in both ML and misled losses. Accordingly, to enhance the PV array performance under different IMSs, it is vital to distribute shade over the entire array surface and that too on a maximum number of rows possible.

4.3 Different PV Array Configurations

In this section, a comprehensive assessment of the physical layouts of various prevalent PV arrangements is carried out. The configurations under scrutiny comprise TCT, B-L, and H-C. In this work, 81 PV modules are intricately arranged in a 9×9 configuration. Consider the current generated by each PV unit to be I_m, the voltage of each module be V_m. Let the cumulative current, voltage, and power of the array be I_a, V_a and P_a respectively.

4.3.1 TCT configured PV Array

This arrangement addresses the drawbacks associated with the SP configuration of PV arrays. It involves an initial parallel alignment of all modules in rows, followed by the sequential connection of these rows. A significant drawback of the TCT connection lies in its substantial wiring needs, attributable to the considerable number of cross-ties. This characteristic diminishes its practical suitability for widespread implementation in large-scale photovoltaic installations. The number of cross-ties required in a 9×9 PV arrangement is 64 as shown in Fig. 4.3(a). Within this arrangement, the voltage spanning each row mirrors the voltage across each module. The collective output voltage of the PV array results from the summation of the distinct voltages within each row. Correspondingly, the PV array's total output current stems from the amalgamation of the individual currents associated with modules within a given row. The cumulative current I_a, voltage V_a and power P_a of this PV arrangement can be estimated as:

$$\begin{aligned} I_a &= I_{\text{row},9} = I_{\text{row},8} = I_{\text{row},7} = \ldots = I_{\text{row},1} = \textstyle\sum_{c=1}^{9} I_{1c} \\ &= I_{11} + I_{12} + I_{13} + \ldots + I_{19} = 9I_m \end{aligned} \tag{4.3}$$

$$\begin{aligned} V_a &= V_{\text{col},9} = V_{\text{col},8} = V_{\text{col},7} = \ldots = V_{\text{col},1} = \textstyle\sum_{r=1}^{9} V_{r1} \\ &= V_{11} + V_{21} + V_{31} + V_{41} + \ldots + V_{91} = 9V_m \end{aligned} \tag{4.4}$$

$$P_a = 9I_m \times 9V_m = 81V_m I_m \tag{4.5}$$

4.3.2 B-L Configured PV Array

In series arrangement when specific cells or modules experience IMSs or malfunctions, there is a significant and pronounced reduction in the overall output voltage of the PV system. The SP topology suffers from the increased occurrence of ML due to a higher quantity of series connections among modules within a string. To alleviate the significant ML incurred in S and SP

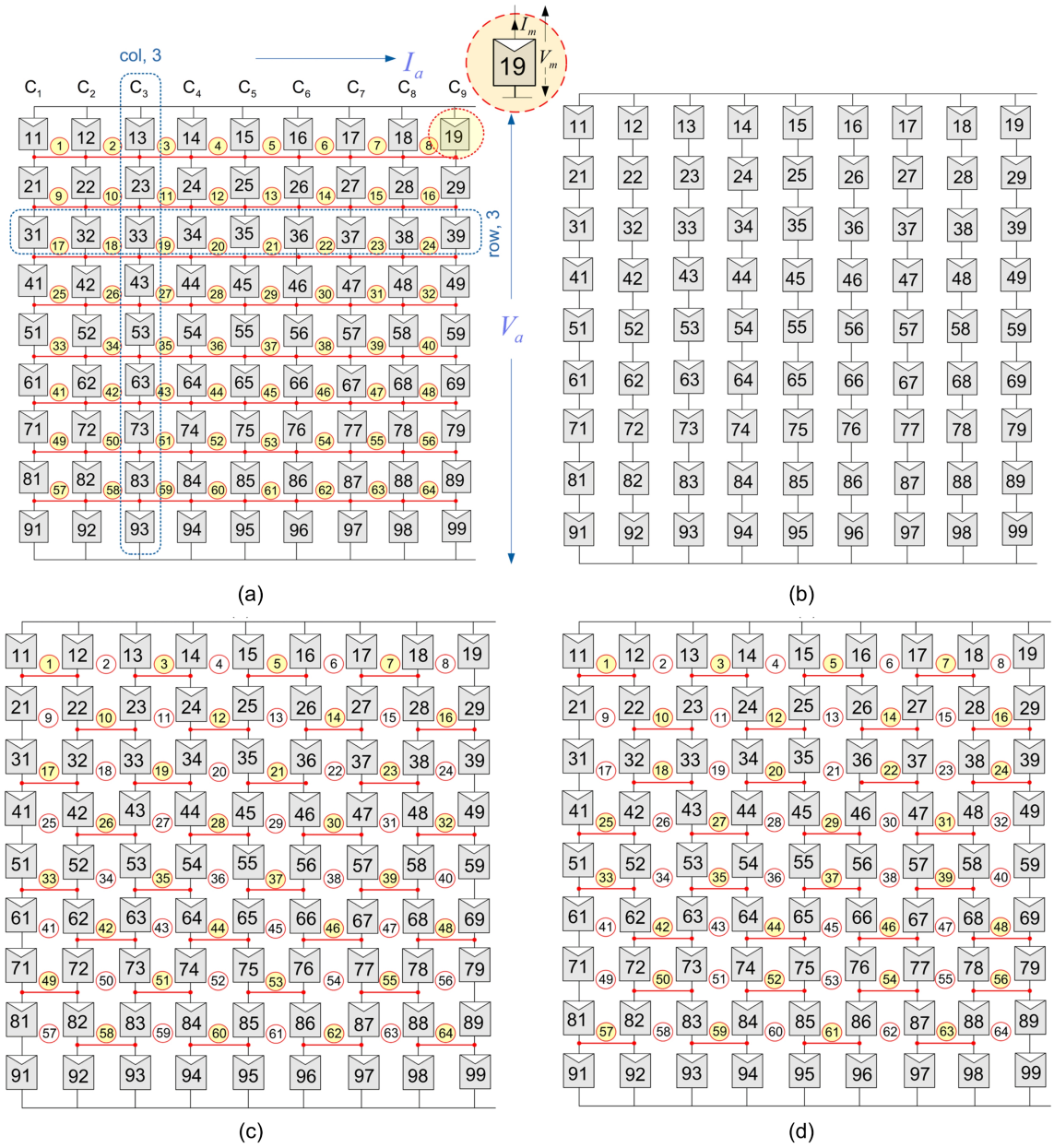

FIGURE 4.3: 9×9 PV array arrangements: (a) TCT configuration (64 cross-ties). (b) SP configuration (0 cross ties). (c) B-L configuration (32 cross-ties). (d) H-C configuration (32 cross ties).

configurations, PV units are interconnected within the array similar to bridge rectifier configuration as depicted in Fig. 4.3(c). The B-L arrangement exhibits higher series interconnection of PV units within the string but fewer than the S and SP arrangements. The total number of cross ties required for interconnecting

PV units in B-L configuration for a 9 × 9 PV array is 32. In this structural arrangement, it becomes evident that a pair of modules within the bridge interconnect sequentially and subsequently parallelize (refer Fig. 4.3(c)). All these interconnected bridges are united to attain the targeted output voltages and currents through the summation of voltages in a sequential manner and currents in a parallel arrangement.

4.3.3 H-C Configured PV Array

In this configuration, the PV units are linked together in a manner reminiscent of the hexagonal structure found in honeycomb architecture. The physical layout of a H-C configured PV array for a 9×9 configuration is shown in Fig. 4.3(d). There are 32 cross-ties in the H-C configuration. The H-C topology exhibits a higher quantity of series connections when contrasted with the TCT and B-L PV setups. However, it features a lower number of series connections compared to S and SP array topologies. Consequently, the ML in the H-C PV array topologies surpasses those in the TCT and B-L PV array topologies but remains lower than those in the S and SP PV array topologies.

4.3.4 Proposed MPVA PV Array

The wiring structure of the proposed reduced cross-tied PV arrangement, MPVA, along with the proposed criteria for selecting cross-ties, is outlined below:

4.3.4.1 Criteria for Selection of Cross-ties

Consider a 2 × 2 PV array setup as shown in Fig. 4.4(i). In Fig. 4.4(ii), an additional cross-tie wire-1-1′is connected in the 2 × 2 PV arrangement. The criteria for selecting or removing a cross-tie are based on the peak power achieved under the tested scenarios. If the global peak power achieved by configuration I (without cross-tie) (refer Fig. 4.4(i)) is equal to that of configuration II (with cross-tie) (refer Fig. 4.4(ii)), the cross-tie can be removed without any loss of power. To develop the proposed reduced cross-tied PV arrangement (MPVA), a simulation analysis of all potential shading scenarios on a 2 × 2 PV array were conducted to assess the necessity of a cross-tie, as

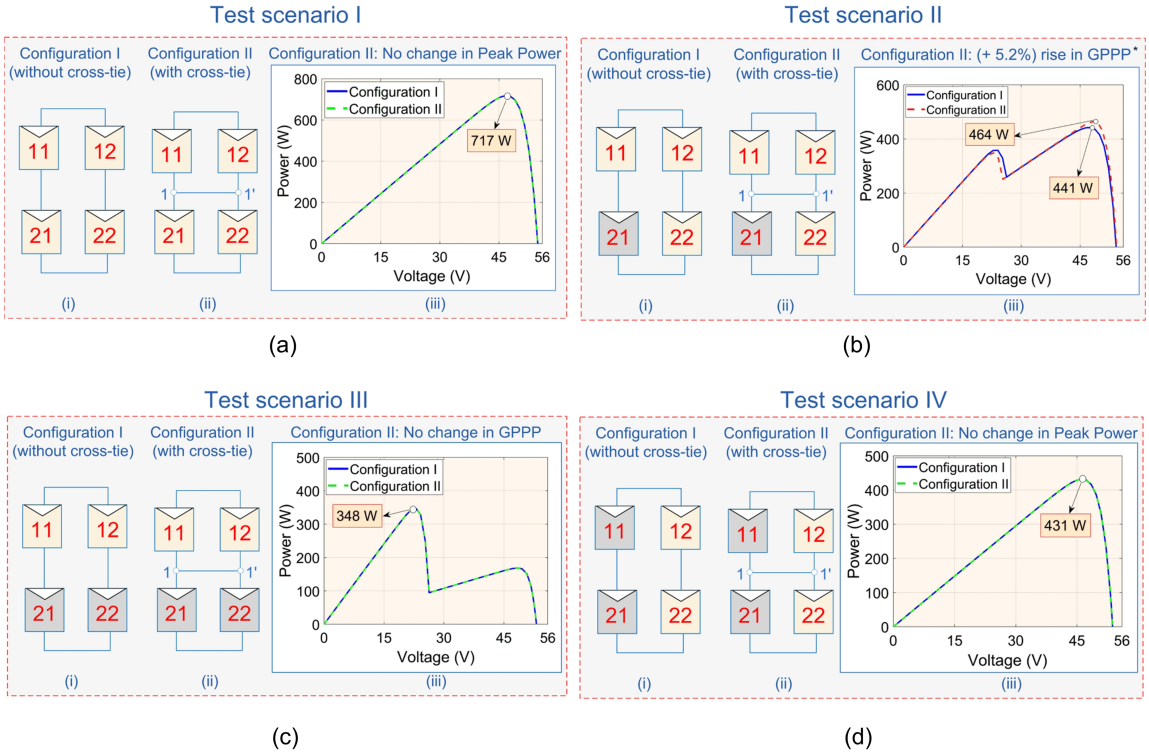

FIGURE 4.4: 2 × 2 PV array: (a) Test Scenario I. (b) Test Scenario II. (c) Test Scenario III. (d) Test Scenario IV.

described below. Each PV module selected for the simulation analysis has a rating of 200 W.

(a) Test Scenario I (Uniform irradiance conditions): All four PV modules of the 2 × 2 PV array in configurations I and II are subjected to the same irradiance profile (i.e., 900 W/m^2) as shown in Fig. 4.4(a). The peak power achieved by configurations I and II is identical, at 717 W, as depicted in Fig. 4.4(a). Therefore, the cross-tie can be eliminated when all four PV modules in a 2 × 2 PV subarray receive uniform insolation.

(b) Test Scenario II (One PV module experiences IMS): One out of four PV modules experiences shading conditions and receives an irradiance of 200 W/m^2, whereas the remaining three PV modules receive an irradiance of 900 W/m^2, as shown in Fig. 4.4(b). The peak power attained by configurations I and II is 441 W and 464 W, respectively. Based on the GPPP values, configuration II, which includes a cross-tie, should be selected as it results in a 5.2% increase in GPPP value, as evident from the power curve depicted in Fig. 4.4(b). Therefore, a cross-tie is

required to extract higher power under this shading case. It must be noted that the rise in the GPPP using the cross-tie will be higher depending on the intensity of shading on the PV module.

(c) Test Scenario III (Two PV Modules Experience IMS - 'Horizontal Shading'): The bottom two modules experience shading conditions and receive an irradiance of 200 W/m^2, whereas the remaining two modules receive an irradiance of 900 W/m^2.The remaining top two PV modules receive an irradiance of 900 W/m^2, as shown in Fig. 4.4(c). The GPPP value attained using configurations I and II is identical at 348 W, as depicted in the P-V curve in Fig. 4.4(c). Hence, the cross-tie can be removed without losing power under this scenario. Similar characteristics are obtained when the top two PV modules experience shading.

(d) Test Scenario IV (Two PV Modules Experience IMS - 'Vertical Shading'): In the 2 $\times$ 2 PV array, under this scenario, the PV modules in the first column receive an irradiance of 200 W/m^2, while the remaining two modules receive 900 W/m^2, as illustrated in Fig. 4.4(d). Configurations I and II both achieve a peak power of 431 W, as shown in the power curve in Fig. 4.4(d). Similarly, shading all PV modules in column II yields a comparable response. Hence, the cross-tie can be removed without affecting the generated power.

(e) Test Scenario V (Two PV Modules Experience IMS - 'Diagonal Shading'): The PV modules positioned diagonally receive an irradiance of 200 W/m^2, while the remaining two modules receive 900 W/m^2, as illustrated in Fig. 4.5(a). The peak power attained by configurations I and II is 347 W and 431 W, respectively. Based on the GPPP values, configuration II, which includes a cross-tie, should be selected as it results in a 24.2% increase in GPPP value, as evident from the power curve depicted in Fig. 4.5(a).Therefore, a cross-tie is required to extract higher power under this shading case.

(f) Test Scenario VI (Three PV Modules Experience IMS): Under this shading case, three PV modules receive irradiance of 200 W/m^2, while the remaining PV module receives 900 W/m^2, as illustrated in Fig. 4.5(b). The GPP attained by configurations I and II is 207 W and 214 W, respectively. Based on the GPPP values, configuration II, which includes a cross-tie, should should be selected as it results in a 3.38% increase in GPPP value, as evident from the power curve depicted in Fig. 4.5(b). Therefore, a cross-tie is required to extract higher power under this shading case.

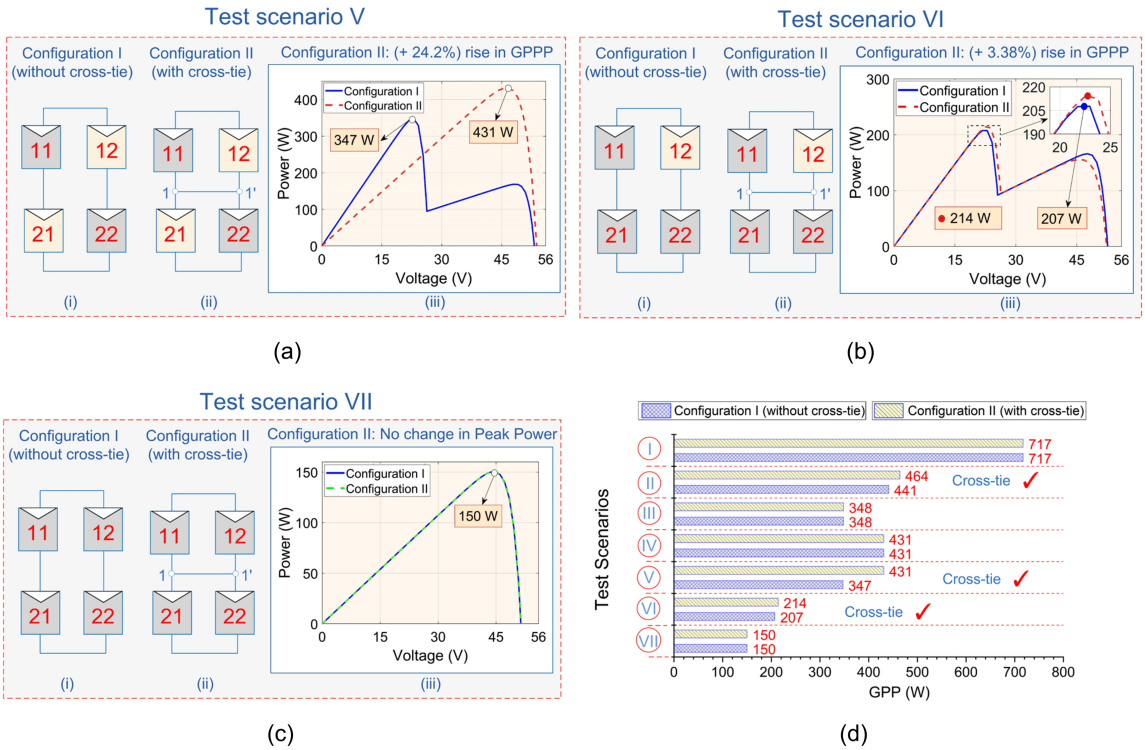

FIGURE 4.5: 2 × 2 PV array: (a) Test Scenario V. (b) Test Scenario VI. (c) Test Scenario VII. (d) Comparative assessment of the necessity of cross tie under different scenarios.

(g) Test Scenario VII (All PV Modules Experience IMS): All four PV modules of the 2×2 PV array in configurations I and II are subjected to the same irradiance profile (i.e., 200 W/m^2) as shown in Fig. 4.5(c). The peak power achieved by configurations I and II is identical, at 150 W, as depicted in the power curve in Fig. 4.5(d). Hence, the presence of a cross-tie is redundant.

From the above simulation analysis, it is evident that to maximize power extraction under IMSs, a cross-tie is essential in a 2×2 PV sub-array under the following conditions and is redundant otherwise:

Condition 1: One of the four modules is under the impact of shading (*Test Scenario II*).

Condition 2: Two diagonally opposite modules are affected by shading (*Test Scenario V*).

Condition 3: Three out of the four PV modules experience shading events (*Test Scenario VI*).

The combined results obtained under all shading scenarios, along with the

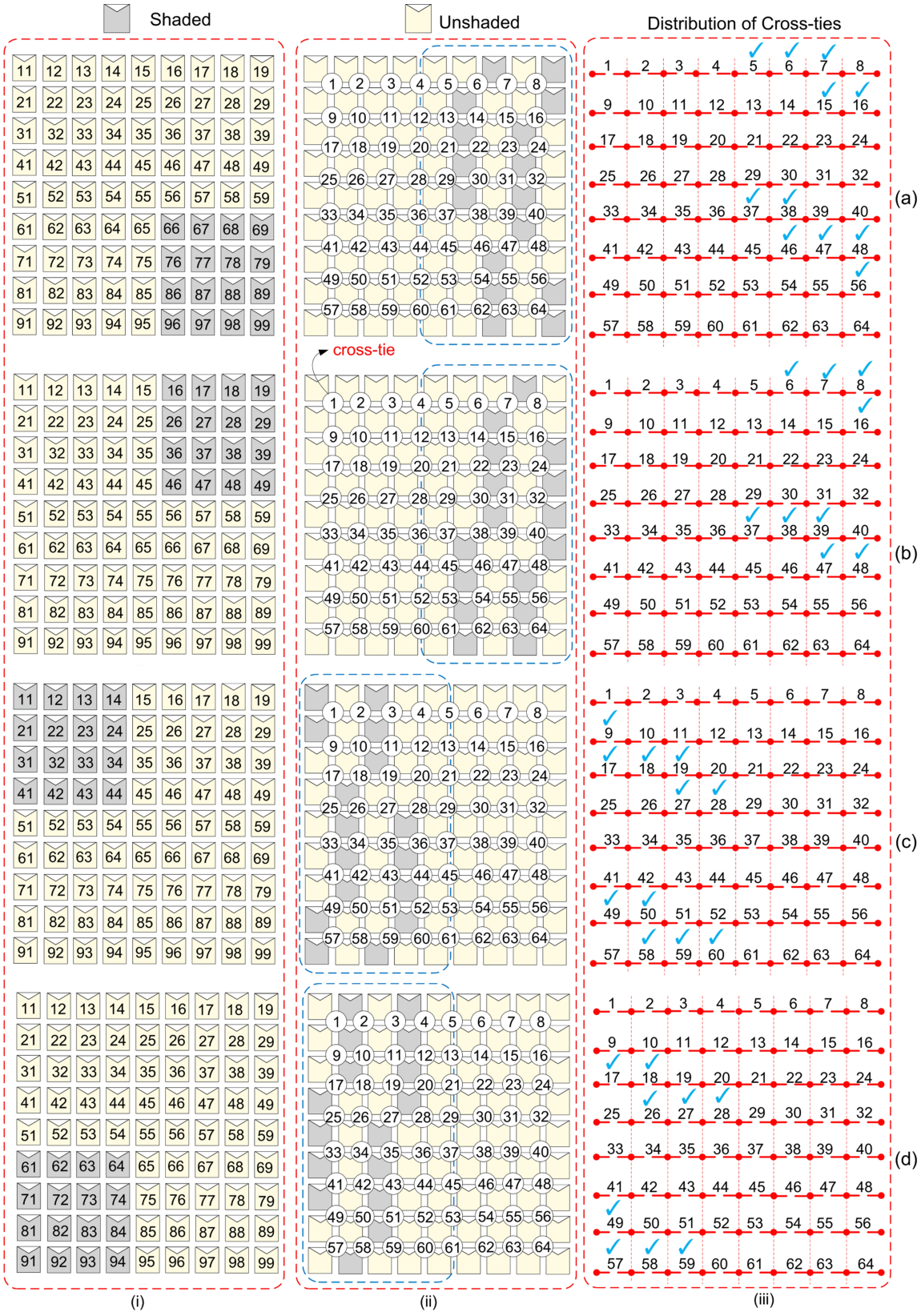

FIGURE 4.6: 9×9 PV array: (i) different IMSs. (ii) SD using the proposed PMSRA. (iii) distribution of cross-ties for: (a) IMS-I. (b) IMS-II. (c) IMS-III. (d) IMS-IV.

indication of the requirement for cross-ties, are also illustrated in Fig. 4.5(d). Using these results, the selection of cross-ties at specific locations in a 9×9 PV array is determined by examining SD achieved by the proposed PMSRA reconfiguration approach under different IMSs and applying any of the three earlier specified conditions (***conditions I, II, and III***). Fig. 4.6 illustrates the shading scenarios considered and the SD achieved using the proposed reconfiguration scheme. Additionally, the specific locations where cross-ties are selected within the array for all shading scenarios are depicted after applying the different conditions. For instance, cross-ties at locations 5 (***condition I*** satisfied), 6 (***condition II*** satisfied), and 7 (***condition I*** satisfied) are selected in the first row of the array under scenario I, as depicted in Fig. 4.6(a). Similarly, cross-ties at other locations are selected. This process is repeated for all the cases. Redundant crossties are removed from the array, leading to the most optimized wiring arrangement for the PV array.

4.3.4.2 Motivation and Novelty

TCT configurations are preferred over SP configurations due to their substantial reduction in shadowing losses. However, the increased wiring complexity in TCT PV setups compared to SP configurations leads to higher wiring costs and additional losses. Thus, there is a need for a new and improved PV arrangement that performs well in shading scenarios while minimizing the extensive wiring requirements typical of TCT configurations. The proposed 9 × 9 MPVA requires only 26 cross-ties, marking a substantial 59.37% reduction in cross-wiring requirements (see Fig. 4.7(b)). The criteria for selecting these cross-ties are straightforward and applicable to PV arrays of varying dimensions without added complexity, ensuring an optimized PV arrangement that maximizes power extraction under IMSs.

4.3.4.3 Wiring structure of the Proposed MPVA

The initial configuration of the array follows a straightforward SP arrangement. Between row 1 and row 2, cross ties are placed at positions 5, 6, 7, and 8, as illustrated in Fig. 4.7(b). Moving on to rows 2 and 3, cross ties are positioned at locations 9, 15, and 16. Subsequently, for rows 3 and 4, cross connections among

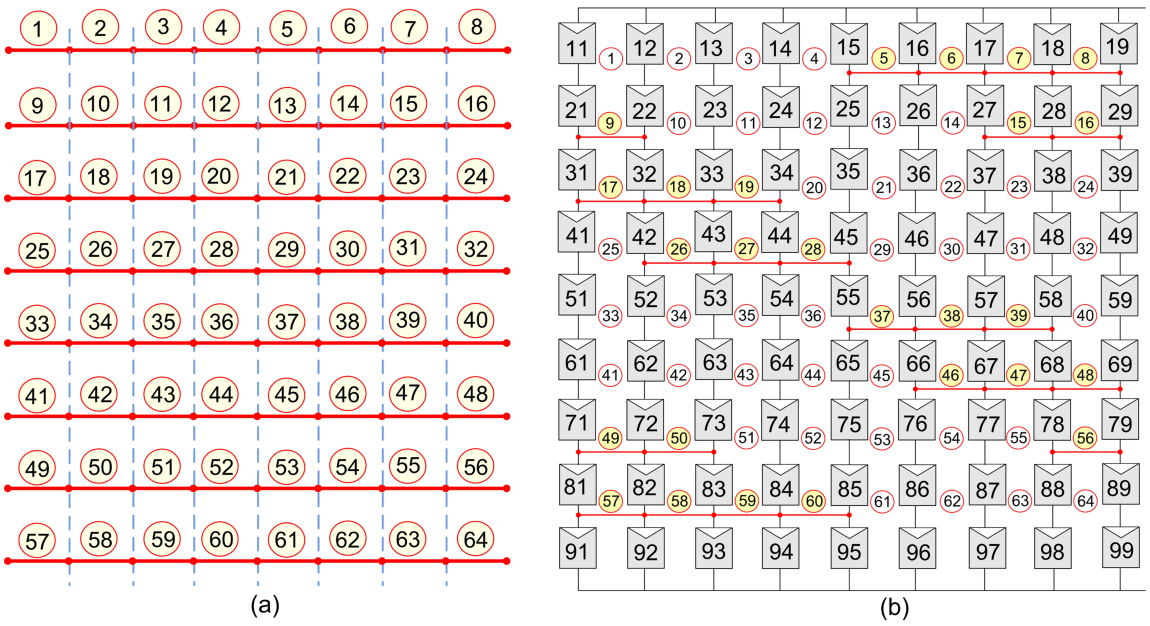

FIGURE 4.7: 9×9 PV configuration for (a) benchmark TCT (64 cross ties). (b) proposed MPVA (26 cross ties).

PV units are established at positions 17, 18, and 19. Similarly, cross ties are introduced at locations 26, 27, and 28 for rows 4 and 5. In the case of rows 5 and 6, PV modules are cross-connected at positions 37, 38, and 39. This pattern continues with cross connections at positions 46, 47, and 48 for rows 6 and 7. Finally, cross ties are established at locations 49, 50, and 56 for rows 7 and 8, and 57, 58, 59, and 60 for rows 8 and 9, respectively.

The output current, voltage, and power relations for a 9×9 MPVA are given as:

$$\begin{aligned} I_a &= I_{\text{row},9} = I_{\text{row},8} = I_{\text{row},7} = \ldots = I_{\text{row},1} = \textstyle\sum_{c=1}^{9} I_{1c} \\ &= I_{11} + I_{12} + I_{13} + \ldots + I_{19} = 9I_m \end{aligned} \tag{4.6}$$

$$\begin{aligned} V_a &= V_{\text{col},9} = V_{\text{col},8} = V_{\text{col},7} = \ldots = V_{\text{col},1} = \textstyle\sum_{r=1}^{9} V_{r1} \\ &= V_{11} + V_{21} + V_{31} + V_{41} + \ldots + V_{91} = 9V_m \end{aligned} \tag{4.7}$$

$$P_a = 9I_m \times 9V_m = 81V_m I_m \tag{4.8}$$

4.4 Progressive Module Shift Rearrangement Approach (PMSRA)

Any PV array, with dimensions $r \times c$, can be effectively reconfigured using the proposed PMSRA algorithm through the systematic procedural steps outlined below. Here ' r ' and ' c ' respectively represent the number of rows and columns present in the PV configuration. The versatility of the proposed approach extends to both symmetrical and unsymmetrical PV structures, accommodating even unequal sizes for ' r ' and ' c '.

A PV module can occupy any position within the array, which can be specified using two digits representing the row and column index positions associated with the module. For example, '25' represents a PV module positioned in the second row and fifth column. In the proposed rearrangement strategy, as only row indices are altered while column indices remain intact, indicating module rearrangement only within a column, the PV module position is represented using a single digit, reflecting only the row index position. In this work, the proposed PMSRA is specifically applied to the suggested MPVA configuration having significantly fewer cross-ties compared to the TCT configuration.

For any $r \times c$ PV array: $r =$ rows; $c =$ columns.

Step 1: Identify the 'master' column, C_j in the PV array.

Case I: ' c ' is an odd number $\{c : c = 2k - 1 \text{ where } k \in N\}$, where ' N ' is a set of natural numbers. The master column is given by $j = \frac{c}{2}$. Here, ' represents the 'ceil' operator. For 9×9 and 5×5 PV arrays, $j = 5$ and $j = 3$ respectively.

Case II: 'c' is an even number $\{c : c = 2k \text{ where } k \in N\}$. $j = \frac{c}{2} + 1$. For 6×6 and 6×4 PV arrays, $j = 4$ and $j = 3$ respectively. Fig. 4.8(a) shows a 9×9 PV array interconnected in an MPVA configuration, with the 'master column' highlighted.

Step 2: Arrange members of the 'master' column sequentially in ascending order, starting from row index ' 1 ' up to the last row index, 9, as depicted in Fig. 4.8(b).

Step 3: Segment the entire PV array into two sections, namely 'section I' and 'section- II', located towards the left and right of the master column, C_j respectively. The members in 'section I' undergo a progressive downward shift,

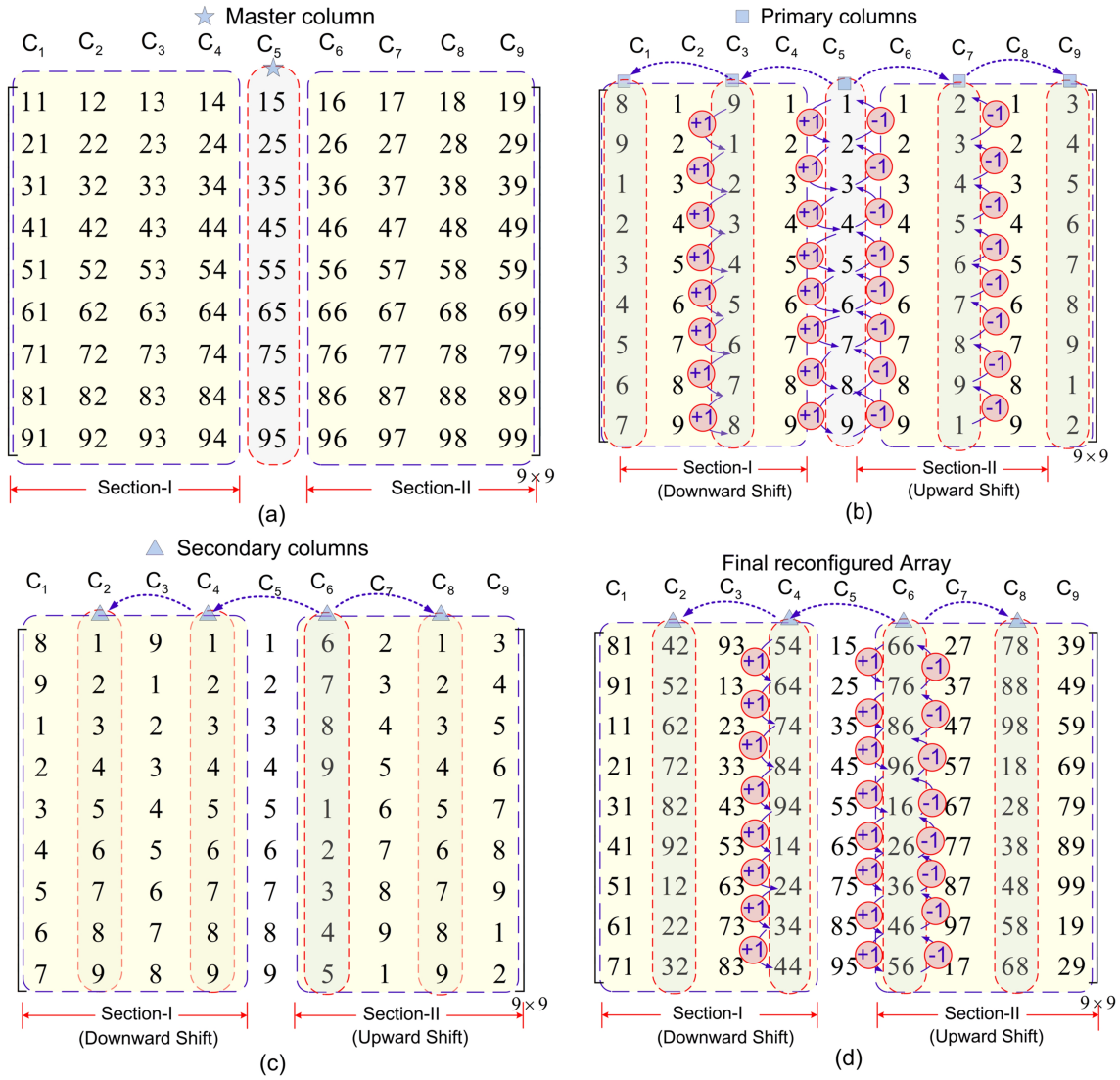

FIGURE 4.8: Layout of the proposed PMSRA rearrangement strategy for a 9 × 9 PV array: (a) Master column identification/ array division into sections. (b) 'primary columns' identification and shift operations. (c) 'secondary columns' identification. (d) remaining shift operations and final reconfigured PV array.

while members in 'section II' undergo a progressive upward shift in their respective columns. (refer Fig. 4.8(b)).

Step 4: Identify 'primary columns', C_p such that $p = j, j+2, j+4, j+6, \ldots \quad \{p : j \leq p \leq c\}$ Therefore, the master column C_5 and other columns i.e. C_7, C_9 of section-II are identified as the 'primary' columns, as shown in Fig. 4.8(b). Likewise, the 'primary' columns, C_p for section-I are determined such that

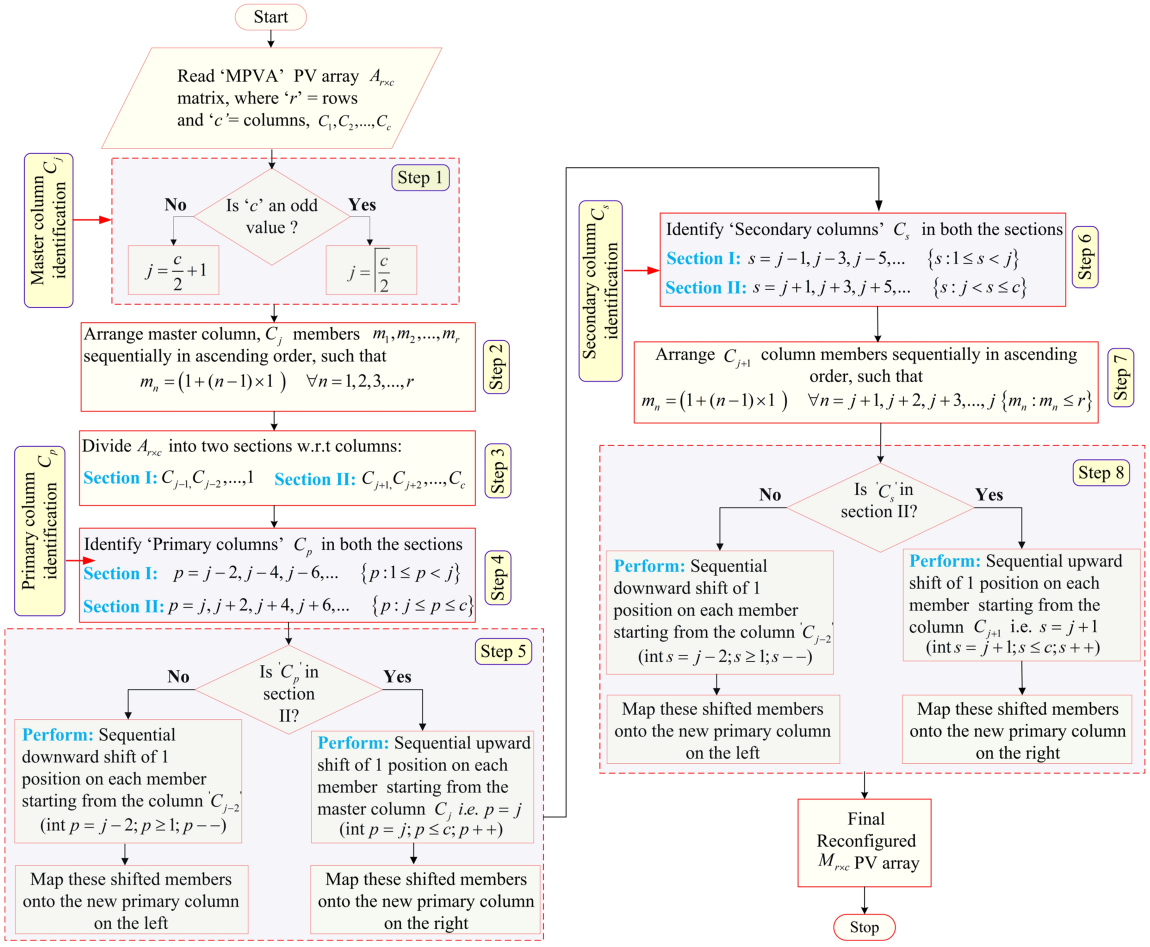

FIGURE 4.9: The complete flow diagram of the proposed approach depicting various operational steps.

$p = j-2, j-4, j-6, \ldots \quad \{p : 1 \le p < j\}$. So, columns C_3 and C_1 are selected as 'primary columns' in section-I (refer Fig. 4.8(b)).

Step 5: All PV units in the 'master' column and section-II 'primary' columns undergo a progressive upward shift of 1 position before being mapped to the new 'primary' column on the right. Similarly, all PV units in the master column and section-I 'primary' columns undergo a progressive downward shift of 1 position before being mapped to the new column on the left, as illustrated in Fig. 4.8(b).

Step 6: Identify the 'secondary' columns, C_s such that $s = j+1, j+3, j+5, \ldots \quad \{s : j < s \le c\}$. Therefore, columns C_6 and C_8 of section-II areidentified as the 'secondary' columns, as shown in Fig. 4.8(c). Likewise, the

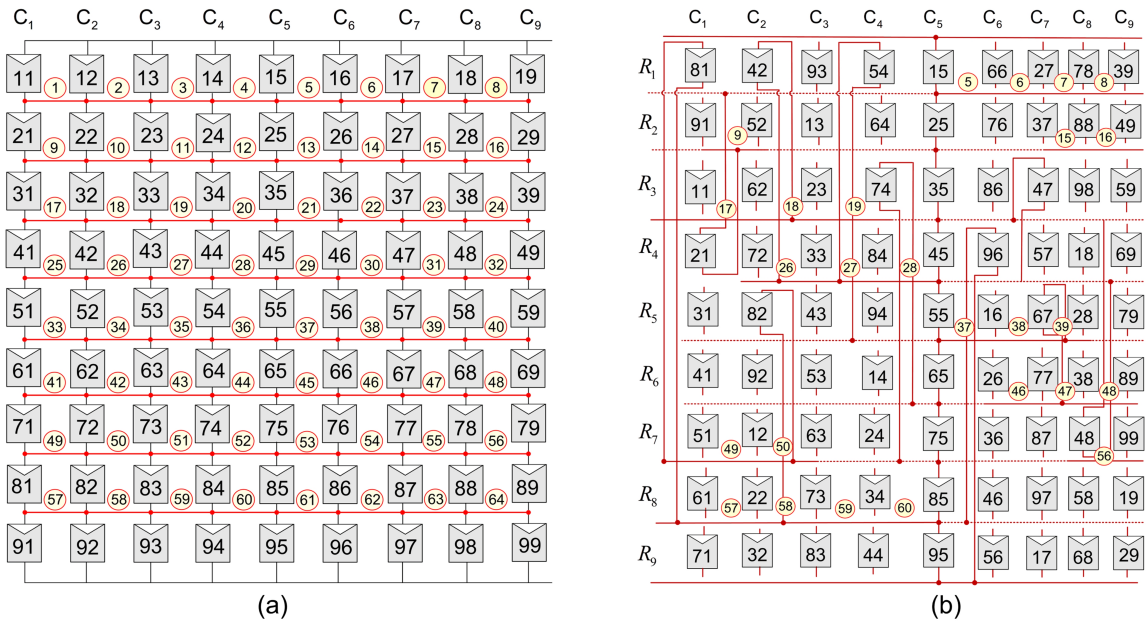

FIGURE 4.10: Wired connection layout of 9×9 PV arrangement for (a) TCT configuration (64 cross-ties). (b) proposed PMSRA (26 cross ties).

'secondary' columns, C_s, for section-I are determined such that $s = j-1, j-3, j-5, \ldots \quad \{s : 1 \leq s < j\}$. So, columns C_4 and C_2 are selected as 'secondary' columns in section-I (refer Fig. 4.8(c)).

Step 7: The precise positions of PV modules in the 'secondary' column, C_{j+1} are determined by sequentially placing the PV modules, starting from $(j+1)^{\text{th}}$ member as the initial PV unit as shown in Fig. 4.8(c).

Step 8: The exact locations of the corresponding PV units in the remaining 'secondary' columns for sections II and I are obtained by applying step 5 w.r.t the 'secondary' column, C_{j+1} The final rearranged MPVA using the proposed PMSRA for a 9×9 PV configuration is depicted in Fig. 4.8(d). The comprehensive flowchart of the proposed approach, depicting key operational steps, is presented in Fig. 4.9. The final reconfigured MPVA has PV units at specific pre-determined locations within the array, achieved using the proposed PMSRA, without disturbing the end-terminal electrical connections. The wiring structure for T-C-T and the proposed PMSRA configuration is shown in Fig. 4.10(a) and (b), respectively. For instance, module '42' in the column, C_2, although now positioned where '12' was originally located, remains electrically connected in parallel to members of the 4th row (4.10(b)).

TABLE 4.1: Technical Specifications of PV Module Used in Simulation and Experiments

Technical Specifications	Simulation	Experimental
Peak Power, P_m(W)	200 W	10 W
Operating voltage @ PPP* *, V_{pm}(V)	23.56 V	19.25 V
Operating current@ PPP, I_{pm}(A)	8.49 A	0.52 A
Short Circuit Current, I_{sc}(A)	9 A	0.55 A
Open Circuit Voltage, V_{oc}(V)	27.76 V	22.50 V
Cell count, N_s	36	36
Physical measurements (mm) (*Length* $\times$ *Width* $\times$ *Height)*	$1490 \times 665 \times 30$	$255 \times 350 \times 22$

4.5 Simulation Analysis and Experimental Validation

This section give details regarding the simulation and experimental analysis conducted.

4.5.1 Simulation Results and Performance Analysis

An exhaustive simulation and experimental analysis have been undertaken, encompassing widely adopted reconfiguration strategies. To enable a thorough comparative assessment, critical performance indicators have been selected to characterize array performance across various IMSs. The prominent metrics chosen include FF, ER, EFF, ML, and PE with respect to the benchmark TCT. The simulation study is executed on an extensive 9×9 PV configuration, comprising 81 modules, each rated at 200 W. The technical specifications are detailed in Table 4.1.

TABLE 4.2: Analytical Computations of Current, Voltage, and Power Attained for CMAP, PRS

IMS	Row Index	CMAP [91]			Row Index	PRS [93]		
		I_m (A)	V_m (V)	P_a (W)		I_m (A)	V_m (V)	P_a (W)
IMS-I: LRCS	R_1	4.9	9	44.1	R_8	5.7	9	51.3
	R_9	5.7	8	**45.6**	R_9	6.5	8	**52**
	R_2	-	-	-	R_6	-	-	-
	R_8	6.5	6	39	R_4	-	-	-
	R_3	-	-	-	R_3	-	-	-
	R_7	7.3	4	29.2	R_1	-	-	-
	R_4	-	-	-	R_7	7.3	3	21.9
	R_6	8.1	2	16.2	R_5	-	-	-
	R_5	-	-	-	R_2	-	-	-
IMS-II: URCS	R_5	5.3	9	47.7	R_5	6	9	**54**
	R_6	6	8	**48**	R_9	6.7	8	53.6
	R_4	-	-	-	R_7	-	-	-
	R_7	6.7	6	40.2	R_6	-	-	-
	R_3	-	-	-	R_3	-	-	-
	R_8	7.4	4	29.6	R_2	-	-	-
	R_2	-	-	-	R_8	7.4	3	22.2
	R_9	8.1	2	16.2	R_4	-	-	-
	R_1	-	-	-	R_1	-	-	-

Table 4.2 (continued)

IMS	Row Index	CMAP [91]			Row Index	PRS [93]		
		I_m (A)	V_m (V)	P_a (W)		I_m (A)	V_m (V)	P_a (W)
IMS-III: ULCS	R_1	5.7	9	**51.3**	R_1	6.3	9	**56.7**
	R_9	6.3	8	50.4	R_9	6.9	8	55.2
	R_2	-	-	-	R_8	-	-	-
	R_8	6.9	6	41.4	R_7	-	-	-
	R_3	-	-	-	R_4	-	-	-
	R_7	7.5	4	30	R_3	-	-	-
	R_4	-	-	-	R_6	7.5	3	23.1
	R_6	8.1	2	16.2	R_5	-	-	-
	R_5	-	-	-	R_2	-	-	-
IMS-IV: LLCS	R_6	5.1	9	45.9	R_2	5.85	9	52.6
	R_7	5.85	8	**46.8**	R_9	6.6	9	**52.8**
	R_5	-	-	-	R_7	-	-	-
	R_8	6.6	6	39.6	R_6	-	-	-
	R_4	7.1	5	35.5	R_5	-	-	-
	R_9	7.6	4	30.4	R_4	-	-	-
	R_3	-	-	-	R_8	7.35	3	22.0
	R_2	8.1	2	15.4	R_3	-	-	-
	R_1	-	-	-	R_1	-	-	-

TABLE 4.3: Analytical Computations of Current, Voltage, and Power Attained for ACMS, PMSRA

IMS	Row Index	ACMS [89] I_m (A)	ACMS [89] V_m (V)	ACMS [89] P_a (W)	Row Index	PMSRA (Proposed) I_m (A)	PMSRA (Proposed) V_m (V)	PMSRA (Proposed) P_a (W)
IMS-I: LRCS	R_4	5.7	9	51.3	R_9	6.5	9	**58.5**
	R_9	6.5	8	**52**	R_8	-	-	
	R_8	-	-	-	R_5	-	-	-
	R_5	-	-	-	R_4	-	-	-
	R_3	-	-	-	R_3	-	-	-
	R_2	-	-	-	R_2	-	-	-
	R_7	7.3	3	21.9	R_1	-	-	-
	R_6	-	-	-	R_7	7.3	2	14.6
	R_1	-	-	-	R_6	-	-	-
IMS-II: URCS	R_7	6	9	**54**	R_9	6.7	9	**60.3**
	R_6	6.7	8	53.6	R_8	-	-	-
	R_5	-	-	-	R_7	-	-	-
	R_3	-	-	-	R_6	-	-	-
	R_2	-	-	-	R_5	-	-	-
	R_1	-	-	-	R_4	-	-	-
	R_9	7.4	3	22.2	R_3	7.4	3	22.2
	R_8	-	-	-	R_2	-	-	-
	R_4	-	-	-	R_1	-	-	-

Table 4.3 (continued)

IMS	Row Index	ACMS [89] I_m (A)	V_m (V)	P_a (W)	Row Index	PMSRA (Proposed) I_m (A)	V_m (V)	P_a (W)
IMS-III: ULCS	R_4	6.3	9	**56.7**	R_9	6.9	9	**62.1**
	R_9	6.9	8	55.2	R_8	-	-	-
	R_8	-	-	-	R_7	-	-	-
	R_6	-	-	-	R_6	-	-	-
	R_3	-	-	-	R_5	-	-	-
	R_2	-	-	-	R_2	-	-	-
	R_7	7.5	3	23.1	R_1	-	-	-
	R_5	-	-	-	R_4	7.5	2	15
	R_1‘	-	-	-	R_3	-	-	-
IMS-IV: LLCS	R_1	5.85	9	52.6	R_7	6.6	9	**59.4**
	R_9	6.6	8	**52.8**	R_6	-	-	-
	R_8	-	-	-	R_5	-	-	-
	R_7	-	-	-	R_4	-	-	-
	R_6	-	-	-	R_3	-	-	-
	R_5	-	-	-	R_2	-	-	-
	R_4	7.35	3	22.0	R_1	-	-	-
	R_3	-	-	-	R_9	7.35	2	15
	R_2	-	-	-	R_8	-	-	-

4.5.1.1 Description of IMSs and Performance Analysis

The PV array is exposed to mismatch scenarios stemming from diverse orientations. To achieve this, four prevalent shading profiles are chosen, namely Lower Right Corner Shading (LRCS), Upper Right Corner Shading (URCS), Upper Left Corner Shading (ULCS), and Lower Left Corner Shading (LLCS).
***(a) IMS-I:LRCS*:** Under this shading scheme, a 16-cell matrix of PV modules located in the lower right quadrant of the 9×9 TCT and the proposed MPVA configured array experiences reduced irradiance input of 100 W/m^2, while the remaining 65 PV units receive an insolation of 900 W/m^2, as shown in Fig. 4.11. The dispersion of shade is accomplished through widely recognized module rearrangement approaches, namely PRS [93], CMAP [91], ACMS [89], DS [66], and the proposed PMSRA as depicted in Fig. 4.11(b), (c), (d), (e), and (f), respectively. The number of shaded PV modules in each row is highlighted in Fig. 4.11 for various rearrangement approaches. Power-voltage (P-V) and current-voltage (I-V) profiles for different methods are shown in Fig. 4.11(g) and (h), respectively. As evident, the proposed method yields a maximum power of 11,656 W and a maximum current of 55.2 A.Analytical computations of current, voltage, and power for each row are conducted for all the aforementioned configurations. The outcomes of the analytical computations for different methods are presented in Table 4.2 and 4.3. The calculations for the TCT configured array are presented below:

$$I_{\text{row},1} = I_{\text{row},2} = I_{\text{row},3} = I_{\text{row},4} = I_{\text{row},5} = 9 \times \left(\frac{900}{1000}\right) I_m \tag{4.9}$$

$$I_{\text{row},6} = I_{\text{row},7} = I_{\text{row},8} = I_{\text{row},9} = 5 \times \left(\frac{900}{1000}\right) I_m + 4 \times \left(\frac{100}{1000}\right) I_m \tag{4.10}$$

The application of the proposed PMSRA reconfiguration scheme to the suggested reduced cross-tied MPVA results in the highest GPPP location of $58.5 \times V_m I_m$ for the examined PV array among all reconfiguration methods (refer Table 4.2 and 4.3). Efficient dispersion of shade across the entire array surface through various reconfiguration approaches is optimally achieved when the disparity of currents among rows is minimized. The maximum difference of currents among rows for any PV array can be used as an effective measure for evaluating the relative

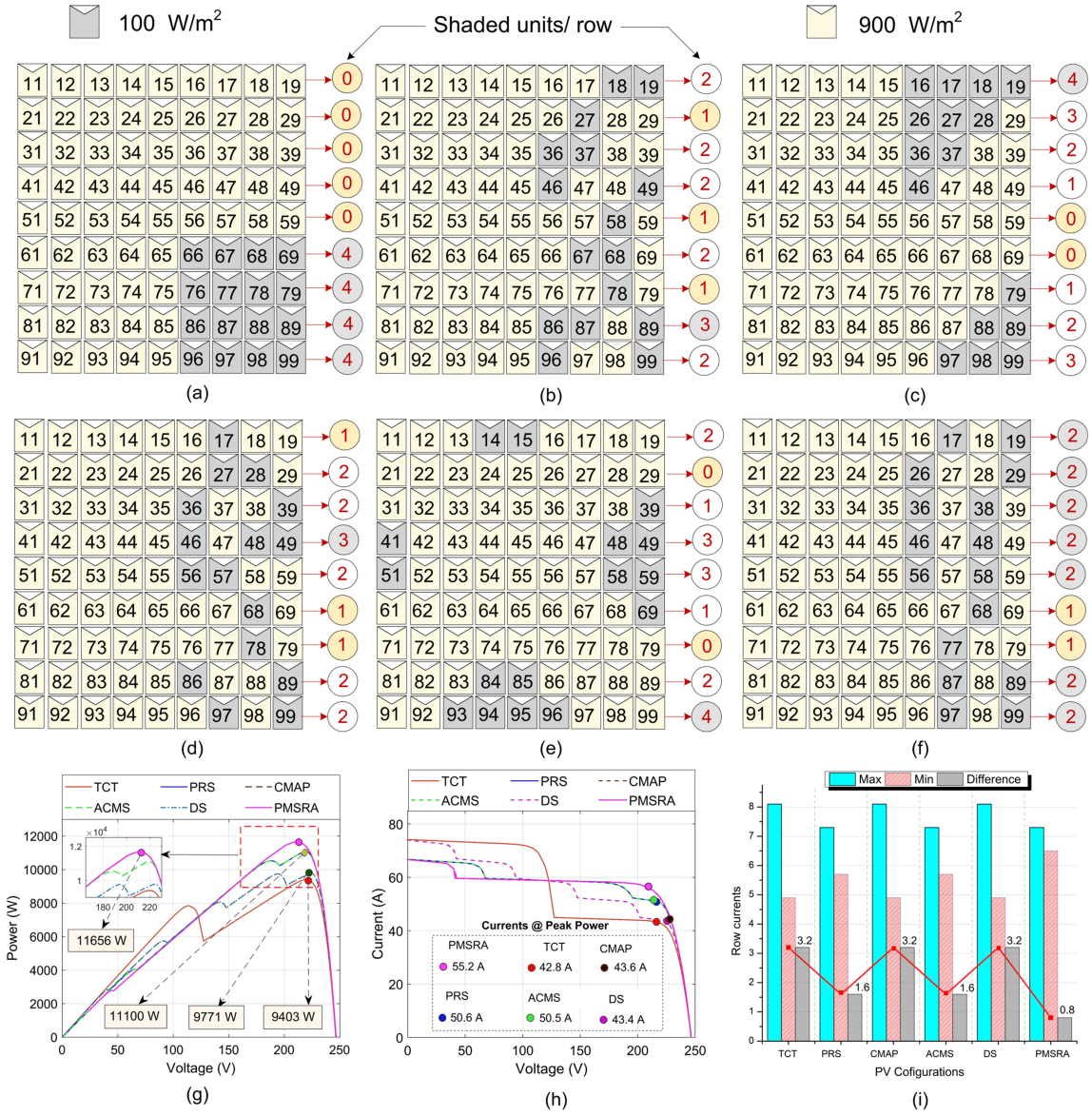

FIGURE 4.11: IMS-I- Lower right corner shading (LRCS) on 9 × 9 PV array: Shade distribution performance with (a) TCT. (b) PRS. (c) CMAP. (d) ACMS. (e) DS. (f) proposed PMSRA. (g) P-V characteristics. (h) I-V characteristics. (i) minimum and maximum row currents generated.

performance of different SD approaches. The maximum difference in row currents, d_{row} is obtained as given below:

$$d_{\text{row}} = I_{row,\,max} - I_{row,min} \tag{4.11}$$

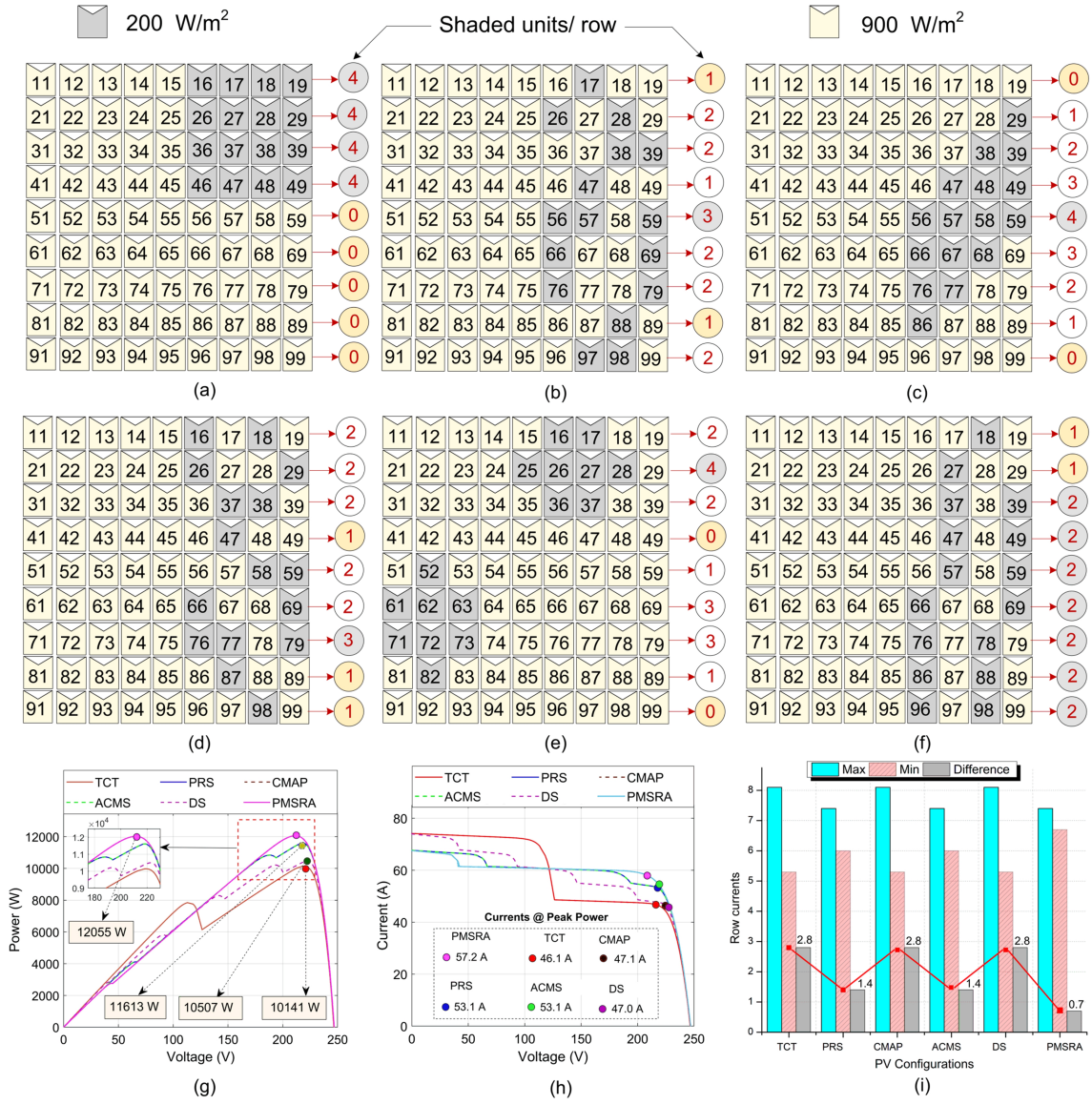

FIGURE 4.12: IMS-II-Upper right corner shading (URCS) on 9 × 9 PV array: Shade distribution performance with (a) TCT. (b) PRS. (c) CMAP. (d) ACMS. (e) DS. (f) proposed PMSRA. (g) P-V characteristics. (h) I-V characteristics. (i) minimum and maximum row currents generated.

The maximum difference in row currents ($d_{\text{row}} = 0.8$)is minimum for the proposed PMSRA, signifying the best SD achieved compared to all other methods as evident from Fig. 4.11(i).

***(b) IMS-II:URCS*:** Under this shading scheme, 16 cell matrix of PV modules

located in the upper right quadrant of the 9×9 TCT configured, and the proposed MPVA array experiences reduced irradiance input of 200 W/m^2, while the remaining 65 PV units insolation of 900 W/m^2, as shown in Fig. 4.12(a).

SD is achieved through well-established module rearrangement methods, including PRS [93], CMAP [91], ACMS [89], DS [66], and the newly introduced PMSRA, illustrated in Fig. 4.12(b), (c), (d), (e) and (f) respectively. The P-V and I-V profiles for different methods are shown in Fig. 4.12(g) and (h) respectively. As evident, the proposed approach delivers a peak power of 12, 055 W and a maximum current of 57.2 A. Analytical calculations for current, voltage, and power are executed individually for every row across all the examined configurations, and results are presented in Tables 4.2 and 4.3. Below are the calculations for the TCT configured PV array:

$$I_{\text{row},5} = I_{\text{row},6} = I_{\text{row},7} = I_{\text{row},8} = I_{\text{row},9} = 9 \times \left(\frac{900}{1000}\right) I_m \tag{4.12}$$

$$I_{\text{row},1} = I_{\text{row},2} = I_{\text{row},3} = I_{\text{row},4} = 5 \times \left(\frac{900}{1000}\right) I_m + 4 \times \left(\frac{200}{1000}\right) I_m \tag{4.13}$$

Implementing the proposed PMSRA reconfiguration strategy on the recommended reduced cross-tied MPVA yields the most favourable GPPP position of $60.3 \times V_m I_m$ within all reconfiguration approaches, as indicated in Tables 4.2 and 4.3. Under, this IMS, again the disparity between the row currents is minimum ($d_{\text{row}} = 0.7$) for the proposed PMSRA, as shown in Fig. 4.12(i).

***(c) IMS-III:ULCS*:** Under this shading scheme, a group of 16 PV modules located in the upper left quadrant of the 9×9 TCT configured, and the proposed MPVA array experiences reduced irradiance input of 300 W/m^2. Meanwhile, the remaining PV units receive an insolation of 900 W/m^2, as shown in Fig. 4.13.SD is achieved through well-established module rearrangement methods, including PRS [93], CMAP [91], ACMS [89], DS [66], and the newly introduced PMSRA, illustrated in Fig. 4.13(b), (c), (d), (e), and (f) respectively. Fig. 4.13(g) and (h) display the P-V and I-V profiles for different methods, respectively. As evident, the presented method delivers a peak power of 12,394 W and a maximum current of 58.4 A.

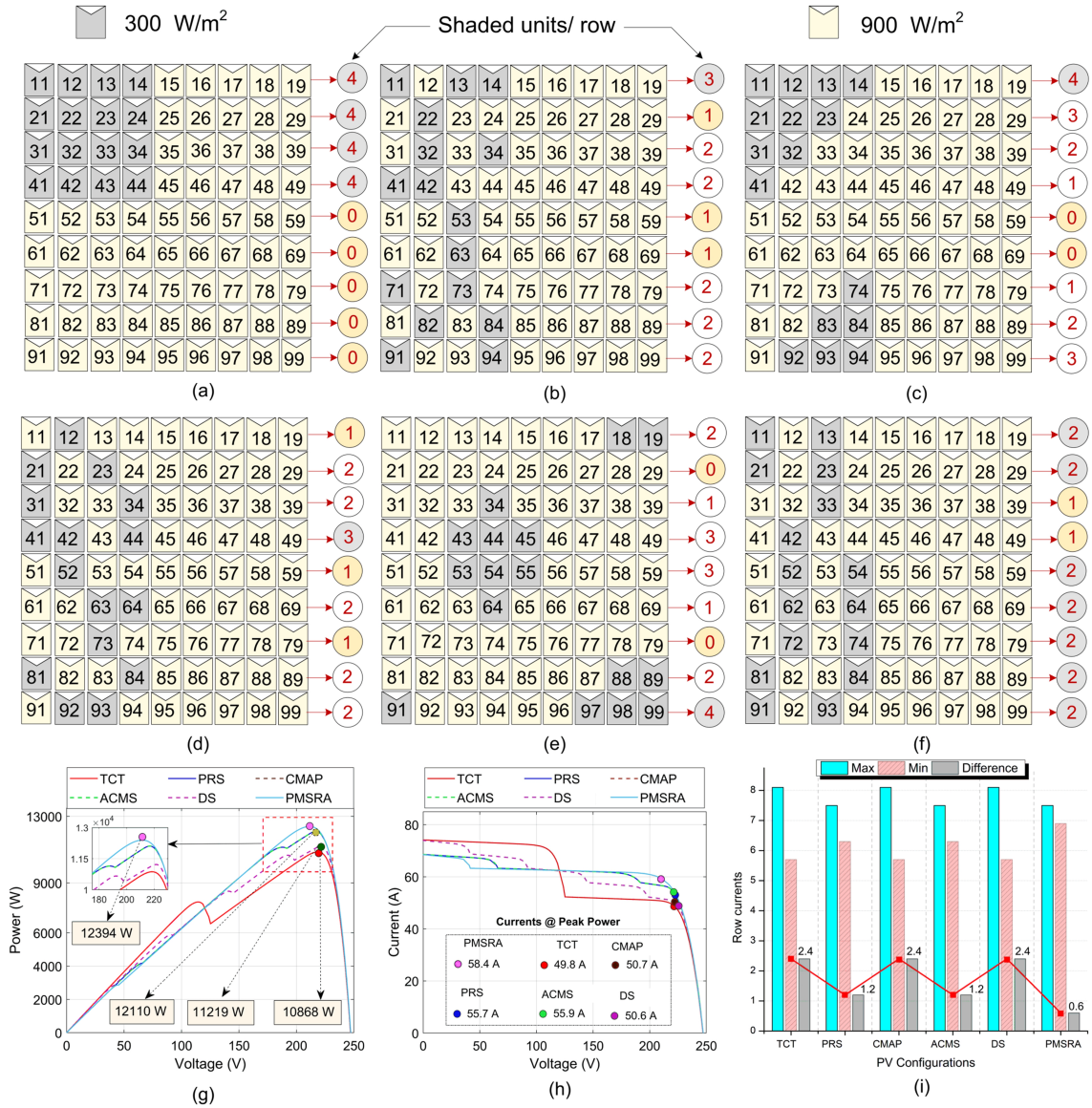

FIGURE 4.13: IMS-III-Upper left corner shading (ULCS) on 9×9 PV array: Shade distribution performance with (a) TCT. (b) PRS. (c) CMAP. (d) ACMS. (e) DS. (f) proposed PMSRA. (g) P-V characteristics. (h) I-V characteristics. (i) minimum and maximum row currents generated.

Analytical calculations for current, voltage, and power are performed separately for each row across all the examined configurations, and the outcomes are presented in Tables 4.2 and 4.3. Below are the calculations for the TCT

configured PV array:

$$I_{\text{row},5} = I_{\text{row},6} = I_{\text{row},7} = I_{\text{row},8} = I_{\text{row},9} = 9 \times \left(\frac{900}{1000}\right) I_m \tag{4.14}$$

$$I_{\text{row},1} = I_{\text{row},2} = I_{\text{row},3} = I_{\text{row},4} = 5 \times \left(\frac{900}{1000}\right) I_m + 4 \times \left(\frac{300}{1000}\right) I_m \tag{4.15}$$

Implementing the proposed PMSRA reconfiguration strategy on the recommended reduced cross-tied MPVA yields the most favourable GPPP position of $62.1 \times V_m I_m$ among all reconfiguration approaches, as indicated in Tables 4.2 and 4.3. Notably, the observed difference between the row currents is minimum ($d_{\text{row}} = 0.6$) for the proposed PMSRA, as shown in Fig. 4.13(i).

***(d) IMS-IV:LLCS*:** Under this shading scheme, a 4×4 grid of PV modules located in the lower left corner of the 9×9 PV array experiences reduced irradiance input of $150\,\text{W/m}^2$, while the remaining PV units receive an insolation of $900\,\text{W/m}^2$, as shown in Fig. 4.14(a). The dispersion of shade is accomplished through widely recognized module rearrangement approaches, namely PRS [93], CMAP [91], ACMS [89], DS [66], and the proposed PMSRA as depicted in Fig. 4.14(b), (c), (d), (e), and (f), respectively. P-V and I-V profiles for different methods are shown in Fig. 4.14(g) and (h), respectively. As evident, the proposed method yields a maximum power of 11,873 W and a peak current of 56.2 A.

Analytical computations of current, voltage, and power for each row are conducted for all the aforementioned configurations. The outcomes of the analytical computations for different methods are presented in Tables 4.2 and 4.3. The calculations for the TCT PV array are shown as follows:

$$I_{\text{row},1} = I_{\text{row},2} = I_{\text{row},3} = I_{\text{row},4} = I_{\text{row},5} = 5 \times \left(\frac{900}{1000}\right) I_m \tag{4.16}$$

$$I_{\text{row},6} = I_{\text{row},7} = I_{\text{row},8} = I_{\text{row},9} = 5 \times \left(\frac{900}{1000}\right) I_m + 4 \times \left(\frac{150}{1000}\right) I_m \tag{4.17}$$

Implementing the proposed PMSRA reconfiguration strategy on the recommended reduced cross-tied MPVA yields the most favourable GPPP position of $59.4 \times V_m I_m$ among all reconfiguration approaches, as indicated in Tables 4.2 and 4.3. Notably, the observed difference between the row currents is

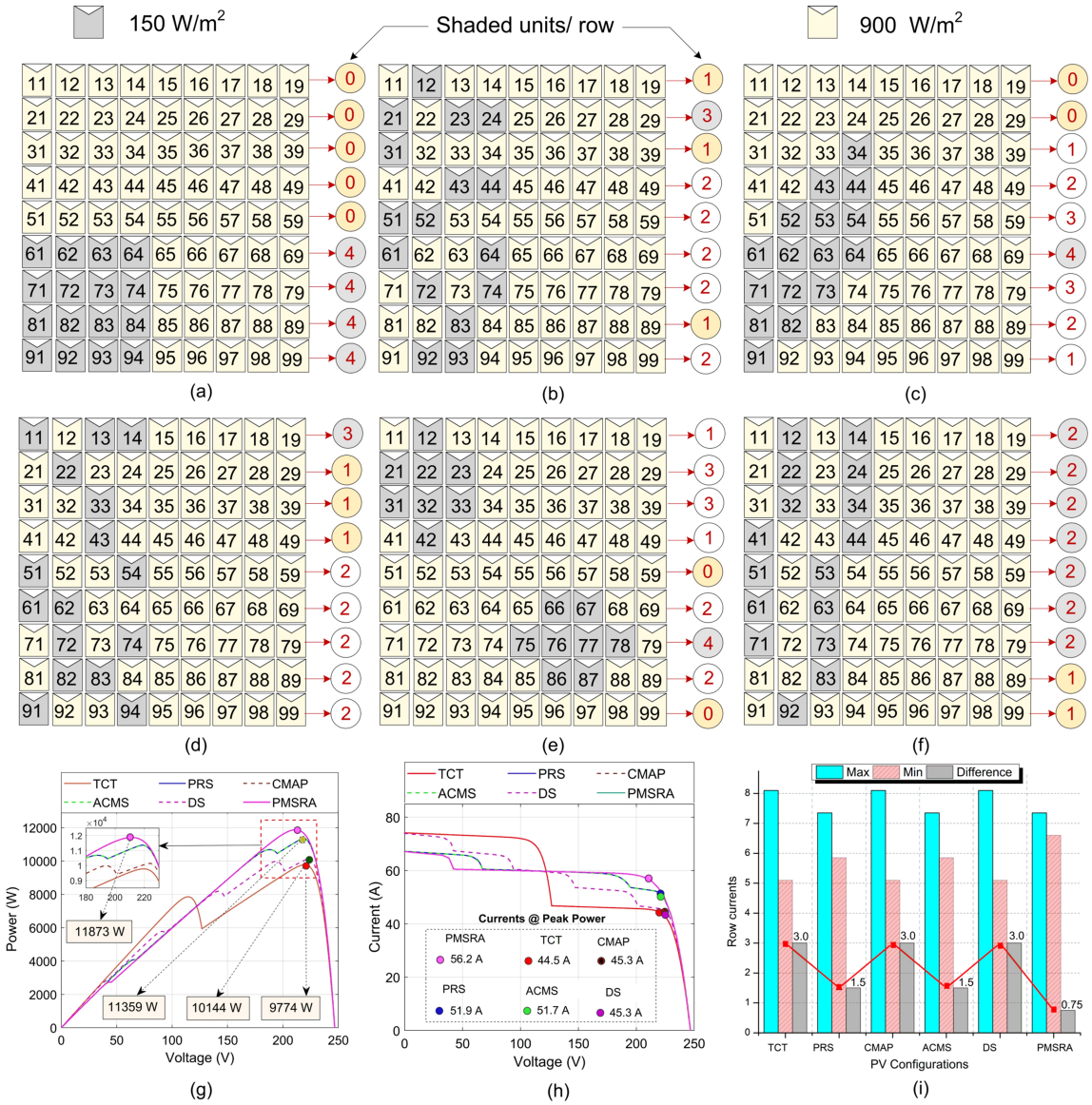

FIGURE 4.14: IMS-IV-Lower left corner shading (LLCS) on 9×9 PV array: Shade distribution performance with (a) TCT. (b) PRS. (c) CMAP. (d) ACMS. (e) DS. (f) proposed PMSRA. (g) P-V characteristics. (h) I-V characteristics. (i) minimum and maximum row currents generated.

minimum, $d_{\text{row}} = 0.75$, for the proposed PMSRA, as shown in Fig. 4.14(i).

4.5.1.2 Performance Metrics

The prominent performance metrics considered in this work are evaluated as shown below:

(a) Fill Factor (FF): The predominant measure for gauging the progression in solar performance is the FF. It is determined as the ratio of peak power extracted from the PV system to the product of current and voltage under short-circuit and open-circuit conditions, respectively at standard test conditions (STC). Ideally, a high-quality PV cell/module should possess an FF close to 1, signifying its proximity to a square having the largest area that can fit into the resulting I-V curve. It is expressed as:

$$\mathrm{FF}(\%) = \frac{(GPP)_{\mathrm{IMS}}}{(V_{\mathrm{oc}} \times I_{\mathrm{sc}})_{\mathrm{STC}}} \times 100 \tag{4.18}$$

The FF values for different configurations are evaluated under varying IMSs as depicted in Fig 4.15. The proposed PMSRA exhibits the highest FF under all considered mismatch scenarios. On averaging the FF values attained under different IMSs, the proposed PMSRA exhibits an FF of 59.3%. Meanwhile, TCT, SP, PRS [93], CMAP [91], ACMS [89], and DS [66] exhibit an average FF value of 49.6%, 46.9%, 57%, 51.4%, 57%, and 51.4%, respectively.

(b) Execution Ratio (ER): It is evaluated as the ratio of peak power attained during IMS to the power attained at STC. As ER improves, the effectiveness of the solar cell also enhances. It can be expressed as:

$$\mathrm{ER}(\%) = \frac{(GPP)_{\mathrm{IMS}}}{(\text{Peak Power})_{\mathrm{STC}}} \times 100 \tag{4.19}$$

Under all considered IMSs, the proposed PMSRA demonstrates the highest ER metric. When averaging the ER values obtained under different IMSs, the proposed PMSRA approach demonstrates an ER value of 74.0%. In contrast, TCT, SP, PRS [93], CMAP [91], ACMS [89], and DS [66] exhibit average ER values of 62.0%, 58.6%, 71.2%, 64.2%, 71.2%, and 64.2%, respectively, as illustrated in Fig. 4.15.

(c) Efficiency (EFF): The precise evaluation of efficiency plays a pivotal role in systematically examining the various reconfiguration approaches under different IMSs. For any $r \times c$ PV configuration, the estimation of EFF (%) is done as

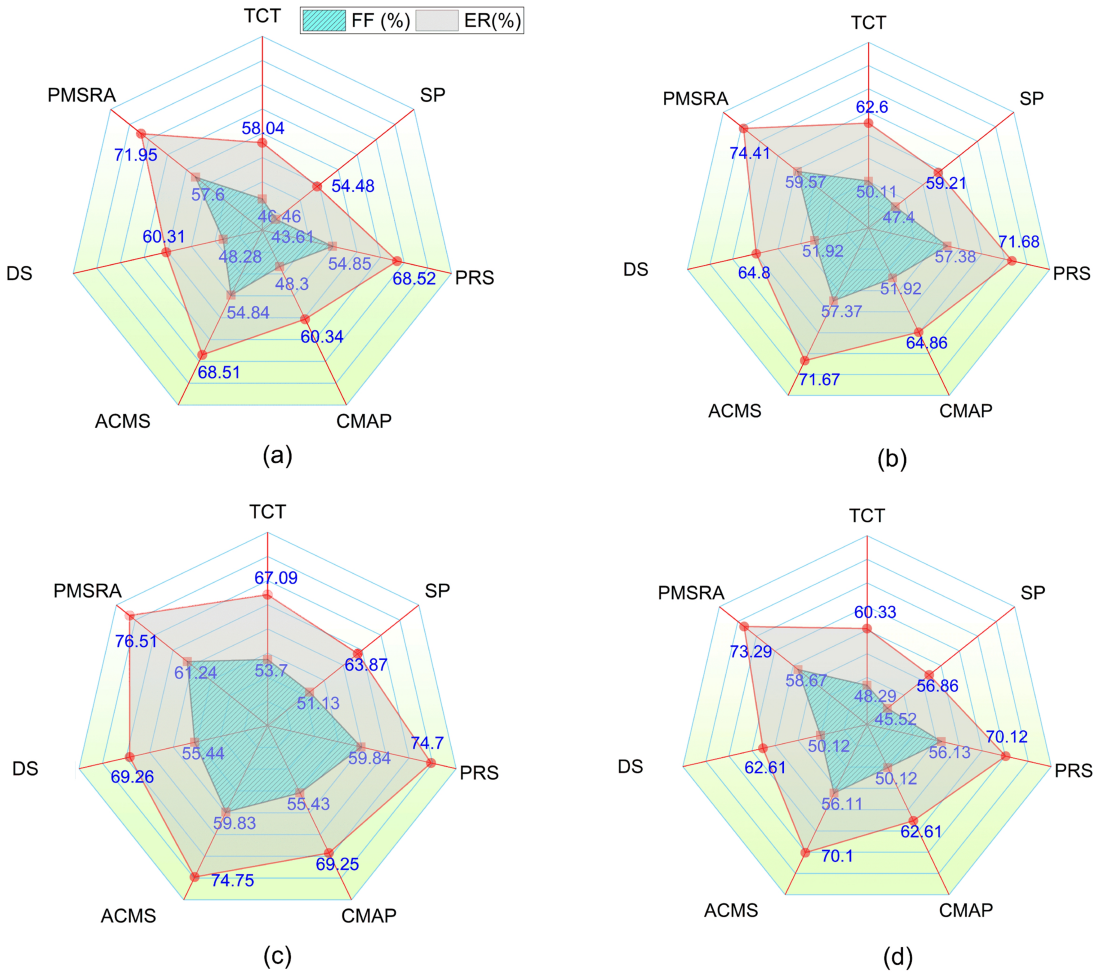

FIGURE 4.15: FF and ER attained values for various considered PV arrangements under different IMSs (a) LRCS. (b) URCS. (c) ULCS. (d) LLCS.

follows:

$$\eta(\%) = \frac{(GPP)_{\text{IMS}}}{\sum_{p=1}^{r}\sum_{q=1}^{c} G_{pq} \times A_m} \times 100 \tag{4.20}$$
$$\forall p = 1,2,3,\ldots,r; \quad \forall q = 1,2,3,\ldots,c$$

where G_{pq} is the irradiance input to the (p,q)-th PV module and A_m is the module area in m². The efficiency is computed for all examined PV configurations under various IMSs as depicted in Fig. 4.16. On taking the mean of all obtained EFF values under different IMSs, it is noteworthy that the proposed PMSRA scheme consistently achieves higher efficiency figures compared to all other reconfiguration approaches. The average EFF figures for

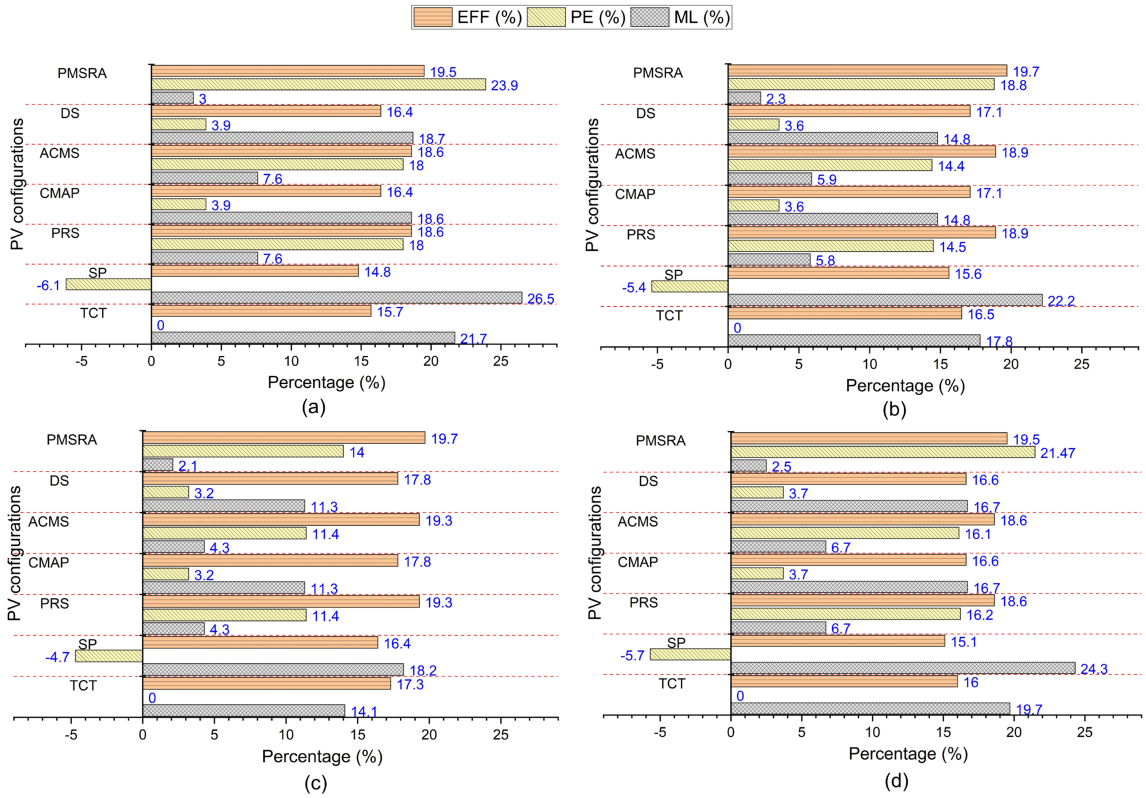

FIGURE 4.16: Performance analysis of various PV setups based on key performance metrics (EFF (%), PE (%), and ML (%)) under various IMSs (a) LRCS. (b) URCS. (c) ULCS. (d) LLCS.

the proposed PMSRA, TCT, SP, PRS [93], CMAP [91], ACMS [89], and DS [66] are 19.6%, 16.3%, 15.4%, 18.8%, 16.9%, 18.8%, and 16.9%, respectively.

(d) Power Enhancement (PE): The percentage power enhancement (w.r.t TCT) is used as a measure to evaluate the various reconfiguration schemes. The PE is estimated as shown:

$$\text{PE}(\%) = \frac{(GPP)_{\text{Reconfiguration Approach}} - (GPP)_{\text{T-C-T}}}{(GPP)_{\text{T-C-T}}} \times 100 \tag{4.21}$$

The PE relative to TCT is assessed for all the rearrangement techniques under different mismatch conditions as shown in Fig. 4.16. It is observed that the proposed PMSRA technique generates maximum PE compared to other methods. The proportionate enhancement of GPPP relative to TCT is calculated for PMSRA, SP, PRS [93], CMAP [91], ACMS [89], and DS [66], resulting in

estimated values of 18.4%, -5.4%, 15%, 3.6%, 14.9%, and 3.6%, respectively. The negative sign for the SP arrangement indicates a decrease in power relative to the TCT topology. These calculations are based on the average of all values computed across various IMSs.

(e) Mismatch Loss (ML): ML is calculated by finding the disparity between the sum of individual peak powers attained by all PV modules in the array and the overall peak power achieved by the entire array under IMS. It is expressed as shown below:

$$ML(\%) = \frac{\sum_{p=1}^{r\times c} P_{m,p} - P_a}{\sum_{p=1}^{r\times c} P_{m,p}} \times 100 \tag{4.22}$$

where $P_{m,p}$ is the peak power generated by ' p_{th}' module and ' P_a ' is the cumulative power generated by the entire PV array under IMS. The proposed PMSRA yields least ML for the 9×9 PV array under consideration under different IMSs as shown in Fig. 4.16. The average of all ML figures attained under the four distinct mismatch scenarios for TCT, SP, PRS [93], CMAP [91], ACMS [89], DS [66] and the proposed PMSRA are 18.3%, 22.8%, 6.1%, 15.3%, 6.1%, 15.3%, and 2.4% respectively.

4.5.2 Experimental Implementation

To empirically assess the proposed approach, a set of 25 PV modules (for technical specifications refer to Table 4.1) are arranged symmetrically in a 5×5 configuration. Furthermore, to validate the effectiveness of the proposed technique in an asymmetrical setup, 24 PV modules are arranged in a 6×4 configuration. Irradiance measurements are conducted using a solar power meter, and current and voltage measurements are taken with a set of multi-meters. The load under consideration consists of two rheostats with a rating of $100\Omega/5$ A each. Various IMSs are created by placing different numbers of transparent plastic sheets, each with a commercial thickness of 250μ m, over the PV modules. This introduces irradiance mismatches within the array for experimental examination. Fig. 4.17 shows the outdoor hardware prototype for experimental implementation. The PV modules are marked with encircled numbers that define module positions. The description of the shading profile used in hardware validation is done utilizing these unique module indices.

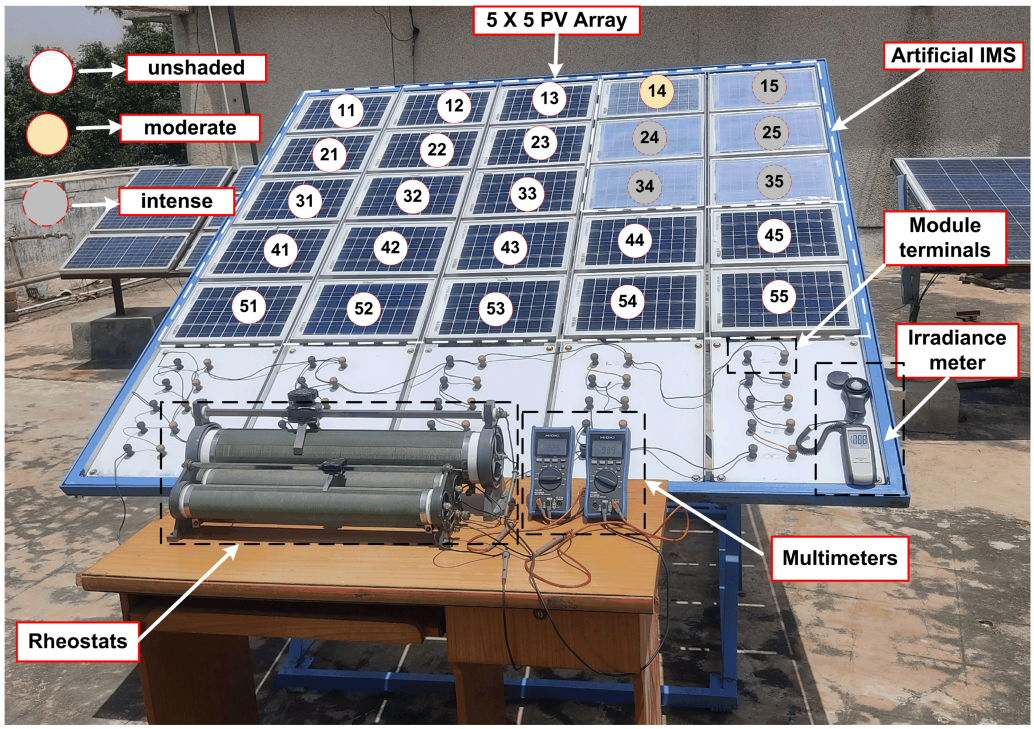

FIGURE 4.17: Hardware prototype for experimental validation configured in 5×5 arrangement (IMS-II).

4.5.2.1 5×5 PV Setup

The 5×5 PV array, configured in the T-C-T topology is depicted alongside the proposed MPVA configuration in Fig. 4.18(a) and (b), respectively. Notably, the proposed configuration exhibits a noteworthy reduction in cross-wiring requirements, amounting to a 37.5% decrease.

The suggested topology is reconfigured using the proposed PMSRA scheme, with terminal connections of each PV module marked as shown in Fig. 4.18(c). The proposed technique's performance is assessed alongside widely used reconfiguration schemes by subjecting the 5×5 PV array to testing under four different IMSs-LRCS, URCS, ULCS, and LLCS. The evaluation of various techniques centers on their effectiveness in distributing shade across the maximum number of rows to mitigate the imbalance in row currents. The experimentally obtained $P-V$ profile plots for different reconfiguration schemes are presented in Fig. 4.19. The SD performance of different techniques under various IMSs for the examined 5×5 PV array is illustrated in Fig. 4.20.

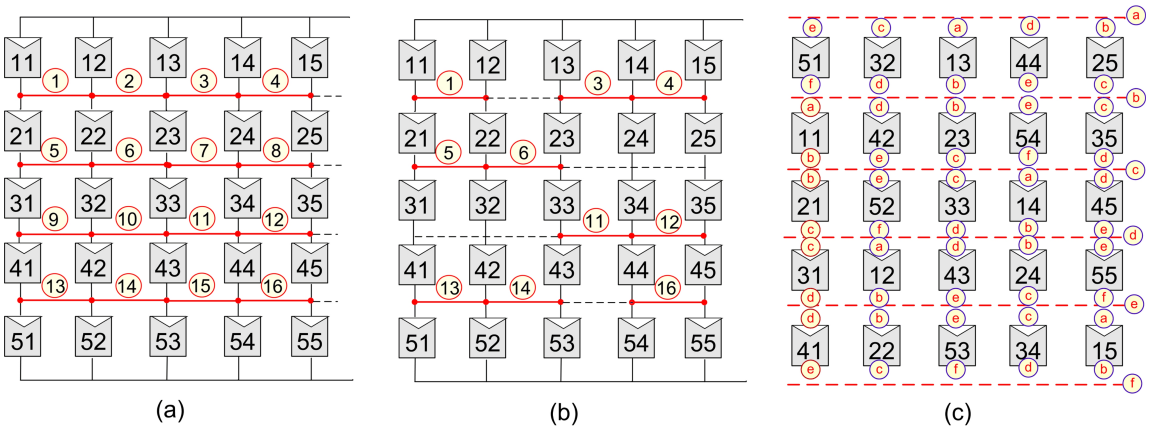

FIGURE 4.18: 5×5 PV arrangement: (a) TCT configuration (16 cross-ties). (b) proposed MPVA (10 cross-ties). (c) proposed PMSRA with marked terminal connections.

Upon conducting a comprehensive analysis of power extraction achieved by different PV arrangements under various considered mismatch conditions, it is evident that the proposed PMSRA strategy leads to a notable power enhancement of nearly 13% compared to the T-C-T framework.

Furthermore, as depicted in Table 4.4, the proposed approach, which involves module rearrangement of an MPVA-configured PV array, surpasses several widely-used rearrangement schemes that involve module rearrangement of a TCT array, which poses significant wiring intricacies. Table 4.5 gives the performance metrics obtained with different PV rearrangement strategies under various IMSs.

Key findings from the experimental validation (5×5 PV array)

The experimental study on a 5×5 PV array reveals that the TCT configuration achieves a GPPP of 154.2 W, 153 W, 158.2 W, and 153.3 W in the four IMSs (refer Fig. 4.19). In contrast, the proposed PMSRA configuration delivers a higher GPPP of 176.3 W, 170.1 W, 178.5 W, and 174.5 W for the same shading cases. This demonstrates that the proposed PMSRA configuration is more effective in all shading scenarios, resulting in power increases of 14.3%, 11.2%, 12.83%, and 13.82%, respectively.

An extensive performance evaluation was conducted using key performance indicators (see Table 4.5) to assess the proposed PMSRA algorithm across different shading scenarios. To comprehensively evaluate various reconfiguration methods across different IMSs, the mean values of all performance metrics are estimated.

The results are as follows:

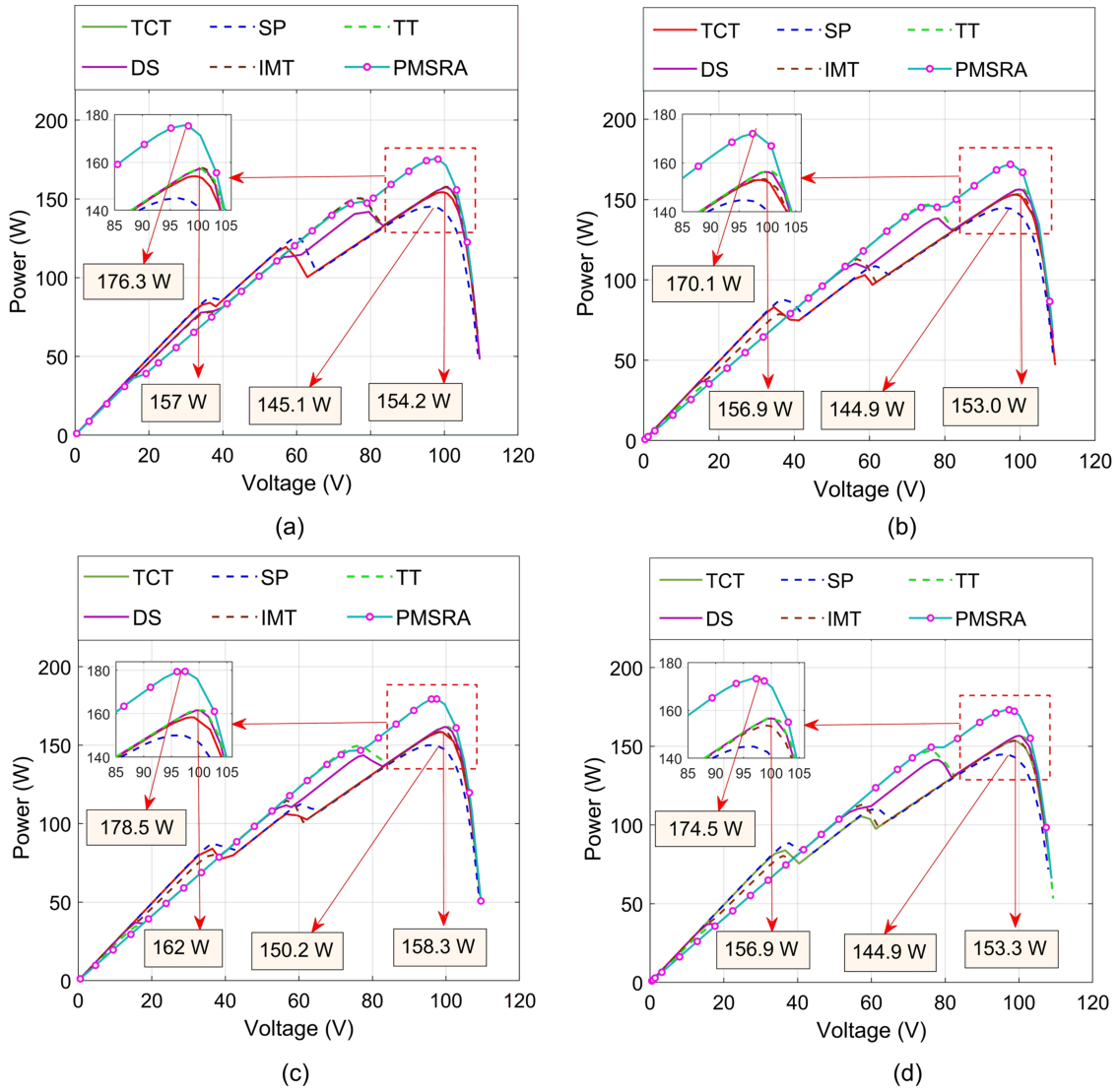

FIGURE 4.19: Experimental voltage versus power curves for different PV configurations (5×5 PV configuration) under different irradiance mismatch conditions (a) IMS-I: LRCS. (b) IMS-II: URCS. (c) IMS-III: ULCS. (d) IMS-IV.

1. The proposed approach, PMSRA, achieves an FF value of 56.5%. In contrast, FF values for the TCT, SP, TT [85], DS [66], and IMT [78] configurations are 50%, 47.3%, 51.1%, 51.0%, and 50.3%, respectively.

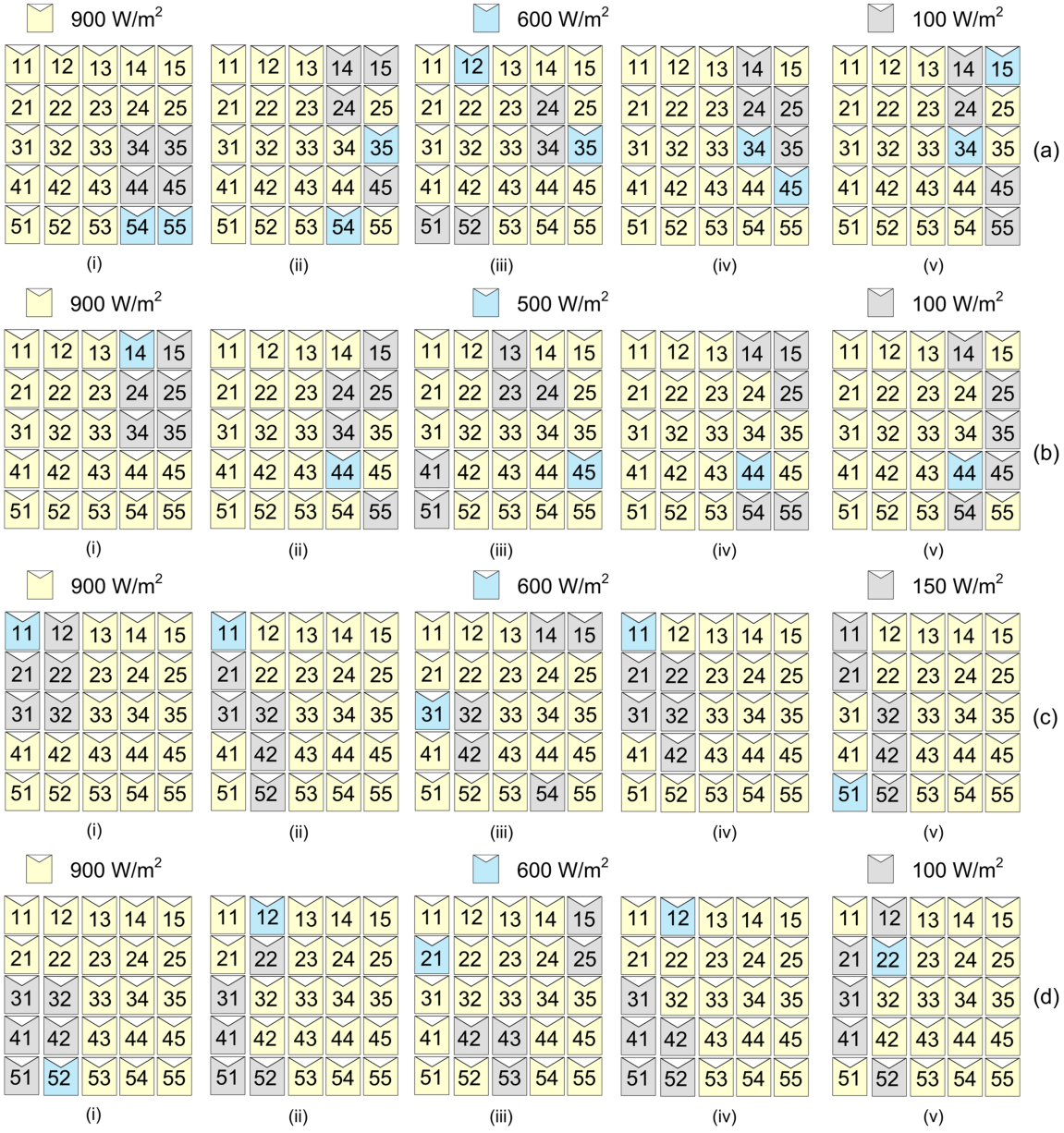

FIGURE 4.20: Shade distribution performance of 5 × 5 PV array with (i) TCT, (ii) TT, (iii) DS, (iv) IMT, (v) proposed PMSRA, under (a) IMS-I. (b) IMS-II. (c) IMS-III. (d) IMS-IV.

2. The proposed configuration yields a lower Mismatch Loss (ML) of 3.8%. In comparison, the TCT, SP, TT [85], DS [66], and IMT [78] configurations exhibit ML values of 15.7%, 20.3%, 13.8%, 13.9%, and 15.14%, respectively.

3. The TCT, SP, TT [85], DS [66], and IMT [78] configurations achieve Energy Ratios (ERs) of 61.8%, 58.5%, 63.3%, 63.1%, and 62.32%, respectively. In

contrast, the proposed approach achieves an impressive ER of 70%.

4. The SP, TT [85], DS [66], and IMT [78] configurations achieve PE values of -5.42%, 2.28%, 2.17%, and 0.7%, respectively, while the proposed method demonstrates a notable PE of 13.02%.

TABLE 4.4: A Comparative Assessment of Different PV Configurations on 5 × 5 Hardware Prototype

Shading scenarios	PV configurations	I_{mp}	V_{mp}	P_{mp}	Shading scenarios	PV configurations	I_{mp}	V_{mp}	P_{mp}
IMS-I	T-C-T	1.55	99.55	154.2	IMS-II	T-C-T	1.54	99.03	153
	SP	1.50	96.63	145.16		SP	1.51	96.26	144.9
	TT [85]	1.58	99.53	157.12		TT [85]	1.57	100.10	156.91
	DS [66]	1.56	100.68	157.33		DS [66]	1.57	99.87	156.35
	IMT [78]	1.56	100.59	157.36		IMT [78]	1.55	98.85	153.55
	PMSRA	**1.82**	**97.0**	**176.34**		PMSRA	**1.75**	**97.22**	**170.10**
IMS-III	T-C-T	1.61	98.31	158.29	IMS-IV	T-C-T	1.55	98.73	153.33
	SP	1.56	96.57	150.21		SP	1.51	96.33	144.99
	TT [85]	1.62	99.70	162.0		TT [85]	1.56	100.51	156.96
	DS [66]	1.61	100.10	161.56		DS [66]	1.56	100.15	156.65
	IMT [78]	1.60	98.92	158.72		IMT [78]	1.55	99.29	153.64
	PMSRA	**1.84**	**97.03**	**178.54**		PMSRA	**1.80**	**96.81**	**174.50**

TABLE 4.5: A Comparative Analysis of Performance Metrics across Different PV Configurations for all Shading Scenarios Using 5×5 Hardware Prototype

Reconfiguration Scheme	FF (%)	ML (%)	ER (%)	EFF (%)	PE (%) w.r.t TCT
IMS I: LRCS					
T-C-T	49.84	17.5	61.68	9.23	-
SP	46.92	22.37	58.04	8.68	-5.86
TT [85]	50.78	15.97	62.84	9.41	1.89
DS [66]	50.85	15.86	62.93	9.42	2.02
IMT [78]	50.86	15.85	62.94	9.42	2.04
PMSRA	**57.00**	**5.70**	**70.53**	**10.56**	**14.35**
IMS II: URCS					
T-C-T	49.45	15.46	61.2	9.47	-
SP	46.83	19.94	57.96	8.96	-5.29
TT [85]	50.71	13.30	62.76	9.71	2.55
DS [66]	50.53	13.61	62.54	9.67	2.18
IMT [78]	49.6	15.16	61.42	9.50	0.3
PMSRA	**54.9**	**6.02**	**68.04**	**10.52**	**11.17**
IMS III: ULCS					
T-C-T	51.16	14.2	63.31	9.58	-
SP	48.55	18.58	60.08	9.09	-5.10
TT [85]	52.36	12.19	64.8	9.81	2.34
DS [66]	52.22	12.43	64.6	9.78	2.06
IMT [78]	51.3	13.97	63.48	9.61	0.27
PMSRA	**57.71**	**3.2**	**71.41**	**10.81**	**12.79**
IMS IV: LLCS					
T-C-T	49.56	15.75	61.33	9.41	-
SP	46.86	20.33	57.99	8.90	-5.43

TT [85]	50.73	13.75	62.78	9.63	2.36
DS [66]	50.63	13.92	62.66	9.61	2.16
IMT [78]	49.66	15.58	61.45	9.43	0.2
PMSRA	**56.4**	**4.1**	**69.8**	**10.71**	**13.8**

4.5.2.2 6×4 PV Setup

The 6 × 4 PV array, structured in the T-C-T topology, is illustrated alongside the proposed MPVA configuration in Fig. 4.21(a) and (b). Remarkably, the suggested configuration demonstrates a significant decrease in cross-wiring requirements, reaching an impressive 80% reduction.

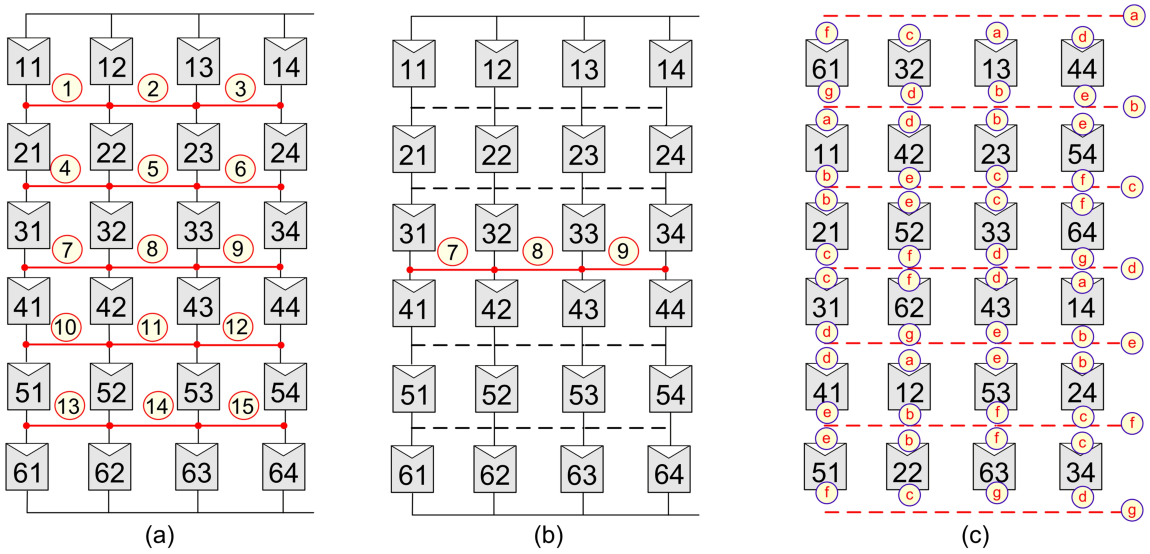

FIGURE 4.21: 6 × 4 PV arrangement: (a) TCT configuration (15 cross-ties). (b) proposed MPVA (3 cross-ties). (c) proposed PMSRA with marked terminal connections.

The recommended topology, MPVA, undergoes reconfiguration through the proposed PMSRA scheme, with the terminal connections of each PV module distinctly labeled, as illustrated in Fig. 4.21(c). The experimentally obtained P-V curves under various IMSs are shown in Fig. 4.22. Following a comprehensive analysis of power extraction achieved by different PV setups amid various mismatch scenarios, it is evident that the recommended PMSRA approach leads to a noteworthy enhancement in power output, amounting to approximately

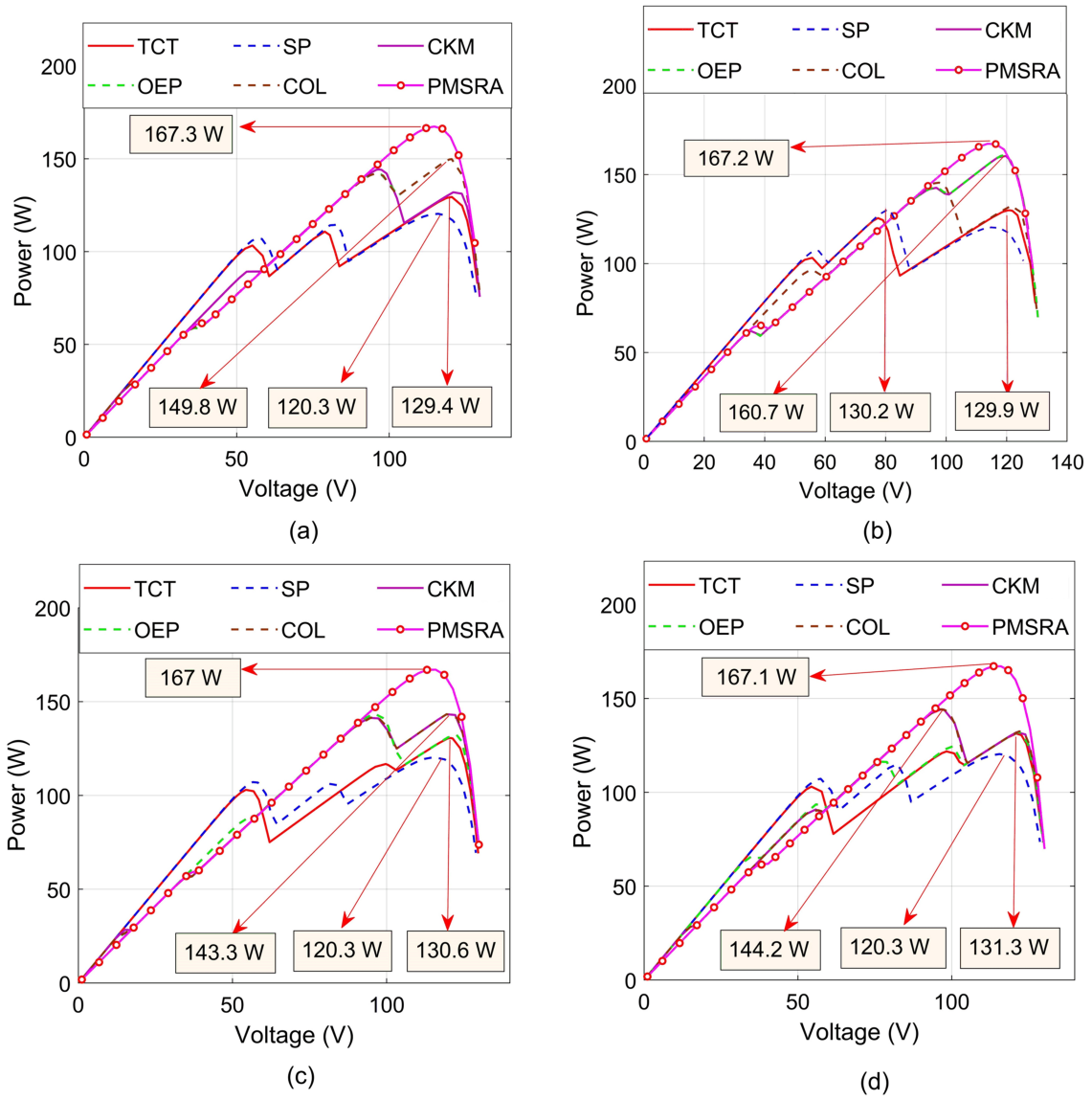

FIGURE 4.22: Experimental voltage versus power curves for different PV configurations (6×4 PV array) under different shading scenarios (a) IMS-I: LRCS. (b) IMS-II: URCS. (c) IMS-III: ULCS. (d) IMS-IV.

28.3% compared to the TCT framework. Fig. 4.23 illustrates the SD performance of various reconfiguration schemes, including the proposed one. Furthermore, as delineated in Table 4.6, the proposed PMSRA, involving the restructuring of PV modules within an MPVA-configured array, outperforms several commonly employed rearrangement strategies that entail the reorganization of modules in a TCT array. The latter poses significant challenges due to the intricate wiring

complexities it introduces.

Key findings from the experimental validation (6 × 4 PV array)

The experimental study on a 6 × 4 PV array reveals that the TCT configuration achieves a GPPP of 129.4 W, 129.9 W, 130.6 W, and 131.3 W in the four IMSs. In contrast, the proposed PMSRA configuration delivers a higher GPPP of 167.3 W, 167.2 W, 167.0 W, and 167.1 W for the same shading cases. This demonstrates that the proposed PMSRA configuration is more effective in all shading scenarios, resulting in power increases of 29.2%, 28.7%, 27.8%, and 27.2%, respectively.

An extensive performance evaluation was conducted using key performance indicators (see Table 4.7) to assess the proposed PMSRA algorithm across different shading conditions. To comprehensively evaluate various reconfiguration methods across different IMSs, the mean values of all performance metrics are estimated. The results are as follows:

1. The proposed approach, PMSRA, achieves an FF value of 56.3%. In contrast, FF values for the TCT, SP, CKM [153], OEP [82], and COL [152] configurations are 43.8%, 41.3%, 49.8%, 48.6%, and 49.0%, respectively.

2. The proposed configuration yields a lower ML of 4.1%. In comparison, the TCT, SP, CKM [153], OEP [82], and COL [152] configurations exhibit ML values of 25.3%, 29.6%, 15.1%, 15.5%, and 16.4%, respectively.

3. The TCT, SP, CKM [153], OEP [82], and COL [152] configurations achieve ERs of 52.1%, 49.1%, 59.2%, 57.7%, and 58.2%, respectively. In contrast, the proposed approach achieves an ER of 66.8%.

4. The SP, CKM [153], OEP [82], and COL [152] configurations achieve PE values of -5.72%, 13.6%, 10.8%, and 11.8%, respectively, while the proposed method demonstrates a notable PE of 28.3%.

A comprehensive quantitative comparative analysis was conducted between the attained performance metrics from simulations and experiments, as presented in Table 4.8. It is apparent from Table 4.8 that the performance metrics do not align perfectly between simulations and experiments. This discrepancy arises because simulations were conducted on a large 9×9 PV array with four distinct IMSs, whereas experimental validations were carried out on both symmetrical (5 × 5)

and asymmetrical (6×4) array configurations. These experiments used different IMSs with varying shading intensities to demonstrate the generalizability of the proposed method across different PV array sizes, which is a unique feature of the approach. Nevertheless, both simulation and experimental validation consistently yield results that follow the same trend.

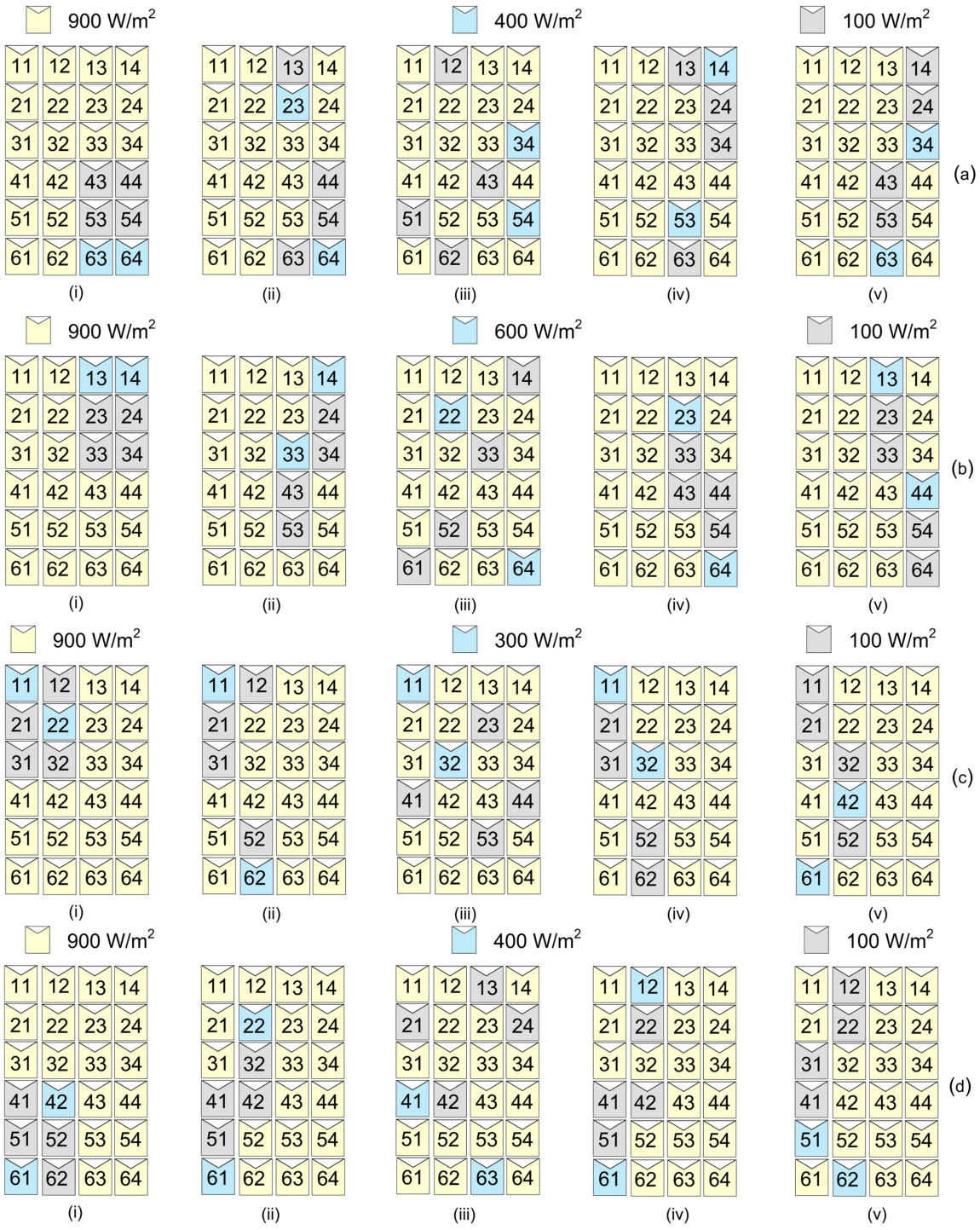

FIGURE 4.23: Shade distribution performance of 6 × 4 PV array with (i) TCT, (ii) CKM, (iii) OEP, (iv) COL, (v) proposed PMSRA, under (a) IMS-I. (b) IMS-II. (c) IMS-III. (d) IMS-IV.

TABLE 4.6: A Comparative Assessment of Different PV Configurations on 6 × 4 Hardware Prototype

Shading scenarios	PV configurations	I_{mp}	V_{mp}	P_{mp}	Shading scenarios	PV configurations	I_{mp}	V_{mp}	P_{mp}
IMS-I	TCT	1.07	120.52	129.43	IMS-II	TCT	1.07	121.09	129.92
	SP	1.04	116.03	120.37		SP	1.62	80.61	130.28
	CKM [153]	1.49	96.63	144.26		CKM [153]	1.34	119.75	160.44
	OEP [82]	1.50	94.60	141.66		OEP [82]	1.35	118.84	160.75
	COL [152]	1.24	120.48	149.80		COL [152]	1.49	97.66	145.46
	PMSRA	**1.46**	**114.77**	**167.36**		PMSRA	**1.47**	**113.58**	**167.26**
IMS-III	TCT	1.08	120.54	130.60	IMS-IV	TCT	1.09	120.96	131.32
	SP	1.04	115.21	120.36		SP	1.04	115.53	120.38
	CKM [153]	1.20	119.44	143.26		CKM [153]	1.49	96.68	144.26
	OEP [82]	1.49	96.26	143.37		OEP [82]	1.08	122.15	131.92
	COL [152]	1.20	119.46	143.29		COL [152]	1.50	96.25	144.23
	PMSRA	**1.44**	**115.89**	**167.02**		PMSRA	**1.47**	**113.62**	**167.18**

TABLE 4.7: A Comparative Analysis of Performance Metrics across Different PV Configurations for all Shading Scenarios Using 6×4 Hardware Prototype.

Reconfiguration Scheme	FF (%)	ML (%)	ER (%)	EFF (%)	PE (%) w.r.t TCT
IMS I: LRCS					
TCT	43.5	25.61	51.77	8.33	-
SP	40.52	30.82	48.14	7.75	-6.99
CKM [153]	48.57	17.09	57.7	9.28	11.45
OEP [82]	47.69	18.58	56.66	9.12	9.44
COL [152]	50.43	13.90	59.92	9.64	15.73
PMSRA	**56.35**	**3.81**	**66.94**	**10.77**	**29.30**
IMS II: URCS					
TCT	43.74	27.01	51.96	8.15	-
SP	43.86	26.80	52.11	8.17	0.27
CKM [153]	54.02	9.86	64.17	10.07	23.49
OEP [82]	54.12	9.69	64.3	10.09	23.72
COL [152]	48.97	18.2	58.18	9.13	11.96
PMSRA	**56.31**	**6.03**	**66.90**	**10.49**	**28.7**
IMS III: ULCS					
TCT	43.97	24.06	52.24	8.48	-
SP	40.52	30	48.14	7.81	-7.84
CKM [153]	48.23	16.7	57.30	9.3	9.69
OEP [82]	48.27	16.64	57.34	9.31	9.77
COL [152]	48.24	16.69	57.31	9.30	9.71
PMSRA	**56.23**	**2.89**	**66.80**	**10.84**	**27.88**
IMS IV: LLCS					
TCT	44.21	24.52	52.52	8.43	-
SP	40.53	30.81	48.15	7.73	-8.33

CKM [153]	48.57	17.09	57.70	9.26	9.85
OEP [82]	44.41	24.18	52.76	8.47	0.45
COL [152]	48.56	17.10	57.69	9.26	9.83
PMSRA	**56.28**	**3.91**	**66.87**	**10.73**	**27.30**

4.6 Summary

This chapter proposed a novel PV configuration referred to as MPVA, featuring a considerable reduction in cross-ties. The primary contributions of this study include:

1. The proposed configuration leads to a substantial decrease in cross-wiring by 59.37% for the 9×9 configuration. Moreover, the modified proposed PV arrangement achieves substantial reductions in cross-tie requirements, with a decrease of 37.5% for the 5×5 array and an impressive 80% for the 6×4 PV arrays.

2. An extensive simulation analysis is conducted using a 9×9 PV array, with key performance indices such as FF, ER, EFF, PE, and ML chosen for evaluation. The proposed PMSRA approach, implemented on an MPVA with reduced wiring intricacy, demonstrates superior performance metrics when compared to various array rearrangement techniques. This approach results in a power enhancement of 18.4% compared to the TCT arrangement on a 9×9 PV setup.

3. A comprehensive comparative analysis reveals the clear dominance of the proposed approach over contemporary reconfiguration methods applied to the benchmark TCT. Additionally, the proposed method yields the lowest ML of 2.4%, compared to 18.3% and 22.8% generated by TCT and SP configurations, respectively.

4. Experimental evaluation on a hardware prototype with PV modules interconnected in both symmetrical and unsymmetrical arrangements demonstrates the highest power extraction for the proposed technique. A

TABLE 4.8: A Quantitative Comparison of the Attained Performance Metrics Between Simulations and Experiments

Performance Metrics	Simulation			Experimental					
	9×9			5×5 (Symmetrical)			6×4 (Unsymmetrical)		
	TCT	SP	Proposed	TCT	SP	Proposed	TCT	SP	Proposed
FF (%)	49.6	46.9	59.3	50.1	47.3	56.5	43.8	41.3	56.3
ML (%)	18.3	22.8	2.4	15.7	20.3	3.8	25.3	29.6	4.1
ER (%)	62	58.6	74	61.8	58.5	70	52.1	49.1	66.8
PE (%)	-	-5.4	18.4	-	-5.42	13.02	-	-5.7	28.3

maximum power boost of 13.03% and 28.3% are respectively realized for the 5×5 and 6×4 PV arrangements.

Overall, this refined approach offers a more efficient and less intricate alternative to existing PV configurations, effectively addressing challenges presented by various IMSs.

Chapter 5

Modeling and Investigation of the Solar PV System Performance Under Sub-Optimal Operating Conditions

5.1 Preamble

The increasing reliance on renewable energy sources, particularly SPV systems, marks a significant shift in the global energy landscape. This transition is driven by the urgent need to reduce greenhouse gas emissions and the declining costs associated with solar technology. However, the integration of SPV systems into the electrical grid presents a unique set of challenges, particularly concerning PQ issues that can arise during operation.

The deployment of power electronic devices within renewable energy systems often leads to substandard PQ, manifesting as harmonic distortion, poor power factor, voltage regulation problems, and load unbalancing. These issues can severely impact the performance of the distribution system and the quality of electricity supplied to end-users, necessitating effective control strategies to mitigate these adverse effects.

A typical grid-tied SPPG system consists of several integral components, including the SPV array, a VSC, interfacing inductors, filters, and both linear and non-linear loads. The VSC serves a crucial function as it operates as an active shunt compensator, addressing various PQ challenges while facilitating the transfer of power from the SPV system to the grid.

To ensure optimal performance and compliance with power quality standards, robust control schemes are essential. In this chapter, a dual-stage SPPG system employing a STF assisted control approach is proposed, which not only enhances the system's ability to harvest maximum power but also improves power quality by minimizing harmonics and correcting power factor.

The effectiveness of the STF control scheme is rigorously evaluated through extensive simulations conducted in the MATLAB/Simulink environment. These simulations reveal significant enhancements in power quality, with grid currents maintaining sinusoidal characteristics and adhering to the IEEE-519 standard, even under varying load conditions.

The remainder of the chapter is as follows: Section 5.2 gives the design of the proposed grid-integrated system. Section 5.3 describes in detail the proposed STF enabled control architecture for the grid-integrated system followed by simulation results and discussions in section 5.4. Finally, section 5.5 concludes the chapter with summary of research findings.

5.2 Design of the Grid Integrated System

The overall system layout is presented in Fig. 5.1. A dual-stage topology is configured here. It comprises a 415V, 50 Hz, 3-phase grid, while the first stage incorporates an SPV array, DC-DC boost converter, and MPOP control (P and O) for optimum power extraction from SPV under varying irradiance conditions. The VSC acting as an active shunt compensator forms the second stage. It is further interfaced with inductors (included one for each phase) to smoothen the injected currents and minimize switching losses. An RC filter is also employed to arrest high-frequency ripples at point of common coupling (PCC) due to the switching action of VSC. The section's upcoming portion elaborates on the design equations and selected values for different constituent elements of the proposed SPPG system. The SPV system is designed for the optimum power rating of 30.8 kW by utilizing 22×7 module array interconnections. All modules in the array are similar, having identical electrical characteristics. Each SPV module employed in this work has a short circuit current rating of 8.21 A and open circuit voltage rating of 32.9 V.

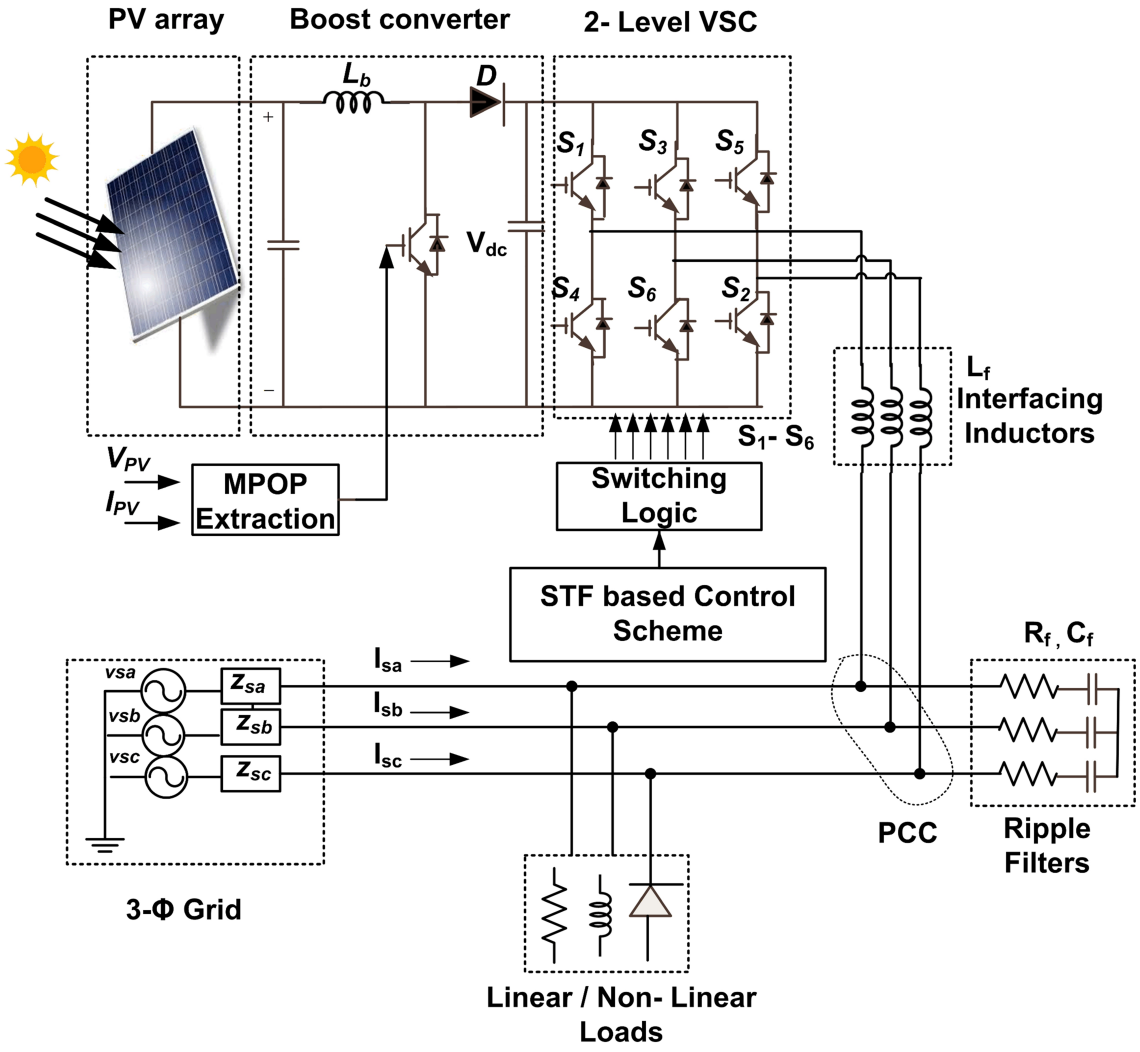

FIGURE 5.1: Schematic representation of grid-tied SPPG system.

The inductor for the stage-I converter (boost converter) is designed for the duty ratio, $D = 0.1734$, as shown in (5.1)

$$L_{\text{boost}} = \frac{V_{\text{mpop}} \times D}{\Delta I_{\text{input}} \times f_{\text{sw}}} = \frac{578.6 \times 0.1734}{2.66 \times 10000} = 3.75\ mH \tag{5.1}$$

where V_{mpop} is the SPV array voltage at MPOP, and ΔI_{input} accounts for the maximum ripple in the SPV current. The input current (SPV current) is estimated as:

$$I_{\text{input}} = \frac{P_{\text{mpop}}}{V_{\text{mpop}}} = \frac{53.27}{578.6} = 3.27\ \text{A}. \tag{5.2}$$

Considering the maximum allowable ripple in the input current to be 5% ($0.05 \times 53.27 = 2.66$ A), the boost inductor value is estimated to be 3.75 mH, as shown in (5.1). In this work, *4 mH* is selected.
The minimal value required for the DC-link voltage should be higher than double the maximum of the phase voltage at point of common coupling (PCC). Consequently, the DC-link voltage is determined as in [154]:

$$V_{\text{dc-link}} = \frac{\sqrt{2} \times V_{\text{L-L}}}{\sqrt{3} \times m} = \frac{\sqrt{2} \times 415}{\sqrt{3} \times 1} = 677.7\,\text{V}, \tag{5.3}$$

where $V_{\text{L-L}}$ is the grid phase-to-phase voltage, and m is the modulation index. A DC-link voltage of 700 V is selected for the proposed system.

The smoothening inductors connected to VSC are estimated as shown below [154]:

$$L_f = \frac{\sqrt{3} \times m_i \times V_{\text{dc-link}}}{12 \times h \times f_{sw} \times \Delta I_{\text{peak}}} = \frac{\sqrt{3} \times 1 \times 700}{12 \times 1.2 \times 10000 \times (60.64 \times .05)} = 2.78\text{mH} \tag{5.4}$$

where h is 1.2 and is termed as overloading factor, f_{sw} is switching frequency (10 kHz)of the VSC. ΔI_{peak} accounts for the ripple (5%) in the peak grid phase current.

$$\Delta I_{peak} = 0.05 \times \sqrt{2} \times \left(\frac{30822}{\sqrt{3} \times 415} \right) = 3.03\ \text{A} \tag{5.5}$$

3 mH is selected for adequate smoothening of injected currents. The value of the dc-link capacitance of VSC is determined as given in (5.6) [154].

$$\begin{aligned} C_{dc-\,\text{link}} &= \frac{\left(P_{mpop}/V_{dc-\,\text{link}}\right)}{2 \times (2 \times \pi \times f) \times \Delta V_{dc-\,\text{link}}} = \left(\frac{30822/700}{2 \times 2 \times \pi \times 50 \times (2/100) \times 700} \right) \\ &= 5005.58\mu\ \text{F} \end{aligned} \tag{5.6}$$

where $\Delta V_{dc-\,\text{link}}\,(2\%)$ is allowable percent ripple in dc link voltage, $V_{dc-link}$. A safe value of 6 mF is chosen for the proposed system to settle the voltage rapidly in the event of system dynamics. The ripple filter component values, R_f, C_f are estimated as calculated in [154] .

5.3 Control Scheme

The control scheme aims to enhance PQ at PCC and feed the optimal power harvested from the PV system to the grid. Additionally, the PV integrated system is highly resistant to the adverse effects of sudden changes in loads and unbalancing effects. The control approach can be subdivided into MPOP tracking control, and grid interfaced VSC control. The MPOP control is implemented by employing a dc-dc boost converter and operating with an adequate duty cycle. Numerous control theories have been advocated in the literature to harvest optimal power from the SPPG system and are deeply investigated in [155, 156]. For the control of VSC, the switching operation is exercised using the indirect current control scheme. The fundamental components of load current and grid voltages are determined using STF. The overall control architecture using STF is shown in Fig. 5.2.

5.3.1 MPOP Tracking Control

As discussed in the earlier section, because of the benefits associated with the P&O control algorithm, it is implemented here for MPOP convergence. The control is simple, and the algorithm observes only the change in power with corresponding perturbations in output voltage. It then decides its next course of action based on SPV power before and after perturbation and consequently alters the converter duty ratio to arrive at the MPOP. The following logic dictates the change in duty cycle: *If*

$$\left.\begin{array}{c} \Delta P_{PV} > 0 \&\& \Delta V > 0 \\ or \\ \Delta P_{PV} < 0 \&\& \Delta V < 0 \end{array}\right\} \rightarrow D(t+1) = D(t) + \Delta D \tag{5.7}$$

else if,

$$\left.\begin{array}{c} \Delta P_{PV} > 0 \&\& \Delta V < 0 \\ or \\ \Delta P_{PV} < 0 \&\& \Delta V > 0 \end{array}\right\} \rightarrow D(t+1) = D(t) - \Delta D \tag{5.8}$$

where $\Delta P_{PV} = P(t+1) - P(t), \Delta V = V(t+1) - V(t)$ and ΔD is the change in duty ratio.

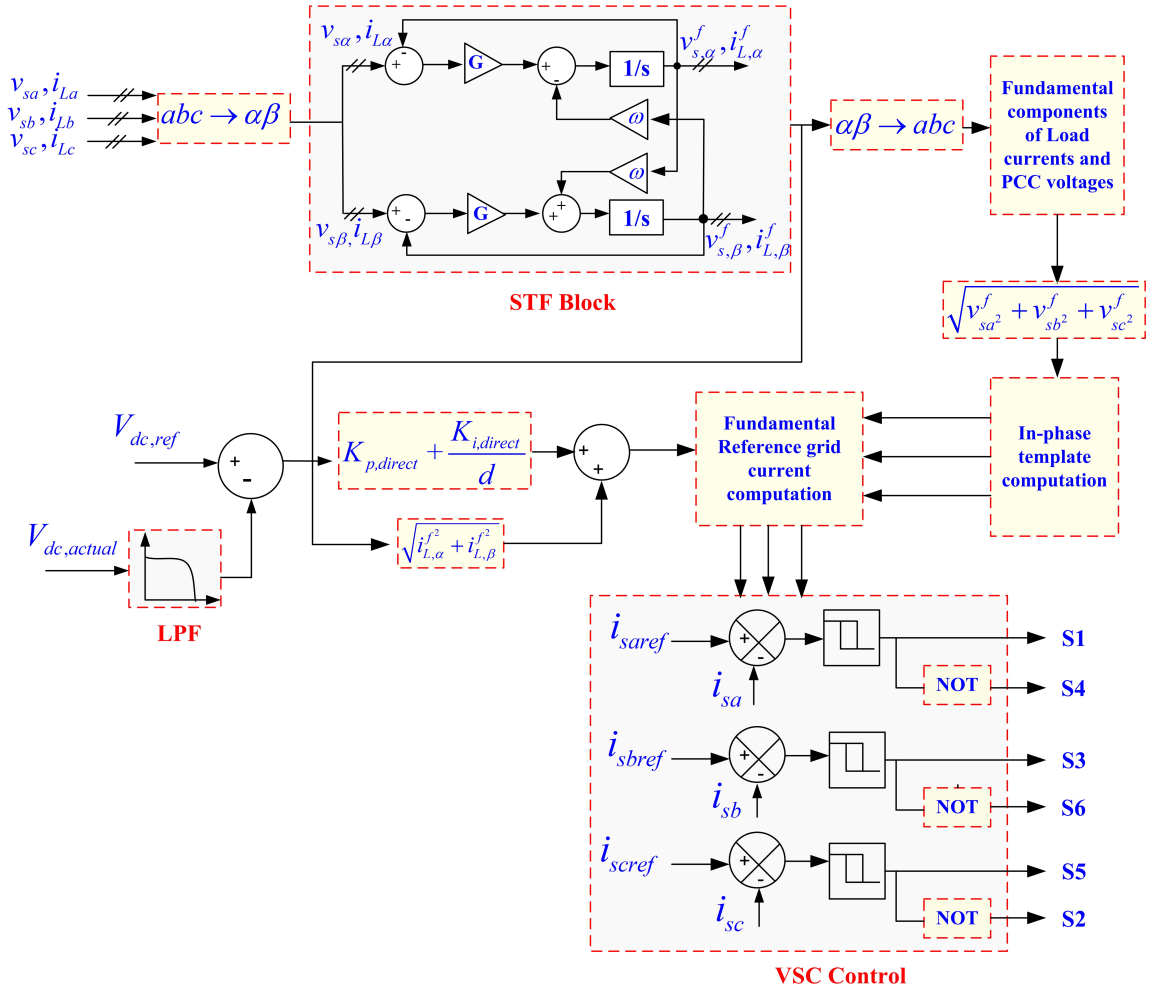

FIGURE 5.2: STF assisted control architecture for SPPG system.

5.3.2 Grid-Tied VSC Control

In this section the overall control architecture is explained. To have a better insight into the control architecture, it is subdivided into five segments elaborated in subsequent sections.

5.3.2.1 STF Module Description

A block schematic of the STF is depicted in Fig. 5.3, and it is evident that it belongs to the class of multiple input multiple output systems. STF exhibits the following

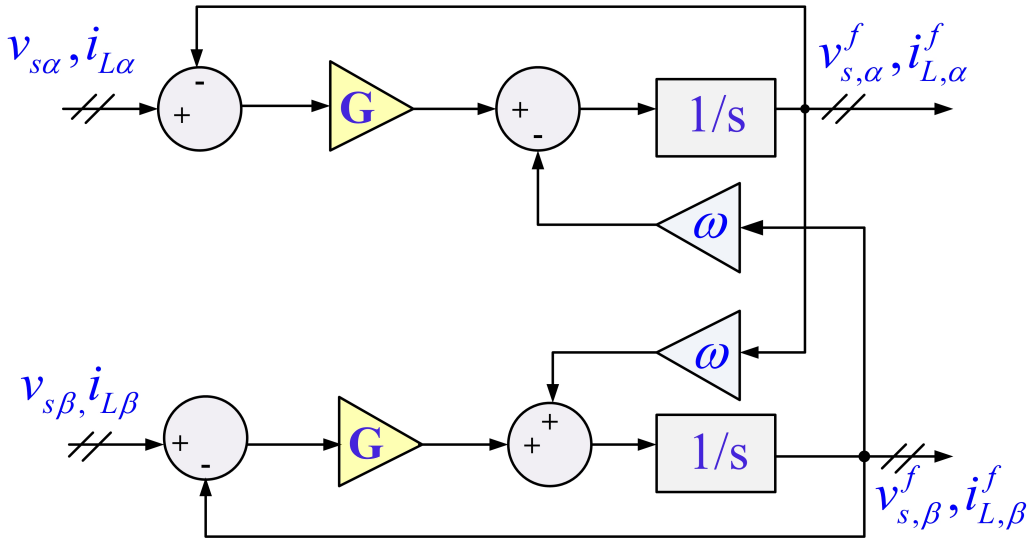

FIGURE 5.3: Block module representation of STF.

transfer function structure [157].

$$G(s) = \frac{C_{xy}(s)}{R_{xy}(s)} = \frac{s + j\omega_0}{s^2 + \omega_0^2} \tag{5.9}$$

where, $C_{xy}(t) = e^{(j\omega t)} \int e^{(j\omega t)} R_{xy}(t) dt$
With a proper selection of gain G, unity magnitude of the transfer function and zero phase delay can be achieved for $\omega = \omega_0$. With the time constant of STF being 1/G, desirable performance in terms of speed of response can be ascertained by properly tuning gain parameter G. Value of the parameter, G, selected in this study is 100 . For this value of G, the STF exhibits zero phase delay and quick response with unity magnitude at $\omega = \omega_0$ (see Fig. 5.4). The fundamental components pertaining to the grid voltages and load currents are extracted using STF by employing Clarke transformation on inputs followed by inverse Clarke transformation as given below:

$$\begin{pmatrix} i_{L\alpha} \\ i_{L\beta} \\ i_{L0} \end{pmatrix} = \sqrt{\frac{2}{3}} \begin{pmatrix} 1 & -\frac{1}{2} & -\frac{1}{2} \\ 0 & \frac{\sqrt{3}}{2} & -\frac{\sqrt{3}}{2} \\ \frac{1}{\sqrt{2}} & \frac{1}{\sqrt{2}} & \frac{1}{\sqrt{2}} \end{pmatrix} \begin{pmatrix} i_{La} \\ i_{Lb} \\ i_{Lc} \end{pmatrix} \tag{5.10}$$

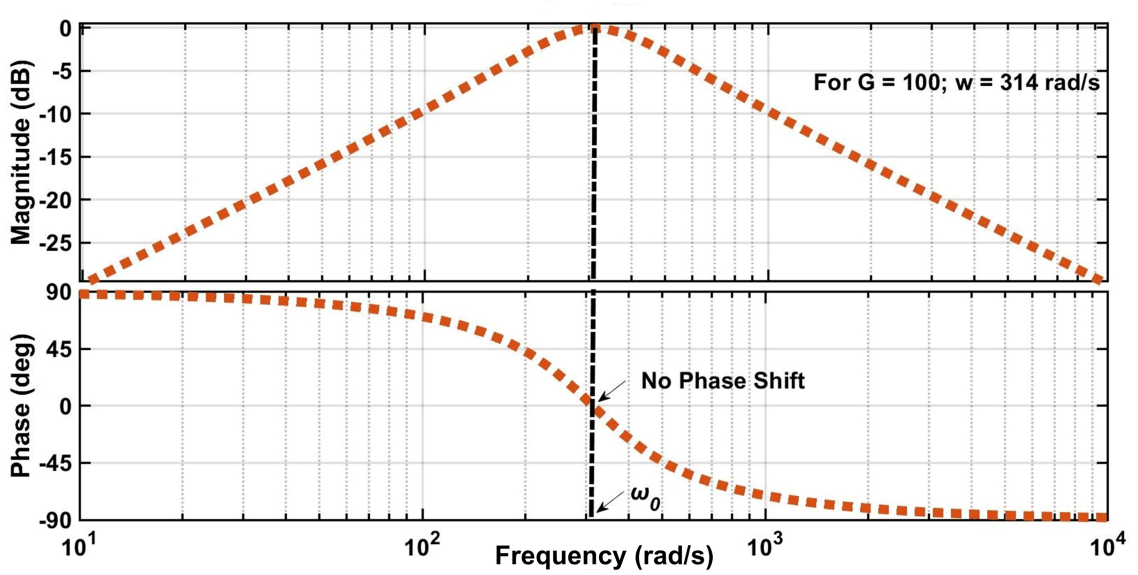

FIGURE 5.4: Bode plot representation of STF for G = 100.

STF operates on the transformed load currents to yield fundamental components of load currents, as shown in the following equations [157]:

$$i^f_{L,\beta} = \frac{1}{s}\left\{G\left(i_{L,\beta} - i^f_{L,\beta}\right) - \omega i^f_{L,\alpha}\right\} \tag{5.11}$$

$$i^f_{L,\alpha} = \frac{1}{s}\left\{G\left(i_{L\alpha} - i^f_{L,\alpha}\right) - \omega i^f_{L,\beta}\right\} \tag{5.12}$$

It is noted that the response of STF is consistent with a bandpass filter.

5.3.2.2 PCC Amplitude and Unit-Template Estimation($V^*, x_{pa}, x_{pb}, x_{pc}$)

The presence of source inductance causes the voltage at PCC to be distorted and non-sinusoidal under non-linear load conditions. So extraction of unit templates from such a system would not result in proper grid synchronization. The sensed grid phase voltages v_{sa}, v_{sb}, v_{sc} are first transformed from a, b, c to $\alpha - \beta$ components. These are applied as inputs to an STF for transforming them into fundamental $\alpha - \beta$ components and finally back to three-phase fundamental grid phase voltages ${v_{sd}}^f, {v_{sb}}^f, {v_{sc}}^f$ using inverse Clarke transformation. In-phase unit templates (x_{pa}, x_{pb} and x_{pc}) are then extracted, making use of the magnitude (V^*) of the fundamental components of grid phase voltages as shown:

$$V^* = \sqrt{\frac{2}{3}\left[\left(v_{sa}^f\right)^2 + \left(v_{sb}^f\right)^2 + \left(v_{sc}^f\right)^2\right]} \tag{5.13}$$

$$x_{pa} = \frac{v_{sa}^f}{V^*}; x_{pb} = \frac{v_{sb}^f}{V^*}; x_{pc} = \frac{v_{sc}^f}{V^*} \tag{5.14}$$

5.3.2.3 Estimation of Active Loss Component

The actual voltage across the dc link (V_{dc}) is measured and corelated with the reference dc-link voltage (V_{dcref}). The error (V_{error}) obtained is passed through a PI controller, which drives the dc-link voltage to the reference value by operating upon the error received. The active loss component ($(I_{\text{loss}}$) is obtained as

$$I_{\text{loss}}^{(k+1)} = I_{\text{loss}}^{k} + K_p\left(\Delta V_{\text{error}}\right) + K_i\left(V_{\text{error}}^{(k+1)}\right) \tag{5.15}$$

where, $\Delta V_{\text{error}} = V^{(k+1)} - V^{(k)}$ is the error difference between two successive instants.

5.3.2.4 Estimation of the Fundamental Active Load Current Component

The fundamental active load current amplitude (I_L^f, active) is estimated from the quadrature current components (${i_L}^f{}_\alpha$ and ${i_L}^f{}_\beta$) obtained from STF as given below:

$$I_{L,active}^f = \sqrt{\left(i_{L,\alpha}^f\right)^2 + \left(i_{L,\beta}^f\right)^2} \tag{5.16}$$

5.3.2.5 Reference Grid Current Extraction

The effective active component (${I_{\text{ref}}}^*$), is obtained as shown under:

$$I_{ref}^* = I_{\text{loss}} + I_{L,active}^f \tag{5.17}$$

The reference grid currents estimated are compared with the measured grid currents, and the resultant error is minimized using a hysteresis current regulator to effectuate switching of the VSC.

5.4 Results and Discussion

A three-phase $415-\mathrm{V}, 50$ Hz, grid integrated SPPG system involving dual-stage configuration is developed and modelled using MATLAB/Simulink toolbox. For assessing the efficacy of the STF enabled control scheme, extensive simulation studies are carried out under varied scenarios. The system is critically investigated in terms of voltages at PCC, V_{sabc} , compensator currents $I_{\text{invabc,}}$, grid currents I_{sabc}, SPV array parameters such as array current I_{pv}, voltage V_{pv}, and power Ppv. The voltage across DC bus V_{dc}, grid reference currents I^*_{ref} and load currents I_{labc}.

5.4.1 Performance Analysis under Balanced Non-Linear Load with SPPG system subjected to Uniform Insolation

Fig. 5.5 demonstrates the performance of the proposed SPPG system under uniform irradiance conditions for the balanced non-linear load conditions. The grid side experiences improved power quality behavior, with the power factor being close to unity and having substantially less harmonic interference.

5.4.2 Performance Analysis under Balanced Linear Load with SPPG system subjected to Non- Uniform Insolation

Fig. 5.6 demonstrates the performance of the proposed SPPG system under balanced loading conditions at variable insolation. For this case, a balanced 20 kW linear load at power factor 0.8 lagging is connected at the distribution end. The dynamic performance is tested under varying insolation from 500 $\mathrm{W/m^2}$ to 1000 $\mathrm{W/m^2}$ at $\mathrm{t} = 0.65$ s. On increment of solar insolation (G), the power extracted out of SPV system $\left(P_{pv}\right)$ increases with subsequent increment in grid currents($\left(I_{sabc}\right)$. This change is observed because the excess power fed from the SPV system after fulfilling the load requirement gets adjusted in incrementing grid current magnitude. Under all operating conditions, the grid currents remain balanced, sustained, and sinusoidal. The dc-link voltage (V_{dc}) is almost constant and is restricted to the desired value. The control scheme operates satisfactorily even for sustained dynamic variation of insolation. MPOP algorithm works well

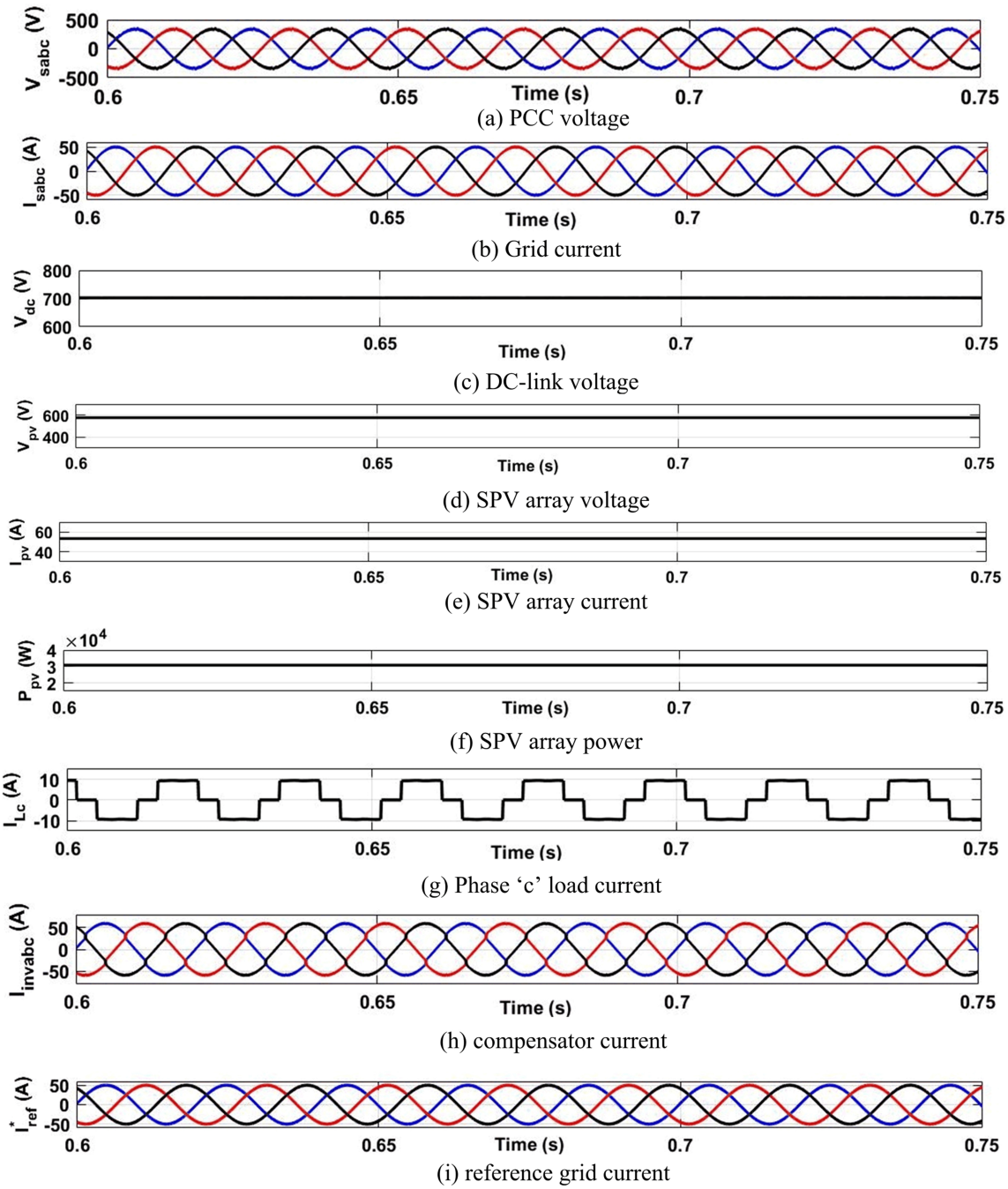

FIGURE 5.5: Performance with balanced non-linear load under uniform insolation.

and ensures maximum power extraction out of the SPV system even when subjected to varying insolation, thus enhancing system utilization.

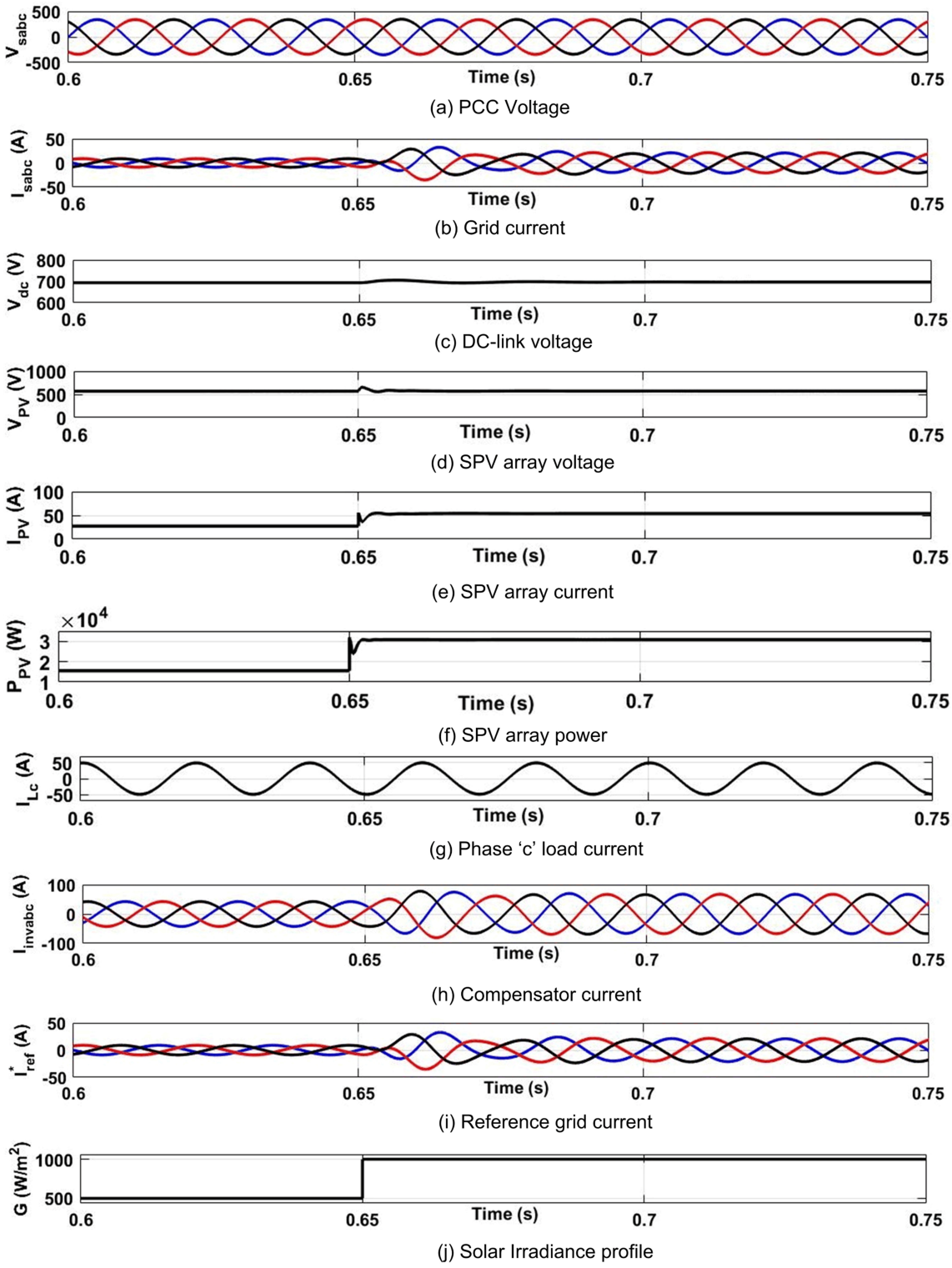

FIGURE 5.6: Performance with balanced linear load subjected to variable insolation.

5.4.3 Performance Analysis under Unbalanced Non-Linear Load with SPV system subjected to Uniform Insolation

Fig. 5.7 shows the performance of the proposed SPPG system for the unbalanced non-linear load (3-ϕ diode bridge rectifier with R-L load) under the influence of steady insolation. The dynamic performance is observed by removing one phase of the balanced load (phase 'c' in this case) from 0.65 s-0.7 s. It can be observed that this unbalancing has a negligible effect on the performance of the proposed system. The control algorithm adapts suitably to this change and enhances power quality at the grid side. The grid currents (Isabc) remain balanced, sustained, and perfectly sinusoidal. The dc-link voltage (Vdc) is maintained at the reference value (700 V) throughout this dynamic condition. MPOP algorithm is extracting maximum power.

5.4.4 Comparative Performance Analysis of Proposed STF Assisted Control Scheme with Popular Conventional and Adaptive Control Schemes

A comparative performance analysis with conventional and adaptive control schemes is performed to investigate the effectiveness of the proposed STF assisted control of VSC compared to different existing and popular control schemes. Table I, shows the percentage THD of PCC voltage and currents. The STF based control scheme for SPV power injection into the grid shows enhanced performance in minimizing harmonic interference at PCC, countering load unbalancing, and ensuring power factor correction. The THD values obtained with STF based control scheme for grid currents (I_{sabc}), PCC voltage (V_{sabc}) and load currents (I_{labc}) are 0.67%, 1.33% and 30.17% respectively. A careful examination of the total harmonic distortion present in the grid side voltage and current indicated in Table I, clearly shows that the proposed SPPG system with STF based control scheme offers better performance. Moreover, the main advantage provided by STF based control scheme is its simple structure. One unit of STF is enough for three-phase applications. PLL-based control schemes such as SRFT results in a more complicated control structure with reduced response time.

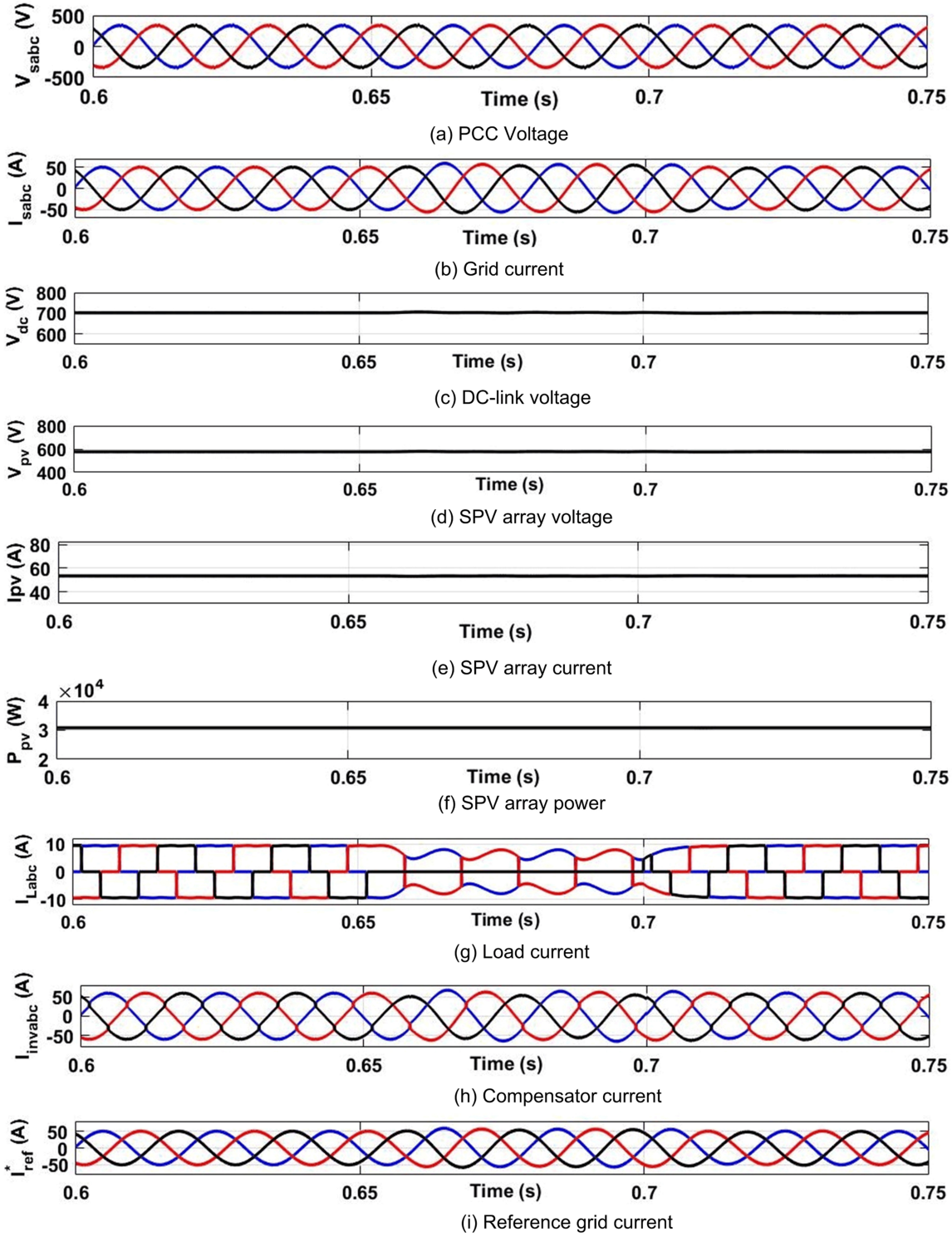

FIGURE 5.7: Dynamic performance with unbalanced non-linear load subjected to uniform insolation.

In contrast, STF based control scheme improves the speed of response and eliminates system complexity.

TABLE 5.1: THD Computations Under Non-Linear Load

Parameters	Grid Current (A)	Grid Voltage (V)	Load Current (A)
1. Proposed Self-Tuning Filter (STF)			
Magnitude	50.25 A	338.6 V	10.31 A
THD	0.67%	1.33%	30.17%
2. Synchronous Reference Frame Theory (SRFT)			
Magnitude	50.26 A	338.5 V	10.31 A
THD	1.29%	3.43%	30.29%
3. Unit Vector Transform (UVT)			
Magnitude	49.84 A	339.1 V	10.34 A
THD	1.38%	1.59%	30.13%
4. Power Balance Theory (PBT)			
Magnitude	50.17 A	339.1 V	10.32 A
THD	1.45%	1.61%	30.21%
5. Least Mean Square (LMS)			
Magnitude	50.13 A	339.2 V	10.32 A
THD	1.21%	1.36%	30.21%
6. Least Mean Fourth (LMF)			
Magnitude	50.13 A	339.2 V	10.32 A
THD	1.19%	1.36%	30.21%

5.5 Summary

The chapter presents a comprehensive study on a dual-stage three-phase grid-tied SPPG system, emphasizing the implementation of an STF assisted control

scheme for a VSC. The integration of solar energy into the grid is increasingly vital due to the economic advantages of solar electricity over conventional sources, alongside the growing efficiency of solar panels. The paper outlines the challenges associated with grid integration, particularly the unpredictable nature of SPPG systems and the need for robust control mechanisms to ensure PQ and reliability. The primary research contributions of this study are:

1. A two-stage SPPG system is developed and modelled in MATLAB/Simulink. Here, the STF assisted control scheme for feeding SPV power to the grid is implemented.

2. The system comprises several key components, including a SPV array, a DC-DC boost converter, and the VSC. These elements work together to optimize power extraction from the solar array and facilitate effective power injection into the grid.

3. The chapter highlights significant PQ issues associated with integrating renewable energy sources into the grid, such as harmonics injection, poor power factor, and voltage regulation problems. These issues can adversely affect end-users in the distribution system.

4. A robust control strategy is proposed to address these PQ challenges. The control scheme is divided into two main components: MPOP tracking control and grid interfaced VSC control. The MPOP control utilizes a DC-DC boost converter to ensure optimal power extraction from the SPV system.

5. Extensive simulations were conducted using MATLAB/Simulink to evaluate the performance of the proposed STF control approach. The results demonstrated that the STF method effectively enhances PQ, achieving harmonic rejection and power factor correction, thus ensuring compliance with PQ standards.

6. The thesis compares the STF control approach with traditional and popular adaptive control methods, showing that the STF method outperforms classical techniques in maintaining sinusoidal grid currents and minimizing harmonic distortion, even under non-linear load conditions.

The proposed STF-assisted control scheme significantly improves the performance of grid-tied solar power systems, making it a valuable contribution to the field of renewable energy integration. The findings emphasize the importance of effective control strategies in enhancing the reliability and efficiency of SPPG systems.

Chapter 6

Conclusions and Future Scopes

This chapter encapsulates the notable outcomes derived from the research, offering overarching conclusions and discussions on the main findings, alongside recommendations for potential future research extensions.

6.1 Conclusions

This thesis presents a comprehensive investigation into innovative strategies addressing critical challenges in PV systems, with a focus on enhancing performance, reliability, and cost-effectiveness under diverse operating conditions. By tackling issues such as HS formation and ML, the research delivers substantial contributions to advancing PV technology.

The first core area of study targets the persistent issue of HS formation, which undermines module reliability and energy efficiency, particularly under PSCs. A novel HSMC is proposed, significantly reducing localized heating and power loss while enhancing thermal stability. Experimental results demonstrate up to an 89.82% reduction in power loss compared to conventional BPDs, highlighting the limitations of standard BPDs in mitigating localized heating during shading events. This work establishes the HSMC as a robust solution for improving system performance and reliability under PSCs.

The research also advances the field through novel static SD and reconfiguration strategies, such as GMRA, GPRS, and CDMRA. These methods optimize power extraction, achieving significant gains in FF, efficiency, and energy yield compared to traditional and contemporary approaches. For example, GMRA demonstrates improvements of up to 29.55% in power output,

while CDMRA reduces ML by 89.9%, showcasing their effectiveness in diverse shading scenarios. A detailed techno-economic analysis further underscores their feasibility and profitability, particularly for large-scale PV installations, with shorter payback periods and higher revenue generation compared to conventional configurations.

Another critical contribution is the development of the MPVA, which achieves significant reductions in cross-tie complexity and wiring requirements, streamlining system design. This configuration enhances power extraction efficiency and reduces MLs, as evidenced by experimental results showing power boosts of up to 28.3%. By offering a more efficient and less intricate alternative to traditional designs, the MPVA addresses key challenges associated with IMSs.

In summary, this thesis makes significant contributions to PV system design by addressing the pressing challenges of shading and MLs. The proposed methods not only enhance energy output and system reliability but also provide practical and cost-effective solutions for large-scale deployment. These findings pave the way for future advancements in PV technology, fostering a more sustainable and efficient energy landscape.

6.2 Contributions

The growing reliance on solar energy as a sustainable and renewable power source has catalyzed significant advancements in PV technology. Despite these advancements, PV systems face persistent challenges such as irradiance mismatch, shading, and temperature variations, which result in power losses, reduced system lifespan, and safety concerns like hot spot formation. This thesis addresses these challenges by proposing innovative solutions to enhance the efficiency, reliability, and safety of PV systems under non-ideal conditions.

The primary contributions of this thesis include the development of advanced reconfiguration techniques and optimized circuit designs aimed at mitigating the adverse effects of irradiance mismatch and hot spots. Additionally, it proposes a dual-stage, three-phase grid-interfaced solar PV system equipped with a self-tuning filter to enhance power quality and ensure efficient grid integration. This

system outperforms traditional control methods. Key highlights include:

1. **Development of the hot spot mitigation circuit:** A novel circuit design that effectively mitigates HS formation and MLs, achieving up to 89.82% reduction in MLs compared to conventional BPDs. This enhancement significantly improves both the reliability and safety of PV arrays under PSCs.

2. **Innovative Reconfiguration Techniques:**
   (a) GMRA and its variant SP-GMRA uniformly distribute shading across PV arrays. These techniques demonstrated a reduction in MLs by up to 76.3% and 27%, respectively, compared to traditional configurations.
   (b) GPRS and its series-parallel variant SP-GPRS are proposed for diverse shading scenarios, showing up to 75.4% reduction in MLs and power generation improvements of up to 31% for TCT configurations and up to 16.1% for SP configurations.
   (c) The proposed CDMRA method optimizes module positioning to minimize shading impacts without altering wiring, achieving significant reductions in mismatch power loss and improved system efficiency across varying IMSs.

3. **Enhanced PV Configurations:**
   (a) A modified PV arrangement (MPVA) is introduced to address wiring complexity in conventional TCT arrays, reducing cross-ties by 59.37% and improving system performance through minimized wiring requirements.
   (b) The PMSRA is presented as a static shade mitigation technique applicable to TCT, SP, and MPVA configurations, achieving up to 86% reduction in MLs compared to conventional TCT arrays.

4. **Dual-Stage Grid-Interfaced System:** A dual-stage three-phase grid-interfaced solar PV power generation system is proposed, incorporating a self-tuning filter to enhance power quality by addressing harmonic rejection and power factor correction. This system outperforms existing control techniques, demonstrating superior VSC control.

   Through these contributions, the research significantly advances the field of PV technology, providing practical and scalable solutions to improve

system performance under non-ideal conditions. Furthermore, the efficient grid integration of PV systems ensures enhanced energy utilization and power quality, supporting the broader adoption of solar energy for sustainable and reliable power generation.

6.3 Future Scopes

Based on the research conducted in this thesis,outlined below are key considerations and prospective areas for future exploration and development in the field of performance enhancement of solar PV systems operating under sub-optimal operating conditions:

1. Using artificial intelligence and machine learning to predict mismatch conditions before they significantly impact system performance, enabling preventive maintenance and reducing downtime.
2. Leveraging big data and analytics to monitor PV system performance and identify patterns in mismatch conditions, leading to more targeted interventions and optimizations.
3. Developing more sophisticated MPPT algorithms and inverters that can adapt dynamically to varying mismatch conditions. This includes machine learning based MPPT techniques that predict and optimize energy yield in real time.
4. Studying the impact of mismatched PV systems on grid stability, particularly in scenarios with high PV penetration. Research could focus on control strategies to ensure stable operation under varying mismatch conditions.
5. Exploring how energy storage systems can be optimized to work with PV systems under mismatch conditions, ensuring that energy generation and storage are both maximized even under non-ideal circumstances.
6. Developing advanced battery management systems (BMS) that can work in tandem with PV systems to mitigate the effects of mismatches, ensuring stable and reliable output.

Bibliography

[1] S. Ghosh and R. Yadav, "Future of photovoltaic technologies: A comprehensive review," *Sustainable Energy Technologies and Assessments*, vol. 47, p. 101410, 2021.

[2] S. Li, W. Liu, S. Hu, and B. Xu, "A method for determining the applicable geographical regions of pv modules field reliability assessment results based on regional clustering of environmental factors and their weights," *Sustainable Energy Technologies and Assessments*, vol. 53, p. 102620, 2022.

[3] S. Ghosh, S. K. Singh, and V. K. Yadav, "Experimental investigation of hotspot phenomenon in pv arrays under mismatch conditions," *Solar Energy*, vol. 253, pp. 219–230, 2023.

[4] B. Liu, L. Chen, K. Sun, X. Wang, and J. Zhao, "A hot spot identification approach for photovoltaic module based on enhanced u-net with squeeze-and-excitation and vgg19," *IEEE Transactions on Instrumentation and Measurement*, 2024.

[5] Y. Singh, B. Singh, and S. Mishra, "An uninterruptable pv array-battery based system operating in different power modes with enhanced power quality," *IEEE Transactions on Industrial Electronics*, vol. 69, no. 4, pp. 3631–3642, 2021.

[6] M. Thuis, N. M. Al Hasan, R. L. Arnold, B. King, A. Maes, D. C. Miller, J. M. Newkirk, L. T. Schelhas, A. Sinha, and K. Terwilliger, "A comparison of emerging nonfluoropolymer-based coextruded pv backsheets to industry-benchmark technologies," *IEEE Journal of Photovoltaics*, vol. 12, no. 1, pp. 88–96, 2021.

[7] I. S. Millah, R. K. Subroto, Y. W. Chang, K. L. Lian, and B.-R. Ke, "Investigation of maximum power point tracking of different kinds of solar panels under

partial shading conditions," *IEEE Transactions on Industry Applications*, vol. 57, no. 1, pp. 17–25, 2020.

[8] J. Zhang, Y. Liu, Y. Li, X. Chen, K. Ding, J. Yan, and X. Chen, "An i–v characteristic reconstruction-based partial shading diagnosis and quantitative evaluation for photovoltaic strings," *Energy*, vol. 300, p. 131480, 2024.

[9] P. Pandian, P. W. David, P. Murugesan, and P. K. Balachandran, "A selective cross-tied array configuration technique for partial shaded solar pv system," *Electrical Engineering*, pp. 1–20, 2024.

[10] V. L. Mishra, Y. K. Chauhan, and K. Verma, "Attenuation of shading loss using a novel solar array reconfigured topology under partial shading conditions," *Solar Energy*, vol. 274, p. 112552, 2024.

[11] D. Debnath and K. Chatterjee, "Two-stage solar photovoltaic-based stand-alone scheme having battery as energy storage element for rural deployment," *IEEE Transactions on Industrial Electronics*, vol. 62, no. 7, pp. 4148–4157, 2014.

[12] S. Krithiga and N. G. A. Gounden, "Power electronic configuration for the operation of pv system in combined grid-connected and stand-alone modes," *IET Power Electronics*, vol. 7, no. 3, pp. 640–647, 2014.

[13] O. M. Akeyo, V. Rallabandi, N. Jewell, and D. M. Ionel, "The design and analysis of large solar pv farm configurations with dc-connected battery systems," *IEEE Transactions on Industry Applications*, vol. 56, no. 3, pp. 2903–2912, 2020.

[14] D. Li, T. Wang, W. Pan, X. Ding, and J. Gong, "A comprehensive review of improving power quality using active power filters," *Electric Power Systems Research*, vol. 199, p. 107389, 2021.

[15] C. Jain and B. Singh, "A three-phase grid tied spv system with adaptive dc link voltage for cpi voltage variations," *IEEE Transactions on Sustainable Energy*, vol. 7, no. 1, pp. 337–344, 2015.

[16] N. Babu, J. M. Guerrero, P. Siano, R. Peesapati, and G. Panda, "An improved adaptive control strategy in grid-tied pv system with active power filter for

power quality enhancement," *IEEE Systems Journal*, vol. 15, no. 2, pp. 2859–2870, 2020.

[17] D. Venkatramanan and V. John, "Dynamic phasor modeling and stability analysis of srf-pll-based grid-tie inverter under islanded conditions," *IEEE Transactions on Industry Applications*, vol. 56, no. 2, pp. 1953–1965, 2019.

[18] G. Acciari, D. Graci, and A. La Scala, "Higher pv module efficiency by a novel cbs bypass," *IEEE transactions on power electronics*, vol. 26, no. 5, pp. 1333–1336, 2010.

[19] K. A. Kim and P. T. Krein, "Reexamination of photovoltaic hot spotting to show inadequacy of the bypass diode," *IEEE Journal of Photovoltaics*, vol. 5, no. 5, pp. 1435–1441, 2015.

[20] V. d'Alessandro, P. Guerriero, and S. Daliento, "A simple bipolar transistor-based bypass approach for photovoltaic modules," *IEEE Journal of Photovoltaics*, vol. 4, no. 1, pp. 405–413, 2013.

[21] P. Bauwens and J. Doutreloigne, "Reducing partial shading power loss with an integrated smart bypass," *Solar Energy*, vol. 103, pp. 134–142, 2014.

[22] S. Daliento, F. Di Napoli, P. Guerriero, and V. d'Alessandro, "A modified bypass circuit for improved hot spot reliability of solar panels subject to partial shading," *Solar Energy*, vol. 134, pp. 211–218, 2016.

[23] T. Ghanbari, "Permanent partial shading detection for protection of photovoltaic panels against hot spotting," *IET Renewable Power Generation*, vol. 11, no. 1, pp. 123–131, 2017.

[24] J. Qian, A. Thomson, A. Blakers, and M. Ernst, "Comparison of half-cell and full-cell module hotspot-induced temperature by simulation," *IEEE Journal of Photovoltaics*, vol. 8, no. 3, pp. 834–839, 2018.

[25] C. Olalla, M. N. Hasan, C. Deline, and D. Maksimović, "Mitigation of hot-spots in photovoltaic systems using distributed power electronics," *Energies*, vol. 11, no. 4, p. 726, 2018.

[26] M. Dhimish, V. Holmes, P. Mather, and M. Sibley, "Novel hot spot mitigation technique to enhance photovoltaic solar panels output power performance," *Solar Energy Materials and Solar Cells*, vol. 179, pp. 72–79, 2018.

[27] S. Ghosh, V. K. Yadav, and V. Mukherjee, "Improvement of partial shading resilience of pv array though modified bypass arrangement," *Renewable energy*, vol. 143, pp. 1079–1093, 2019.

[28] M. Dhimish, "Assessing mppt techniques on hot-spotted and partially shaded photovoltaic modules: Comprehensive review based on experimental data," *IEEE Transactions on Electron Devices*, vol. 66, no. 3, pp. 1132–1144, 2019.

[29] D. P. Winston, "Efficient output power enhancement and protection technique for hot spotted solar photovoltaic modules," *IEEE Transactions on Device and Materials Reliability*, vol. 19, no. 4, pp. 664–670, 2019.

[30] P. Guerriero, P. Tricoli, and S. Daliento, "A bypass circuit for avoiding the hot spot in pv modules," *Solar Energy*, vol. 181, pp. 430–438, 2019.

[31] M. Karimi, H. Samet, T. Ghanbari, and E. Moshksar, "A current based approach for hotspot detection in photovoltaic strings," *International Transactions on Electrical Energy Systems*, vol. 30, no. 9, p. e12517, 2020.

[32] C. E. Clement, J. P. Singh, E. Birgersson, Y. Wang, and Y. S. Khoo, "Hotspot development and shading response of shingled pv modules," *Solar Energy*, vol. 207, pp. 729–735, 2020.

[33] L. Xia, Z. Wen, K. Liao, J. Chen, Q. Li, and X. Luo, "Unveiling the failure mechanism of electrical interconnection in thermal-aged pv modules," *IEEE Transactions on Device and Materials Reliability*, vol. 20, no. 1, pp. 24–32, 2019.

[34] K. Ayache, A. Chandra, and A. Chériti, "An embedded reconfiguration for reliability enhancement of photovoltaic shaded panels against hot spots," *IEEE Transactions on Industry Applications*, vol. 56, no. 2, pp. 1815–1826, 2019.

[35] S. Ghosh, V. K. Yadav, and V. Mukherjee, "A novel hot spot mitigation circuit for improved reliability of pv module," *IEEE Transactions on device and materials reliability*, vol. 20, no. 1, pp. 191–198, 2020.

[36] M. U. Ali, H. F. Khan, M. Masud, K. D. Kallu, and A. Zafar, "A machine learning framework to identify the hotspot in photovoltaic module using infrared thermography," *Solar Energy*, vol. 208, pp. 643–651, 2020.

[37] D. P. Winston, "Design of sustainable pv module for efficient power generation during faults," *IEEE Transactions on components, packaging and manufacturing technology*, vol. 10, no. 3, pp. 389–392, 2020.

[38] A. Wang and Y. Xuan, "Close examination of localized hot spots within photovoltaic modules," *Energy Conversion and Management*, vol. 234, p. 113959, 2021.

[39] S. Tang, Y. Xing, L. Chen, X. Song, and F. Yao, "Review and a novel strategy for mitigating hot spot of pv panels," *Solar Energy*, vol. 214, pp. 51–61, 2021.

[40] C. Cheng, M. Liu, H. Yi, J. Wang, and H. Chen, "Tendency-aided data-driven method for hot spot detection in photovoltaic systems," *IEEE Journal of Emerging and Selected Topics in Industrial Electronics*, vol. 3, no. 4, pp. 901–910, 2022.

[41] W. P. Lamb, D. E. Asnes, J. Kupfer, E. Lickey, J. Bakken, R. C. Haskell, P. N. Saeta, and Q. Yang, "Real-time anticipation and prevention of hot spots by monitoring the dynamic conductance of photovoltaic panels," *IEEE Journal of Photovoltaics*, vol. 12, no. 4, pp. 1051–1057, 2022.

[42] C. Cheng, M. Liu, H. Yi, G. Ran, and H. Chen, "Slow manifold analysis-based detection of hot spots in photovoltaic systems," *IEEE Transactions on Instrumentation and Measurement*, vol. 71, pp. 1–10, 2022.

[43] T. Wei, Y. Zhang, Y. Zhang, R. Miao, J. Kang, and H. Qi, "City-scale roof-top photovoltaic deployment planning," *Applied Energy*, vol. 368, p. 123461, 2024.

[44] V. Kapsalis, C. Maduta, N. Skandalos, M. Wang, S. S. Bhuvad, D. D'Agostino, T. Ma, U. Raj, D. Parker, J. Peng *et al.*, "Critical assessment of large-scale rooftop photovoltaics deployment in the global urban environment," *Renewable and Sustainable Energy Reviews*, vol. 189, p. 114005, 2024.

[45] M. Mehdi, N. Ammari, A. A. Merrouni, S. Elhamaoui, and M. Dahmani, "Innovative design and field performance evaluation of a desert-adapted pv module for enhanced solar energy harvesting and reliability in harsh arid environments," *Applied Energy*, vol. 366, p. 123359, 2024.

[46] F. Belhachat and C. Larbes, "Photovoltaic array reconfiguration strategies for mitigating partial shading effects: Recent advances and perspectives," *Energy Conversion and Management*, vol. 313, p. 118547, 2024.

[47] P. Aravind, D. Prince Winston, S. Sugumar, and M. Pravin, "Optimal battery based electrical reconfiguration technique for partial shaded pv system," *Applied Energy*, vol. 361, p. 122942, 2024.

[48] B. Aljafari, P. R. Satpathy, and S. B. Thanikanti, "Partial shading mitigation in pv arrays through dragonfly algorithm based dynamic reconfiguration," *Energy*, vol. 257, p. 124795, 2022.

[49] A. Fathy, "Butterfly optimization algorithm based methodology for enhancing the shaded photovoltaic array extracted power via reconfiguration process," *Energy Conversion and Management*, vol. 220, p. 113115, 2020.

[50] B. Yang, R. Shao, M. Zhang, H. Ye, B. Liu, T. Bao, J. Wang, H. Shu, Y. Ren, and H. Ye, "Socio-inspired democratic political algorithm for optimal pv array reconfiguration to mitigate partial shading," *Sustainable Energy Technologies and Assessments*, vol. 48, p. 101627, 2021.

[51] E. R. Sanseverino, T. N. Ngoc, M. Cardinale, V. L. Vigni, D. Musso, P. Romano, and F. Viola, "Dynamic programming and munkres algorithm for optimal photovoltaic arrays reconfiguration," *Solar Energy*, vol. 122, pp. 347–358, 2015.

[52] L. Bouselham, A. Rabhi, B. Hajji, and A. Mellit, "Photovoltaic array reconfiguration method based on fuzzy logic and recursive least squares: An experimental validation," *Energy*, vol. 232, p. 121107, 2021.

[53] T. S. Babu, J. P. Ram, T. Dragičević, M. Miyatake, F. Blaabjerg, and N. Rajasekar, "Particle swarm optimization based solar pv array reconfiguration of the maximum power extraction under partial shading

conditions," *IEEE Transactions on Sustainable Energy*, vol. 9, no. 1, pp. 74–85, 2017.

[54] D. Nguyen and B. Lehman, "An adaptive solar photovoltaic array using model-based reconfiguration algorithm," *IEEE Transactions on industrial Electronics*, vol. 55, no. 7, pp. 2644–2654, 2008.

[55] D. Yousri, S. B. Thanikanti, K. Balasubramanian, A. Osama, and A. Fathy, "Multi-objective grey wolf optimizer for optimal design of switching matrix for shaded pv array dynamic reconfiguration," *IEEE Access*, vol. 8, pp. 159 931–159 946, 2020.

[56] M. Alanazi, A. Fathy, D. Yousri, and H. Rezk, "Optimal reconfiguration of shaded pv based system using african vultures optimization approach," *Alexandria Engineering Journal*, vol. 61, no. 12, pp. 12 159–12 185, 2022.

[57] A. M. Nassef, E. H. Houssein, B. E.-d. Helmy, A. Fathy, M. L. Alghaythi, and H. Rezk, "Optimal reconfiguration strategy based on modified runge kutta optimizer to mitigate partial shading condition in photovoltaic systems," *Energy Reports*, vol. 8, pp. 7242–7262, 2022.

[58] X. Zhang, D. Meng, J. Cai, G. Zhang, T. Yu, F. Pan, and Y. Yang, "A swarm based double q-learning for optimal pv array reconfiguration with a coordinated control of hydrogen energy storage system," *Energy*, vol. 266, p. 126483, 2023.

[59] X. Zhang, T. Yu, X. Ma, and L. Guo, "An efficient multi-agent negotiation algorithm for multi-period photovoltaic array reconfiguration with a hydrogen energy storage system," *Energy Conversion and Management*, vol. 256, p. 115376, 2022.

[60] T. N. Ngoc, Q. N. Phung, L. N. Tung, E. R. Sanseverino, P. Romano, and F. Viola, "Increasing efficiency of photovoltaic systems under non-homogeneous solar irradiation using improved dynamic programming methods," *Solar Energy*, vol. 150, pp. 325–334, 2017.

[61] S. N. Deshkar, S. B. Dhale, J. S. Mukherjee, T. S. Babu, and N. Rajasekar, "Solar pv array reconfiguration under partial shading conditions for maximum

power extraction using genetic algorithm," *Renewable and Sustainable Energy Reviews*, vol. 43, pp. 102–110, 2015.

[62] A. M. Ajmal, V. K. Ramachandaramurthy, A. Naderipour, and J. B. Ekanayake, "Comparative analysis of two-step ga-based pv array reconfiguration technique and other reconfiguration techniques," *Energy Conversion and Management*, vol. 230, p. 113806, 2021.

[63] X. Zhang, D. Meng, W. Li, T. Yu, Z. Fan, and Z. Hao, "Evolutionary based pareto optimization algorithms for bi-objective pv array reconfiguration under partial shading conditions," *Energy Conversion and Management*, vol. 271, p. 116308, 2022.

[64] D. Yousri, D. Allam, and M. B. Eteiba, "Optimal photovoltaic array reconfiguration for alleviating the partial shading influence based on a modified harris hawks optimizer," *Energy Conversion and Management*, vol. 206, p. 112470, 2020.

[65] B. I. Rani, G. S. Ilango, and C. Nagamani, "Enhanced power generation from pv array under partial shading conditions by shade dispersion using su do ku configuration," *IEEE Transactions on sustainable energy*, vol. 4, no. 3, pp. 594–601, 2013.

[66] B. Dhanalakshmi and N. Rajasekar, "Dominance square based array reconfiguration scheme for power loss reduction in solar photovoltaic (pv) systems," *Energy conversion and management*, vol. 156, pp. 84–102, 2018.

[67] A. S. Yadav and V. Mukherjee, "Line losses reduction techniques in puzzled pv array configuration under different shading conditions," *Solar Energy*, vol. 171, pp. 774–783, 2018.

[68] M. Horoufiany and R. Ghandehari, "Optimization of the sudoku based reconfiguration technique for pv arrays power enhancement under mutual shading conditions," *Solar Energy*, vol. 159, pp. 1037–1046, 2018.

[69] P. R. Satpathy and R. Sharma, "Power loss reduction in partially shaded pv arrays by a static sdp technique," *Energy*, vol. 156, pp. 569–585, 2018.

[70] R. Pachauri, A. S. Yadav, Y. K. Chauhan, A. Sharma, and V. Kumar, "Shade dispersion-based photovoltaic array configurations for performance enhancement under partial shading conditions," *International Transactions on Electrical Energy Systems*, vol. 28, no. 7, p. e2556, 2018.

[71] I. Nasiruddin, S. Khatoon, M. F. Jalil, and R. Bansal, "Shade diffusion of partial shaded pv array by using odd-even structure," *Solar Energy*, vol. 181, pp. 519–529, 2019.

[72] P. R. Satpathy and R. Sharma, "Power and mismatch losses mitigation by a fixed electrical reconfiguration technique for partially shaded photovoltaic arrays," *Energy conversion and management*, vol. 192, pp. 52–70, 2019.

[73] V. M. R. Tatabhatla, A. Agarwal, and T. Kanumuri, "Performance enhancement by shade dispersion of solar photo-voltaic array under continuous dynamic partial shading conditions," *Journal of cleaner production*, vol. 213, pp. 462–479, 2019.

[74] Manjunath, H. Suresh, and S. Rajanna, "Performance enhancement of hybrid interconnected solar photovoltaic array using shade dispersion magic square puzzle pattern technique under partial shading conditions," *Solar Energy*, vol. 194, pp. 602–617, 2019.

[75] S. G. Krishna and T. Moger, "Optimal sudoku reconfiguration technique for total-cross-tied pv array to increase power output under non-uniform irradiance," *IEEE Transactions on Energy Conversion*, vol. 34, no. 4, pp. 1973–1984, 2019.

[76] G. S. Krishna and T. Moger, "Improved sudoku reconfiguration technique for total-cross-tied pv array to enhance maximum power under partial shading conditions," *Renewable and Sustainable Energy Reviews*, vol. 109, pp. 333–348, 2019.

[77] K. Rajani and T. Ramesh, "Maximum power enhancement under partial shadings using a modified sudoku reconfiguration," *CSEE Journal of Power and Energy Systems*, vol. 7, no. 6, pp. 1187–1201, 2020.

[78] N. Rakesh, S. S. Kumar, and G. Madhusudanan, "Mitigation of power mismatch losses and wiring line losses of partially shaded solar pv array using improvised magic technique," *IET Renewable Power Generation*, vol. 13, no. 9, pp. 1522–1532, 2019.

[79] M. S. S. Nihanth, J. P. Ram, D. S. Pillai, A. M. Ghias, A. Garg, and N. Rajasekar, "Enhanced power production in pv arrays using a new skyscraper puzzle based one-time reconfiguration procedure under partial shade conditions (pscs)," *Solar Energy*, vol. 194, pp. 209–224, 2019.

[80] S. Anjum, V. Mukherjee, and G. Mehta, "Advanced sudoku-based reconfiguration strategies for maximum power extraction from partially shaded solar photovoltaic array," *Journal of Solar Energy Engineering*, vol. 143, no. 6, p. 061003, 2021.

[81] L. El Iysaouy, M. Lahbabi, and A. Oumnad, "A novel magic square view topology of a pv system under partial shading condition," *Energy Procedia*, vol. 157, pp. 1182–1190, 2019.

[82] S. S. Reddy and C. Yammani, "Odd-even-prime pattern for pv array to increase power output under partial shading conditions," *Energy*, vol. 213, p. 118780, 2020.

[83] M. Kumar, "Enhanced solar pv power generation under pscs using shade dispersion," *IEEE Transactions on Electron Devices*, vol. 67, no. 10, pp. 4313–4320, 2020.

[84] V. P. Madhanmohan, M. Nandakumar, and A. Saleem, "Enhanced performance of partially shaded photovoltaic arrays using diagonally dispersed total cross tied configuration," *Energy Sources, Part A: Recovery, Utilization, and Environmental Effects*, pp. 1–19, 2020.

[85] V. M. R. Tatabhatla, A. Agarwal, and T. Kanumuri, "Performance improvement by mitigating the effects of moving cloud conditions," *IEEE Transactions on Power Electronics*, vol. 36, no. 4, pp. 4214–4223, 2020.

[86] R. D. A. Raj and K. A. Naik, "Optimal reconfiguration of pv array based on digital image encryption algorithm: A comprehensive simulation and

experimental investigation," *Energy Conversion and Management*, vol. 261, p. 115666, 2022.

[87] V. R. Krishnan, F. Blaabjerg, A. Sangwongwanich, and R. Natarajan, "Twisted two-step arrangement for maximum power extraction from a partially shaded pv array," *IEEE Journal of Photovoltaics*, vol. 12, no. 3, pp. 871–879, 2022.

[88] D. Yousri, A. Fathy, and E. F. El-Saadany, "Four square sudoku approach for alleviating shading effect on total-cross-tied pv array," *Energy Conversion and Management*, vol. 269, p. 116105, 2022.

[89] R. K. Pachauri, S. B. Thanikanti, J. Bai, V. K. Yadav, B. Aljafari, S. Ghosh, and H. H. Alhelou, "Ancient chinese magic square-based pv array reconfiguration methodology to reduce power loss under partial shading conditions," *Energy Conversion and Management*, vol. 253, p. 115148, 2022.

[90] C. Saiprakash, A. Mohapatra, B. Nayak, T. S. Babu, and H. H. Alhelou, "A novel benzene structured array configuration for harnessing maximum power from pv array under partial shading condition with reduced number of cross ties," *IEEE Access*, vol. 10, pp. 129 712–129 726, 2022.

[91] V. M. R. Tatabhatla, A. Agarwal, and T. Kanumuri, "A chaos map based reconfiguration of solar array to mitigate the effects of partial shading," *IEEE Transactions on Energy Conversion*, vol. 37, no. 2, pp. 811–823, 2021.

[92] V. L. Mishra, Y. K. Chauhan, and K. Verma, "A novel pv array reconfiguration approach to mitigate non-uniform irradiation effect," *Energy Conversion and Management*, vol. 265, p. 115728, 2022.

[93] N. Ramachandra and R. Natarajan, "Productivity enhancement of total-cross-tied pv array under static shade conditions," *IEEE Transactions on Power Electronics*, vol. 38, no. 3, pp. 4053–4060, 2022.

[94] D. Ahluwalia, S. Anjum, and V. Mukherjee, "Boost in energy generation using robust reconfiguration: A novel scheme for photovoltaic array under realistic fractional partial shadings," *Energy Conversion and Management*, vol. 290, p. 117211, 2023.

[95] A. Fathy, D. Yousri, T. S. Babu, and H. Rezk, "Triple x sudoku reconfiguration for alleviating shading effect on total-cross-tied pv array," *Renewable Energy*, vol. 204, pp. 593–604, 2023.

[96] M. F. Jalil, D. Sharma, and R. C. Bansal, "Cross kit reconfiguration algorithm for enhanced output power of pv array during shading mismatch conditions," *Optik*, vol. 288, p. 171218, 2023.

[97] R. K. Pachauri and J. G. Singh, "A novel shadow dispersion approach for solar pv modules in array using chess board game methodology: An experimental study," *Solar Energy*, vol. 265, p. 112098, 2023.

[98] N. D. Kaushika and N. K. Gautam, "Energy yield simulations of interconnected solar pv arrays," *IEEE Transactions on Energy Conversion*, vol. 18, no. 1, pp. 127–134, 2003.

[99] R. Ramaprabha and B. Mathur, "A comprehensive review and analysis of solar photovoltaic array configurations under partial shaded conditions," *International Journal of Photoenergy*, vol. 2012, no. 1, p. 120214, 2012.

[100] C. A. Ramos-Paja, J. D. Bastidas, A. J. Saavedra-Montes, F. Guinjoan-Gispert, and M. Goez, "Mathematical model of total cross-tied photovoltaic arrays in mismatching conditions," in *2012 IEEE 4th Colombian Workshop on Circuits and Systems (CWCAS)*. Ieee, 2012, pp. 1–6.

[101] L. F. L. Villa, D. Picault, B. Raison, S. Bacha, and A. Labonne, "Maximizing the power output of partially shaded photovoltaic plants through optimization of the interconnections among its modules," *IEEE Journal of Photovoltaics*, vol. 2, no. 2, pp. 154–163, 2012.

[102] F. Belhachat and C. Larbes, "Modeling, analysis and comparison of solar photovoltaic array configurations under partial shading conditions," *Solar energy*, vol. 120, pp. 399–418, 2015.

[103] M. Amin, J. Bailey, C. Tapia, and V. Thodimeladine, "Comparison of pv array configuration efficiency under partial shading condition," in *2016 IEEE 43rd Photovoltaic Specialists Conference (PVSC)*. IEEE, 2016, pp. 3704–3707.

[104] S. Mohammadnejad, A. Khalafi, and S. M. Ahmadi, "Mathematical analysis of total-cross-tied photovoltaic array under partial shading condition and its comparison with other configurations," *Solar energy*, vol. 133, pp. 501–511, 2016.

[105] C. T. K. Kho, J. Ahmed, S. Kashem, and Y. L. Then, "A comprehensive review on pv configurations to maximize power under partial shading," in *TENCON 2017-2017 IEEE Region 10 Conference*. IEEE, 2017, pp. 763–768.

[106] S. Bana and R. Saini, "Experimental investigation on power output of different photovoltaic array configurations under uniform and partial shading scenarios," *Energy*, vol. 127, pp. 438–453, 2017.

[107] M. Dhimish, V. Holmes, B. Mehrdadi, M. Dales, B. Chong, and L. Zhang, "Seven indicators variations for multiple pv array configurations under partial shading and faulty pv conditions," *Renewable Energy*, vol. 113, pp. 438–460, 2017.

[108] C. T. K. Kho, J. Ahmed, Y. L. Then, and M. Kermadi, "Mitigating the effect of partial shading by triple-tied configuration of pv modules," in *2018 IEEE PES Asia-Pacific Power and Energy Engineering Conference (APPEEC)*. IEEE, 2018, pp. 532–537.

[109] S. R. Pendem and S. Mikkili, "Modeling, simulation and performance analysis of solar pv array configurations (series, series–parallel and honey-comb) to extract maximum power under partial shading conditions," *Energy Reports*, vol. 4, pp. 274–287, 2018.

[110] P. K. Bonthagorla and S. Mikkili, "Optimal pv array configuration for extracting maximum power under partial shading conditions by mitigating mismatching power losses," *CSEE Journal of Power and Energy Systems*, vol. 8, no. 2, pp. 499–510, 2020.

[111] S. R. Pendem, V. V. Katru, and S. Mikkili, "Hybrid pv array configurations for mitigating the mismatching power loss and number of peaks in the output characteristics under various pscs," in *IECON 2019-45th Annual Conference of the IEEE Industrial Electronics Society*, vol. 1. IEEE, 2019, pp. 2377–2382.

[112] P. K. Bonthagorla and S. Mikkili, "Performance analysis of pv array configurations (sp, bl, hc and tt) to enhance maximum power under non-uniform shading conditions," *Engineering reports*, vol. 2, no. 8, p. e12214, 2020.

[113] R. K. Pachauri, O. P. Mahela, A. Sharma, J. Bai, Y. K. Chauhan, B. Khan, and H. H. Alhelou, "Impact of partial shading on various pv array configurations and different modeling approaches: A comprehensive review," *IEEE Access*, vol. 8, pp. 181 375–181 403, 2020.

[114] Y.-J. Hung, J.-F. Liao, and Y.-C. Cheng, "Series-connected and shade-resilient silicon photovoltaic module for direct laser powering," *IEEE Electron Device Letters*, vol. 41, no. 12, pp. 1798–1801, 2020.

[115] P. K. Bonthagorla and S. Mikkili, "A novel fixed pv array configuration for harvesting maximum power from shaded modules by reducing the number of cross-ties," *IEEE Journal of Emerging and Selected Topics in Power Electronics*, vol. 9, no. 2, pp. 2109–2121, 2020.

[116] T. Ramesh, K. Rajani, and A. K. Panda, "A novel triple-tied-cross-linked pv array configuration with reduced number of cross-ties to extract maximum power under partial shading conditions," *CSEE Journal of Power and Energy Systems*, vol. 7, no. 3, pp. 567–581, 2020.

[117] C. Saiprakash, A. Mohapatra, and B. Nayak, "An a tt array configuration for performance enhancement of pv system under psc," in *2021 1st International Conference on Power Electronics and Energy (ICPEE)*. IEEE, 2021, pp. 1–5.

[118] H. Oufettoul, S. Motahhir, G. Aniba, M. Masud, and M. A. AlZain, "Improved tct topology for shaded photovoltaic arrays," *Energy Reports*, vol. 8, pp. 5943–5956, 2022.

[119] P. Changmai, S. Kumar, S. K. Nayak, and S. K. Metya, "Maximum power estimation of total cross-tied connected pv cells in different shading conditions for high current application," *IEEE Journal of Emerging and Selected Topics in Power Electronics*, vol. 10, no. 4, pp. 3883–3894, 2021.

[120] K. Rajani and T. Ramesh, "Reconfiguration of pv arrays (tct, bl, hc) considering wiring resistance," *CSEE Journal of Power and Energy Systems*, vol. 8, no. 5, pp. 1408–1416, 2022.

[121] S. Kumar, S. K. Nayak, and H. S. Sahu, "A novel gmpp estimation technique for series parallel connected partially shaded pv array," *Solar Compass*, vol. 7, p. 100049, 2023.

[122] S. Shambhu Choudhary, T. Nath Gupta, and I. Hussain, "Intelligent solar grid integration: Advancements in control strategies and power quality enhancement," *International Journal of Circuit Theory and Applications*, 2024.

[123] N. Mukundan, S. B. Q. Naqvi, B. Singh, and P. Jayaprakash, "Multi-functional grid integrated solar power transfer system with improved fagi based control for enhanced performance at non-ideal load conditions," *Electric Power Systems Research*, vol. 225, p. 109885, 2023.

[124] A. Bharatee, P. K. Ray, and A. Ghosh, "Power distribution technique and small-signal modeling of grid-integrated solar pv system with hybrid energy storage systems," *Journal of Energy Storage*, vol. 73, p. 109316, 2023.

[125] M. Shafiullah, S. D. Ahmed, and F. A. Al-Sulaiman, "Grid integration challenges and solution strategies for solar pv systems: a review," *IEEE Access*, vol. 10, pp. 52 233–52 257, 2022.

[126] N. Mukundan and P. Jayaprakash, "Realization of cascaded h-bridge multilevel inverter based grid integrated solar energy system with band stop generalized integral control," *IEEE Transactions on Industry Applications*, vol. 57, no. 1, pp. 764–773, 2020.

[127] K. Zeb, W. Uddin, M. A. Khan, Z. Ali, M. U. Ali, N. Christofides, and H. Kim, "A comprehensive review on inverter topologies and control strategies for grid connected photovoltaic system," *Renewable and Sustainable Energy Reviews*, vol. 94, pp. 1120–1141, 2018.

[128] A. A. Hussein, X. Chen, M. Alharbi, A. A. Pise, and I. Batarseh, "Design of a grid-tie photovoltaic system with a controlled total harmonic distortion and

tri maximum power point tracking," *IEEE Transactions on Power Electronics*, vol. 35, no. 5, pp. 4780–4790, 2019.

[129] R. I. Bojoi, L. R. Limongi, D. Roiu, and A. Tenconi, "Enhanced power quality control strategy for single-phase inverters in distributed generation systems," *IEEE Transactions on Power Electronics*, vol. 26, no. 3, pp. 798–806, 2011.

[130] H. Manoharan, S. Karuppannan, K. Chandrasekaran, and S. Barua, "Power quality improvement of grid-connected solar power plant systems using a novel fractional order proportional integral derivative controller technique," *IET Renewable Power Generation*, 2024.

[131] Ajit and S. Agrawal, "Power quality improvement using a novel simplified adaptive control of solar pv integrated shunt active power filter," *International Journal of Circuit Theory and Applications*, 2024.

[132] M. Chankaya, S. B. Q. Naqvi, I. Hussain, B. Singh, and A. Ahmad, "Power quality enhancement and improved dynamics of a grid tied pv system using equilibrium optimization control based regulation of dc bus voltage," *Electric Power Systems Research*, vol. 226, p. 109911, 2024.

[133] E. Akbari and A. Z. G. Seyyedi, "Power quality enhancement of distribution grid using a photovoltaic based hybrid active power filter with three level converter," *Energy Reports*, vol. 9, pp. 5432–5448, 2023.

[134] R. Boopathi and V. Indragandhi, "Solar photovoltaic-interfaced shunt active power filter implementation for power quality enhancement in grid-connected systems," *International Journal of Circuit Theory and Applications*, vol. 51, no. 11, pp. 5305–5323, 2023.

[135] P. Ray, P. K. Ray, and S. K. Dash, "Power quality enhancement and power flow analysis of a pv integrated upqc system in a distribution network," *IEEE Transactions on Industry Applications*, vol. 58, no. 1, pp. 201–211, 2021.

[136] N. Babu, J. M. Guerrero, P. Siano, R. Peesapati, and G. Panda, "A novel modified control scheme in grid-tied photovoltaic system for power quality enhancement," *IEEE Transactions on Industrial Electronics*, vol. 68, no. 11, pp. 11 100–11 110, 2020.

[137] M. Badoni, A. Singh, A. K. Singh, H. Saxena, and R. Kumar, "Grid tied solar pv system with power quality enhancement using adaptive generalized maximum versoria criterion," *CSEE Journal of Power and Energy Systems*, vol. 9, no. 2, pp. 722–732, 2021.

[138] R. B. Peesapati and G. Panda, "An optimal current control scheme in grid-tied hybrid energy system with active power filter for harmonic mitigation." *International Transactions on Electrical Energy Systems*, vol. 30, no. 3, 2020.

[139] V. Jain and B. Singh, "A multiple improved notch filter-based control for a single-stage pv system tied to a weak grid," *IEEE Transactions on Sustainable Energy*, vol. 10, no. 1, pp. 238–247, 2018.

[140] F. U. Nazir, N. Kumar, B. C. Pal, B. Singh, and B. K. Panigrahi, "Enhanced sogi controller for weak grid integrated solar pv system," *IEEE Transactions on Energy Conversion*, vol. 35, no. 3, pp. 1208–1217, 2020.

[141] P. Verma, R. Garg, and P. Mahajan, "Smooth lms-based adaptive control of spv system tied to grid for enhanced power quality," *IET Power Electronics*, vol. 13, no. 15, pp. 3456–3466, 2020.

[142] A. Kumar, R. Garg, and P. Mahajan, "Control of grid integrated photovoltaic system using new variable step size least mean square adaptive filter," *Electrical Engineering*, vol. 103, no. 6, pp. 2945–2959, 2021.

[143] M. Badoni, A. Singh, B. Singh, and H. Saxena, "Real-time implementation of active shunt compensator with adaptive srlmmn control technique for power quality improvement in the distribution system," *IET Generation, Transmission & Distribution*, vol. 14, no. 8, pp. 1598–1606, 2020.

[144] B. Singh and V. Jain, "Tocf based control for optimum operation of a grid tied solar pv system," *IEEE Transactions on Energy Conversion*, vol. 35, no. 3, pp. 1171–1181, 2020.

[145] S. B. Q. Naqvi, S. Kumar, and B. Singh, "Three-phase four-wire pv system for grid interconnection at weak grid conditions," *IEEE Transactions on Industry Applications*, vol. 56, no. 6, pp. 7077–7087, 2020.

[146] V. Yadav, S. Kewat, B. Singh, and A. Verma, "Control and implementation of multifunctional microgrid with seamless synchronization capability," *Energy Conversion and Economics*, vol. 2, no. 3, pp. 157–168, 2021.

[147] B. Singh, N. Kumar, and B. K. Panigrahi, "Steepest descent laplacian regression based neural network approach for optimal operation of grid supportive solar pv generation," *IEEE Transactions on Circuits and Systems II: Express Briefs*, vol. 68, no. 6, pp. 1947–1951, 2020.

[148] E. I. Batzelis and S. A. Papathanassiou, "A method for the analytical extraction of the single-diode pv model parameters," *IEEE Transactions on Sustainable Energy*, vol. 7, no. 2, pp. 504–512, 2015.

[149] H. K. Mehta, H. Warke, K. Kukadiya, and A. K. Panchal, "Accurate expressions for single-diode-model solar cell parameterization," *IEEE Journal of Photovoltaics*, vol. 9, no. 3, pp. 803–810, 2019.

[150] H. Sharadga, S. Hajimirza, and E. P. Cari, "A fast and accurate single-diode model for photovoltaic design," *IEEE Journal of Emerging and Selected Topics in Power Electronics*, vol. 9, no. 3, pp. 3030–3043, 2020.

[151] H. S. Sahu, S. K. Nayak, and S. Mishra, "Maximizing the power generation of a partially shaded pv array," *IEEE journal of emerging and selected topics in power electronics*, vol. 4, no. 2, pp. 626–637, 2015.

[152] D. S. Pillai, J. P. Ram, M. S. S. Nihanth, and N. Rajasekar, "A simple, sensorless and fixed reconfiguration scheme for maximum power enhancement in pv systems," *Energy conversion and management*, vol. 172, pp. 402–417, 2018.

[153] D. S. Pillai, J. P. Ram, V. Shabunko, and Y.-J. Kim, "A new shade dispersion technique compatible for symmetrical and unsymmetrical photovoltaic (pv) arrays," *Energy*, vol. 225, p. 120241, 2021.

[154] B. Subudhi and R. Pradhan, "A comparative study on maximum power point tracking techniques for photovoltaic power systems," *IEEE transactions on Sustainable Energy*, vol. 4, no. 1, pp. 89–98, 2012.

[155] R. B. Bollipo, S. Mikkili, and P. K. Bonthagorla, "Hybrid, optimal, intelligent and classical pv mppt techniques: A review," *CSEE Journal of Power and Energy Systems*, vol. 7, no. 1, pp. 9–33, 2020.

[156] M. Abdusalam, P. Poure, S. Karimi, and S. Saadate, "New digital reference current generation for shunt active power filter under distorted voltage conditions," *Electric Power Systems Research*, vol. 79, no. 5, pp. 759–765, 2009.

[157] P. Chittora, A. Singh, and M. Singh, "Application of self tuning filter for power quality improvement in three-phase-three-wire distorted grid system," in *2017 7th International Conference on Power Systems (ICPS)*. IEEE, 2017, pp. 313–318.

List of Publications

Papers in Refereed Journals

[1] **Ranjeet Singh**, Vinod Kumar Yadav, and Madhusudan Singh. An Improved Hot Spot Mitigation Approach for Photovoltaic Modules Under Mismatch Conditions. *IEEE Transactions on Industrial Electronics*, 71(5): 4840-4850, 2023. doi:10.1109/TIE.2023.3281684.

[2] **Ranjeet Singh**, Vinod Kumar Yadav, and Madhusudan Singh. Optimal Shade Dispersion Strategy for Enhanced PV Power Extraction Under PSCs. *IEEE Transactions on Power Electronics*, 38(11): 14665-14674, 2023. doi:10.1109/TPEL.2023.3307813.

[3] **Ranjeet Singh**, Vinod Kumar Yadav, and Madhusudan Singh. A Comprehensive Shade Resilient Approach for Enhanced PV Array Performance Under Irradiance Mismatch Conditions. *IEEE Journal of Photovoltaics*, 14(3): 549-556, 2024. doi:10.1109/JPHOTOV.2024.3374069.

[4] **Ranjeet Singh**, Vinod Kumar Yadav, and Madhusudan Singh. Performance Enhancement of a Novel Reduced Cross-Tied PV Arrangement Under Irradiance Mismatch Scenarios. *Applied Energy*, 376(A): 124185, 2024. doi:https://doi.org/10.1016/j.apenergy.2024.124185.

[5] Vinod Kumar Yadav, Anwesh Devratna Behera, **Ranjeet Singh**, Anubhav Maheshwari, Santosh Ghosh, and Abhijeet Prakash. A novel PV array reconfiguration technique based on circular array data structure. *Energy*, 283: 128505, 2023. doi:https://doi.org/10.1016/j.energy.2023.128505.

[6] Vinod Kumar Yadav, Ranjana Yadav, **Ranjeet Singh**, Ish Mishra, Isha Ganvir, and Manish. Reconfiguration of PV array through recursive addition approach for optimal power extraction under PSC. *Energy*

Conversion and Management, 292: 117412, 2023. doi:https://doi.org/10.1016/j.enconman.2023.117412.

[7] Shivam Kushwaha, **Ranjeet Singh**, Ranjana Yadav, Vinod Kumar Yadav, Tanmay, and Shivam Singh. Reconfiguration of PV array for improved performance under different partial shading conditions using Roulette Barrel Shifter approach. *Energy Conversion and Management*, 322: 119151, 2024. https://doi.org/10.1016/j.enconman.2024.119151.

[8] Viraj Jain, **Ranjeet Singh**, Ranjana Yadav, Vinod Kumar Yadav, Vikas, and Shlok Garg. Multi Step Optimization for Reconfiguration of Solar PV Array for Optimal Shade Dispersion. *Electrical Engineering*, 1-37, 2024. https://link.springer.com/article/10.1007/s00202-024-02840-8.

National and International Conference Proceedings

[1] **Ranjeet Singh**, Vinod Kumar Yadav, and Madhusudan Singh. Design and Performance Evaluation of Three-Phase Grid-Tied Solar Power Generation System Using STF based Algorithm. In *2023 International Conference on Power, Instrumentation, Energy and Control (PIECON)*, pages 1-6, 2023. doi:10.1109/PIECON56912.2023.10085865 (***Best Paper Award***)

[2] **Ranjeet Singh**, Vinod Kumar Yadav, and Madhusudan Singh. Optimizing the Shade-Tolerant Performance in a Mismatched PV Array Using Cross-Diagonal Module Rearrangement Approach. In *2024 IEEE Third International Conference on Power Electronics, Intelligent Control and Energy Systems (ICPEICES)*, pages 621-626, 2024. doi:10.1109/ICPEICES62430.2024.10719147.